


Summer 1-1-2017

# Rationalizing the Band Gap Tunability of Semiconductors via Electronic Structure Calculations

Matthew N. Srnec  
*Duquesne University*

Follow this and additional works at: <https://dsc.duq.edu/etd>

 Part of the [Materials Chemistry Commons](#), [Numerical Analysis and Scientific Computing Commons](#), and the [Physical Chemistry Commons](#)

---

## Recommended Citation

Srnec, M. N. (2017). Rationalizing the Band Gap Tunability of Semiconductors via Electronic Structure Calculations (Doctoral dissertation, Duquesne University). Retrieved from <https://dsc.duq.edu/etd/245>

This One-year Embargo is brought to you for free and open access by Duquesne Scholarship Collection. It has been accepted for inclusion in Electronic Theses and Dissertations by an authorized administrator of Duquesne Scholarship Collection. For more information, please contact [phillips@duq.edu](mailto:phillips@duq.edu).

RATIONALIZING THE BAND GAP TUNABILITY OF SEMICONDUCTORS  
VIA ELECTRONIC STRUCTURE CALCULATIONS

A Dissertation

Submitted to the Bayer School of Natural and Environmental Sciences

Duquesne University

In partial fulfillment of the requirements for  
the degree of Doctor of Philosophy

By

Matthew N. Srnec

August 2017

Copyright by  
Matthew N. Snec

2017

RATIONALIZING THE BAND GAP TUNABILITY OF SEMICONDUCTORS  
VIA ELECTRONIC STRUCTURE CALCULATIONS

By

Matthew N. Srnec

Approved June 29, 2017

---

Jeffrey D. Evanseck  
Professor of Chemistry & Biochemistry  
(Committee Chair)

---

M. Rita Mihailescu  
Professor of Chemistry & Biochemistry  
(Committee Member)

---

Jennifer A. Aitken  
Professor of Chemistry & Biochemistry  
(Committee Member)

---

Ralph A. Wheeler  
Chair and Professor, Department of  
Chemistry & Biochemistry  
Northern Illinois University  
(External Committee Member)

---

Philip P. Reeder  
Dean and Professor, Bayer School of  
Natural & Environmental Sciences

---

Ellen S. Gawalt  
Chair and Professor, Department of  
Chemistry & Biochemistry

# ABSTRACT

## RATIONALIZING THE BAND GAP TUNABILITY OF SEMICONDUCTORS VIA ELECTRONIC STRUCTURE CALCULATIONS

By

Matthew N. Srnec

August 2017

Dissertation supervised by Professor Jeffrey D. Evanseck.

The polymorphs of titanium dioxide and various diamond-like semiconductor materials are promising candidates in photovoltaic solar cell applications. Several of these polymorphs have been studied with experimental and computational methods, which often aim at tuning the electronic structure, particularly the band gap value of the crystalline solid. Prior studies report that the addition of a substituent into the structure of titanium dioxide decreases its band gap value, but the reasons for this are unknown. Possible explanations for the change in band gap involve the substituent atom's crystal radius, electronegativity, and ionization energy. Understanding the cause of these changes will provide great insight in designing new materials. The hypothesis of this work is that a substituent atom's crystal radius has a greater impact on the change in band gap of titanium dioxide than the substituent atom's electronegativity. In an aim to test this hypothesis, atoms of differing chemical properties were selected for substitution into the rutile and anatase polymorphs of titanium dioxide. The electronic structure (band structure and density of states) of the substituted

systems was calculated using the full-potential linearized-augmented plane wave approach of density functional theory in the WIEN2k software. Upon calculating the electronic structure, the relationships between the band gap value and various chemical properties were evaluated.

## DEDICATION

To my wife, Amanda; my son, Rush; my parents, Nick and Linda; and my sister, Sarah. I am so grateful for your unwavering support and love you all very much.

In addition, I would like to dedicate this work to my deceased research advisor, Dr. Jeffry D. Madura. You were an amazing example in the classroom and in your research. You will be forever missed.

## ACKNOWLEDGEMENT

I would like to acknowledge Duquesne University, the Bayer School of Natural and Environmental Sciences, the Department of Chemistry and Biochemistry, and the Center for Computational Sciences, all of which provided me the opportunity to conduct this research. A special thanks to Scott Boesch (Center for Computational Sciences) for his support in maintaining the computational resources utilized in this project. Scott has been a great friend, a tremendous help in my time at Duquesne, and continues to be a vital resource as I begin my academic career.

I would also like to acknowledge the National Science Foundation Award 1259941, allowing me to serve as the Department of Chemistry and Biochemistry's Science, Technology, Engineering, and Mathematics (STEM) fellow from 2013-2016. In addition, calculations in this work utilized the Extreme Science and Engineering Discovery Environment (XSEDE), which is supported by National Science Foundation grant number ACI-1548562.

Thank you to those at Duquesne University's Center for Teaching Excellence, for challenging me to critically reflect on my teaching strategies and to develop my teaching philosophy/portfolio. Participation in their Certificate and Advanced Certificate programs prepared me exceptionally well for my teaching career. I would also like to thank the Center for Teaching Excellence for selecting me as the 2016 recipient of Duquesne University's Graduate Student Award for Excellence in Teaching.

I would like to acknowledge the many undergraduate and graduate students that I worked alongside at Duquesne. In particular, a special thanks to Andrew Glaid for his assistance on this project. I am very lucky to have worked with you for three years and to have gained valuable mentoring experience as you completed your undergraduate honors thesis. Many thanks to all of the graduate students (Riley, Emily, Kendy, Mike, Shiv, Amanda, and Bernandie) in the Madura Research Group.



You were truly tremendous colleagues, but continue to be even better friends.

To my research committee: Jeffrey Evanseck, Jennifer Aitken, Rita Mihailescu, and Ralph Wheeler. Thank you very much for the many sacrifices you have made and for your constant support on this journey. Your feedback and discussions were an invaluable contribution to this work.

Last, I would like to thank my research advisor, Dr. Jeffrey D. Madura, who unexpectedly passed away March 14, 2017. Not a day goes by that I don't think about you and how much you are missed. Six years ago, you welcomed me into your group and trained me in a diverse computational chemistry skillset. In addition, you challenged me to think deeply about my project and the way I present and communicate my research. Most importantly, your contributions to my development as a teacher are innumerable and your friendship can never be replaced.

# TABLE OF CONTENTS

Abstract . . . . .	iv
Dedication . . . . .	vi
Acknowledgements . . . . .	vii
List of Tables . . . . .	xii
List of Figures . . . . .	xiii
List of Abbreviations . . . . .	xvii
Chapter 1 Background . . . . .	1
1.1 Motivation . . . . .	1
1.2 Photovoltaic Solar Cells . . . . .	4
1.3 Solids and their Electronic Structure . . . . .	11
1.4 Reciprocal Space . . . . .	15
1.5 Advances in Photovoltaics . . . . .	26
1.6 TiO <sub>2</sub> Literature Review . . . . .	27
1.7 Hypothesis and Specific Aims . . . . .	31
Chapter 2 Computational Methodology . . . . .	32
2.1 Computational Quantum Chemistry . . . . .	32
2.2 Solving Schrödinger's Equation with Python . . . . .	34
2.3 Density Functional Theory . . . . .	39
2.4 Exchange Correlation . . . . .	42
2.5 The modified Becke Johnson Potential . . . . .	44
2.6 FP-LAPW . . . . .	45
2.7 Self-Consistent Field . . . . .	46

2.8	Computational Resources and Workflow . . . . .	48
Chapter 3	Unsubstituted TiO <sub>2</sub> . . . . .	50
3.1	TiO <sub>2</sub> Polymorphs . . . . .	50
3.2	Computational Input Parameters . . . . .	51
3.3	Rutile Electronic Structure . . . . .	53
3.4	Anatase Electronic Structure . . . . .	58
3.5	Brookite Electronic Structure . . . . .	62
3.6	Unsubstituted Electronic Structure Summary . . . . .	65
Chapter 4	Substituted TiO <sub>2</sub> . . . . .	69
4.1	Modeling Supercells . . . . .	69
4.2	Impact of Substituent Position . . . . .	71
4.3	Impact of Substituent Percentage . . . . .	74
4.4	Electronic Structure of Substituted Rutile . . . . .	79
4.5	Electronic Structure of Substituted Anatase . . . . .	83
4.6	Substituent Properties and Changes in Band Gap . . . . .	88
Chapter 5	Electronic Structure of Diamond-like Semiconductors . . . . .	101
5.1	Electronic Structure of $\alpha$ - and $\beta$ - Cu <sub>2</sub> ZnSiS <sub>4</sub> . . . . .	101
5.2	Electronic Structure of the Cu <sub>2</sub> CdSnS <sub>4</sub> and $\alpha/\beta$ - Cu <sub>2</sub> ZnSiS <sub>4</sub> Diamond-like Semiconductors . . . . .	107
5.3	Electronic Structure of a Novel Diamond-like Semiconductor: Li <sub>2</sub> MnSnS <sub>4</sub> . . . . .	111
5.4	Electronic Structure of Mn-Substituted AgInSe <sub>2</sub> Chalcopyrite Semiconductors . . . . .	123
Chapter 6	Broader Impacts . . . . .	132

6.1 Revisiting the Thermodynamic Model from Goldstein et al. (1992) .	132
Chapter 7 Conclusions . . . . .	137
References . . . . .	140
Appendix 1 . . . . .	150
Appendix 2 . . . . .	158
Appendix 3 . . . . .	162
Appendix 4 . . . . .	174

## LIST OF TABLES

Table		Page
1.1	Crystal systems and their lattice parameters . . . . .	12
1.2	TiO <sub>2</sub> computational band gap values from the literature . . . . .	29
1.3	Experimental evidence of band gap narrowing in CuInS <sub>2</sub> . . . . .	30
3.1	Crystallographic information of TiO <sub>2</sub> polymorphs . . . . .	51
3.2	TiO <sub>2</sub> computational input parameters . . . . .	52
3.3	Computational band gap summary . . . . .	67
4.1	Substituents and their chemical properties . . . . .	70
4.2	Substituent position's effect on band gap . . . . .	72
4.3	Substituent % effect on band gap . . . . .	75
4.4	Melting point's effect on rutile's band gap . . . . .	89
4.5	Charge/crystal radius' effect on rutile's band gap . . . . .	90
4.6	Electronegativity's effect on rutile's band gap . . . . .	91
4.7	Crystal radius' effect on rutile's band gap . . . . .	92
4.8	Ionization energy's effect on rutile's band gap . . . . .	93
4.9	Melting point's effect on anatase's band gap . . . . .	94
4.10	Charge/crystal radius' effect on anatase's band gap . . . . .	95
4.11	Electronegativity's effect on anatase's band gap . . . . .	96
4.12	Crystal radius' effect on anatase's band gap . . . . .	97
4.13	Ionization energy's effect on anatase's band gap . . . . .	98
6.1	Cadmium sulfide thermodynamic model input values . . . . .	134
6.2	Melting point and surface tension of metal sulfides . . . . .	135

# LIST OF FIGURES

Figure		Page
1.1	World energy production and consumption . . . . .	1
1.2	CO <sub>2</sub> emissions . . . . .	2
1.3	Temperature anomalies . . . . .	3
1.4	p-type and n-type semiconductors . . . . .	5
1.5	Semiconductor diodes . . . . .	7
1.6	Forward bias in semiconductor diodes . . . . .	7
1.7	Solar cell schematic . . . . .	8
1.8	Equivalent circuit of a solar cell . . . . .	9
1.9	Band structure and density of states . . . . .	15
1.10	2D graphite . . . . .	18
1.11	Real space translation vectors from 30-60-90 right triangle . . . . .	18
1.12	From bulk sample to electronic structure . . . . .	25
2.1	Muffin tin radii approximation . . . . .	46
2.2	Sample SCF iteration . . . . .	47
3.1	Unit cells of TiO <sub>2</sub> polymorphs . . . . .	50
3.2	Rutile input parameter convergence . . . . .	54
3.3	Rutile energy convergence . . . . .	55
3.4	Rutile PBE-GGA electronic structure . . . . .	56
3.5	Rutile electronic structure from literature . . . . .	57
3.6	Rutile mBJ band structure . . . . .	58
3.7	Anatase input parameter convergence . . . . .	59
3.8	Anatase energy convergence . . . . .	59
3.9	Anatase PBE-GGA electronic structure . . . . .	60
3.10	Anatase electronic structure from literature . . . . .	61

3.11	Anatase mBJ band structure . . . . .	62
3.12	Brookite input parameter convergence . . . . .	63
3.13	Brookite energy convergence . . . . .	63
3.14	Brookite PBE-GGA electronic structure . . . . .	64
3.15	Brookite electronic structure from literature . . . . .	65
3.16	Brookite mBJ band structure . . . . .	66
4.1	Sulfur-substituted rutile energy convergence . . . . .	71
4.2	Rutile supercell and various substituent positions . . . . .	72
4.3	Sulfur-substituted rutile PBE-GGA electronic structure . . . . .	73
4.4	Sulfur-substituted rutile mBJ band structure . . . . .	74
4.5	Effect of substituent % on band gap . . . . .	75
4.6	4.2% sulfur-substituted rutile PBE-GGA electronic structure . . . . .	76
4.7	6.3% sulfur-substituted rutile PBE-GGA electronic structure . . . . .	77
4.8	8.3% sulfur-substituted rutile PBE-GGA electronic structure . . . . .	78
4.9	2.1 - 8.3% sulfur-substituted rutile mBJ band structures . . . . .	79
4.10	Fluorine-substituted rutile PBE-GGA electronic structure . . . . .	80
4.11	Nitrogen-substituted rutile PBE-GGA electronic structure . . . . .	81
4.12	Fluorine and nitrogen-substituted rutile mBJ band structures . . . . .	82
4.13	Sulfur-substituted anatase PBE-GGA electronic structure . . . . .	83
4.14	Fluorine-substituted anatase PBE-GGA electronic structure . . . . .	84
4.15	Nitrogen-substituted anatase PBE-GGA electronic structure . . . . .	85
4.16	Tellurium-substituted anatase PBE-GGA electronic structure . . . . .	86
4.17	Sulfur, fluorine, nitrogen, and tellurium-substituted anatase mBJ band structures . . . . .	87
4.18	Melting point's effect on rutile's band gap . . . . .	89
4.19	Charge/crystal radius' effect on rutile's band gap . . . . .	90
4.20	Electronegativity's effect on rutile's band gap . . . . .	91

4.21	Crystal radius' effect on rutile's band gap . . . . .	92
4.22	Ionization energy's effect on rutile's band gap . . . . .	93
4.23	Melting point's effect on anatase's band gap . . . . .	94
4.24	Charge/crystal radius' effect on anatase's band gap . . . . .	95
4.25	Electronegativity's effect on anatase's band gap . . . . .	96
4.26	Crystal radius' effect on anatase's band gap . . . . .	97
4.27	Ionization energy's effect on anatase's band gap . . . . .	98
5.1	$\alpha$ - and $\beta$ - $\text{Cu}_2\text{ZnSiS}_4$ polyhedral views . . . . .	102
5.2	$\alpha$ - and $\beta$ - $\text{Cu}_2\text{ZnSiS}_4$ band structure . . . . .	103
5.3	$\alpha$ - $\text{Cu}_2\text{ZnSiS}_4$ density of states . . . . .	104
5.4	$\beta$ - $\text{Cu}_2\text{ZnSiS}_4$ density of states . . . . .	105
5.5	$\alpha$ - and $\beta$ - $\text{Cu}_2\text{ZnSiS}_4$ band structure (zoomed view) . . . . .	106
5.6	3D DLS structures of $\text{Cu}_2\text{CdSnS}_4$ and $\alpha/\beta$ - $\text{Cu}_2\text{ZnSiS}_4$ . . . . .	108
5.7	$\text{Cu}_2\text{CdSnS}_4$ electronic structure . . . . .	110
5.8	$\alpha$ - $\text{Cu}_2\text{ZnSiS}_4$ electronic structure . . . . .	110
5.9	$\beta$ - $\text{Cu}_2\text{ZnSiS}_4$ electronic structure . . . . .	111
5.10	Polyhedral representations of $\alpha/\beta$ - $\text{Li}_2\text{MnSnS}_4$ . . . . .	112
5.11	Spin up/down band structures of $\alpha$ - $\text{Li}_2\text{MnSnS}_4$ . . . . .	114
5.12	Spin up/down band structures of $\beta$ - $\text{Li}_2\text{MnSnS}_4$ . . . . .	114
5.13	Spin up/down band structures of $\gamma$ - $\text{Li}_2\text{MnSnS}_4$ . . . . .	115
5.14	$\alpha$ - $\text{Li}_2\text{MnSnS}_4$ spin up density of states . . . . .	118
5.15	$\alpha$ - $\text{Li}_2\text{MnSnS}_4$ spin down density of states . . . . .	119
5.16	$\beta$ - $\text{Li}_2\text{MnSnS}_4$ spin up density of states . . . . .	120
5.17	$\beta$ - $\text{Li}_2\text{MnSnS}_4$ spin down density of states . . . . .	121
5.18	$\gamma$ - $\text{Li}_2\text{MnSnS}_4$ spin up density of states . . . . .	122
5.19	$\gamma$ - $\text{Li}_2\text{MnSnS}_4$ spin down density of states . . . . .	123
5.20	$\text{AgInSe}_2$ PBE-GGA electronic structure . . . . .	127



5.21	AgInSe <sub>2</sub> mBJ electronic structure . . . . .	127
5.22	Ag <sub>0.94</sub> Mn <sub>0.06</sub> InSe <sub>2</sub> spin up PBE-GGA electronic structure . . . . .	129
5.23	Ag <sub>0.94</sub> Mn <sub>0.06</sub> InSe <sub>2</sub> spin down PBE-GGA electronic structure . . . . .	129
5.24	Ag <sub>0.94</sub> Mn <sub>0.06</sub> InSe <sub>2</sub> spin up mBJ electronic structure . . . . .	130
5.25	Ag <sub>0.94</sub> Mn <sub>0.06</sub> InSe <sub>2</sub> spin down mBJ electronic structure . . . . .	130
5.26	Ag <sub>0.94</sub> Mn <sub>0.06</sub> InSe <sub>2</sub> spin up mBJ electronic structure with spin-orbit coupling . . . . .	131
5.27	Ag <sub>0.94</sub> Mn <sub>0.06</sub> InSe <sub>2</sub> spin down mBJ electronic structure with spin-orbit coupling . . . . .	131
6.1	Linear fit of melting point and surface tension for metal sulfides . . . . .	136
A2.1	IPython notebook 1 . . . . .	160
A2.2	IPython notebook 2 . . . . .	160
A3.1	Particle in an infinite potential well . . . . .	170
A3.2	Particle in a finite well . . . . .	171
A3.3	Particle in a double finite well (equal depth) . . . . .	171
A3.4	Particle in a double finite well (unequal depth) . . . . .	172
A3.5	Particle in a harmonic well . . . . .	172
A3.6	Particle in a Morse potential energy well . . . . .	173
A3.7	Kronig-Penney finite well . . . . .	173

## LIST OF ABBREVIATIONS

<b>au</b>	atomic units
<b>Bt</b>	billion tons
<b>CdS</b>	cadmium sulfide
<b>CO<sub>2</sub></b>	carbon dioxide
<b>CR</b>	crystal radius
<b>DFT</b>	density functional theory
<b>DLS</b>	diamond-like semiconductors
<b>DOS</b>	density of states
<b>E<sub>g</sub></b>	band gap
<b>eV</b>	electron volt
<b>FP-LAPW</b>	full-potential linearized-augmented plane wave
<b>GW</b>	Green function with screened coulombic term
<b>HSE</b>	Heyd, Scuseria, and Ernzerhof
<b>iBZ</b>	irreducible Brillouin zone
<b>IE</b>	ionization energy
<b>KS</b>	Kohn Sham
<b>LSDA</b>	local spin density approximation
<b>mBJ</b>	Tran Blaha modified Becke Johnson potential
<b>MP</b>	melting point
<b>PBE-GGA</b>	Perdew-Burke-Ernzerhof generalized gradient approximation
<b>PSC</b>	Pittsburgh Supercomputing Center
<b>PV</b>	photovoltaic
<b>RMT</b>	muffin-tin radius
<b>SCF</b>	self consistent field
<b>TiO<sub>2</sub></b>	titanium dioxide

**Ttoe** trillion tons of oil equivalent

**VASP** Vienna *ab initio* software package

**XC** exchange correlation

**XSEDE** Extreme Science and Engineering Discovery Environment

## Chapter 1. Background

### 1.1 Motivation

In materials science research, considerable effort is devoted to the design and engineering of newer and stronger materials for the construction of buildings, the paving of roads, the stability of bridges, and many other applications. However, another focus of today's materials science research is on the development of alternative energy materials, which are being introduced in response to our society's growing energy needs. In Figure 1.1, the total energy production (blue) and consumption (red) are plotted in units of trillion tons of oil equivalent (Ttoe) over the last 15 years.<sup>1</sup> Unquestionably, our society continues to use and produce more energy and, although our energy production has exceeded energy consumption in each of the last 15 years, many question whether we will be able to continue at this pace.

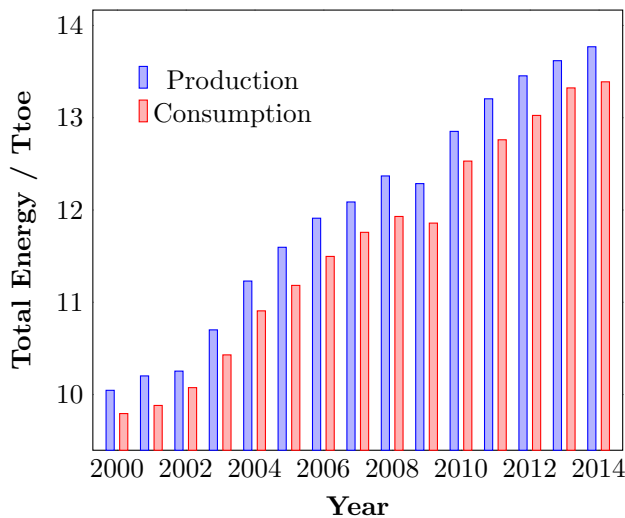


**Figure 1.1:** A plot of total energy production (blue) and consumption (red), in units of Ttoe, over the last 15 years. *Source:* adapted from: Enerdata. Total energy consumption. <https://yearbook.enerdata.net/> (accessed 05/31/2017).

In addition to concerns about our long-term energy production, there is also a concern for the effects of environmental pollution. As more energy is produced and consumed in the form of fossil fuels (petroleum, natural gas, and coal), significant amounts of carbon dioxide ( $\text{CO}_2$ ) are being released into the atmosphere. The  $\text{CO}_2$  emissions, in units of billion tons (Bt), over the last 25 years are plotted in Figure

1.2.<sup>1</sup> This data shows a marked increase in CO<sub>2</sub> emissions over the last 25 years with a pronounced increase over the same 15 year window that is depicted in Figure 1.1. While it is difficult to link the increased CO<sub>2</sub> emissions to the increase in total energy production and consumption, it is quite possible that these two are closely related.

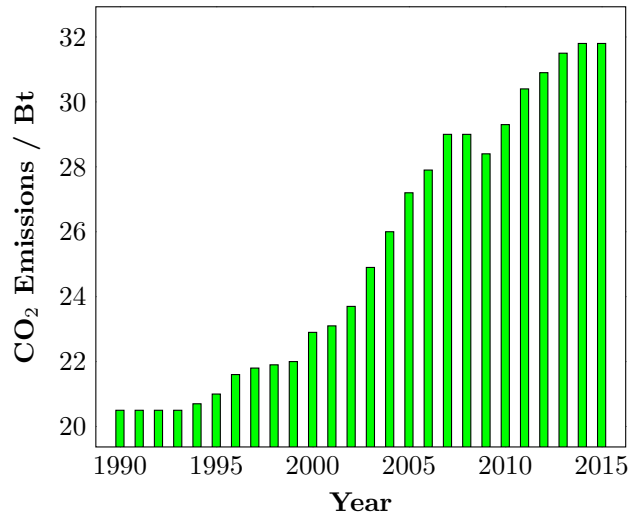


**Figure 1.2:** A plot of CO<sub>2</sub> emissions, in units of Bt, over the last 25 years. *Source:* adapted from: Enerdata. Total energy consumption. <https://yearbook.enerdata.net/> (accessed 05/31/2017).

Researchers have even gone a step further to investigate the impacts of greenhouse gases, e.g. CO<sub>2</sub>, on global climate change.<sup>2</sup> These greenhouse gases have an insulating effect on the planet. As electromagnetic radiation, in the form of ultraviolet and visible rays, strikes Earth’s surface, it loses energy and transitions to the infrared region of the electromagnetic spectrum. These infrared rays, i.e. heat, are reflected away from Earth’s surface, but no longer have sufficient energy to escape the atmosphere. As a result, they are trapped in the atmosphere by greenhouse gases and this buildup of heat warms the planet. Therefore, it is proposed that greater amounts of greenhouse gases in the atmosphere result in an increase to the average surface temperature of the planet. To examine this effect, Figure 1.3 plots the temperature anomaly in units of °C over the last 25 years.<sup>3</sup> In this study by NASA, the temperature anomalies reflect the change in global surface temperature relative to the 1951-1980 average temperature. In other words, the data plotted on the y-axis of Figure 1.3 are determined

by taking the average surface temperature for a particular year, subtracting it from the average surface temperature of the aforementioned 1951-1980 window, and then dividing by that 1951-1980 average surface temperature. NASA's records also trace

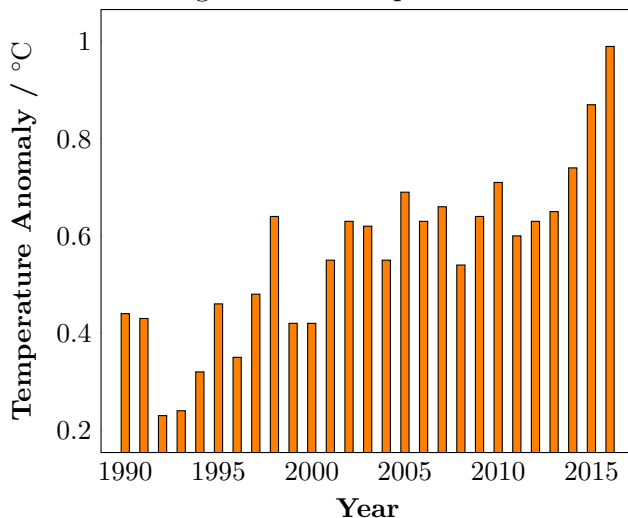


**Figure 1.3:** A plot of temperature anomalies, in units of °C, over the last 25 years. *Source:* adapted from: NASA. Global temperature. <https://climate.nasa.gov/vital-signs/global-temperature/> (accessed 05/31/2017).

this average surface temperature data back to 1880 and, over the last 136 years, 16 of the 17 warmest years have occurred since 2001. It is also important to note that 2016 ranks as the warmest year on record. With respect to global climate change, there are many additional factors to consider, such as the role of ocean currents on CO<sub>2</sub> concentration in the atmosphere and the impact of clouds on the heating and cooling of our planet. Directly linking global climate change to our society's increased energy consumption and production is an ongoing debate. However, there is no denying that energy demands are on the rise and changes in our planet's climate are occurring.

In order to address these challenges, scientists are investigating renewable energy resources, such as wind, geothermal, hydroelectric, thermoelectric, and solar power generation.<sup>4-10</sup> For instance, the Seebeck effect of thermoelectrics allows semiconductor materials to utilize a temperature gradient and generate electricity (i.e. converting waste heat into electrical energy). In photovoltaic (PV) devices, a semiconductor material absorbs photons of light from the sun and produces an electrical

current. However, in both thermoelectric and PV applications, the efficiency of the material is a significant limitation. Ultimately, this efficiency can be tied back to the material's composition and the electronic structure. With this in mind, scientists are searching for new compositions that show promise in these applications. In this project, computational methods are utilized to investigate the electronic structure of a well known PV composition, titanium dioxide ( $\text{TiO}_2$ ), in order to make connections to the physical properties of the material.

## 1.2 Photovoltaic Solar Cells

Each day, the sun emits roughly 10,000 times the energy that is needed on our planet, but a major challenge is capturing and storing that energy.<sup>9</sup> In PV solar cells, some of the best materials for capturing photons of light from the sun and converting them into electrical current are semiconductors. Semiconductors possess electrical conductivity that lies somewhere between that of an insulator and that of a conductor, with a band gap ( $E_g$ ) value between 0 and 4 electron volt (eV). Common semiconducting elements are silicon and germanium. However, for use in PV applications, the pure materials are altered by adding a small amount of impurity to change the conductive properties. For instance, in the top panel of Figure 1.4, an array of silicon atoms is depicted. In this case, silicon's four valence electrons are drawn around the silicon nuclei. Each valence electron participates with valence electrons from neighboring atoms to form bonds within the array. With each of these electrons participating in bonding, they are not free to move throughout the crystal, which results in silicon and germanium's poor electrical conductivity.

In order to improve this electrical conductivity, small amounts of impurities are introduced into the array. In Figure 1.4 (lower left), boron replaces a single silicon atom. Boron possesses three valence electrons and when placed on a silicon site, is only capable of forming three bonds with the valence electrons of neighboring atoms. Due to the absence of the 4th bond, a hole is created and this hole is free to move

about the crystal. With the presence of a positively charged hole in the silicon array, the neighboring electrons within the crystal can move to fill the hole, thus leaving behind another hole from the departure of that electron. In this case, the hole propagates through the material and since the mobile charge carrier is positively charged, materials engineered in this fashion are characterized as p-type semiconductors.<sup>11</sup>

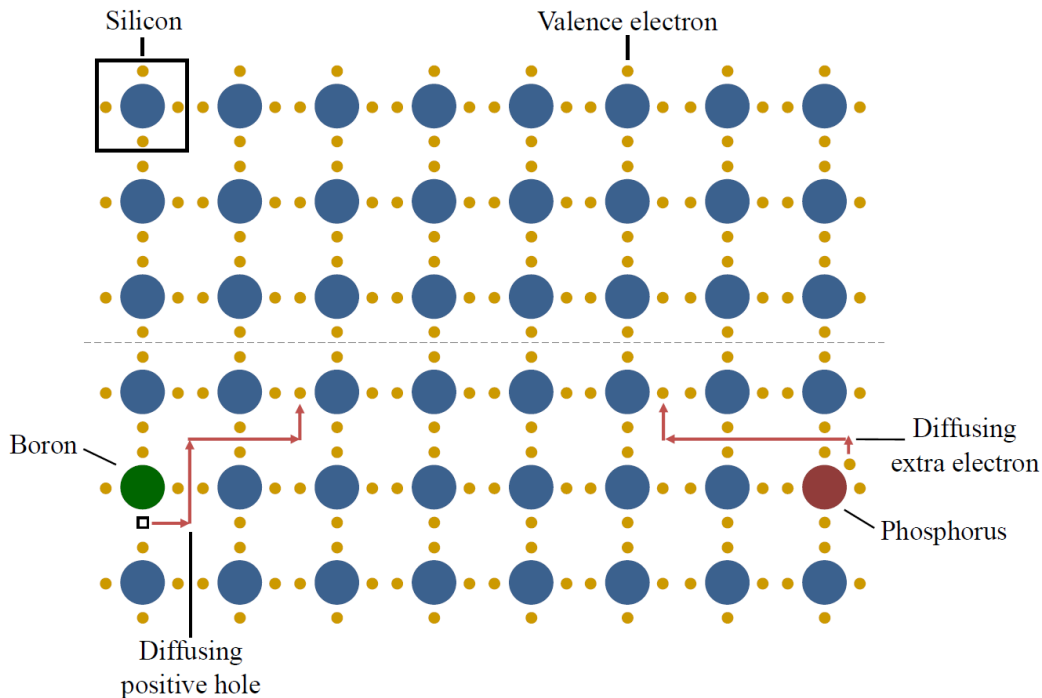


**Figure 1.4:** A pure silicon crystal is depicted in the top panel. Silicon can also be substituted with boron (green) and phosphorus (red) to produce p-type and n-type semiconductors, respectively. In this figure, electrons are displayed in yellow, silicon nuclei in blue, phosphorus nuclei in red, and boron nuclei in green. *Source:* adapted from: Cutnell, J.; Johnson, K. *Physics*, 9th; John Wiley and Sons: Hoboken, NJ, 2012.

In the opposite scenario, an atom with more valence electrons than silicon can be substituted into the array. In Figure 1.4 (lower right), a phosphorus atom has replaced a single silicon atom. In this case, only four of phosphorus' five valence electrons participate in bonding with the neighboring silicon atoms. The fifth, non-bonding valence electron is free to diffuse about the crystal in the same fashion as the positively charged hole in the p-type semiconductor. Since the mobile charge carrier in this scenario is the negatively charged, non-bonding electron, materials engineered



in this fashion are called n-type semiconductors. When multiple phosphorus atoms are substituted into the array, there is a pool of valence electrons that are free to wander about the material, allowing the semiconductor to conduct electricity.<sup>11</sup>

Combining the n-type and p-type semiconducting materials described previously gives rise to a semiconductor diode. Here, the p-type material in Figure 1.5 (top) is shown in red and is characterized by immobile negative charges and mobile positively charged holes. The n-type material in Figure 1.5 (top) is shown in blue and is characterized by immobile positive charges and mobile negatively charged electrons. At the junction between the p-type and n-type semiconductors, mobile electrons and holes combine to produce a negative charge layer within the p-type semiconductor and a positive charge layer within the n-type semiconductor. These charge layers result in a net electric field  $\vec{E}$  that is drawn from the positively charged layer in the n-type semiconductor to the negatively charged layer in the p-type semiconductor, as shown in Figure 1.5 (bottom).<sup>11</sup>

With a battery connected to the semiconductor diode, the junction is in a condition of forward bias when the negative terminal of the battery is connected to the n-type semiconductor and the positive terminal of the battery is connected to the p-type semiconductor. Junctions in forward bias possess a current in the circuit, as shown in Figure 1.6. Electrons in the n-type semiconductor move toward the junction because they are repelled by the negative terminal of the battery. In addition, the positive holes in the p-type semiconductor move toward the junction because they are repelled by the positive terminal of the battery. At the junction, the electrons and holes combine, but the negative terminal of the battery provides a new supply of electrons while the positive terminal provides additional holes by pulling electrons off of the p-type material. In this scenario, a continual flow of charge results and the current is maintained so long as the battery is charged.

If the negative terminal of the battery were connected to the p-type material

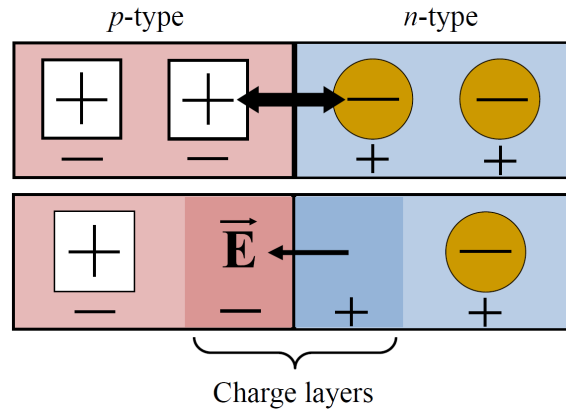


**Figure 1.5:** (top) p-type and n-type semiconductor materials are combined to form a semiconductor diode. (bottom) Mobile electrons and holes combine at the junction between these materials, creating positive and negative charge layers and an electric field  $\vec{E}$ . *Source:* adapted from: Cutnell, J.; Johnson, K. *Physics*, 9th; John Wiley and Sons: Hoboken, NJ, 2012.

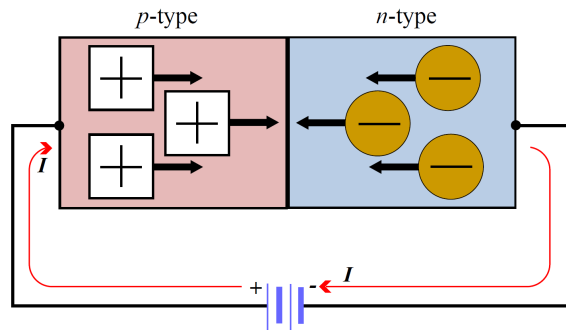


**Figure 1.6:** p-type and n-type semiconductor materials connected to a battery in a condition of forward bias, resulting in a continuous electrical current. *Source:* adapted from: Cutnell, J.; Johnson, K. *Physics*, 9th; John Wiley and Sons: Hoboken, NJ, 2012.

and the positive terminal of the battery were connected to the n-type material, the junction would be in a state of reverse bias. In a condition of reverse bias, the electrons are attracted to the positive terminal of the battery while the holes are attracted to the negative terminal of the battery. Since the holes and electrons are repelled from the junction, no current passes through the diode.<sup>11</sup>

Just as semiconductor diodes possess current when connected to a battery, solar cells convert sunlight directly into electricity via the same p-n junctions. Figure 1.7 shows a simple schematic of a solar cell formed by a p-n junction, where the p-type semiconductor surrounds the n-type semiconductor. As was seen in the semicon-

ductor diode of Figure 1.5, charge layers are formed in both the p-type and n-type semiconductors, giving rise to an electric field  $\vec{E}$  that is oriented from the n-type to the p-type material. The outer covering of the solar cell is made very thin such that photons of light from the sun can pass through, ionize some of the atoms, and cause electrons to be ejected.

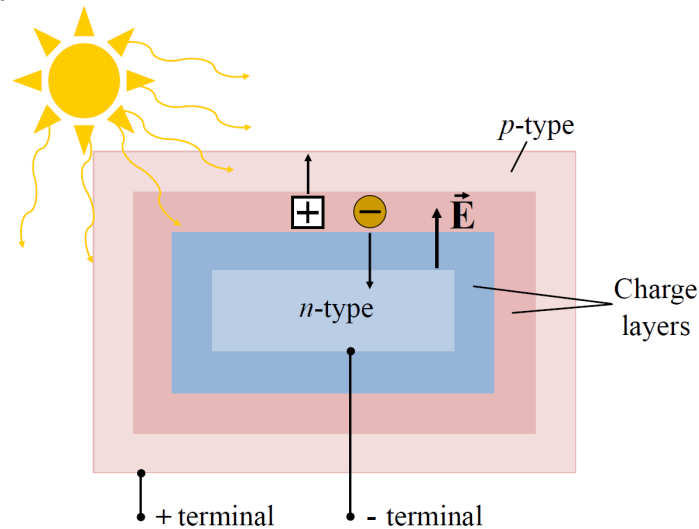


**Figure 1.7:** A schematic of a solar cell, comprised of a p-n semiconductor junction. *Source:* adapted from: Cutnell, J.; Johnson, K. *Physics*, 9th; John Wiley and Sons: Hoboken, NJ, 2012.

Once an electron is ejected, it leaves behind a positive hole, and due to the direction of  $\vec{E}$ , the hole and the ejected electron move away from the junction. However, the electron and the hole do not migrate in the same direction. The electron moves toward the n-type material because it possesses a positive charge layer at the junction while the hole moves toward the p-type material because it possesses a negative charge layer at the junction. Electrodes are also connected to the semiconducting material, such that the electrons and holes will travel through the material until they reach an electrode. As the electrons and holes accumulate at their respective electrodes, a potential is created in each region of localized charge. In order to cancel this potential, charge flows through the material and is harnessed into a usable amount of direct current. Since the current generated from a single solar cell is small, many of these cells are connected into larger panels, and these panels can also be connected

into larger modules, such as those frequently seen in commercial use. Connecting many solar panels in series allows additional current to be harnessed.

The major challenges that current PV research aims to address are improving the efficiency of the cells while also reducing the module production cost. This work focuses solely on the aspect of PV cell efficiency, in particular, the role of the material's electronic structure and  $E_g$  on this efficiency. The overall efficiency of a PV cell is a product of four individual efficiency terms: reflectance efficiency, thermodynamic efficiency, charge carrier separation efficiency, and conductive efficiency.<sup>12</sup> Each of these efficiencies contains many different parameters, which were taken into consideration when Shockley and Queisser proposed the maximum efficiency theoretical limit of 33.16% for p-n junction solar cells in 1961.<sup>12</sup> This theoretical limit correlates with a material's  $E_g$  in the range of 1.0-1.5 eV.<sup>12</sup> For further discussion on the electronic structure, see Section 1.3.

In order to examine the electronic properties of PV solar cells, a model of a solar cell is comprised of a current source in parallel with a diode. A shunt resistance and a series resistance are also added to the model, taking into account that no solar cell is ideal. The model solar cell's equivalent circuit is shown in Figure 1.8. The current

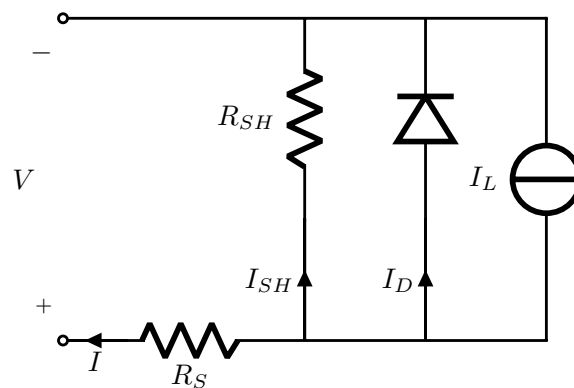


**Figure 1.8:** A model solar cell's equivalent circuit, comprising a current source in parallel with a diode along with shunt and series resistances, which are included to account for the non-ideal behavior of a practical solar cell. *Source:* adapted from: [https://commons.wikimedia.org/wiki/File:Solar\\_cell\\_equivalent\\_circuit.svg](https://commons.wikimedia.org/wiki/File:Solar_cell_equivalent_circuit.svg); prepared using the PSTricks package of L<sup>A</sup>T<sub>E</sub>X.

produced by the solar cell ( $I$ ) is equal to the current produced by the current source ( $I_L$ ) minus the current that passes through the diode ( $I_D$ ) minus the current passing through the shunt resistor ( $I_{SH}$ ). This is summarized in eq 1.1.

$$I = I_L - I_D - I_{SH} \quad (1.1)$$

The corresponding voltage across this circuit is defined as

$$V_j = V + IR_S \quad (1.2)$$

where  $V_j$  is the voltage (in volts) across both the diode and resistor ( $R_{SH}$ ),  $V$  is the voltage (in volts) across the output terminals,  $I$  is the output current (in amperes), and  $R_S$  is the series resistance (in Ohms,  $\Omega$ ). According to the Shockley diode relationship (eq 1.3), the current diverted through the diode is

$$I_D = I_O \left\{ \exp \left[ \frac{V_j}{nV_T} \right] - 1 \right\} \quad (1.3)$$

where  $I_O$  is the reverse saturation current (in amperes),  $n$  is the diode ideality factor (1 for an ideal diode),  $q$  is the elementary charge ( $1.602 \times 10^{-19}$  Coulomb),  $k$  is Boltzmann's constant ( $1.381 \times 10^{-23}$  J K<sup>-1</sup>),  $T$  is the absolute temperature (in Kelvin), and  $V_T = \frac{kT}{q}$  or the thermal voltage, which is  $\approx 0.0259$  V at 25 °C. According to Ohm's law, the current passing through the shunt resistor ( $I_{SH}$ ) is defined as

$$I_{SH} = \frac{V_j}{R_{SH}} \quad (1.4)$$

where  $R_{SH}$  is the shunt resistance. Substituting eqs 1.2, 1.3, and 1.4 into 1.1 relates the solar cell's parameters to the output current and voltage, which is ultimately known as the characteristic equation of a solar cell, shown in eq 1.5

$$I = I_L - I_O \left\{ \exp \left[ \frac{V + IR_S}{nV_T} \right] - 1 \right\} - \frac{V + IR_S}{R_{SH}} \quad (1.5)$$

Proceeding one step further, the reverse saturation current ( $I_O$ ) can be more explicitly written as

$$I_O = DT^3 \exp \left[ \frac{E_g}{kT} \right] \quad (1.6)$$

where  $D$  is the diode diffusion factor,  $T$  is the absolute temperature (in Kelvin),  $k$  is Boltzmann's constant, and  $E_g$  is the material's band gap. Upon examining the characteristic equation of a solar cell, in particular the reverse saturation current ( $I_O$ ), it is evident that the current produced by the PV solar cell is dependent on the  $E_g$  of the material. A larger  $E_g$  produces a larger reverse saturation current ( $I_O$ ), which results in a lower output current of the solar cell according to eq 1.5. It is here that Shockley and Queisser determined that  $E_g$  values in the range of 1.0-1.5 eV corresponded to maximum efficiency of the solar cell.<sup>12</sup>

### 1.3 Solids and their Electronic Structure

Before examining various materials for their PV applications, it is important to first establish the language used to describe their structure and atomic arrangement. The vast majority of PV materials are crystalline solids whose constituent atoms are arranged in an ordered three-dimensional pattern. These crystalline solids possess long-range order and their structure can be described using a collection of points. The individual atoms within the solid reside at these points, which are termed lattice points. The particular arrangement of individual lattice points defines the crystal. Within the larger crystal lattice, which contains all possible atomic points, a select group of points can be used to reproduce the entire lattice. This select group of points is known as the repeat unit or the unit cell. The unit cell is defined by the three axial lengths ( $a$ ,  $b$ , and  $c$ ) and the interaxial angles ( $\alpha$ ,  $\beta$ , and  $\gamma$ ).<sup>13</sup>

Based on the unit cell dimensions, seven unique crystal systems exist: cubic, tetragonal, orthorhombic, monoclinic, triclinic, trigonal, and hexagonal. These crystal systems (with corresponding lattice parameters) are summarized in Table 1.1. Depending on the crystal system, lattice points can reside at different locations. For example, a unit cell containing lattice points at only the corners is defined as primitive (P). A unit cell containing lattice points at each of its corners and its faces is defined as face-centered (F). A unit cell containing lattice points at each of its corners and

at its center is defined as body-centered (I). Last, the orthorhombic and monoclinic crystal systems have unit cells containing lattice points at each of their corners and on two of their six faces (top and bottom), which is defined as C-centered (C). However, each crystal system does not possess all of the previously mentioned lattice types. The combinations of crystal systems and lattice types are also summarized in the last column of Table 1.1, giving rise to the 14 Bravais lattices.<sup>13</sup>

Crystal System	Axial Lengths	Interaxial Angles	# of Lattices
Cubic	$a = b = c$	$\alpha = \beta = \gamma = 90^\circ$	3 (P, I, F)
Tetragonal	$a = b \neq c$	$\alpha = \beta = \gamma = 90^\circ$	2 (P, I)
Orthorhombic	$a \neq b \neq c$	$\alpha = \beta = \gamma = 90^\circ$	4 (P, I, F, C)
Monoclinic	$a \neq b \neq c$	$\alpha = \gamma = 90^\circ, \beta \neq 120^\circ$	2 (P, C)
Triclinic	$a \neq b \neq c$	$\alpha \neq \beta \neq \gamma \neq 90^\circ$	1 (P)
Trigonal	$a = b = c$	$\alpha = \beta = \gamma \neq 90^\circ, < 120^\circ$	1 (P)
Hexagonal	$a = b \neq c$	$\alpha = \beta = 90^\circ, \gamma = 120^\circ$	1 (P)

**Table 1.1:** Names of the seven crystal systems along with their corresponding unit cell axial lengths, interaxial angles, and the number of lattices that exist within each crystal system. The individual lattice types are primitive (P), body-centered (I), face-centered (F) and C-centered (C). *Source:* adapted from: Housecroft, C.; Sharpe, A. *Inorganic chemistry*, 3rd; Prentice Hall: Essex, England, 2008. Copyright 2008 Prentice Hall.

Taking into account the symmetry of the Bravais lattices gives rise to 32 point groups and 230 space groups. The space group contains all of the unique symmetry information and is often used to identify the solid. However, it is important to note that a single chemical composition can give rise to multiple solid structures with different space groups. These solid structures of identical chemical composition but differing 3D arrangement of the constituent atoms are known as polymorphs.<sup>13</sup> For example, in this project, three polymorphic forms of  $\text{TiO}_2$  are investigated. These polymorphic forms (rutile, anatase, and brookite) are introduced in Section 3.1

In order to computationally investigate the electronic structure of semiconducting materials, band structure and density of states (DOS) analyses are commonly used. However, in order to understand this electronic structure, it is useful to first consider some simple general chemistry principles. The chemist typically thinks about atoms

and their electrons, which are confined to atomic orbitals. When these atoms combine to form molecules or compounds, the atomic orbitals can overlap to form molecular orbitals if they are consistent in symmetry and of suitable energy. This allows the chemist to construct molecular orbital diagrams. However, in solids, the number of orbitals becomes so great that bands of orbitals begin to form.

Bands that are filled with electrons are known as valence bands while the bands devoid of electrons are known as the conduction bands. The difference in energy between the highest energy valence band and the lowest energy conduction band is defined as the  $E_g$  value. Based on the magnitude of this energy difference, materials can be classified as conductors, insulators, or semiconductors. Conductors, such as metals, are defined by a  $E_g = 0$  eV; metallic conductivity is the result of electrons moving through a partially filled band. Insulators are defined by a large  $E_g$ , which is responsible for their poor electrical conductivity. Semiconductors are characterized by a small  $E_g$ , which allows electrons to be excited from the valence band to the conduction band (provided sufficient incident energy). This excitation of an electron creates a hole in the valence band and a subsequent electron will move to fill this hole, leaving behind another hole. The process continues and the flow of electrons gives rise to electrical conductivity in these semiconducting materials.<sup>13</sup>

The electronic structure of a molecule or extended solid can be calculated using solid-state physics (plane waves) or orbitals. In this project, the physicist's plane wave approach is implemented and additional details are provided in Chapter 2. A solid-state physicist investigates the molecule or extended solid in the context of a band structure plot, such as Figure 1.9 (left). Band structures depict energy in eV on the y-axis and points of high symmetry in the irreducible Brillouin zone (iBZ) on the x-axis. These points of high symmetry are also known as k-points and will be discussed in detail in Section 1.4. For every molecular orbital, a band is generated in a band structure plot. Important characteristics of the band structure are the



band dispersion (a band's total range in energy) and the direction in which the band runs. Greater overlap of atomic orbitals results in a greater band dispersion and smaller  $E_g$ . Considering the directionality of the bands, the topology of the orbital overlap determines the way a band runs. Regions of a band that are highest in energy correspond to the most antibonding orientation of the orbitals while regions of a band that are lowest in energy correspond to the most bonding orientation of the orbitals.<sup>14</sup>

Another important characteristic for the properties of a material is whether the  $E_g$  is direct or indirect. In order to differentiate between the two, one must first focus on the highest energy valence band and the lowest energy conduction band, which define  $E_g$ . If the highest energy point of the valence band and the lowest energy point of the conduction band occur at the same k-point, the  $E_g$  is direct. If they exist at different k-points, the  $E_g$  is defined as indirect. A direct  $E_g$  infers that the momentum of electrons and holes is the same in both the valence and conduction bands and therefore, a photon can be directly emitted from an electron. With an indirect  $E_g$ , electrons pass through an intermediate state, transfer some of their momentum to the crystal lattice, and therefore, a photon cannot be emitted.

Furthermore, electronic structure calculations include density of states (DOS) analysis as in Figure 1.9 (right). Here, energy is depicted in eV on the y-axis and DOS on the x-axis. This density of states curve is obtained by integrating over the bands in the band structure plot and reflects the number of electronic states per unit volume, or in this case, per unit energy. Flatter regions of a band in a band structure plot correspond to a greater density of states while broader regions of a band correspond to lower density of states. Integrating over the DOS curve up to the Fermi level (reference point that separates empty and filled bands) determines the number of filled bands in the system and multiplying the number of filled bands by two determines the number of electrons in the system.<sup>14</sup> The total DOS can also be partitioned into partial DOS, reflecting which atoms and, more specifically, which

orbitals are contributing to particular regions of the band structure plot. This is extremely useful for tuning the electronic structure via structural substitutions. For instance, if the  $E_g$  is too wide, structural substitutions can be carried out to introduce states into the  $E_g$  region, decreasing its value.

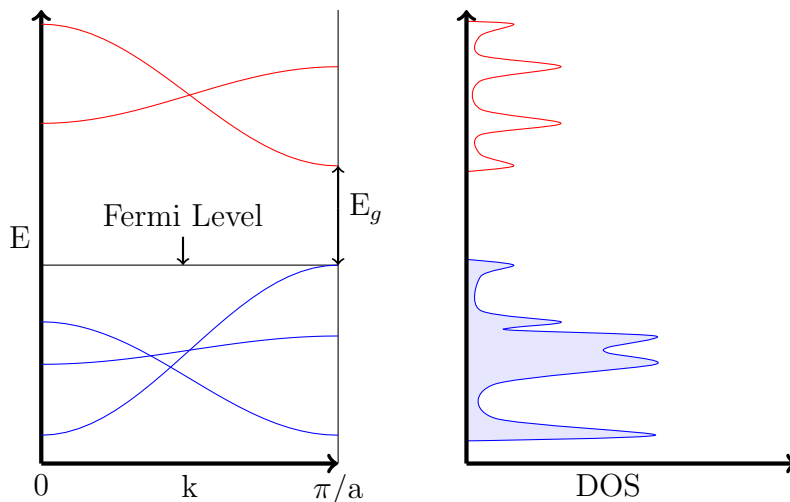


**Figure 1.9:** The electronic structure is comprised of the band structure (left) and DOS (right) analyses. The Fermi level is a reference point that separates the filled valence bands (blue) and the empty conduction bands (red). The energy difference between these two is defined as  $E_g$ . *Source:* adapted from: Hoffmann, R. How chemistry and physics meet in the solid state. *Angew. Chem. Int. Edit.* **1987**, *26*, 846–878; prepared using the PSTricks package of L<sup>A</sup>T<sub>E</sub>X.

## 1.4 Reciprocal Space

This section is partially adapted and reproduced (with permission) from the following manuscript: Srnec, M. et al. Teaching reciprocal space to undergraduates via theory and code components of an IPython notebook. *J. Chem. Educ.* **2016**, *93*, 2106–2109.

As discussed in Section 1.3, the band structure diagram depicts the energy of bands as a function of high symmetry k-points in the iBZ.<sup>16,17</sup> Understanding the meaning of these k-points requires knowledge of: reciprocal space, the mathematical relationship between real and reciprocal space vectors, and the role that these reciprocal space vectors play in determining the physical properties of solids. Several studies have focused on these topics in the literature, but none have mathematically shown the stepwise transformation of the vectors along with a computational tool for automating

the process.<sup>18-20</sup>

Electronic structure calculations have been carried out on a variety of compounds, ranging from simple systems to compositionally complex. To carry out such calculations, several software packages have been developed and utilized.<sup>21-23</sup> However, simple examples can be solved by hand to illustrate the important concepts. In a 1991 J. Chem. Educ. article, Pisanty et al. utilized the Hückel method to determine the band structure of graphite.<sup>24</sup> This provided an excellent example to consider the crystal structure and reciprocal lattice, set up the secular determinant and solve for the energy of the bands, and ultimately, interpret the results. However, the details necessary to make the conversion of real space vectors to reciprocal space vectors in the two-dimensional graphite example are lacking.

The absence of the mathematical details for this vector conversion in Pisanty et al.'s work reflects a larger void in the presentation of the reciprocal space topic to the scientific community. Oftentimes, textbooks and other educational tools in solid-state chemistry define the real space vectors and simply skip ahead to the final reciprocal space vectors, leaving the reader to wonder what mathematical "magic" took place in between. Furthermore, the inclusion of a rotational matrix in the two-dimensional case poses a challenge for readers. Pisanty et al. present such an example (graphite) and the mathematical details are omitted for simplification.<sup>24</sup> As a result, some instructors may choose to omit the topic of reciprocal space from their classroom discussions altogether due to a lack of proper tools for explaining the time consuming examples and abstract nature of the topic. However, with the vast amount of materials science and alternative energy research taking place, students will undoubtedly come across materials and their reciprocal lattices as they investigate electronic properties.

The discussion below and the tools made available on the web (<http://pubs.acs.org/doi/suppl/10.1021/acs.jchemed.6b00392>) aim at bridging the gap between the abstract mathematical nature of reciprocal space and its real world applications.<sup>15</sup>

Below, the work of Pisanty et al. is expanded upon, beginning with an on-paper two-dimensional example for graphite to gain an appreciation for the mathematical details behind the vector conversion. After working through this example, readers are encouraged to apply their knowledge in a Python program (available at <http://pubs.acs.org/doi/suppl/10.1021/acs.jchemed.6b00392>) that more quickly carries out the conversions. In addition, an IPython notebook is included so that instructors can seamlessly integrate the topic in their materials science or physical chemistry courses. The notebook simultaneously implements components of the theory and code, providing an efficient means of presenting the topic while also working examples in class. This hands-on experience will help build future solid-state chemists and bridge the gap between the topic's abstract nature and real world applications.

As previously mentioned, the work of Pisanty et al. provided the reciprocal space vectors for the two dimensional graphite case, however, much of the mathematical detail for this conversion was omitted. As a result, highlighted below is the detailed mathematical process for converting two real space translation vectors of graphite to the corresponding reciprocal space vectors. The two-dimensional graphite lattice (Figure 1.10) and its unit cell, defined by the  $\mathbf{a}$  and  $\mathbf{b}$  lattice parameters, is utilized to select the real space translation vectors. In this example, the real space translation vectors  $\mathbf{r}_1$  and  $\mathbf{r}_2$  are selected as depicted in Figure 1.11a.

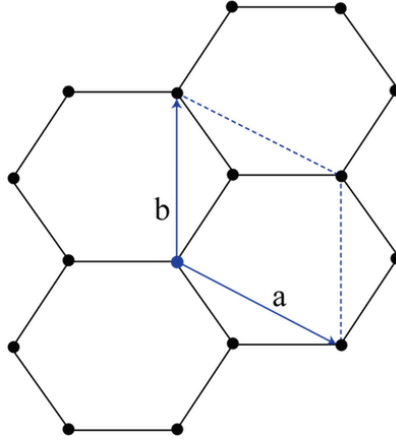


**Figure 1.10:** Two-dimensional representation of the graphite lattice with the hexagonal unit cell depicted in blue. The **a** and **b** lattice parameters define the unit cell. *Source:* prepared using Adobe Illustrator.

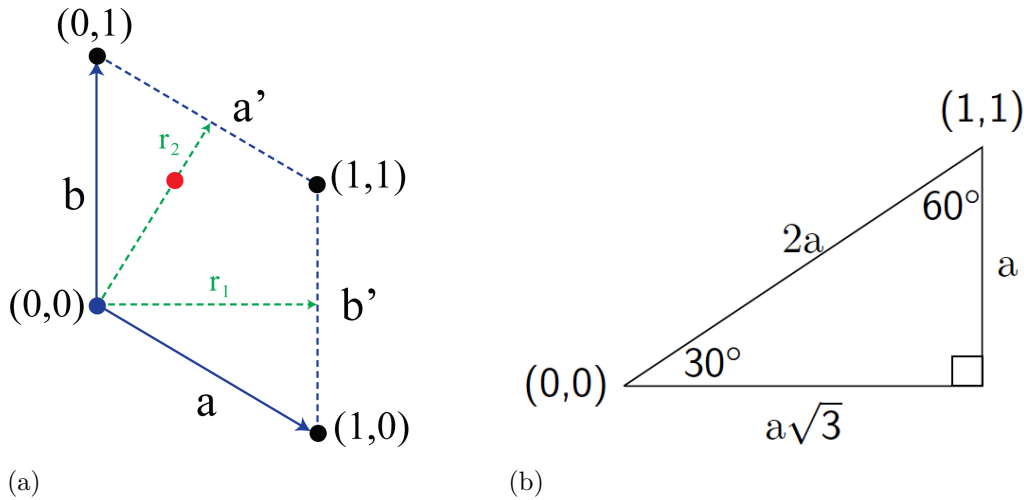


**Figure 1.11:** (a) The hexagonal unit cell of graphite with the real space translation vectors  $\mathbf{r}_1$  and  $\mathbf{r}_2$  (in green). (b) The conventional 30-60-90 right triangle with the corresponding crystal coordinates from the graphite unit cell included at the 30 and 60 degree angles. Visual inspection of the hexagonal unit cell of graphite indicates that it is composed of four 30-60-90 right triangles and these are utilized to determine the coordinates of the real space translation vectors  $\mathbf{r}_1$  and  $\mathbf{r}_2$ . *Source:* part (a) prepared using Adobe Illustrator and part (b) prepared using the PSTricks package of L<sup>A</sup>T<sub>E</sub>X.

The crystal coordinates are also provided in parentheses. For example, point (1,1) represents translating one unit in the x-direction of the unit cell and one unit in the y-direction of the unit cell. The coordinates, determined from the dimensions of a 30-60-90 right triangle (Figure 1.11b), of the real space translation vectors are provided in eq 1.7. There are many other real space translation vectors that could be selected,

but those provided in eq 1.7 are selected because of their similarity to the vectors used in Pisanty et al.'s paper.

$$\mathbf{r}_1 = a \left( \frac{\sqrt{3}}{2}, 0 \right); \quad \mathbf{r}_2 = a \left( \frac{1}{2}, \frac{\sqrt{3}}{2} \right) \quad (1.7)$$

The  $\mathbf{r}_1$  and  $\mathbf{r}_2$  real space translation vectors are then converted to reciprocal space vectors using the formulas provided in eq 1.8 for a two-dimensional system

$$\mathbf{k}_1 = \frac{2\pi\gamma\mathbf{r}_2}{\mathbf{r}_1^T\gamma\mathbf{r}_2}; \quad \mathbf{k}_2 = \frac{2\pi\gamma^T\mathbf{r}_1}{\mathbf{r}_1^T\gamma\mathbf{r}_2} \quad (1.8)$$

where  $\gamma$  is a clockwise ( $\theta = -90^\circ$ ) rotational matrix (eq 1.9) and superscript ‘‘T’’ indicates the transpose of the matrix.

$$\gamma = \begin{bmatrix} \cos \theta & -\sin \theta \\ \sin \theta & \cos \theta \end{bmatrix} = \begin{bmatrix} 0 & 1 \\ -1 & 0 \end{bmatrix} \quad (1.9)$$

Next, the  $\mathbf{k}_1$  and  $\mathbf{k}_2$  expressions are evaluated from eq 1.8. Beginning with the denominator of eq 1.8 for  $\mathbf{k}_1$  leads to eq 1.10.

$$\mathbf{r}_1^T\gamma\mathbf{r}_2 = \begin{bmatrix} \frac{a\sqrt{3}}{2} & 0 \end{bmatrix} \times \begin{bmatrix} \cos \theta & -\sin \theta \\ \sin \theta & \cos \theta \end{bmatrix} \times \begin{bmatrix} \frac{a}{2} \\ \frac{a\sqrt{3}}{2} \end{bmatrix} \quad (1.10)$$

Evaluating the product of the last two matrices in eq 1.10 gives rise to eq 1.11

$$\mathbf{r}_1^T\gamma\mathbf{r}_2 = \begin{bmatrix} \frac{a\sqrt{3}}{2} & 0 \end{bmatrix} \times \begin{bmatrix} 0 \left(\frac{a}{2}\right) + 1 \left(\frac{a\sqrt{3}}{2}\right) \\ -1 \left(\frac{a}{2}\right) + 0 \left(\frac{a\sqrt{3}}{2}\right) \end{bmatrix} \quad (1.11)$$

which is further simplified to eq 1.12

$$\mathbf{r}_1^T\gamma\mathbf{r}_2 = \begin{bmatrix} \frac{a\sqrt{3}}{2} & 0 \end{bmatrix} \times \begin{bmatrix} \frac{a\sqrt{3}}{2} \\ -\frac{a}{2} \end{bmatrix} \quad (1.12)$$

Finally, the product of the two remaining matrices in eq 1.12 is evaluated and simpli-

fied to give the final denominator expression for  $\mathbf{k}_1$  of eq 1.8. The result is provided in eq 1.13.

$$\mathbf{r}_1^T \gamma \mathbf{r}_2 = \frac{a\sqrt{3}}{2} \left( \frac{a\sqrt{3}}{2} \right) + 0 \left( -\frac{a}{2} \right) = \frac{3a^2}{4} \quad (1.13)$$

With the denominator expression determined, the full  $\mathbf{k}_1$  expression is now evaluated as shown in eq 1.14

$$\mathbf{k}_1 = \frac{2\pi \gamma \mathbf{r}_2}{\mathbf{r}_1^T \gamma \mathbf{r}_2} = \frac{2\pi \times \begin{bmatrix} 0 & 1 \\ -1 & 0 \end{bmatrix} \times \begin{bmatrix} \frac{a}{2} \\ \frac{a\sqrt{3}}{2} \end{bmatrix}}{\frac{3a^2}{4}} \quad (1.14)$$

Combining the denominator with the  $2\pi$  coefficient and evaluating the product of the two matrices in the numerator of eq 1.14 gives rise to eq 1.15

$$\mathbf{k}_1 = \frac{8\pi}{3a^2} \times \begin{bmatrix} 0 \left( \frac{a}{2} \right) + 1 \left( \frac{a\sqrt{3}}{2} \right) \\ -1 \left( \frac{a}{2} \right) + 0 \left( \frac{a\sqrt{3}}{2} \right) \end{bmatrix} \quad (1.15)$$

which is then simplified to give the resulting coordinates of the  $\mathbf{k}_1$  reciprocal space vector in eq 1.16.

$$\mathbf{k}_1 = \left( \frac{8\pi a\sqrt{3}}{3a^2}, \frac{-8\pi a}{3a^2} \right) = \left( \frac{4\pi\sqrt{3}}{3a}, \frac{-4\pi}{3a} \right) = \frac{2\pi}{a} \left( \frac{2\sqrt{3}}{3}, -\frac{2}{3} \right) \quad (1.16)$$

In comparing the  $\mathbf{k}_1$  and  $\mathbf{k}_2$  expressions from eq 1.8, it is apparent that the denominators are equivalent, which allows the  $\mathbf{k}_2$  reciprocal space vector to be evaluated in a similar fashion as above (eq 1.17).

$$\mathbf{k}_2 = \frac{2\pi \gamma^T \mathbf{r}_1}{\mathbf{r}_1^T \gamma \mathbf{r}_2} = \frac{2\pi \times \begin{bmatrix} 0 & -1 \\ 1 & 0 \end{bmatrix} \times \begin{bmatrix} \frac{a\sqrt{3}}{2} \\ 0 \end{bmatrix}}{\frac{3a^2}{4}} \quad (1.17)$$

Again, the denominator of eq 1.17 is combined with the  $2\pi$  coefficient in the numerator

and the product of the two remaining matrices gives rise to eq 1.18.

$$\mathbf{k}_2 = \frac{8\pi}{3a^2} \times \begin{bmatrix} 0 \left( \frac{a\sqrt{3}}{2} \right) + -1(0) \\ 1 \left( \frac{a\sqrt{3}}{2} \right) + 0(0) \end{bmatrix} \quad (1.18)$$

Eq 1.18 is then simplified to give the resulting coordinates of the  $\mathbf{k}_2$  reciprocal space vector, which are provided in eq 1.19.

$$\mathbf{k}_2 = \left( 0, \frac{8\pi a\sqrt{3}}{3a^2 2} \right) = \left( 0, \frac{4\pi\sqrt{3}}{3a} \right) = \frac{2\pi}{a} \left( 0, \frac{2\sqrt{3}}{3} \right) \quad (1.19)$$

Finally, the correct  $\mathbf{k}_1$  and  $\mathbf{k}_2$  expressions are confirmed by evaluating the dot products of the real and reciprocal space vectors, which must satisfy the relationships provided in eq 1.20.

$$\mathbf{r}_1 \cdot \mathbf{k}_1 = \mathbf{r}_2 \cdot \mathbf{k}_2 = 2\pi; \quad \mathbf{r}_1 \cdot \mathbf{k}_2 = \mathbf{r}_2 \cdot \mathbf{k}_1 = 0 \quad (1.20)$$

The dot product of  $\mathbf{r}_1$  and  $\mathbf{k}_1$  is evaluated in eq 1.21 - 1.23.

$$\mathbf{r}_1 \cdot \mathbf{k}_1 = \mathbf{r}_{1x}\mathbf{k}_{1x} + \mathbf{r}_{1y}\mathbf{k}_{1y} \quad (1.21)$$

$$\mathbf{r}_1 \cdot \mathbf{k}_1 = \left( \frac{a\sqrt{3}}{2} \right) \left( \frac{4\pi\sqrt{3}}{3a} \right) + (0 \cdot a) \left( -\frac{4\pi}{3a} \right) \quad (1.22)$$

$$\mathbf{r}_1 \cdot \mathbf{k}_1 = 2\pi + 0 = 2\pi \quad (1.23)$$

The dot product of  $\mathbf{r}_2$  and  $\mathbf{k}_2$  is evaluated in eq 1.24 - 1.26.

$$\mathbf{r}_2 \cdot \mathbf{k}_2 = \mathbf{r}_{2x}\mathbf{k}_{2x} + \mathbf{r}_{2y}\mathbf{k}_{2y} \quad (1.24)$$

$$\mathbf{r}_2 \cdot \mathbf{k}_2 = \left( \frac{a}{2} \right) \left( \frac{2\pi \cdot 0}{a} \right) + \left( \frac{a\sqrt{3}}{2} \right) \left( \frac{4\pi\sqrt{3}}{3a} \right) \quad (1.25)$$

$$\mathbf{r}_2 \cdot \mathbf{k}_2 = 0 + 2\pi = 2\pi \quad (1.26)$$

The dot product of  $\mathbf{r}_1$  and  $\mathbf{k}_2$  is evaluated in eq 1.27 - 1.29.

$$\mathbf{r}_1 \cdot \mathbf{k}_2 = \mathbf{r}_{1x}\mathbf{k}_{2x} + \mathbf{r}_{1y}\mathbf{k}_{2y} \quad (1.27)$$

$$\mathbf{r}_1 \cdot \mathbf{k}_2 = \left( \frac{a\sqrt{3}}{2} \right) \left( \frac{2\pi \cdot 0}{a} \right) + (0 \cdot a) \left( \frac{4\pi\sqrt{3}}{3a} \right) \quad (1.28)$$



$$\mathbf{r}_1 \cdot \mathbf{k}_2 = 0 + 0 = 0 \quad (1.29)$$

The dot product of  $\mathbf{r}_2$  and  $\mathbf{k}_1$  is evaluated in eq 1.30 - 1.32.

$$\mathbf{r}_2 \cdot \mathbf{k}_1 = r_{2x}k_{1x} + r_{2y}k_{1y} \quad (1.30)$$

$$\mathbf{r}_2 \cdot \mathbf{k}_1 = \left(\frac{a}{2}\right) \left(\frac{4\pi\sqrt{3}}{3a}\right) + \left(\frac{a\sqrt{3}}{2}\right) \left(\frac{-4\pi}{3a}\right) \quad (1.31)$$

$$\mathbf{r}_2 \cdot \mathbf{k}_1 = \frac{4\pi a\sqrt{3}}{6a} - \frac{4\pi a\sqrt{3}}{6a} = 0 \quad (1.32)$$

After working the above two-dimensional vector conversion by hand, readers are encouraged to revisit the secular determinant solution from Pisanty et al.'s work and then work an additional case for practice. For example, one can set up the necessary real space translation vectors for MoS<sub>2</sub> (molybdenum (IV) sulfide) and convert them to reciprocal space vectors. In working this problem, the following questions can be utilized to enhance understanding:

- What do **a** and **b** represent in Figure 1.10?
- What are the values of **a** and **b** for graphite? Use the scientific literature.
- What is the crystal system of graphite? What is the crystal system of MoS<sub>2</sub>?
- How does the crystal system of these two compounds govern the reciprocal space vector calculation setup and results?
- Briefly comment on how the reciprocal space vectors of MoS<sub>2</sub> differ from those of graphite (assume you selected the same real space vectors to begin).
- Use the IPython notebook or Reciprocal.py program available at <http://pubs.acs.org/doi/suppl/10.1021/acs.jchemed.6b00392> to verify your results.

For additional practice, other compounds, whose crystal systems are different than that of graphite and MoS<sub>2</sub>, can be independently selected. Here, readers begin by

setting up the unit cell, select real space translation vectors, and ultimately convert them to reciprocal space vectors. In a similar fashion as above, the Python program can be used to verify the results. The Reciprocal.py program is written in version 2.7 of the Python programming language.<sup>25</sup> This program runs on Windows, OS X, and Linux operating systems. For Python installation instructions, please refer to Appendix 1. Additionally, a pedagogical framework is provided in Appendix 2 for instructors who wish to implement this topic and the tools provided on the web (<http://pubs.acs.org/doi/suppl/10.1021/acs.jchemed.6b00392>) in their classrooms.

Although the two-dimensional graphite example lends itself well to understanding the mathematical process of reciprocal vector transformations, the bulk solids of interest for alternative energy applications are three-dimensional systems. However, the process for converting real space translation vectors to reciprocal space vectors for three-dimensional systems is more straightforward than the two-dimensional example discussed above. The corresponding formulas necessary to carry out this conversion in three dimensions are provided in eq 1.33.

$$\mathbf{k}_1 = \frac{2\pi\mathbf{r}_2 \times \mathbf{r}_3}{\mathbf{r}_1 \cdot (\mathbf{r}_2 \times \mathbf{r}_3)}; \quad \mathbf{k}_2 = \frac{2\pi\mathbf{r}_1 \times \mathbf{r}_3}{\mathbf{r}_2 \cdot (\mathbf{r}_1 \times \mathbf{r}_3)}; \quad \mathbf{k}_3 = \frac{2\pi\mathbf{r}_1 \times \mathbf{r}_2}{\mathbf{r}_3 \cdot (\mathbf{r}_1 \times \mathbf{r}_2)} \quad (1.33)$$

In the three-dimensional case, the dot products of the real and reciprocal space vectors must satisfy the conditions in eq 1.34.

$$\mathbf{r}_1 \cdot \mathbf{k}_1 = \mathbf{r}_2 \cdot \mathbf{k}_2 = \mathbf{r}_3 \cdot \mathbf{k}_3 = 2\pi; \quad \mathbf{r}_1 \cdot \mathbf{k}_2 = \mathbf{r}_2 \cdot \mathbf{k}_1 = \mathbf{r}_1 \cdot \mathbf{k}_3 = \mathbf{r}_3 \cdot \mathbf{k}_1 = \mathbf{r}_2 \cdot \mathbf{k}_3 = \mathbf{r}_3 \cdot \mathbf{k}_2 = 0 \quad (1.34)$$

As an exercise, the following real space translation vectors (eq 1.35) should be converted to reciprocal space vectors for a three-dimensional system and the correct reciprocal space vectors should be validated using the dot products in eq 1.34.

$$\mathbf{r}_1 = a(1, 0, 0); \quad \mathbf{r}_2 = a\left(\frac{1}{2}, \frac{\sqrt{3}}{2}, 0\right); \quad \mathbf{r}_3 = a(0, 0, 2) \quad (1.35)$$

Once calculated, the reciprocal space vectors can be used to construct the first Brillouin zone of a solid. Within the first Brillouin zone, a smaller volume element of

reciprocal space is defined as the iBZ. This iBZ can be translated symmetrically to reproduce the full Brillouin zone of the solid. Individual points, known as k-points, exist within the iBZ. The k-points lying on symmetry operators are known as the high-symmetry k-points or special k-points. These high symmetry k-points can then be substituted into the Bloch equations (see Section 2.3), which are solved to produce the band structure diagram. From the solid's band structure,  $E_g$  can be determined, which plays a significant role in the material's effectiveness in PV applications. Figure 1.12 shows this overall progression, beginning with a bulk sample, identifying the real space translation vectors from the material's unit cell, calculating the reciprocal space vectors from the real space translation vectors, constructing the Brillouin zone and iBZ, and then utilizing the high-symmetry k-points to solve the Bloch equations for the band structure and DOS.

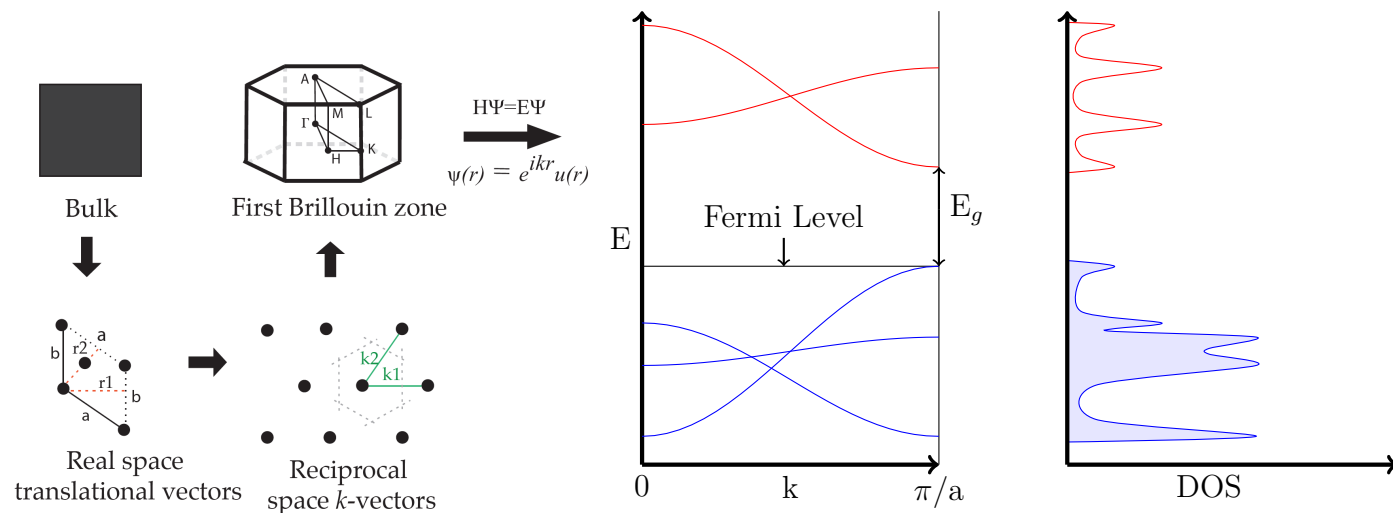


**Figure 1.12:** A progression from bulk solid to determining the real space translation vectors, calculating the corresponding reciprocal space vectors, constructing the Brillouin zone, and utilizing the iBZ's high symmetry  $k$ -points in solving the Bloch equations for the band structure and DOS. *Sources:* part (a) adapted from: Lee, J. *Computational materials science, an introduction*; CRC Press Taylor and Francis Group: Florida, 2012; prepared by Amanda Dumi using Adobe Illustrator. Part (b) adapted from: Hoffmann, R. How chemistry and physics meet in the solid state. *Angew. Chem. Int. Edit.* **1987**, *26*, 846–878; prepared using the PSTricks package of L<sup>A</sup>T<sub>E</sub>X.

## 1.5 Advances in Photovoltaics

In an aim to approach the Shockley Queisser limit discussed in Section 1.2, many studies have been carried out to identify materials with this ideal  $E_g$  range while also optimizing the other terms in the characteristic equation. One of the most popular materials utilized in solar cell applications is amorphous silicon thin-film technology, which allows for cell efficiencies in the range of 5-7% for double-junction designs and 8-10% for triple-junction designs.<sup>27</sup> A triple-junction amorphous silicon structure, prepared via the roll-to-roll continuous deposition process, achieved an efficiency of 13%.<sup>27</sup> Multi-crystalline silicon solar cells that are commercially available possess efficiencies in the range of 14-19%.<sup>28</sup> Lipiński et al. achieved an efficiency of 12% in a double-porous silicon layer formed by acid chemical etching on the top surface of multi-crystalline silicon.<sup>29</sup>

Several groups have investigated the use of cadmium telluride (CdTe) with efficiencies greater than 15% and cadmium sulfide (CdS), but face challenges in the sense that cadmium is highly toxic and tellurium supplies are limited.<sup>30,31</sup> Copper indium diselenide ( $\text{CuInSe}_2$ ) and copper indium gallium diselenide ( $\text{CuInGaSe}_2$  or CIGS) were also investigated for their PV applications due to their high optical absorption coefficients and electrical characteristics. Here, a high efficiency of 20% was achieved with the CIGS composition; however, the biggest concern with this candidate is the shortage of indium.<sup>32,33</sup> Aside from these compositions, several other materials have been investigated for PV applications: organic solar cells,<sup>34</sup> hybrid amorphous/crystalline silicon,<sup>35</sup> light absorbing dyes,<sup>36</sup> and carbon nanotubes.<sup>37</sup>

Although very expensive, gallium arsenide (GaAs) holds the world record for single-junction solar cell efficiency of 28.8%.<sup>38</sup> Building upon the GaAs work, Solar Junction (a San Jose-based solar company) set a new efficiency record of 44% with a multi-junction (triple) cell, consisting of GaAs, germanium, and gallium indium diphosphide ( $\text{GaInP}_2$ ).<sup>39</sup> While the efficiency achievements made in GaAs and multi-

junction solar cells are noteworthy, it is still important to point out that each contains a highly toxic component (arsenic) and the indium shortage also poses an issue in these systems.

For the reasons above, dye-sensitized solar cells have received considerable attention because they are less toxic, their constituents are not in shortage, and they can be made relatively cheap.<sup>36</sup> A major component of the dye-sensitized solar cells is  $\text{TiO}_2$ , whose  $E_g$  lies outside the ideal range for PV applications. However, numerous studies in the literature have proposed structural modifications to  $\text{TiO}_2$  that aim at tuning the electronic structure, particularly the  $E_g$  value, for improved PV efficiency. These studies are summarized in Section 1.6 and further understanding the structural substitutions is the primary focus of this work.

## 1.6 $\text{TiO}_2$ Literature Review

Considering the application of  $\text{TiO}_2$  in dye-sensitized solar cells, the electronic structure of this composition has been studied by a variety of experimental and computational techniques. In 2008, Reyes-Coronado et al. reported the phase-pure nanoparticle synthesis of rutile, anatase, and brookite polymorphs of  $\text{TiO}_2$ . In this study, amorphous titania was used as a starting material and was reacted with acetic acid, utilizing hydrothermal treatment at elevated temperatures, to produce anatase nanoparticles. Hydrochloric acid was used as a reactant to produce phase-pure rutile and brookite nanoparticles. The three polymorphs were characterized using X-ray diffraction and UV-visible reflectance spectroscopy. The UV-visible reflectance experiments indicated  $E_g$  values of 3.00, 3.21, and 3.13 eV for rutile, anatase, and brookite, respectively. In addition, the authors report *ab initio* band structure calculations with  $E_g$  values of 1.44, 1.68, and 1.86 eV for rutile, anatase, and brookite phases, respectively.<sup>40</sup>

The experimental  $E_g$  values of Reyes-Coronado et al. are supported by other studies in the literature. Pascual et al. and Amtout et al. each reported a  $E_g$  approx-

imately equal to 3.00 eV for the rutile polymorph via polarization-dependent absorption spectroscopy and photoluminescence spectroscopy, respectively.<sup>41,42</sup> Tang et al. reported a  $E_g$  approximately equal to 3.40 eV for the anatase polymorph via polarized optical transmission measurements.<sup>43</sup> For brookite, Mattsson and Österlund reported a  $E_g$  approximately equal to 3.30 eV via UV-visible reflectance spectroscopy.<sup>44</sup>

While the experimental  $E_g$  values in the literature are in relatively good agreement, computational studies indicate significant variability in the  $E_g$  calculation. For example, in the Reyes-Coronado work discussed previously, a significant  $E_g$  underestimation was apparent in their *ab initio* results. This underestimation is a result of the computational methods utilized and will be discussed in detail in Section 2.4. However, with the development of more accurate computational methods,  $E_g$  calculations have improved markedly. A summary of these computational results is provided below in Table 1.2. The work of Landmann et al. incorporates several methodologies within the Vienna *ab initio* software package (VASP), all of which are summarized in Table 1.2: density functional theory (DFT)/Perdew-Burke-Ernzerhof generalized gradient approximation (PBE-GGA), DFT/Heyd, Scuseria, and Ernzerhof (HSE), PBE-GGA/Green function with screened coulombic term (GW), and HSE/GW.<sup>45</sup> In addition, the results of Reyes-Coronado (discussed previously) are included, which utilized the DFT/PBE-GGA methodology of the SIESTA software package.<sup>40</sup> A study by Gong et al.,<sup>46</sup> utilized the DFT/PBE-GGA/Tran Blaha modified Becke Johnson potential (mBJ) methodology within VASP.<sup>22</sup> Last, the results of Tosoni et al. are also included,<sup>47</sup> utilizing the same methodology as Gong et al. but using the WIEN2k software (see Section 2.6) instead.<sup>21</sup>

From these studies, it is apparent that the HSE and GW methods slightly overestimate the  $E_g$  for all three polymorphs compared to the experimental results. Moreover, the standard DFT/PBE-GGA methodology implemented by Reyes-Coronado et al. significantly underestimates the  $E_g$ . Results utilizing the DFT/PBE-GGA/mBJ

Method	Rutile $E_g$ /eV	Anatase $E_g$ /eV	Brookite $E_g$ /eV
DFT/PBE-GGA <sup>40</sup>	1.44	1.68	1.86
DFT/PBE-GGA <sup>45</sup>	1.88	1.94	1.86
DFT/PBE-GGA/mBJ <sup>46</sup>	2.60	3.00	NA
DFT/PBE-GGA/mBJ <sup>47</sup>	2.60	3.00	2.90
DFT/HSE <sup>45</sup>	3.39	3.60	3.30
PBE-GGA/GW <sup>45</sup>	3.46	3.73	3.45
HSE/GW <sup>45</sup>	3.73	4.05	3.68

**Table 1.2:** A summary of computational studies investigating the electronic structure and  $E_g$  values for the rutile, anatase, and brookite polymorphs. Methods are summarized in the first column followed by the respective  $E_g$  values in subsequent columns. Method abbreviations are highlighted in the text. *Source:* references for each study are provided in the method column.

methodology agree well with the experimental results, especially for the anatase and brookite polymorphs. Considering the favorable results reported with this methodology, it was selected for the computations carried out in this work.

It is also important to point out that  $E_g$  values for the pure, unsubstituted polymorphs of  $\text{TiO}_2$  are significantly higher than the ideal range of 1.0-1.5 eV proposed by Queisser and Shockley for PV applications.<sup>12</sup> In an aim to address this, several studies in the literature have investigated the ability to tune the electronic structure of these polymorphs with the primary goal of narrowing the  $E_g$ . This tuning can be accomplished via transition metal substitution on the titanium sites in the lattice or via nonmetal substitution on the oxygen sites. For example, the work of Navas et al. reported  $E_g$  narrowing to 2.1 eV in copper-substituted anatase.<sup>48</sup> Khan et al. reported a sequential  $E_g$  narrowing with increasing vanadium concentration substituted on titanium sites.<sup>49</sup> The effects of chromium, iron, and vanadium substitutions in anatase were investigated via UV-visible reflectance spectroscopy and photoconductivity measurements.<sup>50</sup> In addition, the ferromagnetism of chromium, manganese, iron, cobalt, nickel, and copper-substituted rutile was investigated by Sangaletti et al., but the respective  $E_g$  values were not reported.<sup>51</sup>

A variety of nonmetal substitutions have also been carried out on the polymorphs of  $\text{TiO}_2$ . Muhich et al. reported an increase in photocatalytic activity for boron,



carbon, and nitrogen-substituted anatase.<sup>52</sup> In addition, Zheng et al. demonstrated  $E_g$  narrowing for sulfur, selenium, and tellurium-substituted anatase.<sup>53</sup> Wang et al. discovered  $E_g$  narrowing to 2.35 eV in carbon-substituted rutile.<sup>54</sup> Carbon, nitrogen, sulfur, and fluorine mono- and co-substituted anatase were investigated by Xi et al. and also confirmed  $E_g$  narrowing.<sup>55</sup> This  $E_g$  narrowing has also been experimentally demonstrated in  $\text{CuInS}_2$ , another PV application candidate that was discussed in Section 1.5. The results of this unpublished work from the Aitken research group are provided below in Table 1.3.<sup>56</sup> While many studies have demonstrated  $E_g$  narrowing, there is still a lack of understanding in the scientific community regarding the cause of this change. The work of Chen et al. suggests that the magnitude of the  $E_g$  change is dependent upon the ionization energy (IE) of the substituent element.<sup>57</sup> In 2015, Pan et al. studied scandium, yttrium, lanthanum, zirconium, hafnium, vanadium, niobium, and tantalum-substituted anatase, suggesting a linear relationship between the  $E_g$  and the substituent’s melting point (MP).<sup>58</sup> However, other chemical properties, such as the substituent’s electronegativity and crystal radius (CR) should also be considered. Due to the absence of this clear understanding of the causes of  $E_g$  change upon structural modification, this work sets out to further investigate which chemical properties had the greatest impact via the hypothesis and specific aims outlined in Section 1.7.

Structural Formula	$E_g$ / eV
$\text{CuInS}_2$	1.36
$\text{CuIn}_{(0.9875)}\text{Co}_{(0.0125)}\text{S}_2$	1.20
$\text{CuIn}_{(0.975)}\text{Co}_{(0.025)}\text{S}_2$	1.21
$\text{CuIn}_{(0.95)}\text{Co}_{(0.050)}\text{S}_2$	1.22
$\text{CuIn}_{(0.90)}\text{Co}_{(0.10)}\text{S}_2$	1.17
$\text{CuIn}_{(0.85)}\text{Co}_{(0.15)}\text{S}_2$	1.21
$\text{CuIn}_{(0.80)}\text{Co}_{(0.20)}\text{S}_2$	1.15

**Table 1.3:** The increase in cobalt concentration in the  $\text{CuInS}_2$  structure leads to a decrease in the material’s  $E_g$  value. The experimental study was a cationic substitution of indium with varying percentages of cobalt.

## 1.7 Hypothesis and Specific Aims

Based upon the previous studies in the literature (outlined in Section 1.6), the hypothesis of this project is:

*A substituent atom's crystal radius has a greater impact on the change in  $E_g$  of  $\text{TiO}_2$  than the substituent atom's electronegativity.*

In order to test this hypothesis, the following specific aims were constructed:

1. Determine the impact of computational input parameters on the  $E_g$  of  $\text{TiO}_2$  polymorphs to assure that  $E_g$  changes are a reflection of structural differences.
2. Calculate the electronic structure of **unsubstituted**  $\text{TiO}_2$  polymorphs and investigate the DOS to identify substitution possibilities.
3. Calculate the electronic structure of **substituted**  $\text{TiO}_2$  polymorphs, comparing these values to the parent composition.
4. Determine the relationship between the substituent's chemical properties and the  $E_g$  of **substituted**  $\text{TiO}_2$  polymorphs.

## Chapter 2. Computational Methodology

### 2.1 Computational Quantum Chemistry

Computational quantum chemistry is one way of investigating the electronic structure of solids. Using quantum mechanics, one can study how the world works at small scales. This atomic level understanding of materials gives insight to their physical properties, which is particularly useful for systems that are hard to study by experiment, or simply aiding to speed up experimental work. In quantum mechanics, Schrödinger's equation is written as

$$\hat{H}\psi = E\psi \quad (2.1)$$

where  $\hat{H}$  is the Hamiltonian operator,  $\psi$  is the eigenvector or wavefunction, and  $E$  is the eigenvalue or energy of the system.<sup>59</sup> This equation can be solved for the energy ( $E$ ), or the electronic wave function ( $\psi$ ) can be interpreted to produce many different spectra: electronic, vibrational, rotational, nuclear magnetic resonance, etc.

Some of quantum mechanics' simplest problems can be solved using numerical methods, such as the shooting or linear finite difference methods.<sup>60</sup> For example, Section 2.2 highlights several cases of utilizing a three-point finite-difference method for numerically solving various quantum mechanics problems in undergraduate physical chemistry. However, in many-electron systems, more complex computational methods are implemented, often running calculations on multi-processor computers. In this case, many different methods or flavors of quantum computations are available. Included are: various *ab initio* methods (Hartree-Fock, Møller Plesset, configuration interaction, coupled cluster, and Quantum Monte Carlo), semiempirical methods, as well as density functional theory methods.

In the Hartree-Fock (HF) method, electron electron repulsion (referred to as electronic correlation) is not taken into consideration, leading to energies that are always equal to or greater than the exact energy.<sup>61-63</sup> HF computations scale on the order of

$N^4$ , where the system size is defined relatively as  $N$ .<sup>61–64</sup> For example, if the number of electrons in the system is doubled, the calculation time increases  $2^4$  or 16 times per iteration. The other *ab initio* methods mentioned are considered post-Hartree-Fock methods. In the Møller-Plesset (MP) perturbation method, the Hartree-Fock method is improved upon by adding electron correlation via the Rayleigh-Schrödinger perturbation theory.<sup>63,65</sup> Second, third, and fourth order energy corrections are made in the MP2, MP3, and MP4 methods, which scale at  $N^4$  or  $N^5$ ,  $N^6$ , and  $N^7$ , respectively.<sup>63,65</sup> Configuration interaction (CI) methods approximate the electron correlation with a variational wavefunction, comprised of spin orbitals that make up a linear combination of configuration state functions.<sup>66</sup> CI methods scale in the range of  $N^6$ - $N^{10}$ .<sup>63</sup> Coupled cluster (CC) methods account for electron correlation by constructing multi-electron wavefunctions via the exponential cluster operator.<sup>67,68</sup> CC methods scale at  $N^6$ .<sup>63</sup> In addition to the above approaches, Quantum Monte Carlo methods are classified as *ab initio*, but they avoid Hartree-Fock’s variational overestimation. These methods evaluate integrals numerically via Monte Carlo integration, can be very time consuming, and their accuracy significantly depends on the many-body wavefunction initial guesses.<sup>63,69,70</sup> In cases where the full Hartree-Fock treatment is too expensive, semi-empirical methods are often utilized, obtaining some parameters from experimental data.<sup>71–74</sup>

Considering the complexity of the systems of interest in this project, extended solids, many of the post-Hartree-Fock methods described previously are unsuitable because of their scaling. However, DFT methods (as described in Section 2.3) pose several advantages when studying solids. These methods utilize functionals (a function of functions), thus the total energy of the system can be represented as a function of the electron density, which is a function of the electron positions.<sup>63</sup> DFT computations scale on the order of Hartree-Fock methods, which is an advantage compared to the post-Hartree-Fock methods, and electron correlation is included,

whereas it is absent in HF.<sup>63</sup> However, DFT computations lack dispersion effects and severely underestimated  $E_g$  values in the method's early stages, as evidenced in Table 1.2. With the recent development of several functionals, DFT calculations are now producing  $E_g$  results that compare well with experimental data. As a result, the DFT/PBE-GGA/mBJ methodology was selected for this work and is outlined in Sections 2.3-2.7.

## 2.2 Solving Schrödinger's Equation with Python

This section is partially adapted and reproduced (with permission) from the following manuscript: Srnec, M. et al. A python program for solving Schrödinger's equation in undergraduate physical chemistry. *J. Chem. Educ.* **2017**, *94*, 813–815.

In undergraduate physical chemistry, Schrödinger's equation is solved for a variety of cases. In doing so, the energies and wavefunctions of the system are interpreted to provide connections with the physical system being studied. Solving this equation by hand for a one-dimensional system is a manageable task, but becomes time-consuming once various changes are made to investigate the impact of those changes on the results. To address this challenge, numerical methods, such as the shooting and linear finite-difference methods, have been utilized to quickly solve Schrödinger's equation. Outlined below and made available at <http://pubs.acs.org/doi/suppl/10.1021/acs.jchemed.7b00003>, the Python programming environment and the three-point finite-difference numerical method are utilized to find the solutions and plot the results (wavefunctions or probability densities) for a particle in an infinite, finite, double finite, harmonic, Morse, and Kronig-Penney finite potential energy well. These tools are designed to educate undergraduates on the basic tools of computer programming, data analysis, and making connections between mathematical models and the physical systems they are associated with.

In quantum chemistry, Schrödinger's equation is written as shown in eq 2.1.<sup>59</sup> The Hamiltonian operator is comprised of kinetic and potential energy terms, where the

kinetic energy component contains the Laplacian operator. For many of the cases addressed in undergraduate physical chemistry, the form of the Laplacian operator is one dimensional in the  $x$  direction. By solving Schrödinger's equation, the energies and wavefunctions of the system can be interpreted by students to make connections with the physical system being studied. For example, the particle in a finite potential energy well can be used to represent an atom and its ionization potential.

In the *J. Chem Educ.* literature, various tools (BASIC, Mathematica, Mathcad, Microsoft Excel Spreadsheets, and Fortran with Java) have been utilized to find numerical solutions to the Schrödinger equation.<sup>76-84</sup> These have provided valuable contributions to chemical education, but are all limited in the number of cases and variables that students can investigate. For instance, Lang and Towns' use of Mathematica to visualize wavefunctions focused on the two-dimensional particle-in-a-box, harmonic oscillator, and particle on a sphere models. However, they did not address the double finite well, Morse potential, and Kronig-Penney cases. The Python program discussed below provides a single resource for students to utilize and investigate many cases (infinite, finite, double finite of equal depth, double finite of unequal depth, harmonic, Morse, and Kronig-Penney potentials) that they encounter in their physical chemistry curriculum.

The Schrödinger program is coded in Python,<sup>25</sup> a modern scientific coding language that is free to users, in order to provide a tool that science students will be familiar with if they are taking introductory programming courses as part of their undergraduate curriculum. High-resolution graphical output is also provided for data analysis and inclusion in written reports. Moreover, in hopes that others will incorporate this tool in their physical chemistry classrooms, several tools are made available to aid in accomplishing this. Most notably, the IPython notebook feature of the Python programming environment is utilized, providing a novel approach to teaching Schrödinger's equation in the physical chemistry classroom. Utilizing the IPython

notebooks, instructors have the ability to teach theory and code components from a single resource, rather than juggling lecture notes and a separate window for running their code. In addition, a pedagogical framework for utilizing the IPython notebooks in the classroom is provided below. An example assignment and pre-/post-assignment survey questions (see Appendix 4) are also provided to study the project's impact on student learning. Together, instructors' use of the IPython notebooks coupled with the students' use of the full Schrodinger.py program will allow undergraduates to numerically solve Schrödinger's equation and graphically visualize the wavefunctions and their energies.

The computer program is divided into three components: the main Python code (Schrodinger.py), a utilities program written in version 2.7 of the Python programming language (utils2.py), and a utilities program written in version 3.5 of Python (utils3.py). The utilities programs detect which version of Python a user is running and also contain various functions and subroutines that are called by the main Schrodinger.py code. The Schrodinger.py program runs on Windows, OS X, and Linux operating systems and the use of Anaconda is strongly advised. Instructors and students can find explicit installation instructions in Appendix 1. Comments are also provided to explain various aspects within the code.

In order to run the Schrodinger.py program, Windows users can open an Anaconda prompt, navigate to the directory where they have saved the program, and run the program using the command **python Schrodinger.py**. Likewise, OS X users would do the same, but run the program from the terminal window. In both the Anaconda prompt and terminal window, the program provides interactive feedback to the user, prompting various inputs. Users also have the option to save a high-resolution png graphic of their results from each case for inclusion in write-ups/reports.

After prompting the user for several inputs (length of potential energy well, depth of potential energy well, and distance between potential energy wells), the program

then utilizes a three-point finite-difference method,<sup>60</sup>

$$f''(x) \approx \frac{f(x+h) - 2f(x) + f(x-h)}{h^2} \quad (2.2)$$

to construct a matrix representation of the Laplacian differential operator. Here,  $h$  is some small number and represents a change in  $x$ . It is also important to note that the mass of the particle ( $m$ ) and  $\hbar$  are set equal to one in all cases for the sake of calculating energies in atomic units (au). With this in mind, users are also prompted to enter the length, distance between, and depth of potential energy wells in units of au, recalling that  $1 \text{ \AA} = 1.89 \text{ au}$ . Next, the Hamiltonian is calculated and SciPy's built-in "eigh" function is utilized to determine the eigenvectors (wavefunctions) and eigenvalues (energies). SciPy is a Python-based ecosystem of open-source-software for mathematics, science, and engineering.<sup>85</sup> The program then plots (see Appendix 3) the results for students to interpret and answer several fundamental questions in each case. It is also important to note that students and instructors have the option to plot wavefunctions or the probability density at the conclusion of each calculation.

To use these tools in the classroom, instructors should take advantage of the IPython notebooks provided for the six cases addressed in the Schrodinger.py program. These notebooks are located within the Python\_Files folder of the supporting information (<http://pubs.acs.org/doi/suppl/10.1021/acs.jchemed.7b00003>). The notebooks are named Case1-6.ipynb, where Case1 = infinite well, Case2 = finite well, Case3 = double finite well of equal depth, Case4 = double finite well of unequal depth, Case5 = harmonic well, Case6 = Morse well, Case7 = Kronig-Penney. Following the installation instructions document in Appendix 1, instructors are encouraged to open the IPython notebooks via Jupyter<sup>86</sup> on their Windows or OS X computer. The notebooks are divided into "Code" sections that run the corresponding Schrodinger.py program and "Markdown" sections where the instructor is capable of typing up their lecture notes for classroom presentation. Here, the theory/lecture components of the IPython notebooks have been left blank so that instructors can



customize these sections to their desired format. In order to do so, instructors simply click on a cell in their IPython notebook, then find the “Insert” tab at the top of their Jupyter window, and lastly, select insert cell above or below. It is important that instructors designate the new cell as “Markdown” format instead of “Code” before they begin populating their lecture content. For a brief guide on getting started with “Markdown” notation, users are encouraged to utilize the links provided at the end of Appendix 1. Due to the significant variability in syntax, each instructor is left to populate their own lecture content.

Once the IPython notebooks are complete, instructors can utilize them in their classroom as they would their normal lecture slides. This provides a novel approach to teaching Schrödinger’s equation in the physical chemistry classroom because it utilizes a single, clear resource for presenting theory and code content to students. Rather than alternating between lecture notes and another window for running their code, the IPython notebooks allow instructors to present the material in an organized fashion, ultimately allowing students to better focus on the content.

Accompanying the IPython notebooks are a pre-assignment survey (to be administered to students prior to beginning the assignment), an example assignment corresponding to the various cases included in the Schrodinger.py program, and a post-assignment survey (to be administered to students following completion of the assignment). These documents are available in Appendices 3/4 (and on the web) and should be utilized to evaluate the program’s impact on student learning. Instructors are encouraged to modify these three documents as they see fit.

In summary, this section presents a Python program for solving Schrödinger’s equation for a particle in an infinite, finite, double finite, harmonic, Morse, and Kronig-Penney finite potential energy well. The Schrodinger.py program provides students experience with the Python programming language and numerical approximations for solving differential equations. In addition, a novel approach to teaching

Schrödinger’s equation in undergraduate physical chemistry courses is introduced through the use of IPython notebooks. Using the provided assignment (Appendix 3), students then communicate their findings through a written report. All supporting information for this work is available at <http://pubs.acs.org/doi/suppl/10.1021/acs.jchemed.7b00003>.

### 2.3 Density Functional Theory

Today, DFT is one of physicists and chemists most popular methods for carrying out electronic structure calculations. The basis of DFT was formed in 1964 when Hohenberg and Kohn discovered that an electron gas’ ground state total energy, of density  $\rho$ , can be calculated exactly in the presence of an external potential ( $v_{\text{ext}}$ ) if the electron density is known.<sup>87</sup> The electron gas’ total ground state energy ( $E$ ) is defined as a unique functional of the density  $\rho$  and is shown below in eq 2.3

$$E \equiv E[\rho(\mathbf{r})] \quad (2.3)$$

This introduces the definition of a functional, which is a function of a function. DFT gained its name because the total energy  $E$  is a function of the electron density  $\rho$ , and that electron density is a function of the positions  $\mathbf{r}$  of the electrons. Assuming that a system (subjected to an external potential) possesses  $N$  electrons, its Hamiltonian  $\hat{H}$  can be written as

$$\hat{H} = \hat{T} + \hat{V}_{ee} + \sum_{i=1}^N v_{\text{ext}}(\mathbf{r}_i) \quad (2.4)$$

where  $\hat{T}$  is defined as the kinetic energy operator,  $\hat{V}_{ee}$  is the electron-electron interaction operator, and  $v_{\text{ext}}$  is the external potential, which is defined as the sum of all nucleus-electron interactions in the solid. Next, a universal function ( $f$ ) of the density is defined in such a way that it is independent of the system and external potential choice. This universal function is provided in eq 2.5, where  $\psi$  is the wavefunction of an occupied orbital

$$f[\rho] = \min_{|\psi|^2 \rightarrow \rho} \langle \psi | \hat{T} + \hat{V}_{ee} | \psi \rangle \quad (2.5)$$

The Hohenberg-Kohn theorems<sup>87</sup> state that the total energy  $E[\rho]$  is

$$E[\rho] = f[\rho] + \int v_{\text{ext}}(\mathbf{r})\rho(\mathbf{r})d\mathbf{r} \geq E_0 \quad (2.6)$$

where  $E_0$  is the electronic system's ground state total energy. The theorems also state the following equality, taking into account the ground state electron density,  $\rho_0(\mathbf{r})$ :

$$f[\rho_0] + \int v_{\text{ext}}(\mathbf{r})\rho_0(\mathbf{r})d\mathbf{r} = E_0 \quad (2.7)$$

By variationally minimizing the energy in eq 2.6, all the information about the system's ground state can be determined by simply knowing the external potential ( $v_{\text{ext}}$ ) and a functional ( $f[\rho]$ ). As opposed to the  $3N$  variables associated with the many-electron wavefunction, DFT possesses a significant advantage in dealing with the density ( $\rho$ ) of the system, which is a function of only three spatial variables. This reduction in spatial variables is responsible for the favorable scaling of DFT methods compared to the *ab initio* methods discussed at the end of Section 2.1. However, DFT only computes ground state properties and is incapable of studying excited states.

In order to apply the DFT method to solids, an appropriate expression for the functional  $f[\rho]$  must be established. This is provided in eq 2.8

$$f[\rho] = T_s[\rho] + E_H[\rho] + E_{XC}[\rho] \quad (2.8)$$

where  $T_s[\rho]$  is the kinetic energy of the electrons,  $E_H[\rho]$  is the Hartree classical Coulomb repulsion energy, and  $E_{XC}[\rho]$  is the exchange correlation energy. The Hartree energy can be evaluated via its corresponding potential

$$V_H(\mathbf{r}) = \frac{E_H[\rho(\mathbf{r})]}{\delta\rho(\mathbf{r})} = \frac{e^2}{2} \int \frac{\rho(\mathbf{r}')}{|\mathbf{r} - \mathbf{r}'|} d\mathbf{r}' \quad (2.9)$$

where  $e$  is the elementary charge of an electron. However, the kinetic energy and exchange correlation functionals in eq 2.8 are not exactly known. While some success has been achieved in the functional determination of the exchange correlation energy, the kinetic energy functional remains a formidable challenge. As a result, the Hohenberg-Kohn formulation of DFT is often impractical.

Shortly after the work of Hohenberg and Kohn, Kohn and Sham introduced the idea that the many-body quantum mechanical problem could be reduced to a set of equivalent one-electron equations.<sup>88</sup> These equations were then solved self-consistently. As a derivative of Hohenberg and Kohn's work, Kohn and Sham came up with a total energy functional expression (eq 2.10) for an external potential (for a set of doubly occupied orbitals,  $\psi_i$ ) acting on an electron gas.

$$E[\psi_i] = 2 \left[ \frac{\hbar^2}{2m_e} \right] \sum_i \int \psi_i \nabla^2 \psi_i d\mathbf{r} + E_H[\rho] + E_{XC}[\rho] + \int v_{\text{ext}} \rho(\mathbf{r}) d\mathbf{r} \quad (2.10)$$

Here,  $\hbar$  is reduced Planck's constant and  $m_e$  is the mass of an electron. This external potential still includes the kinetic, Hartree, and correlation energies that were introduced in eq 2.8, but now the kinetic energy functional is replaced by an exact analytical expression acting on the set of orbitals  $\psi_i$ . The Kohn Sham (KS) electron density is more explicitly written as

$$\rho(\mathbf{r}) = 2 \sum_i |\psi_i(\mathbf{r})|^2 \quad (2.11)$$

In addition, the external potential  $v_{\text{ext}}$  of a crystalline solid is equal to the nuclei electron interactions as defined in eq 2.12

$$v_{\text{ext}} \equiv V_{\text{ion}} \quad (2.12)$$

In order to determine the ground state total energy of the electronic system, the KS equations (2.13) are solved self-consistently to determine the set of orbitals  $\psi_i(\mathbf{r})$  that minimizes the KS energy functional in eq 2.10.

$$\left[ -\frac{\hbar^2}{2m_e} \nabla^2 + V_{\text{ion}}(\mathbf{r}) + V_H(\mathbf{r}) + V_{XC}(\mathbf{r}) \right] \psi_i(\mathbf{r}) = \varepsilon_i \psi_i(\mathbf{r}) \quad (2.13)$$

In eq 2.13,  $\varepsilon_i$  is the KS eigenvalue associated with state  $i$ ,  $V_H$  is the Hartree potential, which is defined in eq 2.14,

$$V_H(\mathbf{r}) = e^2 \int \frac{\rho(\mathbf{r}')}{|\mathbf{r} - \mathbf{r}'|} d^3\mathbf{r}' \quad (2.14)$$

$V_{\text{ion}}$  is the ionic potential describing the nuclei electron attraction, and  $V_{XC}$  is the

exchange correlation potential, which can be defined by its functional derivative as shown in eq 2.15

$$V_{XC}(\mathbf{r}) = \frac{\delta E_{XC}[\rho(\mathbf{r})]}{\delta \rho(\mathbf{r})} \quad (2.15)$$

Ultimately, the relationships derived by Kohn and Sham were a reformulation of the Hohenberg-Kohn problem, but instead mapped a many-electron system onto a system of noninteracting particles. These noninteracting particles experience an effective potential due to the neighboring electrons and the interactions between those electrons and the nuclei.

## 2.4 Exchange Correlation

As was introduced in eq 2.8,  $E_{XC}[\rho]$  is defined as the exchange correlation energy term. This term along with the kinetic energy functional are not precisely known, thus are subject to approximation. As defined by the Pauli exclusion principle, electrons with equivalent spins must occupy different quantum states due to the anti-symmetry of the wavefunction. The spatial separation of the two electrons gives rise to an “exchange” energy that lowers the total energy of the system. In addition, the electrons in the system are equivalently charged and repel one another, thus the movement of a single electron is impacted by the movement of the neighboring electrons. As a result, the electron movements are “correlated.” Within DFT both exchange and correlation effects are taken into account via approximations that come in two flavors: local density and generalized gradient approximations.<sup>26</sup>

The simplest approximation is the local spin density approximation (LSDA), which assumes that the overall electron density is the same as the local electron density.<sup>26</sup> This over-simplistic approach serves as a good starting approximation, but leads to  $E_g$  underestimation by approximately 50%. Adding a gradient of the electron density at a given point accounts for the fact that real systems have varying density around the electrons. Methods introducing this gradient are known as generalized gradient methods. However, this approximation was also found to underestimate  $E_g$

by approximately 50%. The PBE-GGA is an improved generalized gradient that adds a second-order gradient term.<sup>89-91</sup> This approximation is considered to be highly accurate, computationally efficient, and is one of the most frequently used functionals in solids.<sup>26</sup>

PBE-GGA can be described by considering a separation of the exchange and correlation components.<sup>89-91</sup> The exchange functional is expressed as:<sup>89-91</sup>

$$E_X^{GGA} = \int d^3\mathbf{r} \rho(\mathbf{r}) \varepsilon_X^{unif}(\rho) F_X(s) \quad (2.16)$$

where  $\rho(\mathbf{r})$  is the total electron density;  $\varepsilon_X^{unif}(\rho)$  is the Slater exchange energy density in the uniform gas approximation, which is equal to  $\frac{-3k_F}{4\pi}$ ;  $k_F$  is the local Fermi wave vector, which is equal to  $3\pi^2\rho(\mathbf{r})^{\frac{1}{3}}$ ,  $F_X(s)$  is an enhancement factor; and  $s$  is a dimensionless density gradient, which is equal to  $\frac{|\nabla\rho|}{2k_F\rho}$ . The exchange functional enhancement factor for the PBE-GGA method  $F_X^{PBE}(s)$  is provided in eq 2.17

$$F_X^{PBE}(s) = 1 + \kappa - \frac{\kappa}{1 + \frac{\mu}{\kappa}s^2} \quad (2.17)$$

where  $\kappa = 0.804$  (the minimum value allowed by the Lieb-Oxford bound on the exchange correlation) and  $\mu = 0.21951$ . The correlation functional is expressed as:<sup>89-91</sup>

$$E_C^{GGA}[n_\uparrow, n_\downarrow] = \int d^3\mathbf{r} n[\varepsilon_C^{unif}(r_s, \zeta) + H(r_s, \zeta, t)] \quad (2.18)$$

where  $n_\uparrow$  and  $n_\downarrow$  are the numbers of spin up and down electrons respectively,  $r_s$  is the local Seitz radius with a mean volume per atom in the solid;  $\zeta$  is the relative spin polarization, which is equal to  $\frac{n_\uparrow - n_\downarrow}{n}$ ;  $t$  is a dimensionless density gradient, which is equal to  $\frac{|\nabla n|}{2\phi k_s n}$ ;  $\phi(\zeta)$  is a spin scaling factor, which is equal to  $[(1 + \zeta)^{\frac{2}{3}} + (1 - \zeta)^{\frac{2}{3}}]/2$ ; and  $k_s$  is the Thomas-Fermi screening wave number, which is equal to  $\sqrt{(4k_F)/(\pi a_0)}$  with  $a_0 = (\hbar^2/m_e e^2)$ . In addition, ‘‘H’’ is the gradient contribution:

$$H = \left(\frac{e^2}{a_0}\right) \gamma \phi^3 \ln \left\{ 1 + \frac{\beta}{\gamma} t^2 \left[ \frac{1 + At^2}{1 + At^2 + A^2 t^4} \right] \right\} \quad (2.19)$$

where A is defined as

$$A = \frac{\beta}{\gamma} \left\{ \exp(-\varepsilon_C^{unif}/[\gamma \phi^3 e^2/a_0]) - 1 \right\}^{-1} \quad (2.20)$$

In PBE-GGA, the constants of  $\alpha$ ,  $\beta$ , and  $\gamma$  are 0.0716, 0.066725, and 0.031091, respectively. The energy over the local exchange can then be written as:

$$E_{XC}^{GGA}[n_{\uparrow}, n_{\downarrow}] = \int d^3\mathbf{r} n \varepsilon_X^{unif}(n) F_{XC}(r_s, \zeta, s) \quad (2.21)$$

## 2.5 The modified Becke Johnson Potential

The mBJ potential is an exchange potential that improves  $E_g$  calculations in insulators and semiconductors.<sup>92,93</sup> The potential is defined as:

$$v_{x,\sigma}^{BJ}(\mathbf{r}) = cv_{x,\sigma}^{BR}(\mathbf{r}) + (3c - 2) \frac{1}{\pi} \sqrt{\frac{5}{6}} \sqrt{\frac{t_{\sigma}(\mathbf{r})}{\rho_{\sigma}(\mathbf{r})}} \quad (2.22)$$

where  $\rho_{\sigma}(\mathbf{r})$  is the electron density,  $t_{\sigma}(\mathbf{r})$  is the kinetic energy density, and  $v_{x,\sigma}^{BR}(\mathbf{r})$  is the Becke-Roussel exchange potential, which is used to model the Coulomb potential that is created by the exchange hole as defined in eq 2.23:

$$v_{x,\sigma}^{BR}(\mathbf{r}) = - \left( \frac{8\pi\rho_{\sigma}}{x_{\sigma}^3 e^{-x_{\sigma}}} \right)^{1/3} \left( 1 - e^{-x_{\sigma}(\mathbf{r})} - \frac{1}{2} x_{\sigma}(\mathbf{r}) e^{-x_{\sigma}(\mathbf{r})} \right) \quad (2.23)$$

where  $x_{\sigma}$  is calculated by a nonlinear equation with the gradients of the electron density with respect to  $t_{\sigma}$  and  $c$  introduces relative weights in the form of

$$c = \alpha + \beta \left( \frac{1}{V_{\text{cell}}} \int_{\text{cell}} \frac{|\nabla\rho(\mathbf{r}')|}{\rho(\mathbf{r}')} d^3\mathbf{r}' \right) \quad (2.24)$$

where  $V_{\text{cell}}$  is the unit cell volume,  $\alpha$  is -0.012, and  $\beta$  is  $1.023 \text{ bohr}^{\frac{1}{2}}$ .

In the literature, the mBJ potential has been utilized to analyze the electronic structures of various semiconductors, comparing  $E_g$  to experimental results.<sup>94</sup> The method provides accurate  $E_g$  calculations for germanium (0.85 eV), scandium nitride (0.90 eV), silicon (1.17 eV), and gallium arsenide (1.64 eV); compared to experimental values of 0.74, 0.90, 1.17, and 1.52 eV, respectively. The method was also successfully applied to other semiconductor and insulator materials, as summarized in Tran and Koller's work.<sup>92,93</sup> This evidence in the literature, coupled with the favorable results presented in Section 1.6, made this a suitable choice for the calculations carried out in this work.

## 2.6 FP-LAPW

The two divisions of plane wave DFT methods are all-electron and pseudopotential methods. In pseudopotential methods, i.e. frozen core methods, the valence electrons are assumed to be responsible for the chemical and physical properties of molecules and solids. Here, the core electrons are fixed and only the valence electrons are explicitly treated in the self consistent field (SCF) calculation. In all-electron methods, the plane waves around each atomic site are augmented locally with radial functions in order to describe the core region’s oscillatory wavefunction behavior. These all-electron methods are described as “mixed basis set” methods.<sup>95</sup>

One such example of an all-electron, mixed basis set method is the full-potential linearized-augmented plane wave (FP-LAPW) method within the WIEN2k computational software.<sup>96</sup> In this method, a sphere is centered around the nucleus of the atoms. The sphere size is determined by a parameter called the muffin-tin radius (RMT), which is depicted in Figure 2.1. Electrons within the sphere region are treated with a linear combination of radial functions and spherical harmonics while electrons outside the sphere region are calculated using plane waves, which take the form of

$$\psi_i(\mathbf{r}) = u_{\mathbf{k}}(\mathbf{r})e^{i\mathbf{k}\mathbf{r}} \quad (2.25)$$

where  $u_{\mathbf{k}}$  is a periodic potential and  $e^{i\mathbf{k}\mathbf{r}}$  is a plane wave, which is a function of the reciprocal space vector  $k$  and the real space translation vector  $r$ . Inside an atomic sphere  $t$  of radius  $R_t$ , the linear combination of radial functions and spherical harmonics ( $Y_{lm}(r)$ ) takes on the following form:

$$\phi_{\mathbf{k}_n} = \sum_{lm} [A_{lm,\mathbf{k}_n} u_l(r, E_l) + B_{lm,\mathbf{k}_n} \dot{\mathbf{u}}_l(r, E_l)] Y_{lm}(\hat{\mathbf{r}}) \quad (2.26)$$

where  $u_l(r, E_l)$  is the regular solution of the radial Schrödinger equation for energy  $E_l$ ,  $\dot{\mathbf{u}}_l(r, E_l)$  is the energy derivative of  $u_l$  evaluated at energy  $E_l$ , the coefficients  $A_{lm}$  and  $B_{lm}$  are a function of  $\mathbf{k}_n$ , and the functions  $u_l$  and  $\dot{\mathbf{u}}_l$  are obtained from numerical integration of the radial Schrödinger equation. In the interstitial region, a plane wave



expansion is used, which takes on the following form:

$$\phi_{\mathbf{k}_n} = \frac{1}{\sqrt{\omega}} e^{i\mathbf{k}_n \mathbf{r}} \quad (2.27)$$

where  $\mathbf{k}$  represents the reciprocal lattice vectors. A basis set of LAPW's is combined according to the linear variation method in order to find the solutions to the KS equations. It should be noted that the radius of each atom does not govern the corresponding RMT values. The separation energy between core and valence states specifies a designation/cutoff for where higher and lower level calculations take place in the system. This simplifies the calculation and reduces computational resources.

Linear combination of radial functions and spherical harmonics

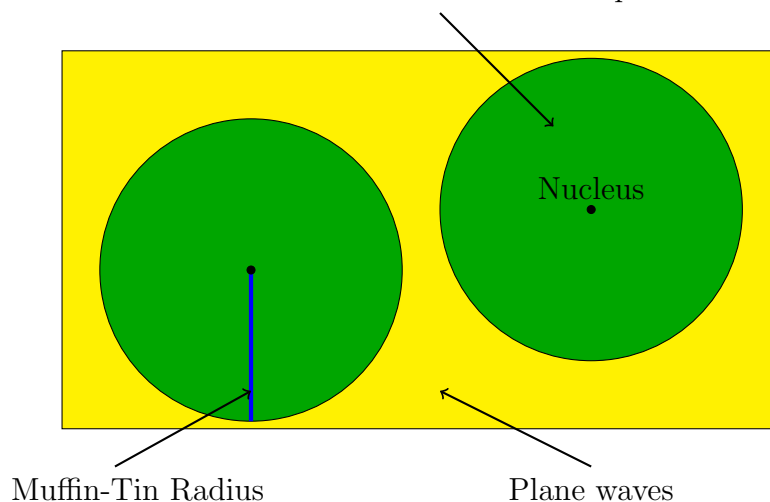


**Figure 2.1:** The RMT approximation within the FP-LAPW method. The RMT is depicted in blue within the green sphere. Electrons within the sphere are treated with a linear combination of radial functions and spherical harmonics while electrons outside the sphere are treated with plane waves. *Source:* adapted from: Blaha, P. et al. WIEN2k: an augmented plane wave plus local orbitals program for calculating crystal properties user's Guide.; prepared using the PSTricks package of L<sup>A</sup>T<sub>E</sub>X.

## 2.7 Self-Consistent Field

Discussed throughout Sections 2.3 and 2.6 was the aspect of solving the KS equations self-consistently. This suggests that the calculations run in cycles until convergence is achieved. An example of this cycle is provided in Figure 2.2. The convergence depends on user input criteria defined at the beginning of the cycle, e.g. energy and charge. In the case of DFT, the energy as a function of the ground state electron

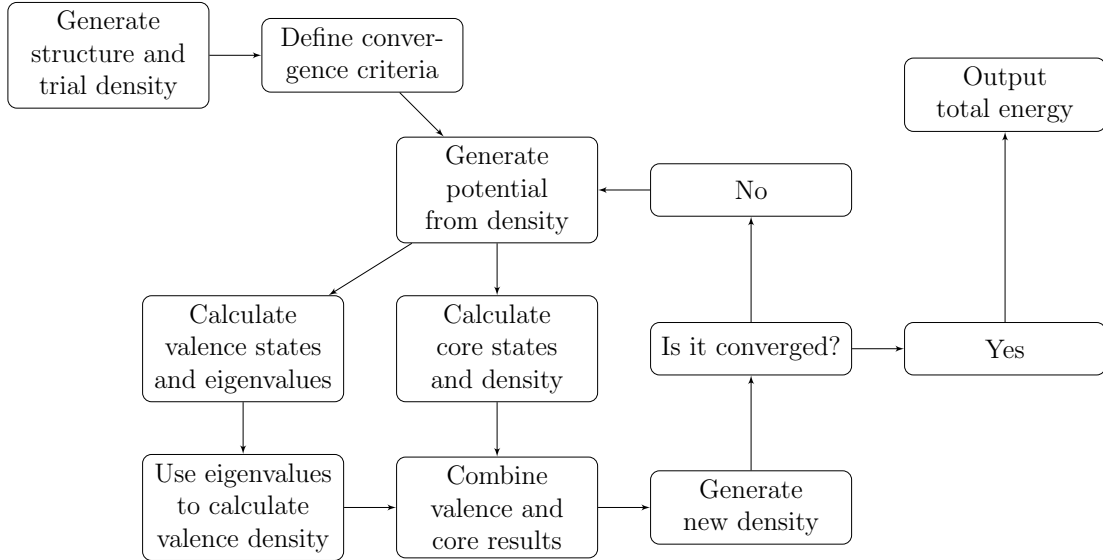


**Figure 2.2:** The self-consistent field cycle is summarized to illustrate the steps involved within the WIEN2k computations for determining the ground state electron density. *Source:* adapted from: Blaha, P. et al. WIEN2k: an augmented plane wave plus local orbitals program for calculating crystal properties user’s Guide.; prepared using the PSTricks package of L<sup>A</sup>T<sub>E</sub>X.

density is computed. Before the SCF calculation, the basis set is built with a specified kinetic energy cutoff for the plane wave functions. Next, a trial electron density is constructed from a superposition of atomic-like densities localized on each atomic site. From the trial electron density, the total density functional Hamiltonian  $H[\rho(\mathbf{r})]$  is built, which includes the ionic, Hartree, and exchange correlation potentials, as presented in Section 2.3.

With the built Hamiltonian, it is then diagonalized to compute the energies. Then, a new charge density is computed by updating the basis set coefficients. At this point, the new charge density is compared back to the convergence criteria specified at the beginning of the SCF calculation and, if it is within the defined threshold, the calculation stops. If, however, the new charge density does not fall within the threshold, a new input density is created (usually by mixing some percentage of the old density with a percentage of the new density), a new SCF cycle begins, the Hamiltonian is constructed from the new charge density, it is diagonalized, and another density is calculated to check for self-consistency.

## 2.8 Computational Resources and Workflow

The computations carried out in this work utilized a variety of resources. The unsubstituted calculations of Chapter 3 were performed on a dual-hexacore Linux box with twelve processors. The substituted calculations of Chapter 4 were performed on several Extreme Science and Engineering Discovery Environment (XSEDE) resources.<sup>97</sup> These resources included Blacklight at the Pittsburgh Supercomputing Center (PSC), Comet at the San Diego Supercomputer Center, and Bridges at PSC. All computations were carried out using 12-48 processors via the parallel compiled WIEN2k software (version 14) from the Vienna University of Technology.<sup>21</sup>

Prior to the SCF calculation, the following computational input parameters were optimized for each case: separation energy, k points, nearest neighbor distance factor, rkmax, and the exchange correlation functional. The separation energy is the energy difference (in units of Rydberg, Ry) between the valence and core states. The nearest neighbor distance factor calculates nearest neighbor distances up to a specified value and determines the atomic sphere radii. The number of k-points correspond to the number of points within the iBZ of reciprocal space, where the wavefunctions are evaluated. Rkmax determines the number of basis functions (the size of the matrix) and is a product of the RMT (smallest of all atomic sphere radii) and  $K_{\max}$  (the plane wave cutoff). Last, the exchange correlation functional is the approximation to the electron electron interaction energy, as discussed in Section 2.4.

SCF calculations were carried out on all systems with the energy convergence criteria set to 0.1 mRy. In the substituted systems, geometry optimizations were implemented in the SCF calculations via the multi-secant minimization protocol with a total force convergence criteria of  $1 \frac{mRy}{au}$ . Following converged SCF calculations, the electron density, band structure, and density of states were calculated for each system. XCrysDen, a WIEN2k add-on package, was utilized for electron density plots, geometry optimization analysis, and k-point path selection for band structure

plots.<sup>98</sup> All crystallographic images were generated using: CrystalMaker<sup>®</sup>: a crystal and molecular structures program for Mac and Windows. CrystalMaker Software Ltd, Oxford, England ([www.crystalmaker.com](http://www.crystalmaker.com)).

## Chapter 3. Unsubstituted $\text{TiO}_2$

### 3.1 $\text{TiO}_2$ Polymorphs

In nature,  $\text{TiO}_2$  exists in many different polymorphic forms. In this project, the most naturally occurring polymorphs (rutile and anatase) were selected for computational investigation because they are most frequently used in PV applications (Sections 1.5 and 1.6). These polymorphs have been extensively studied in the literature via computational and experimental methods (see Section 1.6), which makes them ideal candidates for method validation prior to the substitution studies of Chapter 4. In this chapter, unsubstituted brookite calculations were also included to further validate the method. However, the brookite polymorph was excluded from the substituted calculations because of its increased computational cost. In addition, this polymorph is rarely used in industrial applications due to its rareness and difficult preparation.<sup>45</sup> The increase in computational cost for brookite is due to its crystallization in the orthorhombic crystal system, which possesses less symmetry than that tetragonal crystal system of rutile and anatase. Unit cells of these structures can be seen in Figure 3.1 and their corresponding crystallographic information (space group, lattice parameters, and atomic coordinates) is summarized in Table 3.1.

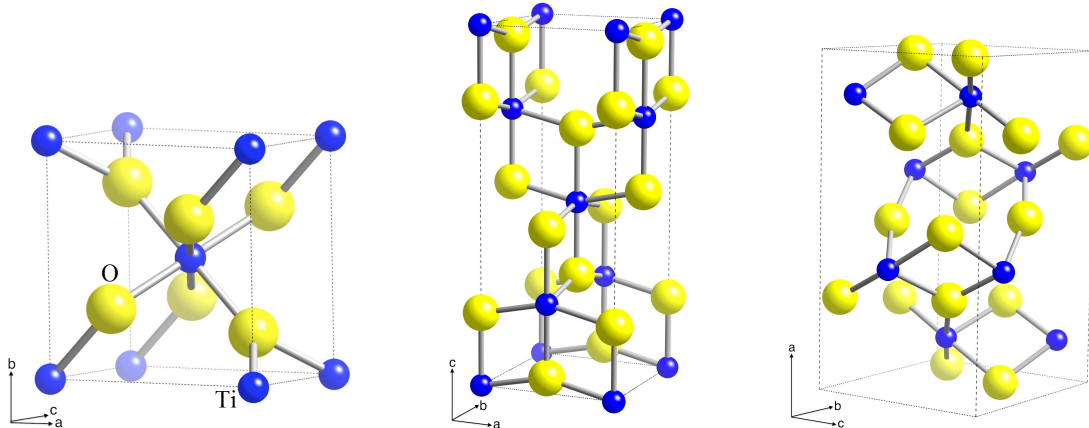


**Figure 3.1:** The unit cells of rutile (left), anatase (middle), and brookite (right) with their corresponding crystallographic axes. Within the unit cells, titanium and oxygen atoms are represented via blue and yellow spheres, respectively. *Source:* prepared using CrystalMaker<sup>®</sup>: a crystal and molecular structures program for Mac and Windows. CrystalMaker Software Ltd, Oxford, England ([www.crystallmaker.com](http://www.crystallmaker.com)).

	<b>Rutile</b> <sup>100</sup>	<b>Anatase</b> <sup>101</sup>	<b>Brookite</b> <sup>45</sup>
Space group	$P4_2/mnm$	$I4_1/amd$	$Pbca$
a / Å	4.5937	3.7842	9.16
b / Å	4.5937	3.7842	5.43
c / Å	2.9581	9.5146	5.13
$\alpha, \beta, \gamma / ^\circ$	90	90	90
Atomic coordinates / a.u.	Ti: (0, 0, 0) O: (0.3053, 0.3053, 0)	Ti: (0, 0, 0) O: (0, 0, 0.2066)	Ti: (0.1290, 0.0972, -0.1371) O1: (0.0101, 0.1486, 0.1824) O2: (0.2304, 0.1130, 0.4629)

**Table 3.1:** The crystallographic information of rutile, anatase, and brookite polymorphs. Each polymorph. Note that the brookite polymorph possesses two crystallographically unique oxygen atoms.

### 3.2 Computational Input Parameters

The calculations in this chapter were initialized in WIEN2k using the aforementioned lattice parameters and the atomic coordinates as reported in Table 3.1.<sup>45,100,101</sup> As discussed in Section 2.8, appropriate values for the separation energy, nearest neighbor distance factor, the number of k-points, the rkmax value, and the exchange correlation (XC) functional computational input parameters were determined. According to the WIEN2k software, the default values for each of these input parameters are: 6.0 Ry, 2.0, 2000 k-points, 7.0, and PBE-GGA, respectively.<sup>21</sup> However, rather than simply selecting the default input parameters, a systematic investigation of all input parameters was carried out. Here, a range of values was selected for each of the above parameters. For all numeric input parameters, a value above and below the default was selected. For the separation energy, values of 5.0, 6.0, and 7.0 Ry were selected. The nearest neighbor distance factor was set to values of 1.5, 2.0, and 2.5. For the number of k-points, values of 1200, 3600, and 6000 k-points were selected. The rkmax value was set to 5.0, 7.0, and 9.0. For the XC functional, the LSDA, PBE-sol (a generalized gradient approximation designed for solids), and PBE-GGA functionals were selected. In all calculations, the RMT values of titanium were set to 1.92, 1.93, and 1.84 for rutile, anatase, and brookite, respectively. The RMT values of oxygen were set to 1.74, 1.74, and 1.66, respectively. When selecting the RMT values for a particular atom across multiple polymorphs, the goal was to keep them

as similar as possible while preventing software input errors for core electron leakage out of the RMT spheres.

With the five input parameters and the three variations of each parameter discussed above, a total of 243 ( $3^5$ ) SCF and  $E_g$  calculations were carried out. The results of these calculations are summarized in Table 3.2. Data presented in the table are  $\Delta E_g$ , compared to an experimental  $E_g$  of 3.00 eV.<sup>40</sup> Therefore, values closest to zero would reflect optimal computational input parameters that produce  $E_g$  values in best agreement with the experimental data while greater values reflect larger deviations from the experimental data.

		rkmax1			rkmax2			rkmax3		
		XC1	XC2	XC3	XC1	XC2	XC3	XC1	XC2	XC3
<b>nn1</b>	<b>k1</b>	1.18	1.13	1.10	1.15	1.11	1.07	1.18	1.13	1.10
	<b>k2</b>	1.18	1.13	1.10	1.15	1.11	1.07	1.18	1.13	1.10
	<b>k3</b>	1.18	1.13	1.10	1.15	1.11	1.07	1.18	1.13	1.10
<b>nn2</b>	<b>k1</b>	1.18	1.13	1.10	1.15	1.11	1.07	1.18	1.13	1.10
	<b>k2</b>	1.18	1.13	1.10	1.15	1.11	1.07	1.18	1.13	1.10
	<b>k3</b>	1.18	1.13	1.10	1.15	1.11	1.07	1.18	1.13	1.10
<b>nn3</b>	<b>k1</b>	1.18	1.13	1.10	1.15	1.11	1.07	1.18	1.13	1.10
	<b>k2</b>	1.18	1.13	1.10	1.15	1.11	1.07	1.18	1.13	1.10
	<b>k3</b>	1.18	1.13	1.10	1.15	1.11	1.07	1.18	1.13	1.10

**Table 3.2:** Matrix of computational input parameter combinations for the rutile SCF calculation. The values reported are  $\Delta E_g$ , compared to the experimental  $E_g$  of 3.00 eV.<sup>40</sup> The above data resulted from a separation energy of 6.0 Ry and various combinations of the following input parameters: nn1 = 1.5, nn2 = 2.0, nn3 = 2.5, k1 = 1200, k2 = 3600, k3 = 6000, rkmax1 = 5.0, rkmax2 = 7.0, rkmax3 = 9.0, XC1 = LSDA, XC2 = PBE-sol, and XC3 = PBE-GGA.

Table 3.2 is one of three matrices (81 calculations each) of data for the input parameter combinations outlined above. This table reports the input parameter combinations for only one separation energy, 6.0 Ry. Similar tables were also prepared for separation energies of 5.0 and 7.0 Ry; however, they were excluded because the  $\Delta E_g$  values were identical to those reported in Table 3.2. This indicates that the  $E_g$  value is independent of the separation energy computational input parameter. Variations in the rkmax and XC functionals are organized along the top rows of the table while

variations in the nearest neighbor distance factor and the number of k-points are organized in the far left column of the table.

Upon inspection of the data, it was evident that  $\Delta E_g$  was independent of the nearest neighbor distance factor and the number of k-points. This is evidenced by the constant  $\Delta E_g$  value moving down each column of Table 3.2. Moving across each row of the table, the  $\Delta E_g$  values were dependent on the rkmax and XC functional selected. It was also apparent that rkmax2 produced the smallest  $\Delta E_g$  values, i.e. in best agreement with the experimental data. In addition, within the rkmax2 column, the  $\Delta E_g$  values got smaller as the calculations progress from LSDA to PBE-sol to PBE-GGA. This is as expected given the XC discussions of Section 2.4 and the PBE-GGA functional producing  $E_g$  values in best agreement with experimental data. From the data presented in Table 3.2, the optimal computational input parameters were determined to be separation energy = 6.0 Ry, nn = 2.0, number of k-points = 3600, rkmax = 7.0, and XC = PBE-GGA. This provided a good starting point for the computational input parameter determination, but the convergence of  $E_g$  with respect to each input parameter was also investigated. These results are presented along with the SCF convergence and electronic structure of each polymorph in Sections 3.3-3.5.

### 3.3 Rutile Electronic Structure

Expanding upon the input parameter determination of Section 3.2, each parameter was varied by itself to investigate the convergence of the  $E_g$  value. In this case, rkmax was varied from 4.0-11.0 in increments of 1.0. The number of k-points was varied from 500-4,000 in increments of 500. The separation energy was varied from 5.0-12.0 in increments of 1.0. The nearest neighbor distance factor was varied from 0.5-4.0 in increments of 0.5. The XC functionals selected were: LSDA, WC-GGA, PBE-sol, and PBE-GGA. The LSDA and PBE-GGA functionals were discussed in Section 2.4, the PBE-sol functional was introduced in Section 3.2, and WC-GGA is a generalized gradient variation devised by Wu and Cohen.



The results of these convergence calculations are provided below in Figure 3.2. The top panel, again, indicates that the  $E_g$  values are independent of the separation energy, the nearest neighbor distance factor, and the number of k-points. This is further supported by the results obtained in the data matrix of computational input parameters in Section 3.2. In addition, similar to the results obtained in Section 3.2, the  $E_g$  value gets closer to the experimental  $E_g$  as the XC functional progresses from LSDA to PBE-GGA. With respect to rkmax, the  $E_g$  value plateaus around  $\text{rkmax} = 7.0$ . These results indicate that the XC approximation and the rkmax input parameters have the greatest impact on the calculated  $E_g$ . This is as expected considering the discussion in Section 2.4 on the importance of the XC energy term as well as the fact that rkmax is a reflection of the basis set size. This basis set size governs whether enough plane waves are used in the calculations. These results further validate the input parameters established in section 3.2 for the rutile polymorph.

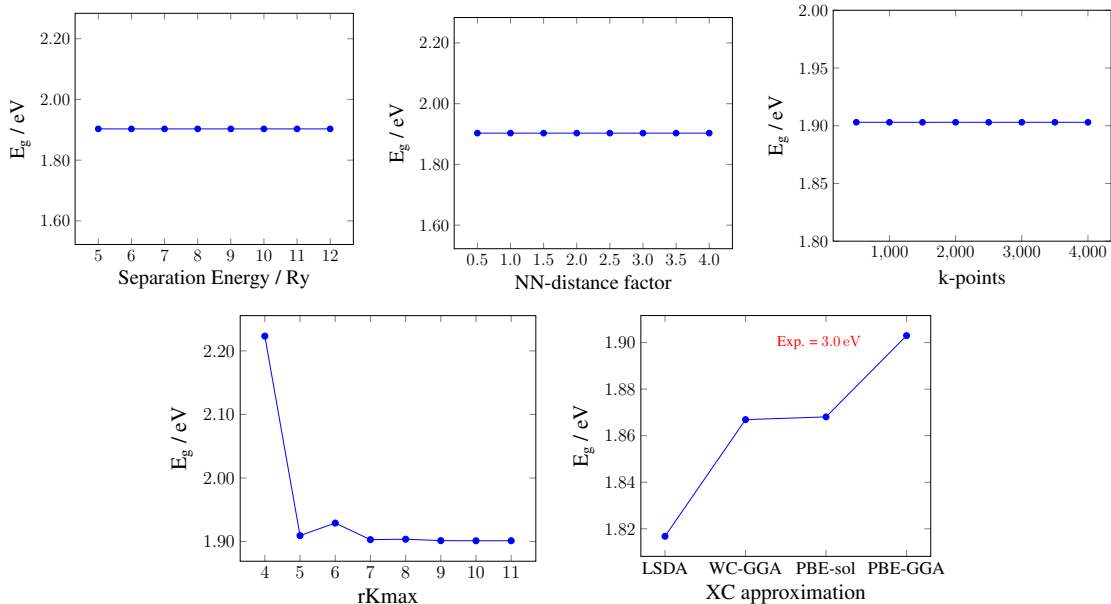


**Figure 3.2:**  $E_g$  convergence plots as a function of varying separation energy, nearest neighbor distance factor, number of k-points, rkmax, and the XC approximation. *Source:* prepared using the PSTricks package of L<sup>A</sup>T<sub>E</sub>X.

Following the computational input parameter determination, a SCF calculation was carried out on the rutile polymorph with the convergence criteria specified in

Section 2.8. The results of this SCF calculation are provided in Figure 3.3, which plots  $\Delta E$  (in units of Ry) on the y-axis and SCF iteration on the x-axis. This calculation was determined to be converged with respect to energy after 17 iterations with a final total energy of the system equal to  $-4018.0619$  Ry.

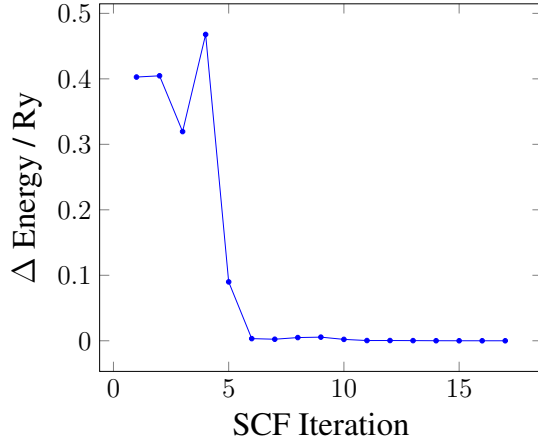


**Figure 3.3:** A plot of rutile’s energy convergence as a function of SCF iteration. The energy convergence criteria was set to 0.1 mRy, and convergence was achieved after 17 iterations. *Source:* prepared using the PSTricks package of L<sup>A</sup>T<sub>E</sub>X.

With the converged electron density and energy from the SCF calculation, the band structure and partial DOS of the system were calculated. The electronic structure results are provided in Figure 3.4. Both the band structure and DOS plots depict energy (in eV) on the y-axis. In the band structure plot, k-points are plotted on the x-axis while the DOS depicts the number of states on the x-axis. The Fermi level (signified by the brown dashed line in all three panels) was found to be 0.3844 eV, which was then set as the zero energy reference point in Figure 3.4. From the band structure, a direct  $E_g$  of 1.90 eV was determined at the  $\Gamma$  point, as evidenced by the valence band maximum and conduction band minimum occurring at the same k-point. This  $E_g$  compared relatively well with the experimental  $E_g$  of 3.00 eV obtained via UV-visible spectroscopy,<sup>40</sup> but was still underestimated, as expected from the discussion in Section 2.4. The  $E_g$  also compared relatively well with previous calculations in the literature, which reported  $E_g = 1.88$  eV using the DFT/PBE-GGA method,  $E_g = 3.39$  eV using the DFT/HSE method,  $E_g = 3.46$  eV

using the PBE-GGA/GW method,  $E_g = 3.73$  eV using the HSE/GW method, and  $E_g = 2.65$  eV using the PBE-GGA+U method.<sup>45,47</sup>

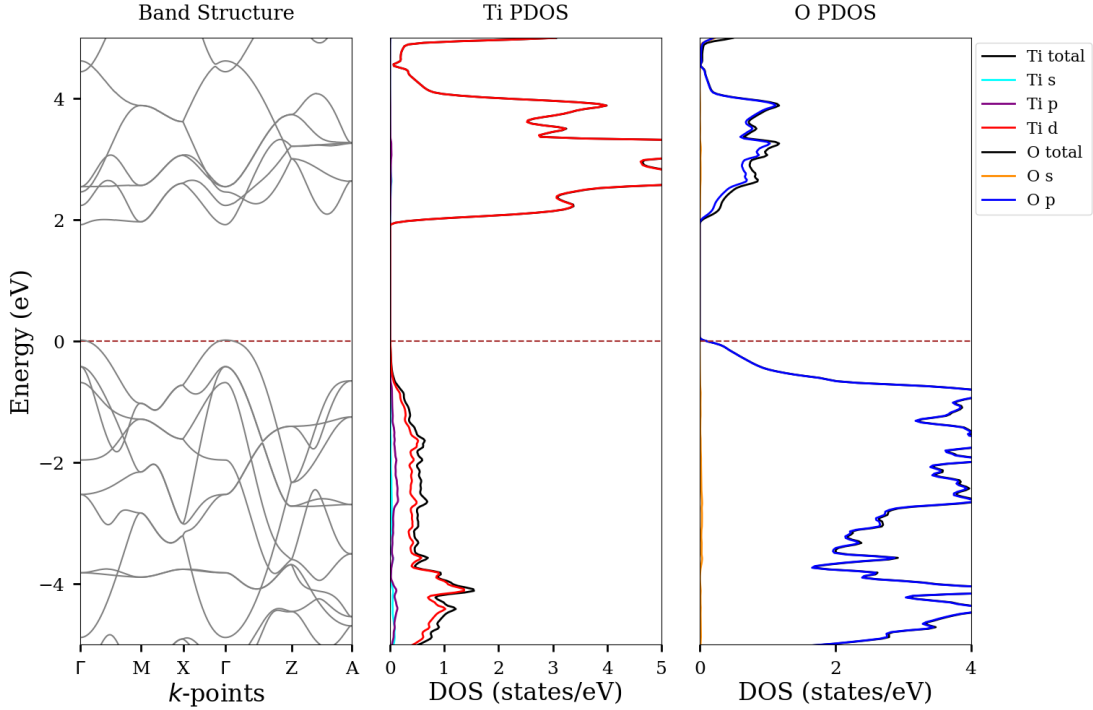


**Figure 3.4:** The band structure (left) of rutile along with its partial DOS diagrams for titanium (center) and oxygen (right). *Source:* prepared using: Python Software Foundation. Python Language Reference, version 2.7. Available at <http://www.python.org>.

The partial DOS analysis was used to investigate the atomic and orbital contribution to the bands near  $E_g$ . The total DOS of titanium and oxygen are depicted in black in their respective DOS diagrams. Titanium-s, -p, and -d state contributions are depicted in cyan, purple, and red, respectively. Oxygen-s and -p state contributions are depicted in orange and blue. The DOS results indicate predominant contributions from the oxygen-p states in the valence band region (-5 to 0 eV). In addition, titanium-s, -p, and -d states provide minor contributions in the valence band region. In the conduction band region (2-5 eV), titanium-d states and oxygen-p states comprise the major DOS contributions. Inspection of the DOS provides great insight to how the  $E_g$  of the material can be tuned. For example, as previously discussed in Sections 1.6 and 1.7, the  $E_g$  value of  $\text{TiO}_2$  is too wide for PV applications. Narrowing

$E_g$  could be accomplished by either adding higher energy valence band states or lower energy conduction band states. This has been the primary focus of the substitutional studies summarized in section 1.6 and will be further discussed with the calculations of Chapter 4. Additionally, this work’s electronic structure of rutile is accompanied by that from previous calculations in the literature (Figure 3.5).<sup>45</sup> Their band structure reported a direct  $E_g$  of 1.88 eV and primary DOS contributions from oxygen-p states in the valence band and titanium-d states in the conduction band,,<sup>45</sup> all of which compare very well with calculations from this work.

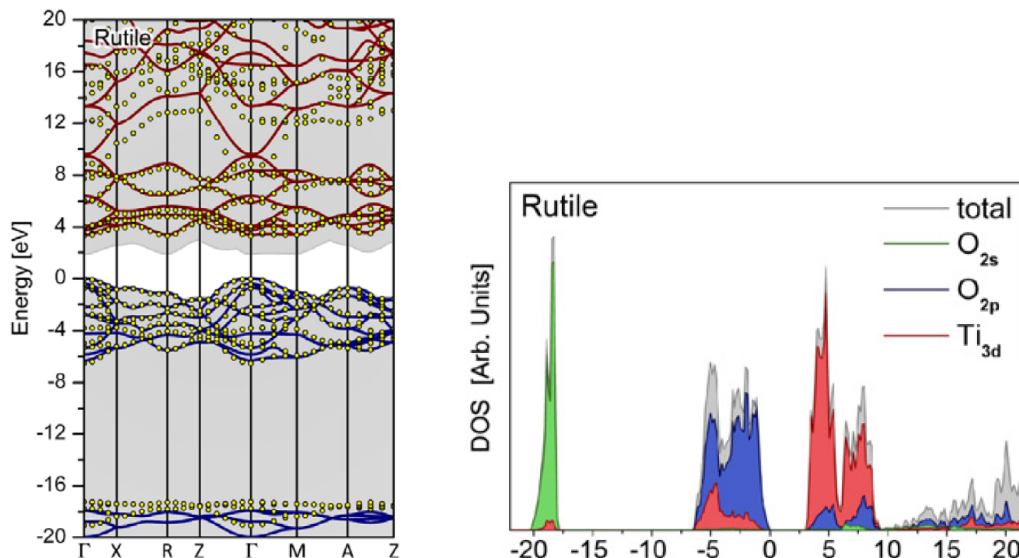


**Figure 3.5:** The band structure (left) of rutile and partial DOS (right) reported in the literature using the HSE06 XC functional. *Source:* reprinted with permission from: Landmann, M. et al. The electronic structure and optical response of rutile, anatase and brookite  $\text{TiO}_2$ . *J. Phys.: Condens. Matter* **2012**, *24*, 195503 (1–6).

In addition to the PBE-GGA band structure (repeated in Figure 3.6 left) the mBJ potential was also added for improved  $E_g$  calculation (Figure 3.6 right). The mBJ calculation resulted in a direct  $E_g$  of 2.61 eV at the  $\Gamma$  point. It is important to note that the topology of the bands via mBJ is very similar to that determined using solely PBE-GGA, confirming the mBJ potential’s ability to improve the  $E_g$  calculation while not compromising other components of the electronic structure.

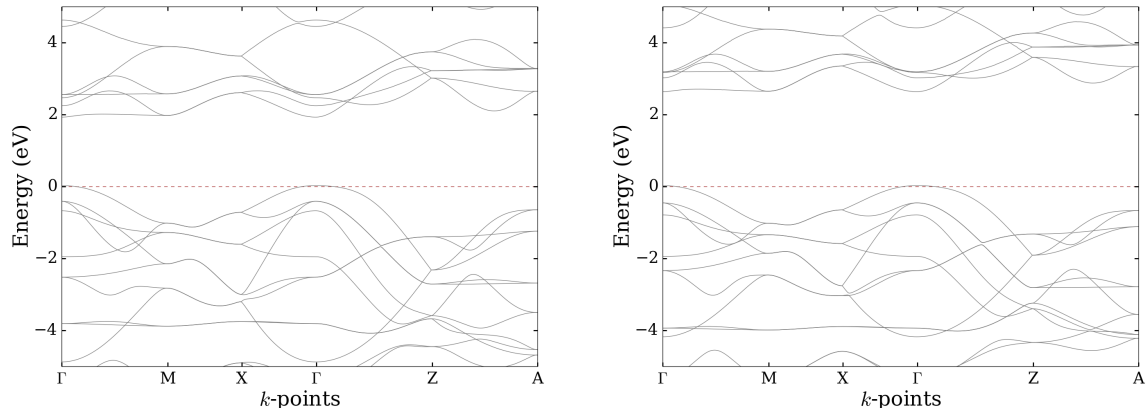


**Figure 3.6:** The band structures of rutile with the PBE-GGA XC functional (left) and the PBE-GGA + mBJ potential (right). *Source:* prepared using: Python Software Foundation. Python Language Reference, version 2.7. Available at <http://www.python.org>.

### 3.4 Anatase Electronic Structure

Before calculating the electronic structure of the anatase polymorph of  $\text{TiO}_2$ , an identical input parameter determination was carried out, as was done for rutile in Section 3.3. See Section 3.3 for an outline of the various input parameter values. The results of the anatase input parameter convergence calculations are provided below in Figure 3.7. The top panel, again, indicates that the  $E_g$  values are independent of the separation energy, the nearest neighbor distance factor, and the number of k-points. This result is in agreement with those obtained for the rutile polymorph in Section 3.3. In addition, similar results as rutile were obtained for the XC functional, where the  $E_g$  value gets closer to the experimental  $E_g$  progressing from LSDA to PBE-GGA. With respect to rkmax, the  $E_g$  value plateaus around  $\text{rkmax} = 8.0$ . These results again indicate that the XC approximation and the rkmax input parameter have the greatest impact on the calculated  $E_g$ . With these results, the following computational input parameters were established for the anatase polymorph: separation energy = 6.0 Ry, nearest neighbor distance factor = 2.0, number of k-points = 2000, rkmax = 8.0, and XC = PBE-GGA.

Following the computational input parameter determination, a SCF calculation was carried out on the anatase polymorph with the convergence criteria specified in

Section 2.8. The results of this SCF calculation are provided in Figure 3.8. This calculation was determined to be converged with respect to energy after 23 iterations with a final total energy of the system equal to  $-4018.0946$  Ry.

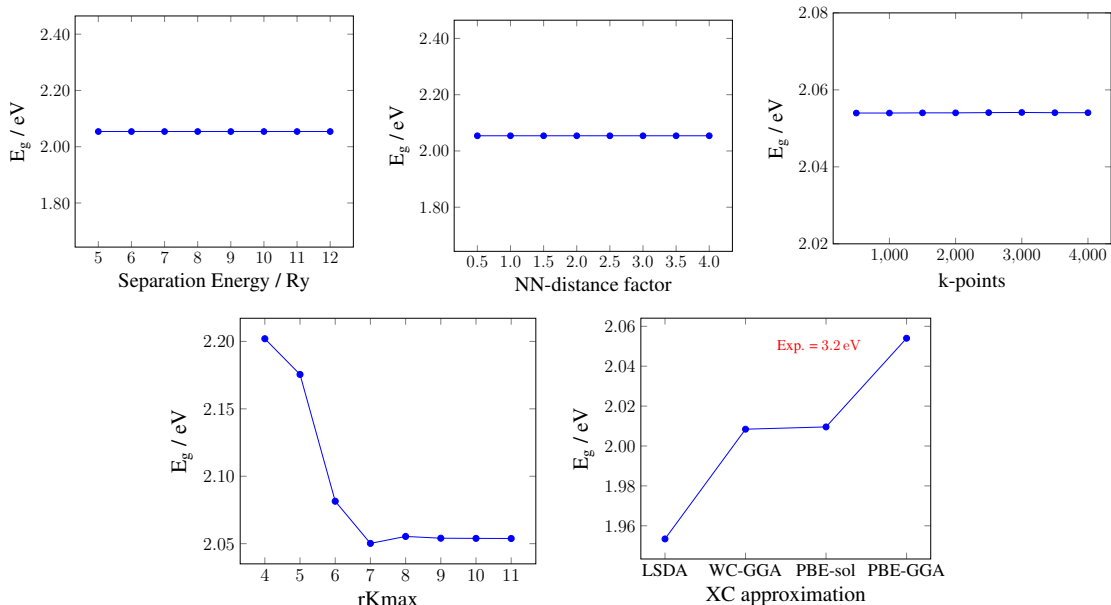


**Figure 3.7:**  $E_g$  convergence plots as a function of varying separation energy, nearest neighbor distance factor, the number of k-points, rKmax, and the XC approximation. *Source:* prepared using the PSTricks package of L<sup>A</sup>T<sub>E</sub>X.

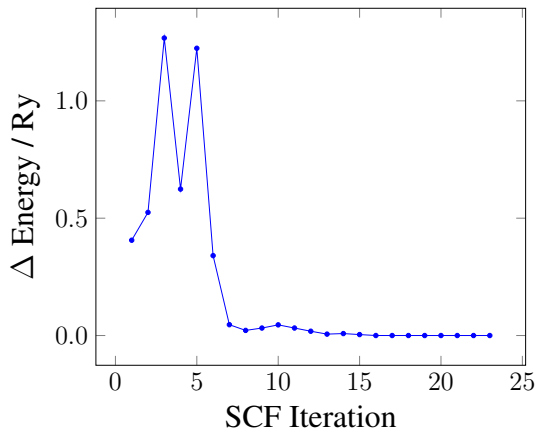


**Figure 3.8:** A plot of anatase's energy convergence as a function of SCF iteration. The energy convergence criteria was set to 0.1 mRy, and convergence was achieved after 23 iterations. *Source:* prepared using the PSTricks package of L<sup>A</sup>T<sub>E</sub>X.

Next, the band structure and partial DOS was calculated and these results are depicted in Figure 3.9. The Fermi level (signified by the brown dashed line in all three panels) was found to be 0.2709 eV, which was then set as the zero energy reference point. From the band structure, an indirect  $E_g$  of 2.05 eV was determined, as evidenced by the valence band maximum and conduction band minimum occurring at different k-points. In this case, the valence band maximum occurs at the X k-point while the conduction band minimum occurs at the  $\Gamma$  k-point. This  $E_g$  compared relatively well with the experimental  $E_g$  of 3.20 eV obtained via UV-visible spectroscopy,<sup>40</sup> but was still underestimated, as previously discussed. The  $E_g$  also compared relatively well with previous calculations in the literature, which reported  $E_g = 1.94$  eV using the DFT/PBE-GGA method,  $E_g = 3.60$  eV using the DFT/HSE method,  $E_g = 3.73$  eV using the PBE-GGA/GW method,  $E_g = 4.05$  eV using the HSE/GW method, and  $E_g = 3.00$  eV using the PBE-GGA+U method.<sup>45,47</sup>

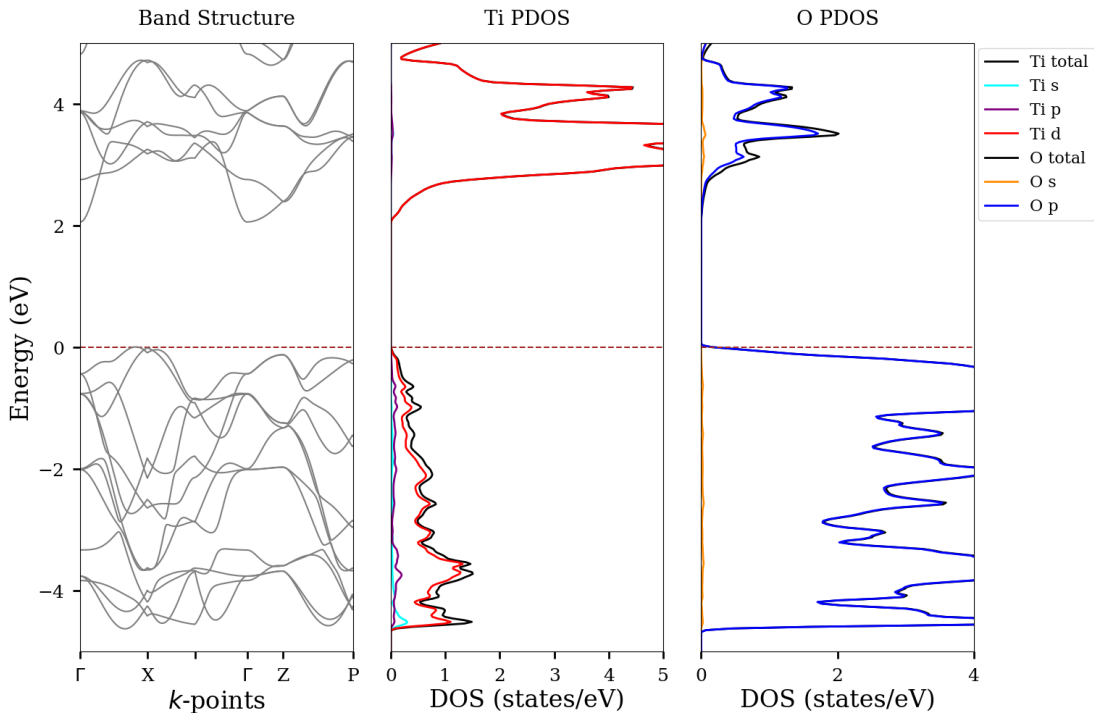


**Figure 3.9:** The band structure (left) of anatase along with its partial DOS diagrams for titanium (center) and oxygen (right). *Source:* prepared using: Python Software Foundation. Python Language Reference, version 2.7. Available at <http://www.python.org>.

The DOS results are provided in Figure 3.9 (center and right). The total DOS of titanium and oxygen are depicted in black in their respective DOS diagrams. Titanium-s, -p, and -d state contributions are depicted in cyan, purple, and red, respectively. Oxygen-s and -p state contributions are depicted in orange and blue. The DOS results indicate predominant contributions from the oxygen-p states in the valence band region (-5 to 0 eV) and minor contributions from the titanium-s, -p, and -d states. In the conduction band region (2-5 eV), titanium-d states and oxygen-p states comprise the major DOS contributions. The band structure and partial DOS of anatase compared very well with that previously published in the literature (Figure 3.10).<sup>45</sup> Their band structure reported an indirect  $E_g$  of 1.94 eV and primary PDOS contributions from oxygen-p states in the valence band and titanium-d states in the conduction band.<sup>45</sup>

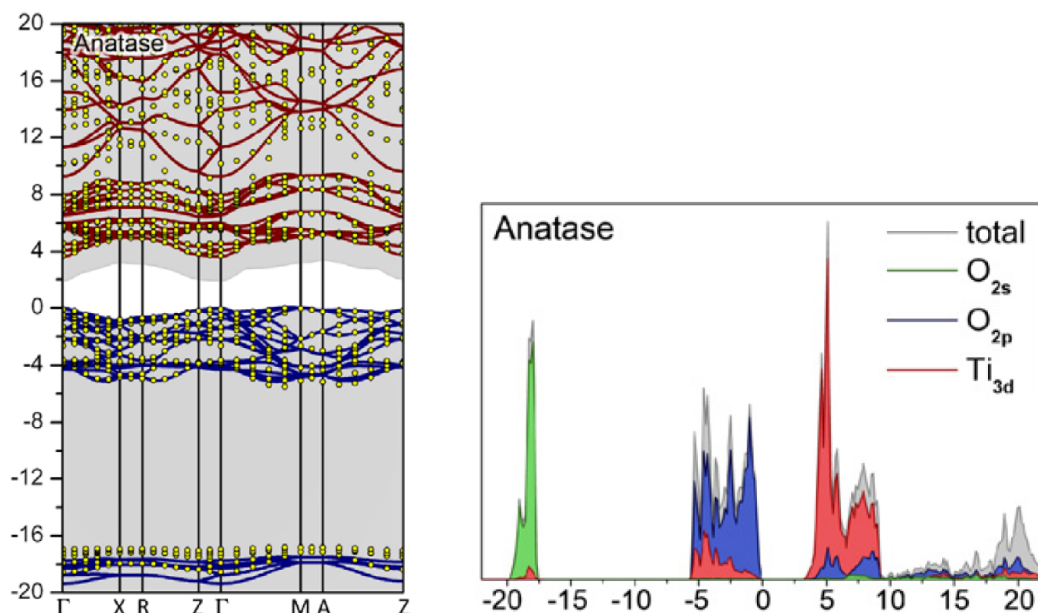


**Figure 3.10:** The band structure (left) of anatase and partial DOS (right) reported in the literature using the HSE06 XC functional. *Source:* reprinted with permission from: Landmann, M. et al. The electronic structure and optical response of rutile, anatase and brookite TiO<sub>2</sub>. *J. Phys.: Condens. Matter* **2012**, *24*, 195503 (1–6).

In addition to the PBE-GGA band structure (repeated in Figure 3.11 left), the mBJ potential was also added for improved  $E_g$  calculation (Figure 3.11 right). The mBJ calculation resulted in an indirect  $E_g$  of 2.88 eV. It is also important to note that



the topology of the bands via mBJ is again similar to that determined using solely PBE-GGA, again confirming the reliability of the mBJ method.

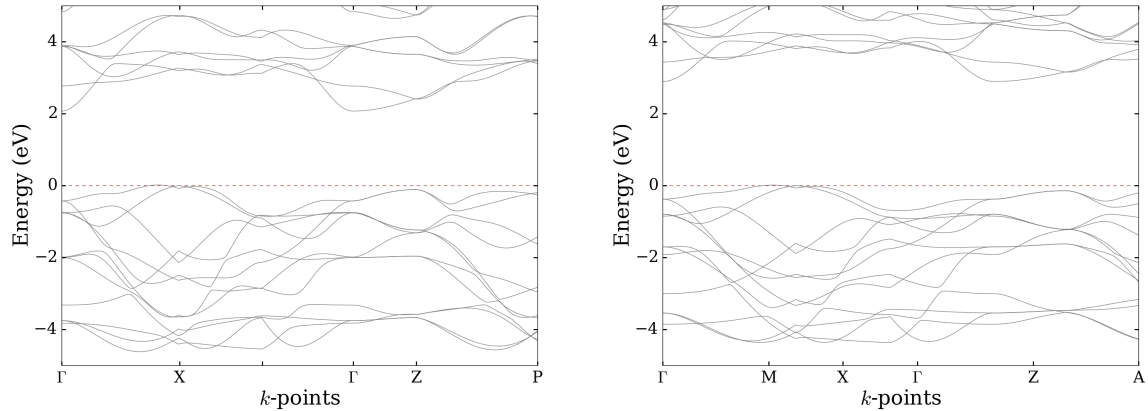


**Figure 3.11:** The band structures of anatase with the PBE-GGA XC functional (left) and the PBE-GGA + mBJ potential (right). *Source:* prepared using: Python Software Foundation. Python Language Reference, version 2.7. Available at <http://www.python.org>.

### 3.5 Brookite Electronic Structure

Due to the compositional complexity and the increased computational cost of the brookite polymorph computations, only the rkmax input parameter was optimized for this polymorph. Given the previous results, this was justified due to the fact that  $E_g$  was independent of the separation energy, nearest neighbor distance factor, and the number of k-points. In this case, rkmax was varied from 4.0-11.0 in increments of 1.0. In addition, due to the PBE-GGA XC functional producing the most accurate results compared to experimental data for the rutile and anatase polymorphs, this XC functional was immediately selected for the brookite electronic structure calculation. The results of the rkmax convergence are provided below in Figure 3.12.

Following the computational input parameter determination, a SCF calculation was carried out on the brookite polymorph with the convergence criteria specified in Section 2.8. The results of this SCF calculation are provided in Figure 3.13. This calculation was determined to be converged with respect to energy after 25 iterations with a final total energy of the system equal to  $-16\,072.3638$  Ry.

Next, the band structure and DOS were calculated and these results are depicted

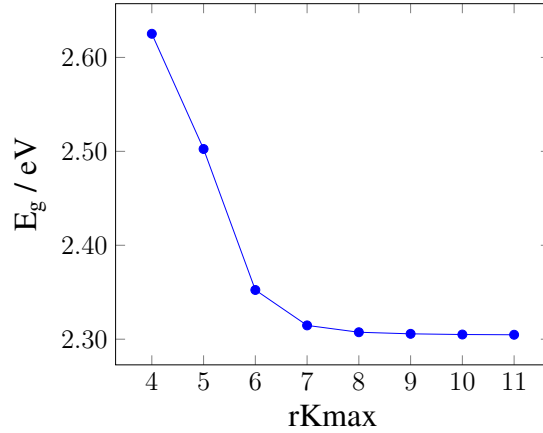


**Figure 3.12:**  $E_g$  convergence plot as a function of varying rkmax. *Source:* prepared using the PSTricks package of  $\text{\LaTeX}$ .

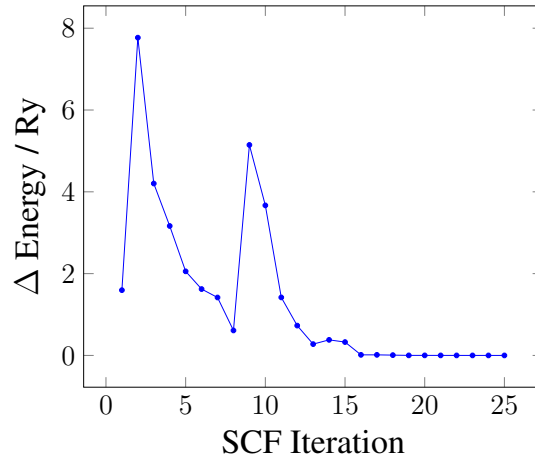


**Figure 3.13:** A plot of brookite’s energy convergence as a function of SCF iteration. The energy convergence criteria was set to 0.1 mRy, and convergence was achieved after 25 iterations. *Source:* prepared using the PSTricks package of  $\text{\LaTeX}$ .

in Figure 3.14. The Fermi level (signified by the brown dashed line in all three panels) was found to be 0.3746 eV, which was then set as the zero energy reference point. From the band structure, a direct  $E_g$  of 2.31 eV was determined at the K1 k-point. This  $E_g$  compared relatively well with the experimental  $E_g$  of 3.10 eV obtained via UV-visible spectroscopy,<sup>40</sup> but was still underestimated, as previously discussed. The  $E_g$  also compared relatively well with previous calculations in the literature, which reported  $E_g = 1.86$  eV using the DFT/PBE-GGA method,  $E_g = 3.30$  eV using the DFT/HSE method,  $E_g = 3.45$  eV using the PBE-GGA/GW method,  $E_g = 3.68$  eV

using the HSE/GW method, and  $E_g = 2.90$  eV using the PBE-GGA+U method.<sup>45,47</sup>

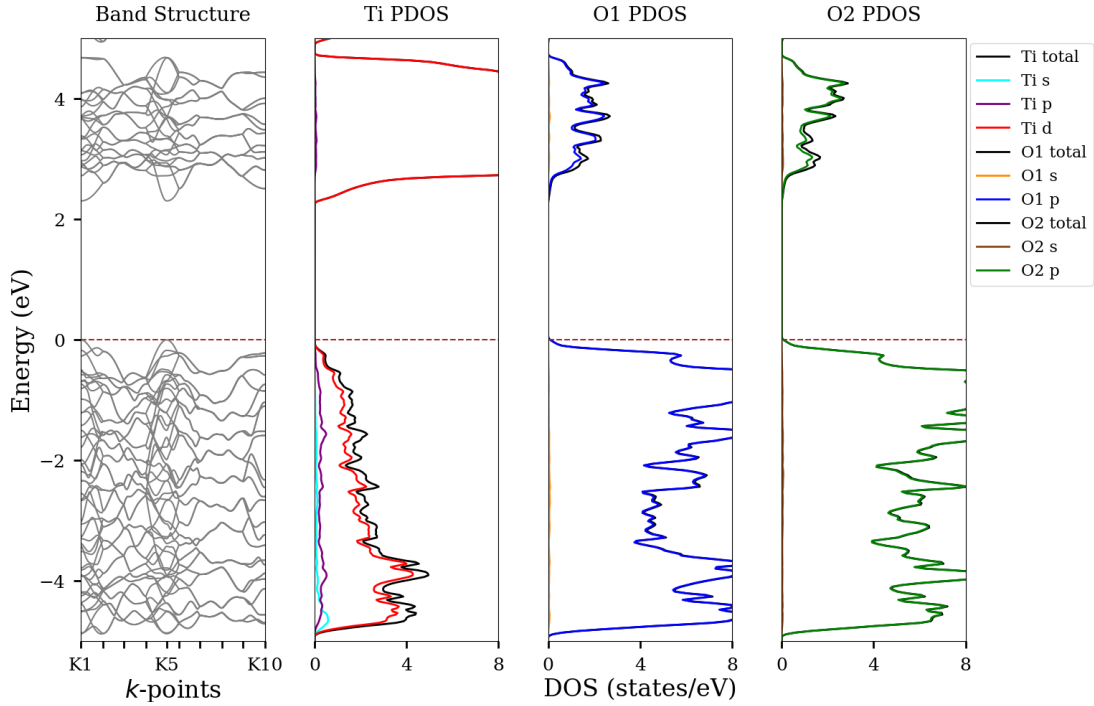


**Figure 3.14:** The band structure (left) of brookite along with its partial DOS diagrams for titanium (left center), oxygen1 (right center), and oxygen2 (right). *Source:* prepared using: Python Software Foundation. Python Language Reference, version 2.7. Available at <http://www.python.org>.

The DOS results are provided in Figure 3.14 (left center, right center, and right). The total DOS of titanium and oxygen are depicted in black in their respective DOS diagrams. However, in the case of brookite, there are two crystallographically unique oxygen atoms. Although very similar, the DOS contributions from each of these oxygen atoms are shown separately. Titanium-s, -p, and -d state contributions are again depicted in cyan, purple, and red, respectively. Oxygen1-s and -p state contributions are depicted in orange and blue. Oxygen2-s and -p state contributions are depicted in brown and green. The DOS results indicate predominant contributions from the oxygen-p states in the valence band region (-5 to 0 eV) along with minor contributions from the titanium-s, -p, and -d states. In the conduction band region (2-5 eV), titanium-d states and oxygen-p states comprise the major DOS contributions. The partial DOS of rutile compared very well with that previously published in the

literature (Figure 3.15).<sup>45</sup> Their band structure reported a direct  $E_g$  of 1.86 eV and primary DOS contributions from oxygen-p states in the valence band and titanium-d states in the conduction band.

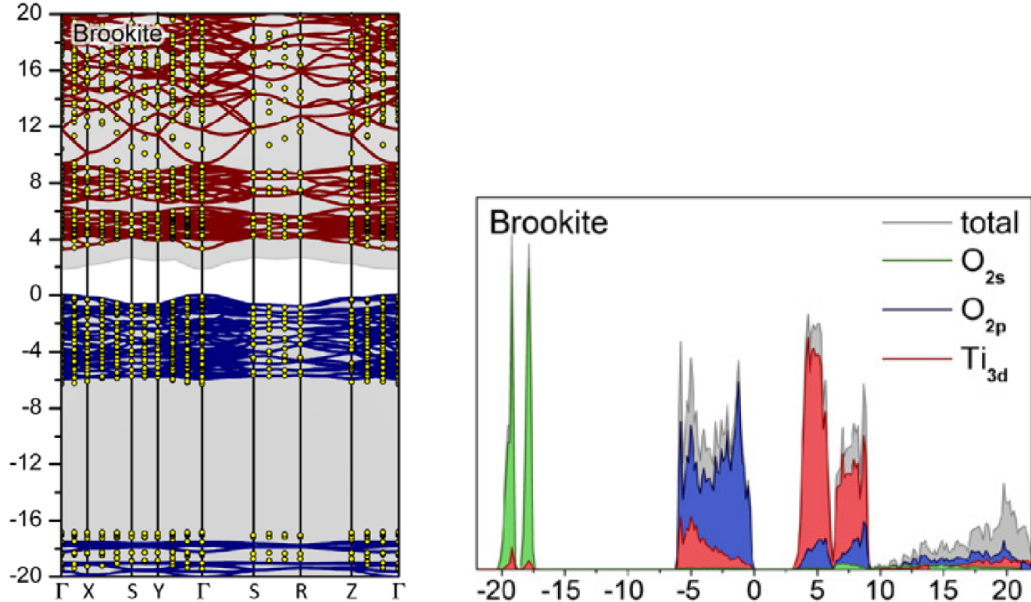


**Figure 3.15:** The band structure (left) of brookite and partial DOS (right) reported in the literature using the HSE06 XC functional. *Source:* reprinted with permission from: Landmann, M. et al. The electronic structure and optical response of rutile, anatase and brookite  $\text{TiO}_2$ . *J. Phys.: Condens. Matter* **2012**, *24*, 195503 (1–6).

In addition to the PBE-GGA band structure (repeated in Figure 3.16 left), the mBJ potential was also added for improved  $E_g$  calculation (Figure 3.16 right). The mBJ calculation resulted in an direct  $E_g$  of 3.10 at the  $\Gamma$  k-point. It is again important to note that the topology of the bands via mBJ is very comparable to that determined using solely PBE-GGA.

### 3.6 Unsubstituted Electronic Structure Summary

Although the  $E_g$  values calculated (using the PBE-GGA XC functional) for rutile, anatase, and brookite compared relatively well with previous calculations and experimental data, it was evident that the computed values were noticeably underestimated. This was attributed to the inability to accurately account for the XC energy in the SCF calculations. A variety of methods have been proposed to circumvent this challenge and more accurately calculate  $E_g$  values. One such method, as utilized in

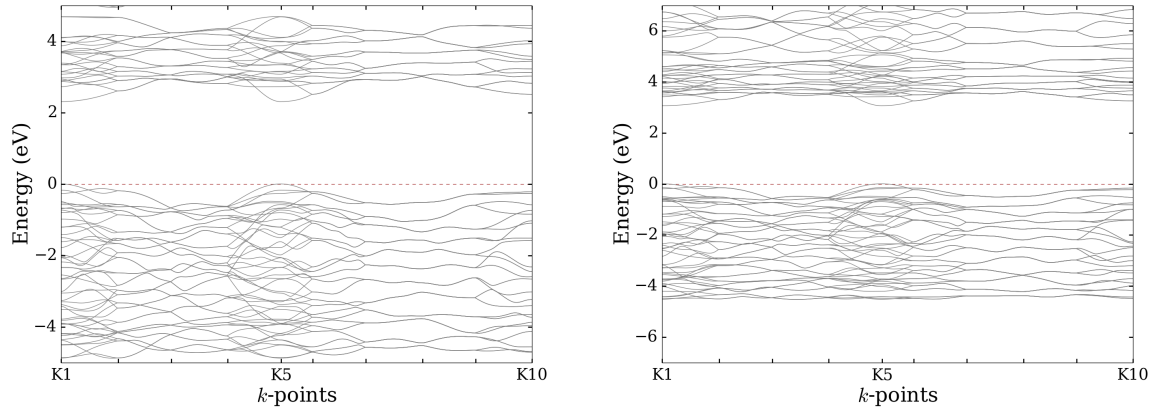


**Figure 3.16:** The band structures of brookite with the PBE-GGA XC functional (left) and the PBE-GGA + mBJ potential (right). *Source:* prepared using: Python Software Foundation. Python Language Reference, version 2.7. Available at <http://www.python.org>.

this work, is the mBJ exchange potential.<sup>93,94</sup> The benefits of this potential are that it leads to band structure calculations nearly as cheap as LSDA or PBE-GGA, allowing it to be efficiently applied to very large systems while more expensive methods, such as hybrid or GW, have size limitations.<sup>94</sup> These advantages make the mBJ method extremely appealing for future calculations, especially considering the size of the substituted systems that are promising PV candidates. However, one drawback of this potential is that its implementation in cases with ferromagnetic metals (iron, cobalt, and nickel) leads to very large magnetic moments, which the authors attribute to insufficient screening of the enhanced exchange term.<sup>93</sup> Although the computations carried out in this work did not involve ferromagnetic metals, several diamond-like semiconductors (DLS) with interesting PV, optical, and thermoelectric properties contain ferromagnetic metals. Therefore, future work in this field must continue to investigate other exchange potentials for accurate  $E_g$  calculations.

Results of the mBJ calculations for rutile, anatase and brookite produced  $E_g$  values of 2.61, 2.88 and 3.06 eV, respectively. Compared to the standard band structure calculation of rutile with PBE-GGA (discussed above), these results showed significant improvement in the  $E_g$  underestimation. The values calculated here also compare very well with experimental UV-visible spectroscopy  $E_g$  and the other computational

methods reported in the literature. However, the method still has limitations, as evidenced in this work. For instance, the PBE-GGA + mBJ method does not produce the same qualitative order of the  $E_g$  values compared to experiment while other methods in the literature (see Table 3.3) do predict the correct order.

The dependence of  $E_g$  on geometry optimization of the unit cells was also investigated in this work. The geometry of the atoms within the unit cell were allowed to relax with the force convergence criteria specified in Section 2.8. Results of geometry optimization (row 4 of Table 3.3) indicated no change in the calculated  $E_g$ . Although the data is not shown, the impact of volume optimization on  $E_g$  calculations was also investigated. Upon optimizing the volume with constant a:b:c ratios, the  $E_g$  values for the three polymorphs of  $\text{TiO}_2$  became less accurate when comparing to the experimental data. The results of geometry and volume optimization suggest that carrying out a DFT/PBE-GGA calculation (using the experimental lattice parameters from X-ray diffraction) followed by implementation of the mBJ potential is sufficient for accurate  $E_g$  calculations. However, in the case where structural data is not present for a system of interest, volume and geometry optimizations must be implemented to determine the most favorable structure. Results of band structure calculations and  $E_g$  data are summarized in Table 3.3, where rows 3-5 summarize the calculations carried out in this work and the last two rows summarize similar reports in the literature.

<b>Method</b>	<b>Rutile <math>E_g</math> (eV)</b>	<b>Anatase <math>E_g</math> (eV)</b>	<b>Brookite <math>E_g</math> (eV)</b>
Experimental <sup>40</sup>	3.00	3.21	3.13
PBE-GGA	1.90	2.05	2.31
PBE-GGA + geom opt	1.90	2.05	2.31
PBE-GGA + mBJ	2.61	2.88	3.06
Reported with VASP <sup>47</sup>	2.65	3.01	2.94
Reported with WIEN2k <sup>46</sup>	2.60	3.01	NA

**Table 3.3:** A summary of the  $E_g$  calculations carried out in this work compared to experimental data and other calculations from the literature.

Furthermore, the DOS results of Sections 3.3, 3.4, and 3.5 agreed very well with

those reported in the literature. The agreement between calculations of unsubstituted TiO<sub>2</sub> polymorphs in this work and those reported in the literature provided validation of the method prior to the substituted systems of interest in Chapter 4. Inspection of the DOS near the  $E_g$ , particularly in the valence band region, revealed a significant oxygen-p state contribution. In attempt to decrease the  $E_g$  of the TiO<sub>2</sub> polymorphs, the oxygen-p state contributions serve as a likely target. Here, substituents possessing a higher ionization energy than oxygen would potentially shift the valence band contributions to higher energy, narrowing the  $E_g$ . The impact of substituent properties is further investigated in Chapter 4.

## Chapter 4. Substituted TiO<sub>2</sub>

### 4.1 Modeling Supercells

With the electronic structure of unsubstituted rutile, anatase, and brookite successfully calculated in Chapter 3, the effects of atomic substitutions in these polymorphs were investigated. As explained previously, due to the high computational cost of the brookite polymorph, only the rutile and anatase polymorphs were subject to substitution in this study. Aiming to tune the electronic structure, particularly the  $E_g$  value, various elements were chosen for anionic (oxygen site) substitution in the polymorphs' lattices. It should be noted that cationic (titanium site) substitutions are also possible in these systems and have been previously studied in the literature.<sup>48-51</sup> However, due to the significant evidence of oxygen-p state DOS contributions to the valence band region of unsubstituted rutile, anatase, and brookite (Figures 3.4, 3.9, and 3.14), the anionic substitutions were primarily studied in this work. Future work will aim to investigate the effects of cationic substitutions.

A summary of the substituents selected for this work is provided in Table 4.1. The selected substituents were fluorine, nitrogen, sulfur, and tellurium. It should be noted that oxygen is included in the data set and does not reflect another calculation, but merely represents the calculated  $E_g$  values for the unsubstituted compositions. Accompanying each of the substituents in Table 4.1 is a variety of each atom's chemical properties. As discussed in the hypothesis and specific aims of Section 1.7, the primary goal of the substitution studies presented herein is to identify what chemical property of the substituent gives rise to the change in electronic structure, particularly the  $E_g$  value. The chemical properties selected are a reflection of proposed ideas in the literature as well as intuition regarding the material's electronic structure. For instance, the work of Chen et al. proposed a possible  $E_g$  dependence on the IE of the substituent atom.<sup>57</sup> The work of Pan et al. suggested a linear relationship between the  $E_g$  value and the substituent's MP.<sup>58</sup> In addition, Hoffmann's conceptual discussion



Substituent	MP / °C	Z/CR	$\chi$	CR / Å	IE / eV
F	-220	0.74	3.98	1.16	17.42
O	-218	1.43	3.44	1.22	13.62
N	-210	1.75	3.04	1.32	14.53
S	113	1.09	2.58	1.70	10.36
Te	449	0.90	2.10	2.07	9.01

**Table 4.1:** Substituents selected for substitution into the rutile and anatase polymorphs. Various chemical properties are also provided for each substituent, where MP is the melting point, Z/CR is the charge to radius ratio,  $\chi$  is the electronegativity, CR is the crystallographic radius, and IE is the ionization energy. *Source:* data reproduced from: Pauling, L. The nature of the chemical bond. IV. The energy of single bonds and the relative electronegativity of atoms. *J. Am. Chem. Soc.* **1932**, *54*, 3570–3582; Shannon, R. Revised effective ionic radii and systematic studies of interatomic distances in halides and chalcogenides. *Acta Cryst.* **1976**, *A32*, 751–767; *CRC handbook of chemistry and physics*, 97th ed.; CRC Press: Boca Raton, FL, 2017.

of band structures identified the CR and electronegativity governing the topology of bands.<sup>14</sup> Each of these chemical properties were included in this study along with a charge/CR ratio. It should be noted that Pauling’s electronegativity and Shannon’s crystal radii were utilized in this work.<sup>102–104</sup> In addition, IE and MP values of the substituents were obtained from the CRC handbook.<sup>105</sup>

In order to carry out the aforementioned substitutions, 2x2x2 supercells of each polymorph were generated using CrystalMaker.<sup>99</sup> From CrystalMaker, a crystallographic information file was exported and converted to a WIEN2k structure file using the cif2struct command. The supercells of rutile and anatase each contained 48 atoms. Following supercell generation, individual oxygen atoms within the supercell were replaced with the substituents outlined in Table 4.1. Upon substitution, the symmetry of each polymorph was broken and the supercells adopted the P1 space group. Next, a SCF calculation was carried out on each substituted system. In the substituted cases, geometry optimizations were performed within the SCF cycle to relax the atomic positions, particularly those surrounding the substitution site. An example of the energy convergence for sulfur-substituted rutile is shown below in Figure 4.1. As expected with the increase in system size and the overall number

of electrons, the sulfur-substituted supercell took many more SCF iterations to converge. In this case, the calculation converged after 262 iterations with a total energy of  $-32\,792.2220$  Ry.

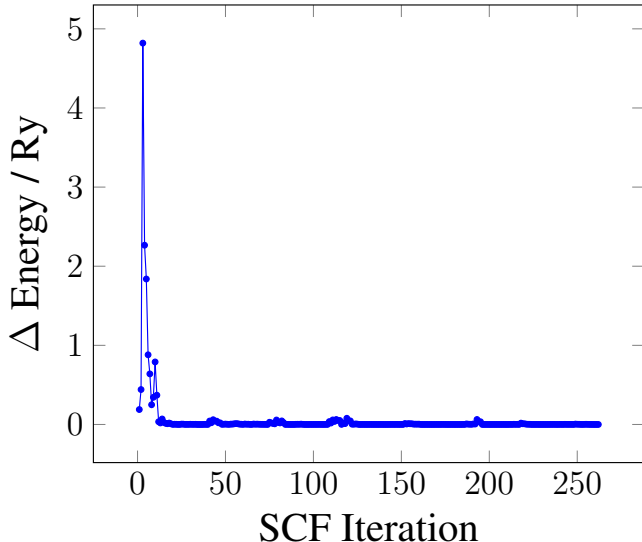


**Figure 4.1:** Sulfur-substituted rutile’s energy convergence as a function of SCF iteration. The energy convergence criteria was set to 0.1 mRy and convergence was achieved after 262 iterations. *Source:* prepared using the PSTricks package of L<sup>A</sup>T<sub>E</sub>X.

## 4.2 Impact of Substituent Position

In order to determine the impact of substituent position on the calculated  $E_g$  value, a variety of oxygen sites in the supercell were selected for anionic substitution. Sulfur was selected for testing the effects of substituent position as highlighted in Figure 4.2. The  $E_g$  values of sulfur-substituted rutile were calculated using both PBE-GGA and PBE-GGA + mBJ. The results of these calculations are summarized in Table 4.2, demonstrating that the position of the substituent within the supercell does not govern the  $E_g$  value. The calculated  $E_g$  values were approximately 1.37 and 1.87 eV for the PBE-GGA and PBE-GGA + mBJ methods, respectively. The band structure of sulfur-substituted rutile is provided in Figure 4.3 (left) and indicates a direct  $E_g$  at the K1 and K4 k-points. Compared to the band structures of the unsubstituted polymorphs in Chapter 3, many more bands exist in the band structures of the substituted systems. This arises from the additional atoms present in the supercell,

which introduces extra electrons and electronic states. Due to the fact that the electronic structures of the five different substituent positions were identical, only one is shown here.

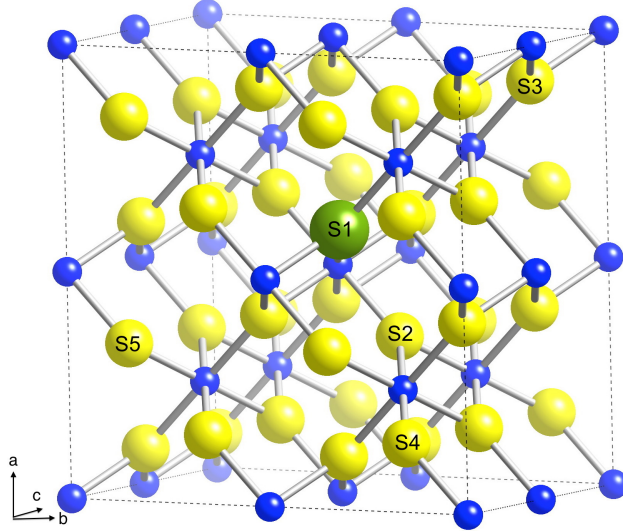


**Figure 4.2:** A 2x2x2 supercell of rutile with five oxygen sites highlighted for sulfur substitution. These sites were selected to determine the impact of substituent position on the calculated  $E_g$ . *Source:* prepared using CrystalMaker<sup>®</sup>: a crystal and molecular structures program for Mac and Windows. CrystalMaker Software Ltd, Oxford, England ([www.crystallmaker.com](http://www.crystallmaker.com)).

Position	PBE-GGA $E_g$ / eV	mBJ $E_g$ / eV
S1	1.37	1.87
S2	1.36	1.87
S3	1.36	1.87
S4	1.36	1.87
S5	1.36	1.87

**Table 4.2:** PBE-GGA and PBE-GGA + mBJ calculated  $E_g$  values for the five oxygen-site substitutions outlined in Figure 4.2. A single sulfur substitution was carried out in each calculation.

The partial DOS analysis (Figure 4.3 left center, right center, and right) was used to investigate the atomic and orbital contribution to the bands near  $E_g$ . The total DOS of titanium, oxygen, and sulfur are depicted in black in their respective DOS diagrams. Titanium-s, -p, and -d state contributions are depicted in cyan, purple, and red, respectively. Oxygen-s and -p state contributions are depicted in orange and blue. Sulfur-s and -p state contributions are depicted in green and yellow. The DOS

results indicate predominant contributions from the oxygen and sulfur-p states in the valence band region (-5 to 0 eV) along with minor contributions from the titanium-s, -p, and -d states. In the conduction band region (2-5 eV), titanium-d states and oxygen-p states comprise the major DOS contributions. Upon sulfur substitution, the  $E_g$  decreased from 1.90 eV (unsubstituted rutile) to 1.37 eV. Reports in the literature characterize the lone band near the Fermi level as a mid-gap state; however, this band still defines the valence band maximum and  $E_g$  is therefore measured from here to the conduction band minimum.<sup>55</sup>

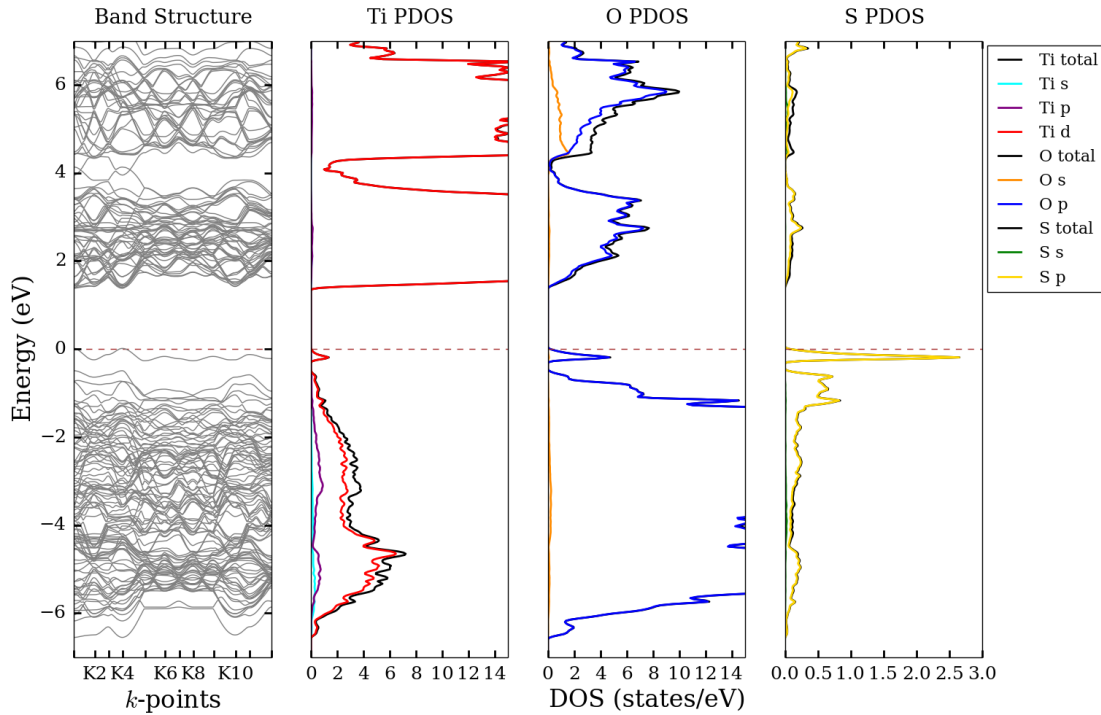


**Figure 4.3:** The band structure (left) of sulfur-substituted rutile along with its partial DOS diagrams for titanium (left center), oxygen (right center), and sulfur (right). *Source:* prepared using Python Software Foundation. Python Language Reference, version 2.7. Available at <http://www.python.org>.

In addition to the PBE-GGA band structure, the mBJ potential was also added for improved  $E_g$  calculation (Figure 4.4). The mBJ calculation resulted in a direct  $E_g$  of 1.87 eV at the K1 k-point. It is also important to note that the topology of the bands via mBJ is again similar to that determined using solely PBE-GGA. It is also important to note that a similar decrease in  $E_g$  was observed upon sulfur substitution

with the mBJ potential as was observed with PBE-GGA alone.

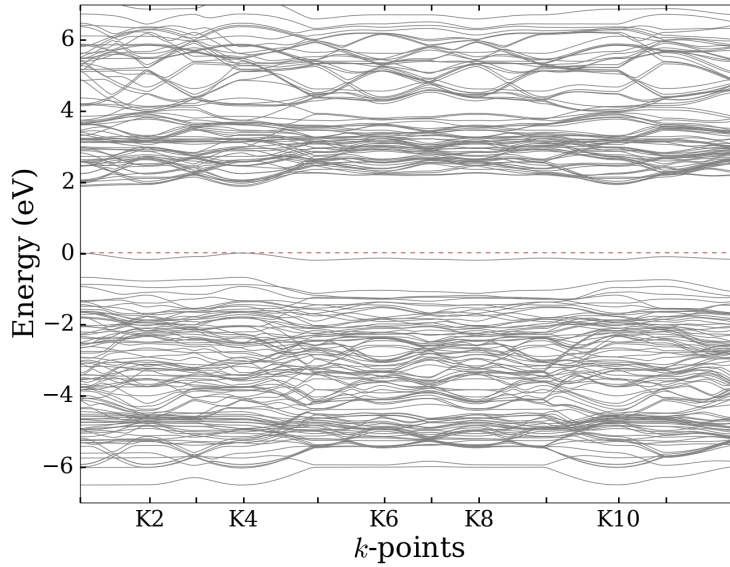


**Figure 4.4:** The band structure of sulfur-substituted rutile with the PBE-GGA + mBJ potential. *Source:* prepared using: Python Software Foundation. Python Language Reference, version 2.7. Available at <http://www.python.org>.

### 4.3 Impact of Substituent Percentage

The impact of substituent percentage was also investigated in this work. Increasing substituent percentage was achieved by adding additional sulfur atoms on oxygen sites within the supercell. A single oxygen atom exchanged for sulfur resulted in a 2.1% sulfur substitution. This percentage is calculated by totaling all of the atomic contributions in the supercell, considering that atoms located on the supercell’s corners count for 1/8, atoms on edges count for 1/4, atoms on faces count for 1/2, and body-centered atoms count for 1. Upon assigning each of the fractional contributions, these are then summed for each atom before reducing the chemical formula. Therefore, a 2.1% sulfur substitution corresponds to the structure  $\text{TiO}_{1.9375}\text{S}_{0.0625}$ . Adding a second, third, and 4th sulfur atom to the supercell resulted in substitutions of 4.2, 6.3, and 8.3%, respectively. This data is summarized in Table 4.3 and Figure 4.5.

As evidenced in Figure 4.5, the  $E_g$  value decreases in a linear fashion with the the 2.1, 4.2, and 6.3% sulfur substitutions. However, upon increasing the sulfur substitution percentage to 8.3%, the  $E_g$  value plateaus and does not experience further

Structure	Substitution %	PBE-GGA $E_g$ /eV	mBJ $E_g$ /eV
TiO <sub>2</sub>	0	1.90	2.57
TiO <sub>1.9375</sub> S <sub>0.0625</sub>	2.1	1.37	1.87
TiO <sub>1.875</sub> S <sub>0.125</sub>	4.2	0.97	1.41
TiO <sub>1.75</sub> S <sub>0.25</sub>	6.3	0.58	0.96
TiO <sub>1.5</sub> S <sub>0.5</sub>	8.3	0.57	1.02
TiS <sub>2</sub>	NA	0.26†	NA

**Table 4.3:** The structural formulas, substitution percentages, and calculated  $E_g$  values for various degrees of sulfur substitution.  $E_g$  values are reported in both PBE-GGA (blue) and PBE-GGA + mBJ (red) methodologies. †The  $E_g$  of a fully-substituted lattice is also provided, which results in the structure TiS<sub>2</sub>.<sup>106</sup>

decrease, suggesting that the extent of  $E_g$  narrowing has a threshold limit. Overall, the trend of  $E_g$  decreasing with increasing substituent % was observed in both the PBE-GGA and PBE-GGA + mBJ methodologies. In addition, error bars were added

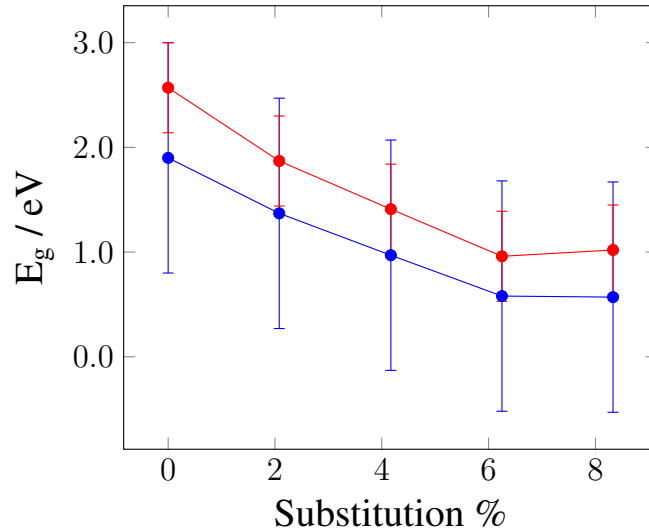


**Figure 4.5:** The calculated  $E_g$  values as a function of various degrees of sulfur substitution.  $E_g$  values are reported in both PBE-GGA (blue) and PBE-GGA + mBJ (red) methodologies. *Source:* prepared using the PSTricks package of L<sup>A</sup>T<sub>E</sub>X.

to the data points in Figure 4.5. In 2016, Crowley et al. reported a total mean absolute deviation of 1.10 eV for the PBE-GGA method by comparing the calculated  $E_g$  values of 64 compounds to their respective experimental values.<sup>107</sup> This PBE-GGA deviation was taken into consideration in this work and is indicated via blue error bars. In 2012, Camargo-Martínez and Baquero reported total mean absolute deviations of 0.43 eV for the PBE-GGA + mBJ method by comparing the calculated  $E_g$  values

of 41 compounds to their respective experimental values.<sup>108</sup> This mBJ deviation was taken into consideration in this work and is indicated via red error bars.

The electronic structures (band structure and DOS) for each of the above substitutions are provided in Figures 4.3 (2.1%), 4.6 (4.2%), 4.7 (6.3%), and 4.8 (8.3%). See Section 4.2 for Figure 4.3 (2.1% sulfur-substituted rutile electronic structure). The band structure of 4.2% sulfur-substituted rutile (Figure 4.6 left) revealed a direct  $E_g$  of 0.97 eV at the K1 and K4 k-points. The partial DOS analysis (Figure

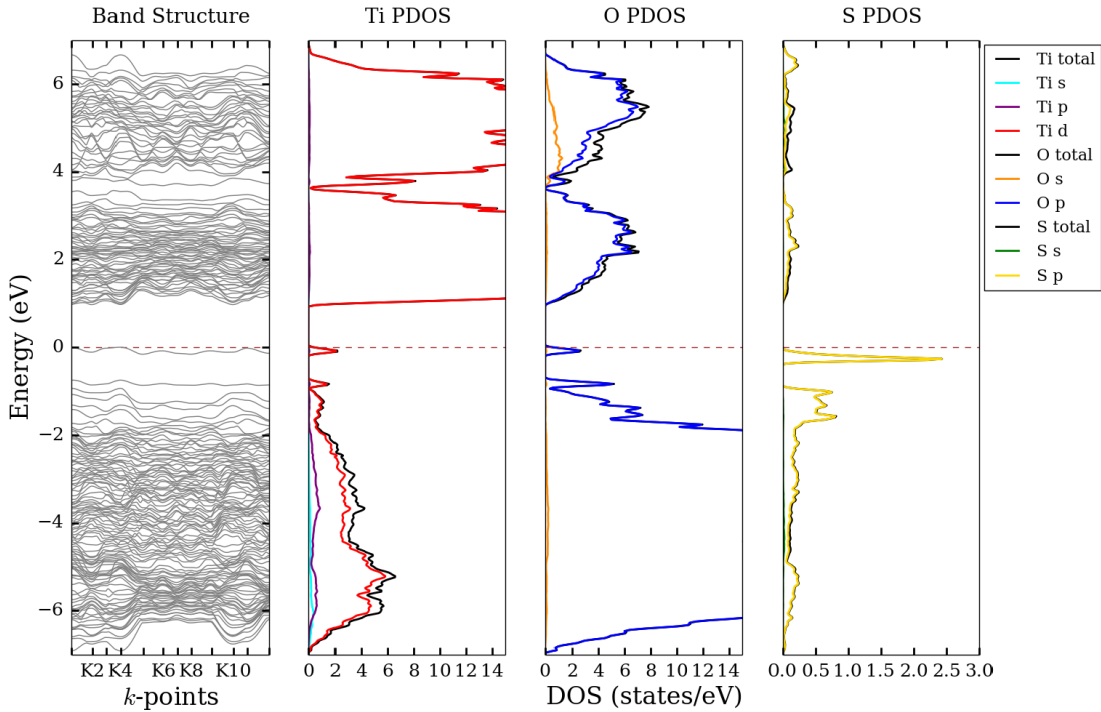


**Figure 4.6:** The band structure (left) of 4.2% sulfur-substituted rutile along with its partial DOS diagrams for titanium (left center), oxygen (right center), and sulfur (right). *Source:* prepared using Python Software Foundation. Python Language Reference, version 2.7. Available at <http://www.python.org>.

4.6 left center, right center, and right) indicates predominant contributions from the oxygen (blue) and sulfur-p (yellow) states in the valence band region (-5 to 0 eV). In addition, titanium-s, -p, and -d states provide minor contributions in the valence band region. In the conduction band region (2-5 eV), titanium-d states and oxygen-p states comprise the major DOS contributions. Overall, the  $E_g$  value decreased from 1.37 eV (2.1% sulfur substitution) to 0.97 eV (4.3% sulfur substitution).

The band structure of 6.3% sulfur-substituted rutile (Figure 4.7 left) revealed a direct  $E_g$  of 0.58 eV at the K1 and K4 k-points. The partial DOS analysis (Figure 4.7 left center, right center, and right) was very similar to those discussed for the 2.1 and 4.2% substitutions. However, in this case, a very interesting phenomenon occurs in the DOS near the  $E_g$  value. While there is still a distinct, sharp peak below the

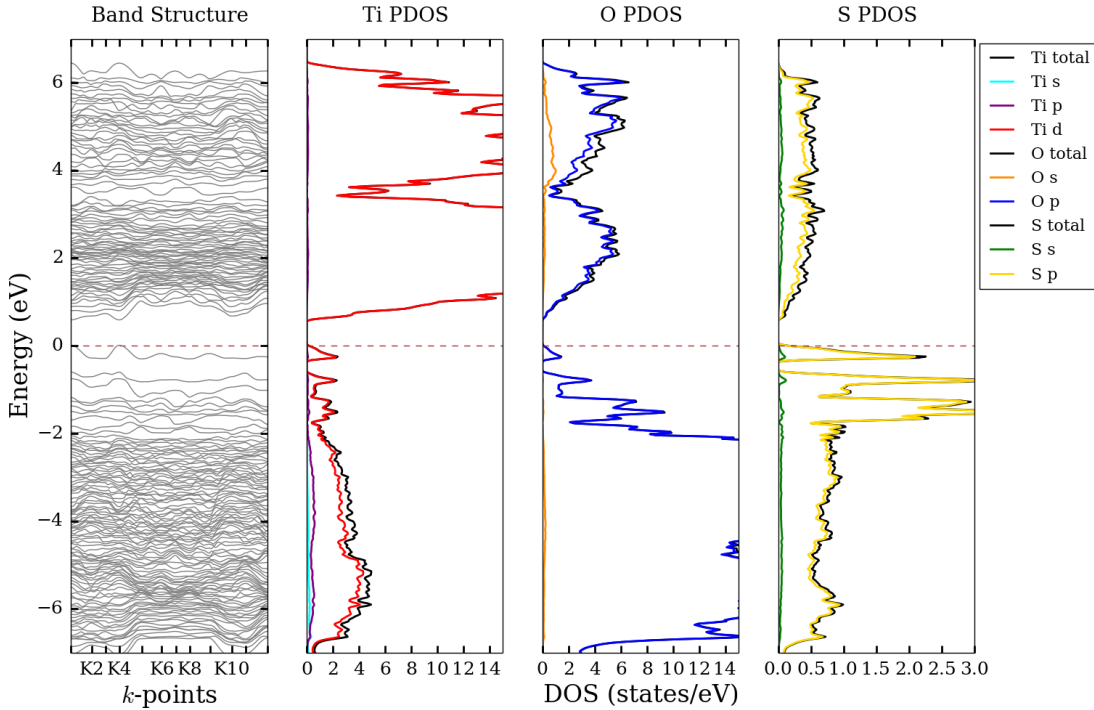


**Figure 4.7:** The band structure (left) of 6.3% sulfur-substituted rutile along with its partial DOS diagrams for titanium (left center), oxygen (right center), and sulfur (right). *Source:* prepared using Python Software Foundation. Python Language Reference, version 2.7. Available at <http://www.python.org>.

Fermi level, resulting from the sulfur-p states, there is now a much greater sulfur-p state contribution below this sharp peak in the valence band region. These sulfur-p states in the range of  $-0.5$  eV to  $-1.0$  eV are much greater than those observed in the same energy range of the 2.1 and 4.2% sulfur-substituted cases. Despite this marked change in the sulfur DOS, the overall magnitude of  $E_g$  still decreased linearly from 0.97 eV (4.3% sulfur substitution) to 0.58 eV (6.3% sulfur substitution).

The band structure of 8.3% sulfur-substituted rutile (Figure 4.8 left) revealed an indirect  $E_g$  of 0.57 eV. The partial DOS analysis (Figure 4.8 left center, right center,



and right) again indicated contributions very similar to those discussed for the 2.1, 4.2, and 6.3% substitutions. However, in the case of 8.3% substitution, significantly

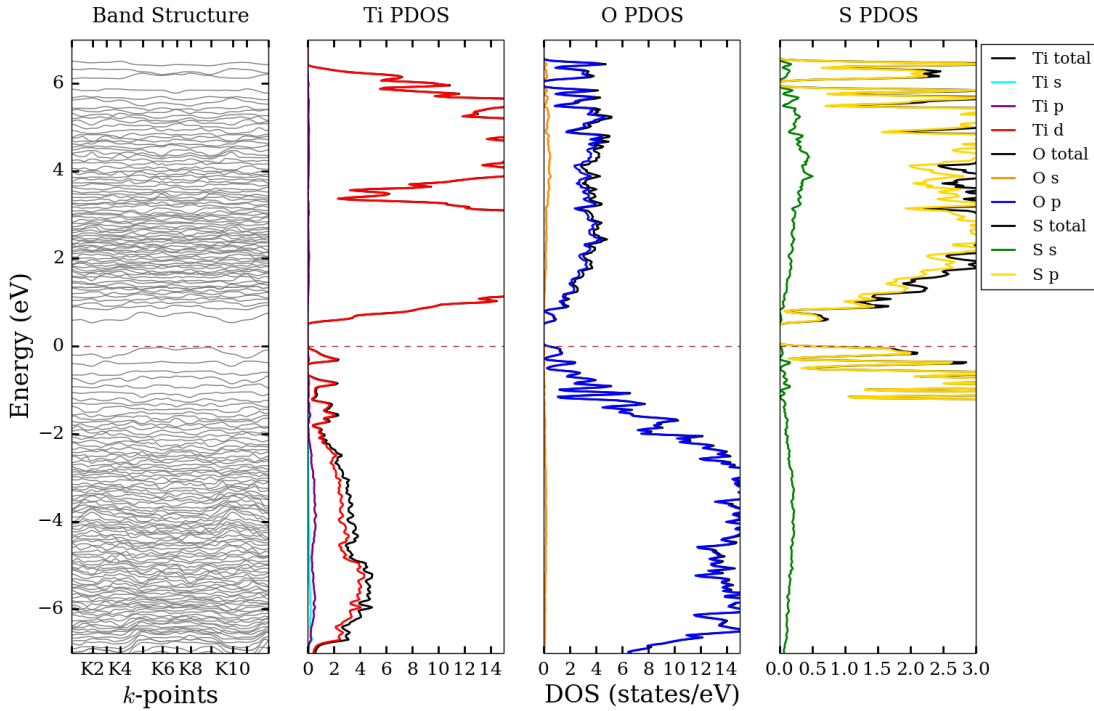


**Figure 4.8:** The band structure (left) of 8.3% sulfur-substituted rutile along with its partial DOS diagrams for titanium (left center), oxygen (right center), and sulfur (right). *Source:* prepared using Python Software Foundation. Python Language Reference, version 2.7. Available at <http://www.python.org>.

greater sulfur-p state contributions were evident in the valence and conduction bands. These sulfur-p states in the range of 0 eV to 6.0 eV are much greater than those observed in the same energy range of the previous substitution percentages. Despite this marked change in the sulfur DOS, the overall magnitude of  $E_g$  remained relatively constant, decreasing only from 0.58 eV (6.3% sulfur substitution) to 0.57 eV (8.3% sulfur substitution).

In addition to the PBE-GGA band structures, the mBJ potential was also added for improved  $E_g$  calculation and the results are provided in Figure 4.9. The mBJ calculations resulted in  $E_g$  values of 1.87, 1.41, 0.96, and 1.02 eV for the 2.1, 4.2, 6.3, and 8.3% substitutions, respectively. It is again important to note that the topology of the bands via mBJ is very comparable to that determined using solely

PBE-GGA. As was observed with the PBE-GGA functional, a similar decrease in  $E_g$  was observed with increasing sulfur substitution percentage upon incorporating the mBJ potential. This decreasing of the  $\text{TiO}_2$   $E_g$  brings its value closer to that desired for PV applications.

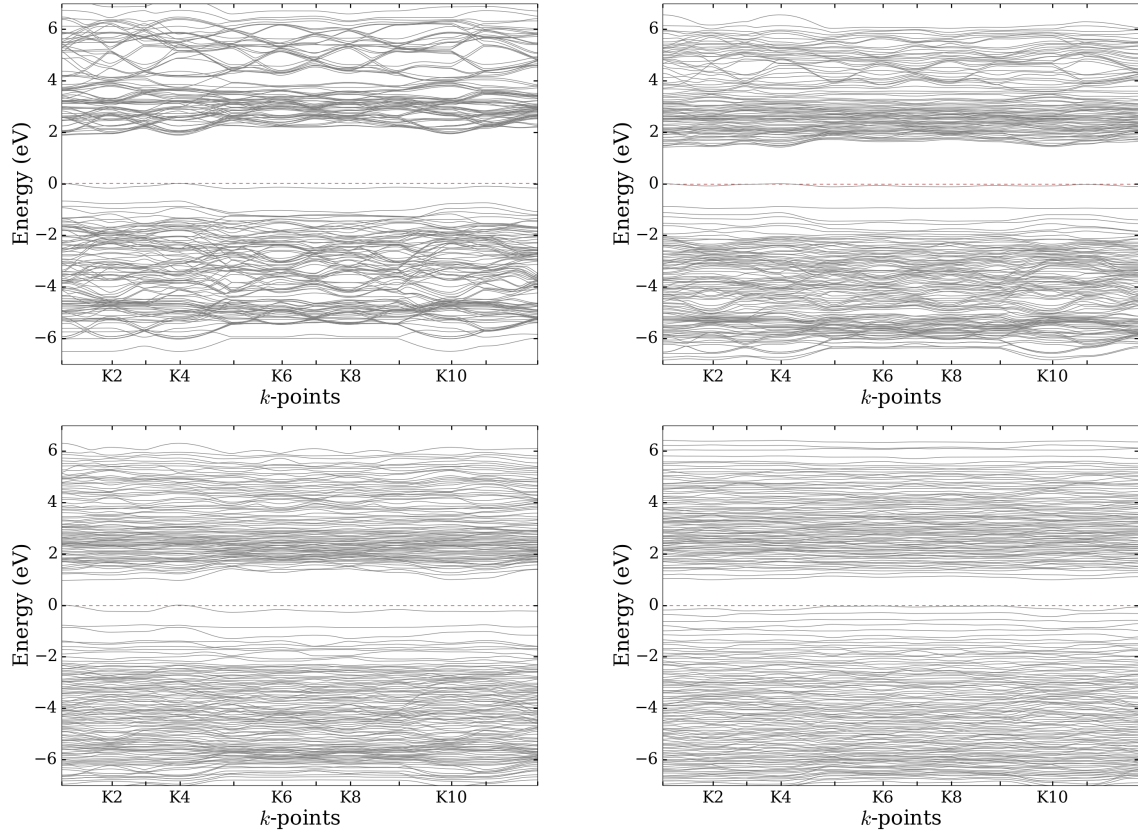


**Figure 4.9:** The band structure of 2.1% (upper left), 4.2% (upper right), 6.3% (lower left) and 8.3% (lower right) sulfur-substituted rutile with the PBE-GGA + mBJ potential. *Source:* prepared using: Python Software Foundation. Python Language Reference, version 2.7. Available at <http://www.python.org>.

#### 4.4 Electronic Structure of Substituted Rutile

In addition to the sulfur-substituted electronic structures discussed in Sections 4.2 and 4.3, the fluorine- and nitrogen-substituted electronic structure of rutile was also calculated. SCF attempts on tellurium-substituted rutile were unsuccessful, as the energy of these calculations oscillated without convergence, indicating the possibility of an unstable system. The band structure of fluorine-substituted rutile (Figure 4.10 left) revealed a direct  $E_g$  of 1.95 eV at the K1 and K4 k-points. The partial

DOS analysis (Figure 4.10 left center, right center, and right) indicated predominant contributions from the oxygen (blue) and fluorine-p (yellow) states in the valence band region (-5 to 0 eV). In addition, titanium-s, -p, and -d states provide minor contributions in the valence band region. In the conduction band region (2-5 eV), titanium-d states and oxygen-p states comprise the major DOS contributions. As opposed to the  $E_g$  narrowing observed in sulfur-substituted rutile, fluorine substitution results in a slight widening of the  $E_g$  from 1.90 eV (unsubstituted) to 1.95 eV (fluorine-substituted).

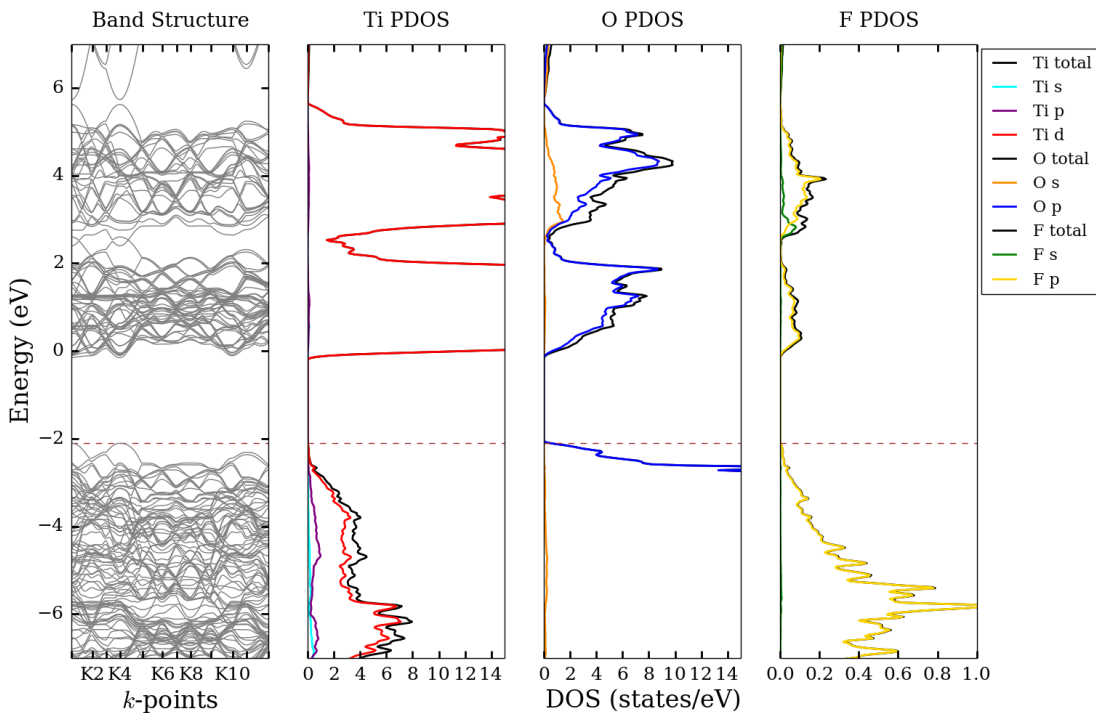


**Figure 4.10:** The band structure (left) of fluorine-substituted rutile along with its partial DOS diagrams for titanium (left center), oxygen (right center), and fluorine (right). *Source:* prepared using Python Software Foundation. Python Language Reference, version 2.7. Available at <http://www.python.org>.

The  $E_g$  widening in fluorine-substituted rutile can be rationalized by considering the chemical properties of fluorine. Fluorine possesses an extremely high electronegativity and ionization energy compared to the other substituents, which could have an effect on some of the electronic states in the band structure. For instance, fluorine substitution could drive some of the valence bands to lower energy or some of the

conduction bands to higher energy, thus widening the  $E_g$ . It is also important to point out that in the case of fluorine substitution, there is no observation of the lone band (mid-gap state) that was present in the sulfur-substituted systems. An explanation of this can again be tied back to the ionization energy of the fluorine substituent. With fluorine’s ionization energy being so high, the potential mid-gap state may not have fallen within the  $E_g$  region as it did in sulfur’s case. This is further supported by the fact that sulfur possesses an ionization energy that is closer to that of oxygen (parent composition).

The band structure of nitrogen-substituted rutile (Figure 4.11 left) revealed a direct  $E_g$  of 1.62 eV at the K1 and K4 k-points. The partial DOS analysis (Figure

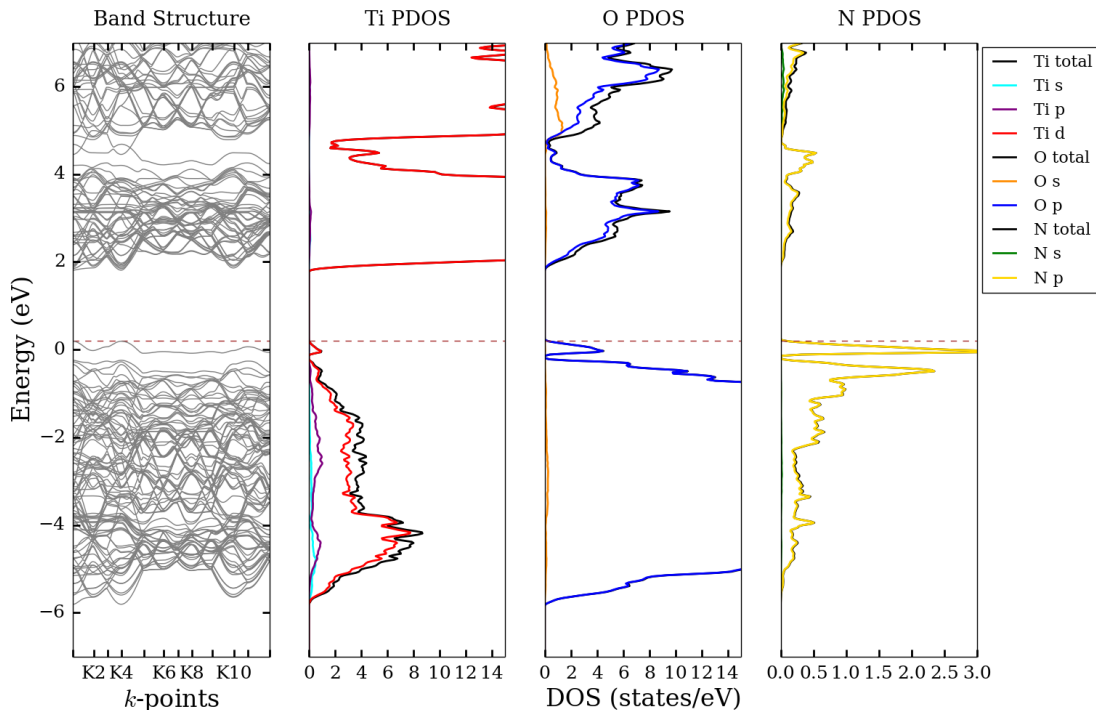


**Figure 4.11:** The band structure (left) of nitrogen-substituted rutile along with its partial DOS diagrams for titanium (left center), oxygen (right center), and nitrogen (right). *Source:* prepared using Python Software Foundation. Python Language Reference, version 2.7. Available at <http://www.python.org>.

4.11 left center, right center, and right) indicated predominant contributions from the oxygen (blue) and nitrogen-p (yellow) states in the valence band region (-5 to 0 eV). In addition, titanium-s, -p, and -d states provide minor contributions in the valence band

region. In the conduction band region (2-5 eV), titanium-d states and oxygen-p states comprise the major DOS contributions. Similar to the results of sulfur substitution, the  $E_g$  narrowing also occurred upon nitrogen substitution, but to a lesser extent than sulfur. In this case,  $E_g$  decreased from 1.90 eV (unsubstituted) to 1.62 eV (nitrogen-substituted). The nitrogen-substituted band structure also indicates the presence of the lone band (mid-gap state) that was observed in the sulfur-substituted case. The features of these lone bands near the Fermi level raise several questions regarding the chemical properties of the substituents and their impact on  $E_g$ . These discussions will be revisited in Section 4.6.

In addition to the PBE-GGA band structures, the mBJ potential was also added for improved  $E_g$  calculation and the results are provided in Figure 4.12. The mBJ

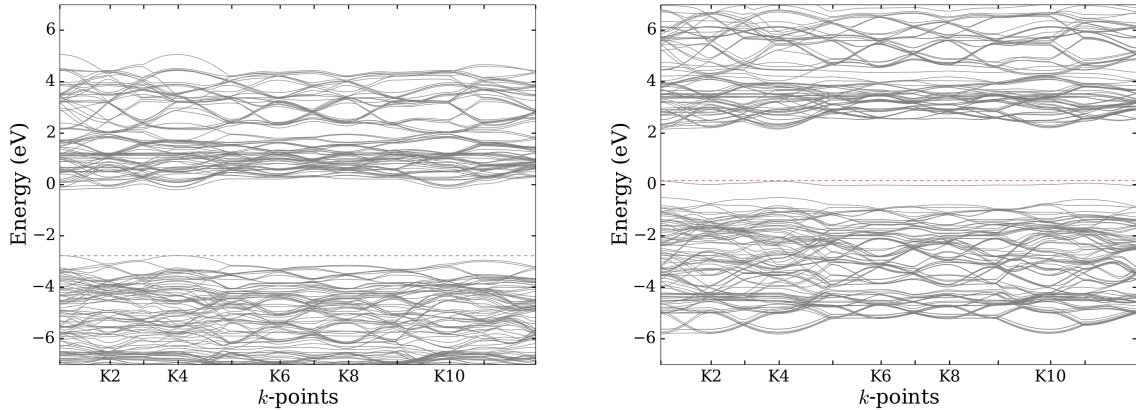


**Figure 4.12:** The band structure of fluorine (left) and nitrogen-substituted (right) rutile with the PBE-GGA + mBJ potential. *Source:* prepared using: Python Software Foundation. Python Language Reference, version 2.7. Available at <http://www.python.org>.

calculations resulted in direct  $E_g$  values of 2.56 and 2.02 eV for fluorine- and nitrogen-substituted rutile, respectively. It is again important to note that the topology of the bands via mBJ is very comparable to that determined using solely PBE-GGA. As was observed with the PBE-GGA functional, an increase in  $E_g$  was observed with fluorine substitution and a decrease in  $E_g$  was observed with nitrogen substitution in the mBJ calculations.

## 4.5 Electronic Structure of Substituted Anatase

The same substitutions were also carried out in the anatase polymorph. Unlike the rutile case, SCF attempts on tellurium-substituted anatase were successful and the results are included in this section. The band structure of sulfur-substituted anatase (Figure 4.13 left) revealed a direct  $E_g$  of 1.38 eV at the K1 and K5 k-points. It is

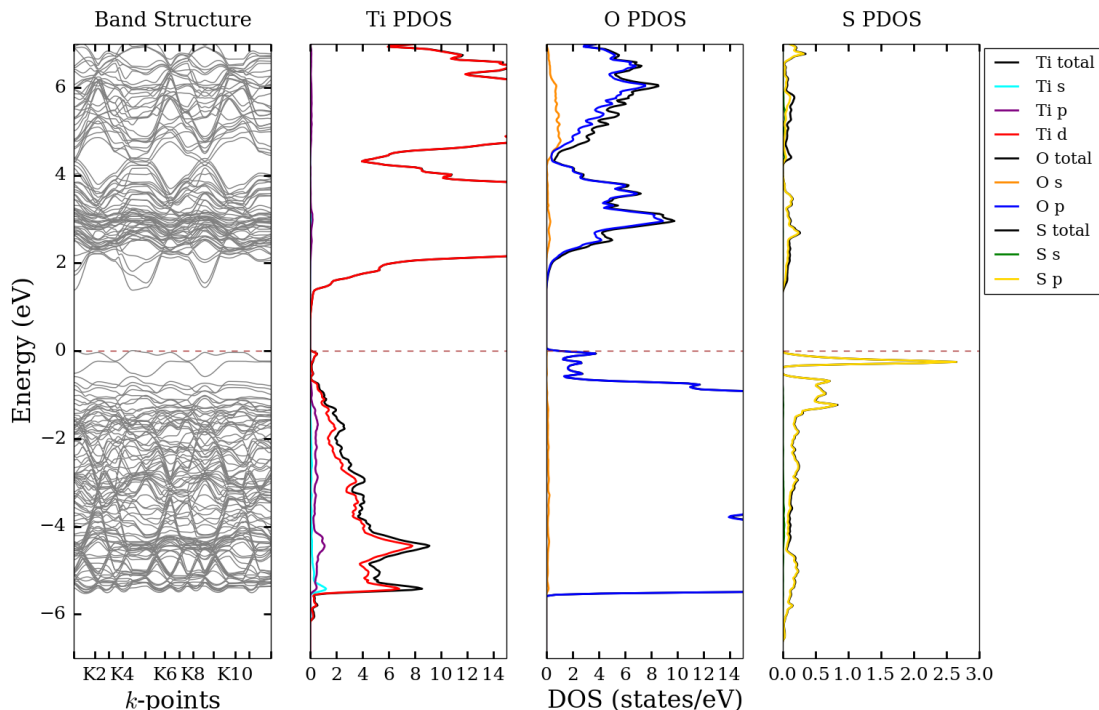


**Figure 4.13:** The band structure (left) of sulfur-substituted anatase along with its partial DOS diagrams for titanium (left center), oxygen (right center), and sulfur (right). *Source:* prepared using Python Software Foundation. Python Language Reference, version 2.7. Available at <http://www.python.org>.

important to note that the unsubstituted anatase polymorph possesses an indirect  $E_g$ . Thus, upon sulfur substitution, the  $E_g$  value transitions from indirect to direct. The partial DOS analysis (Figure 4.13 left center, right center, and right) indicated predominant contributions from the oxygen (blue) and sulfur-p (yellow) states in the valence band region (-5 to 0 eV). In addition, titanium-s, -p, and -d states provide minor contributions in the valence band region. In the conduction band region (2-5 eV), titanium-d states and oxygen-p states comprise the major DOS contributions. Again, the sulfur-substituted states appear to give rise to lone bands near the Fermi

level, indicating mid-gap states, just as observed in the sulfur-substituted rutile calculations. Overall, an  $E_g$  narrowing from 2.05 eV (unsubstituted) to 1.38 eV was observed upon sulfur substitution.

The band structure of fluorine-substituted anatase (Figure 4.14 left) revealed a direct  $E_g$  of 2.19 eV at the K1 and K5 k-points. Again, substitution was responsible for transitioning the  $E_g$  value from indirect to direct. The partial DOS analysis (Figure 4.14 left center, right center, and right) indicated predominant contributions from the oxygen (blue) and fluorine-p (yellow) states in the valence band region (-5 to 0 eV). In addition, titanium-s, -p, and -d states provide minor contributions in the valence band region. In the conduction band region (2-5 eV), titanium-d states and oxygen-p states comprise the major DOS contributions. As opposed to the  $E_g$  narrowing observed in

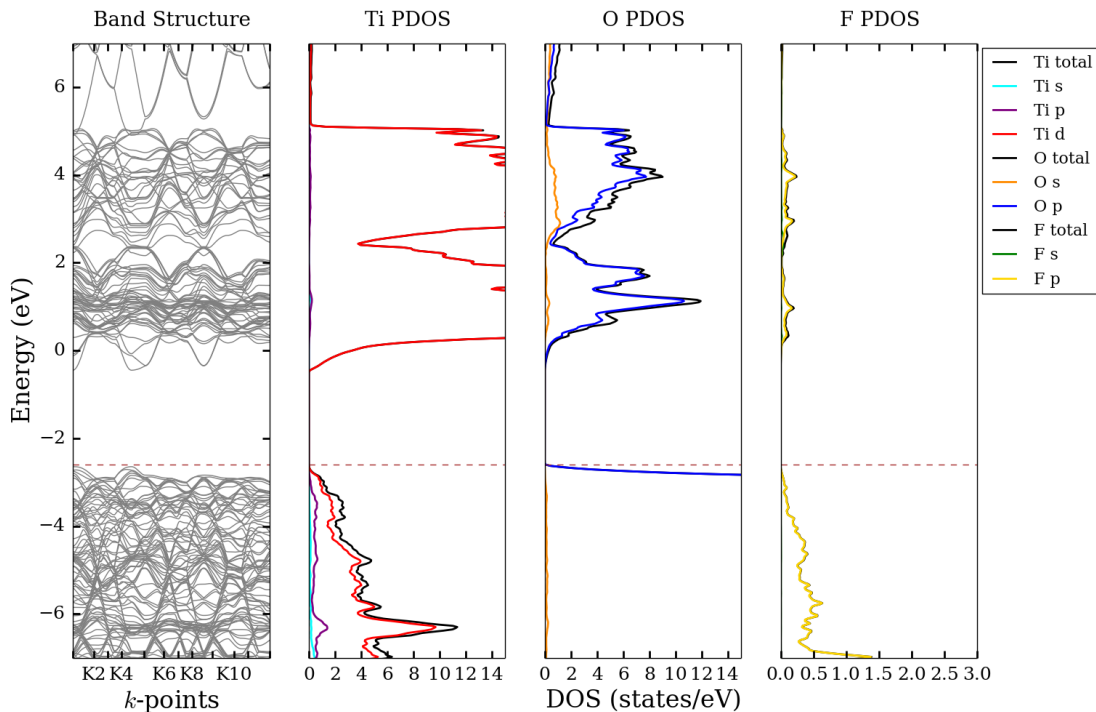


**Figure 4.14:** The band structure (left) of fluorine-substituted anatase along with its partial DOS diagrams for titanium (left center), oxygen (right center), and fluorine (right). *Source:* prepared using Python Software Foundation. Python Language Reference, version 2.7. Available at <http://www.python.org>.

sulfur-substituted anatase, fluorine substitution results in a slight widening of the  $E_g$  from 2.05 eV (unsubstituted) to 2.19 eV (fluorine-substituted). It is also important

to point out that in the case of fluorine substitution, there is no observation of the lone band (mid-gap state) that was present in the sulfur-substituted systems. Both of these results are in agreement with that observed for rutile, again suggesting the possibility that the ionization energy of the substituent dictates where the bands fall and whether a mid-gap state is present.

The band structure of nitrogen-substituted anatase (Figure 4.15 left) revealed a direct  $E_g$  of 0.52 eV at the K1 and K4 k-points. Again, substitution was responsible for transitioning the  $E_g$  value from indirect to direct. The partial DOS analysis (Figure 4.15 left center, right center, and right) indicated predominant contributions from the oxygen (blue) and nitrogen-p (yellow) states in the valence band region (-5 to 0 eV). In

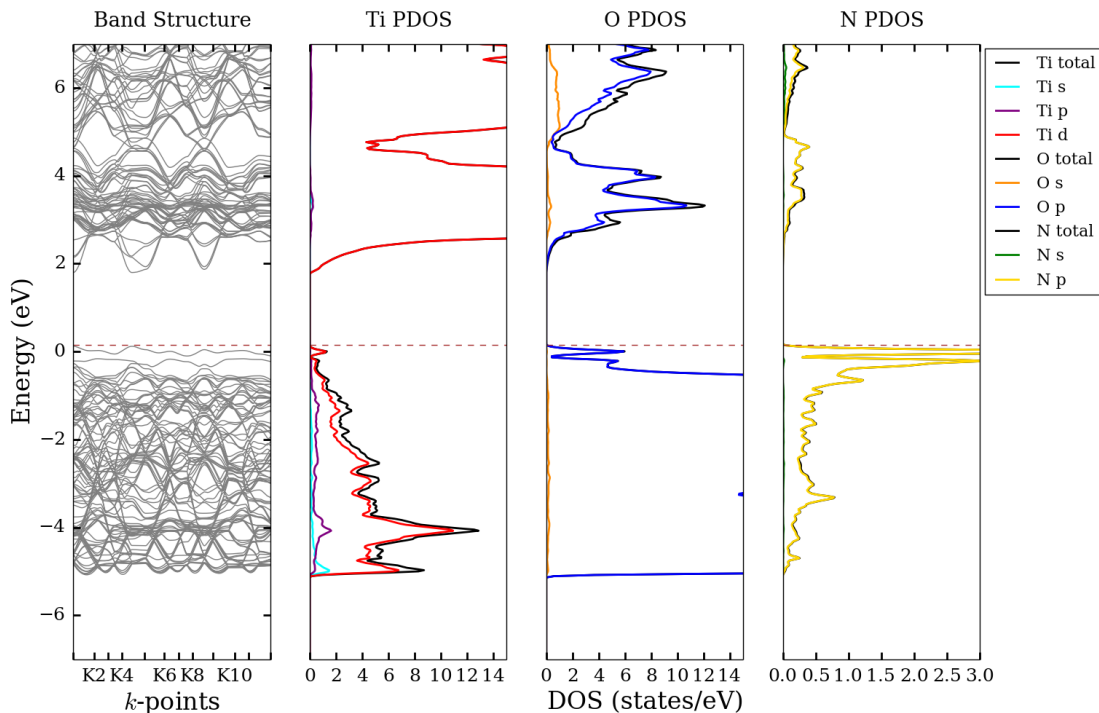


**Figure 4.15:** The band structure (left) of nitrogen-substituted anatase along with its partial DOS diagrams for titanium (left center), oxygen (right center), and nitrogen (right). *Source:* prepared using Python Software Foundation. Python Language Reference, version 2.7. Available at <http://www.python.org>.

addition, titanium-s, -p, and -d states provide minor contributions in the valence band region. In the conduction band region (2-5 eV), titanium-d states and oxygen-p states comprise the major DOS contributions. Similar to the results of sulfur substitution,



the  $E_g$  narrowing also occurred upon nitrogen substitution, but to a lesser extent than sulfur. In this case,  $E_g$  decreased from 2.05 eV (unsubstituted) to 1.68 eV (nitrogen-substituted). The nitrogen-substituted band structure also indicates the presence of the lone band (mid-gap state) that was observed in the sulfur-substituted case.

The band structure of tellurium-substituted anatase (Figure 4.16 left) revealed a direct  $E_g$  of 0.52 eV at the K1 and K4 k-points with a similar transition from indirect  $E_g$  to direct. The partial DOS analysis (Figure 4.16 left center, right center, and right) indicated predominant contributions from the oxygen (blue) and tellurium-p (yellow) states in the valence band region (-5 to 0 eV). In addition, titanium-s, -p, and

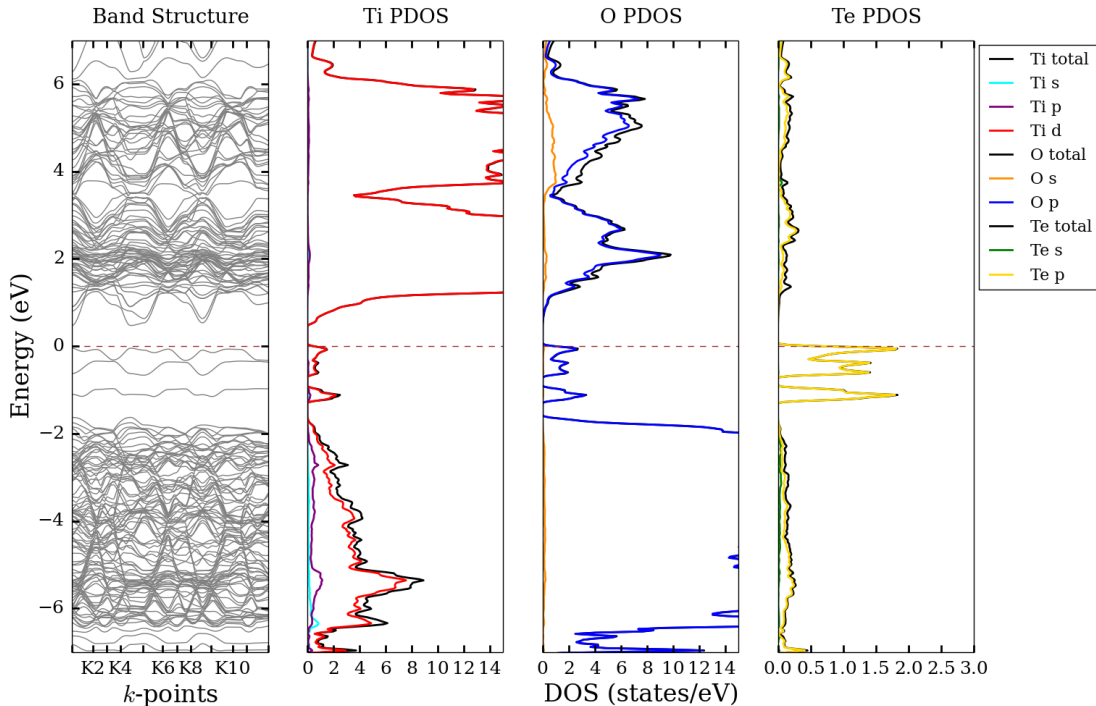


**Figure 4.16:** The band structure (left) of tellurium-substituted anatase along with its partial DOS diagrams for titanium (left center), oxygen (right center), and tellurium (right). *Source:* prepared using Python Software Foundation. Python Language Reference, version 2.7. Available at <http://www.python.org>.

-d states provide minor contributions in the valence band region. In the conduction band region (2-5 eV), titanium-d states and oxygen-p states comprise the major DOS contributions. Similar to the results of sulfur and nitrogen substitutions, the  $E_g$  narrowing also occurred upon tellurium substitution, but to a much greater extent

than the others. In this case,  $E_g$  decreased from 2.05 eV (unsubstituted) to 0.52 eV (nitrogen-substituted). The tellurium-substituted band structure also indicates the presence of the lone band (mid-gap state) that was observed in the sulfur-substituted case. In this case, many more lone bands reside in the  $E_g$  region, which arise from tellurium-p states. The extra mid-gap states are responsible for the greater extent of  $E_g$  narrowing.

In addition to the PBE-GGA band structures, the mBJ potential was also added for improved  $E_g$  calculation and the results are provided in Figure 4.17. The mBJ

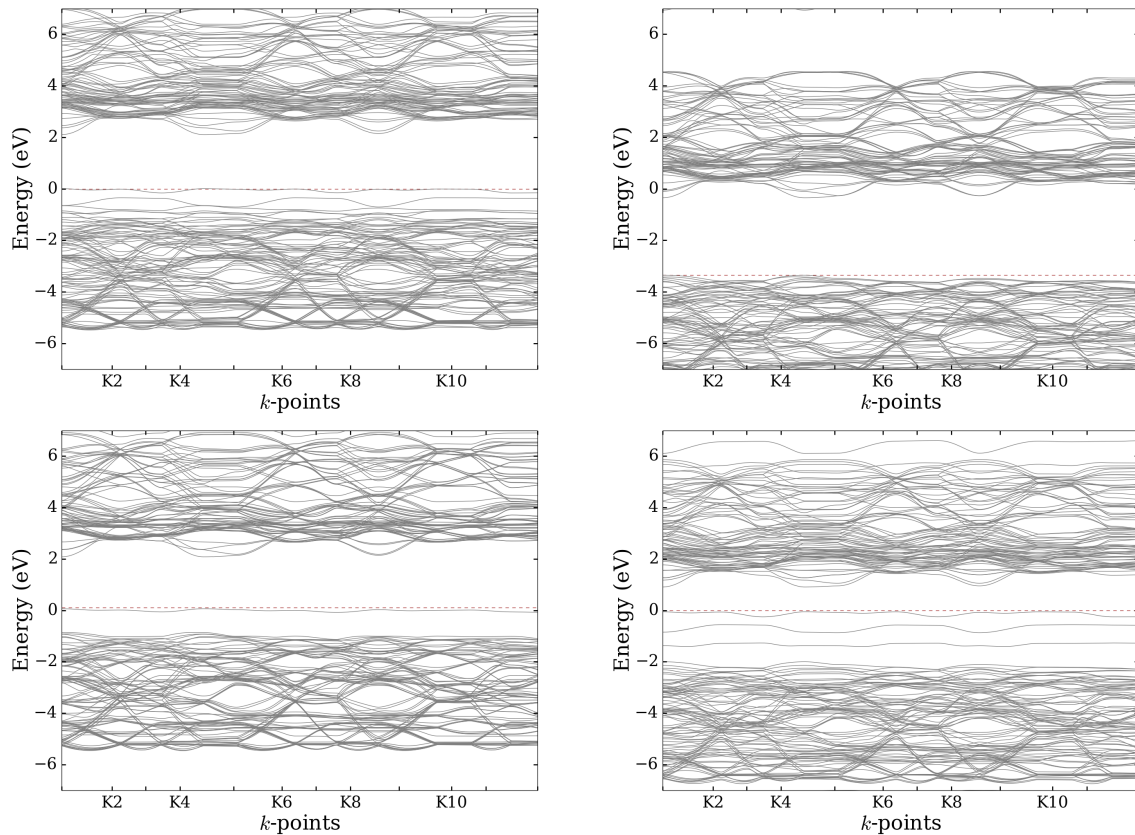


**Figure 4.17:** The band structure of sulfur- (upper left), fluorine- (upper right), nitrogen- (lower left) and tellurium- (lower right) substituted anatase with the PBE-GGA + mBJ potential. *Source:* prepared using: Python Software Foundation. Python Language Reference, version 2.7. Available at <http://www.python.org>.

calculations resulted in  $E_g$  values of 3.00, 2.02, 2.10, and 0.97 eV for fluorine-, nitrogen-, sulfur-, and tellurium-substituted anatase, respectively. It is again important to note that the topology of the bands via mBJ is very comparable to that determined using

solely PBE-GGA. As was observed with the PBE-GGA functional, an increase in  $E_g$  was observed with fluorine substitution and a decrease in  $E_g$  was observed with nitrogen and sulfur substitutions in the mBJ calculations. In addition, tellurium substitution in the anatase polymorph also resulted in  $E_g$  narrowing, but data for this substitution was not available in the rutile polymorph.

#### **4.6 Substituent Properties and Changes in Band Gap**

As observed in Sections 4.3-4.5, the various substitutions in the rutile and anatase polymorphs give rise to characteristic changes in the band structure and DOS. In particular, the  $E_g$  shifted to varying extents depending upon the identity of the substituent. As a result, various analyses were performed to shed light on the chemical property of the substituent and its potential role in the observed  $E_g$  change.

Table 4.4 and Figure 4.18 summarize the effect of melting point (MP) on the change in  $E_g$  of substituted rutile. In Table 4.4, the MP of each substituent is provided along with the calculated  $E_g$  values using both the PBE-GGA and PBE-GGA + mBJ methods. Figure 4.18 plots the changes in  $E_g$  as a function of the substituent’s MP. Error bars, as summarized in Section 4.3, are also included. While no linear relationship existed, generally speaking, the  $E_g$  value decreased with increasing MP of the substituent. However, according to the conceptual discussions of Hoffmann, rationalizing this  $E_g$  change as a result of substituent MP from a structural perspective does not have much merit.<sup>14</sup>

Substituent	F	O	N	S	Te
$E_g$ (PBE-GGA) / eV	1.95	1.90	1.62	1.37	TBD
$E_g$ (mBJ) / eV	2.56	2.61	2.02	1.87	TBD
MP / °C	-220	-218	-210	113	449

**Table 4.4:** The PBE-GGA and PBE-GGA + mBJ calculated  $E_g$  values of substituted rutile along with the substituent’s MP. *Source:* MP values reprinted from: *CRC handbook of chemistry and physics*, 97th ed.; CRC Press: Boca Raton, FL, 2017.

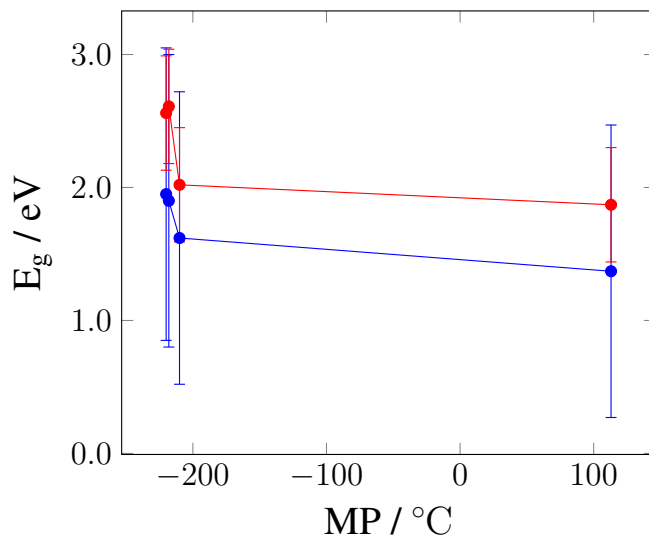


**Figure 4.18:** The PBE-GGA and PBE-GGA + mBJ calculated  $E_g$  values of substituted rutile along with the substituent’s MP. *Source:* prepared using the PSTricks package of L<sup>A</sup>T<sub>E</sub>X.

Table 4.5 and Figure 4.19 summarize the effect of charge/crystal radius ( $Z/CR$ ) ratio on the change in  $E_g$  of substituted rutile. In Table 4.5, the  $Z/CR$  ratio of each substituent is provided along with the calculated  $E_g$  values using both the PBE-GGA and PBE-GGA + mBJ methods. Figure 4.19 plots the changes in  $E_g$  as a function of the substituent’s  $Z/CR$  ratio. Error bars, as summarized in Section 4.3, are also included. No linear relationship was observed between  $E_g$  value and the  $Z/CR$  ratio of the substituent. It should also be pointed out that the order of substituents varies in each table as a result of organizing them in ascending order with respect to the chemical property being examined, so as to match the data points progressing from left to right across the x-axis each figure.

Substituent	F	Te	S	O	N
$E_g$ (PBE-GGA) / eV	1.95	TBD	1.37	1.62	2.05
$E_g$ (mBJ) / eV	2.56	TBD	1.87	2.61	2.02
$Z/CR$	0.74	0.90	1.09	1.43	1.75

**Table 4.5:** The PBE-GGA and PBE-GGA + mBJ calculated  $E_g$  values of substituted rutile along with the substituent’s  $Z/CR$  ratio. *Source:* CR values reprinted from: Shannon, R. Revised effective ionic radii and systematic studies of interatomic distances in halides and chalcogenides. *Acta Cryst.* **1976**, *A32*, 751–767.

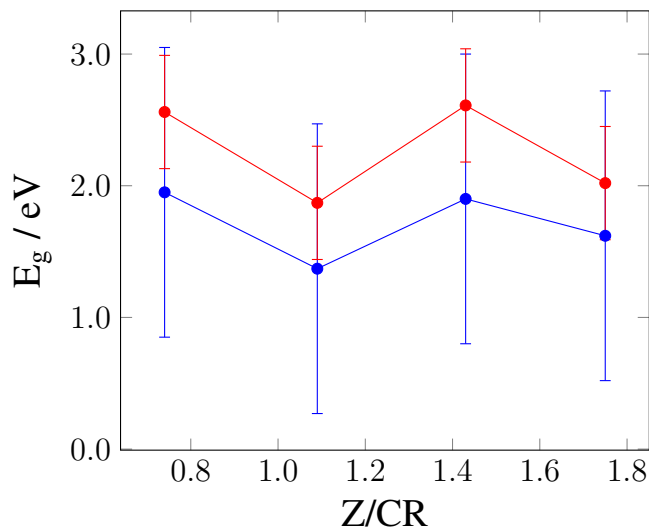


**Figure 4.19:** The PBE-GGA and PBE-GGA + mBJ calculated  $E_g$  values of substituted rutile along with the substituent’s  $Z/CR$ . *Source:* prepared using the PSTricks package of L<sup>A</sup>T<sub>E</sub>X.

Table 4.6 and Figure 4.20 summarize the effect of electronegativity ( $\chi$ ) on the change in  $E_g$  of substituted rutile. In Table 4.6, the electronegativity of each substituent is provided along with the calculated  $E_g$  values using both the PBE-GGA and PBE-GGA + mBJ methods. Figure 4.20 plots the changes in  $E_g$  as a function of the substituent's  $\chi$ . Error bars, as summarized in Section 4.3, are also included. In this case, the  $E_g$  value clearly increased with increasing electronegativity of the substituent. The trend in electronegativity is further discussed at the end of this section.

Substituent	Te	S	N	O	F
$E_g$ (PBE-GGA) / eV	TBD	1.37	1.62	1.90	1.95
$E_g$ (mBJ) / eV	TBD	1.87	2.02	2.61	2.56
$\chi$	2.10	2.58	3.04	3.44	3.98

**Table 4.6:** The PBE-GGA and PBE-GGA + mBJ calculated  $E_g$  values of substituted rutile along with the substituent's electronegativity ( $\chi$ ). *Source:*  $\chi$  values reprinted from: *CRC handbook of chemistry and physics*, 97th ed.; CRC Press: Boca Raton, FL, 2017.

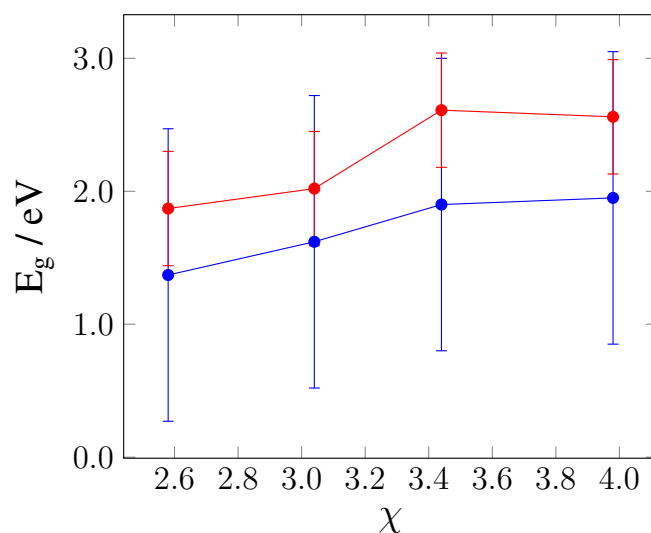


**Figure 4.20:** The PBE-GGA and PBE-GGA + mBJ calculated  $E_g$  values of substituted rutile along with the substituent's electronegativity ( $\chi$ ). *Source:* prepared using the PSTricks package of L<sup>A</sup>T<sub>E</sub>X.

Table 4.7 and Figure 4.21 summarize the effect of CR on the change in  $E_g$  of substituted rutile. In Table 4.7, the crystal radius of each substituent is provided along with the calculated  $E_g$  values using both the PBE-GGA and PBE-GGA + mBJ methods. Figure 4.21 plots the changes in  $E_g$  as a function of the substituent’s CR. Error bars, as summarized in Section 4.3, are also included. In this case, the  $E_g$  value decreased with increasing CR of the substituent. One exception to this trend occurred with the oxygen data point in the mBJ data set (red). The trend in crystal radius is further discussed at the end of this section.

Substituent	F	O	N	S	Te
$E_g$ (PBE-GGA) / eV	1.95	1.90	1.62	1.37	TBD
$E_g$ (mBJ) / eV	2.56	2.61	2.02	1.87	TBD
CR / Å	1.16	1.22	1.32	1.70	2.07

**Table 4.7:** The PBE-GGA and PBE-GGA + mBJ calculated  $E_g$  values of substituted rutile along with the substituent’s CR. *Source:* Crystal radii reprinted from: Shannon, R. Revised effective ionic radii and systematic studies of interatomic distances in halides and chalcogenides. *Acta Cryst.* **1976**, *A32*, 751–767.

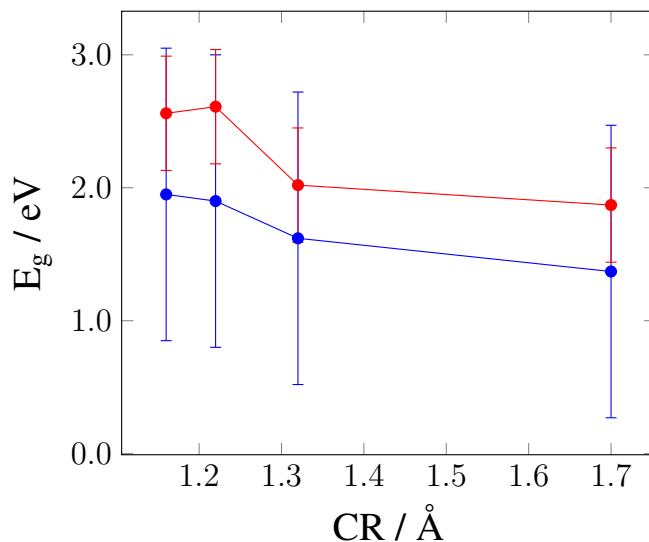
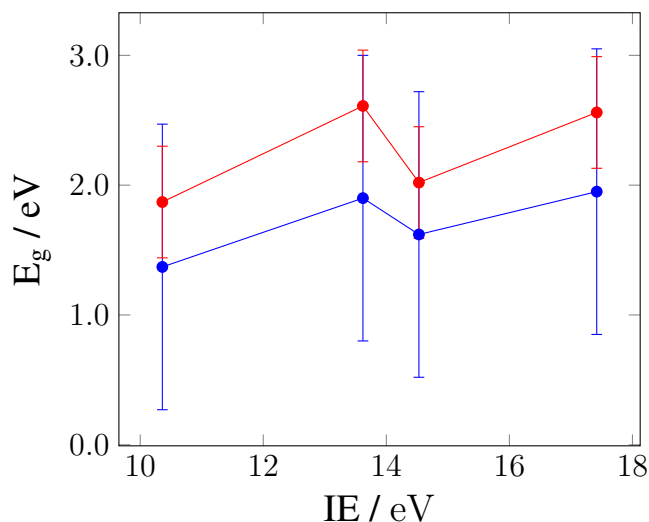


**Figure 4.21:** The PBE-GGA and PBE-GGA + mBJ calculated  $E_g$  values of substituted rutile along with the substituent’s CR. *Source:* prepared using the PSTricks package of L<sup>A</sup>T<sub>E</sub>X.

Table 4.8 and Figure 4.22 summarize the effect of IE on the change in  $E_g$  of substituted rutile. In Table 4.8, the ionization energy of each substituent is provided along with the calculated  $E_g$  values using both the PBE-GGA and PBE-GGA + mBJ methods. Figure 4.22 plots the changes in  $E_g$  as a function of the substituent’s IE. Error bars, as summarized in Section 4.3, are also included. In this case, no clear trend was observed between the calculated  $E_g$  value and the IE of the substituent.

Substituent	Te	S	O	N	F
$E_g$ (PBE-GGA) / eV	TBD	1.37	1.90	1.62	1.95
$E_g$ (mBJ) / eV	TBD	1.87	2.61	2.02	2.56
IE / eV	9.01	10.36	13.62	14.53	17.42

**Table 4.8:** The PBE-GGA and PBE-GGA + mBJ calculated  $E_g$  values of substituted rutile along with the substituent’s IE. *Source:* IE values reprinted from: *CRC handbook of chemistry and physics*, 97th ed.; CRC Press: Boca Raton, FL, 2017.



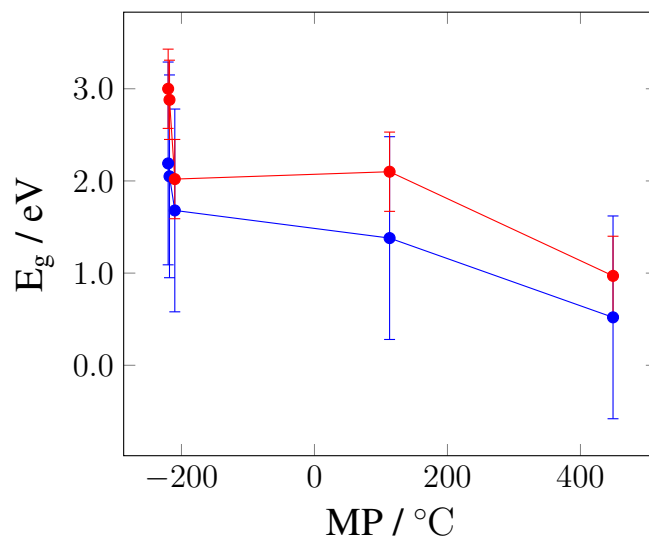
**Figure 4.22:** The PBE-GGA and PBE-GGA + mBJ calculated  $E_g$  values of substituted rutile along with the substituent’s IE. *Source:* prepared using the PSTricks package of L<sup>A</sup>T<sub>E</sub>X.



Table 4.9 and Figure 4.23 summarize the effect of MP on the change in  $E_g$  of substituted anatase. In Table 4.9, the MP of each substituent is provided along with the calculated  $E_g$  values using both the PBE-GGA and PBE-GGA + mBJ methods. Figure 4.23 plots the changes in  $E_g$  as a function of the substituent’s MP. Error bars, as summarized in Section 4.3, are also included. While no linear relationship existed, generally speaking, the  $E_g$  value decreased with increasing MP of the substituent. One exception to this trend occurred for the sulfur-substituted case in the mBJ data set.

Substituent	F	O	N	S	Te
$E_g$ (PBE-GGA) / eV	2.19	2.05	1.68	1.38	0.52
$E_g$ (mBJ) / eV	3.00	2.88	2.02	2.10	0.97
MP / °C	-220	-218	-210	113	449

**Table 4.9:** The PBE-GGA and PBE-GGA + mBJ calculated  $E_g$  values of substituted anatase along with the substituent’s MP. *Source:* MP values reprinted from: *CRC handbook of chemistry and physics*, 97th ed.; CRC Press: Boca Raton, FL, 2017.



**Figure 4.23:** The PBE-GGA and PBE-GGA + mBJ calculated  $E_g$  values of substituted anatase along with the substituent’s MP. *Source:* prepared using the PSTricks package of L<sup>A</sup>T<sub>E</sub>X.

Table 4.10 and Figure 4.24 summarize the effect of the Z/CR ratio on the change in  $E_g$  of substituted anatase. In Table 4.10, the Z/CR ratio of each substituent is provided along with the calculated  $E_g$  values using both the PBE-GGA and PBE-GGA + mBJ methods. Figure 4.24 plots the changes in  $E_g$  as a function of the substituent's Z/CR ratio. Error bars, as summarized in Section 4.3, are also included. No linear relationship was observed between  $E_g$  value and the Z/CR ratio of the substituent.

Substituent	F	Te	S	O	N
$E_g$ (PBE-GGA) / eV	2.19	0.16	1.38	2.05	1.68
$E_g$ (mBJ) / eV	3.00	0.07	2.10	2.88	2.02
Z/CR	0.74	0.90	1.09	1.43	1.75

**Table 4.10:** The PBE-GGA and PBE-GGA + mBJ calculated  $E_g$  values of substituted anatase along with the substituent's Z/CR. *Source:* CR values reprinted from: Shannon, R. Revised effective ionic radii and systematic studies of interatomic distances in halides and chalcogenides. *Acta Cryst.* **1976**, *A32*, 751–767.

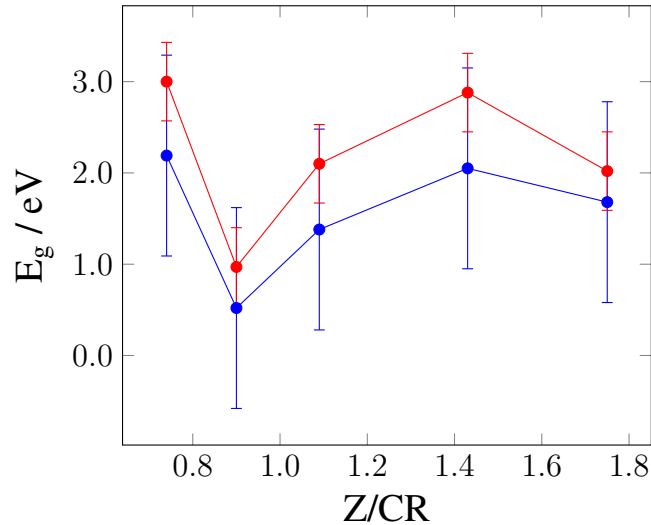


**Figure 4.24:** The PBE-GGA and PBE-GGA + mBJ calculated  $E_g$  values of substituted anatase along with the substituent's Z/CR. *Source:* prepared using the PSTricks package of L<sup>A</sup>T<sub>E</sub>X.

Table 4.11 and Figure 4.25 summarize the effect of  $\chi$  on the change in  $E_g$  of substituted anatase. In Table 4.11, the electronegativity of each substituent is provided along with the calculated  $E_g$  values using both the PBE-GGA and PBE-GGA + mBJ methods. Figure 4.25 plots the changes in  $E_g$  as a function of the substituent's  $\chi$ . Error bars, as summarized in Section 4.3, are also included. In this case, the  $E_g$  value clearly increased with increasing electronegativity of the substituent. One exception to this trend was the nitrogen-substituted point in the mBJ data set. The trend in electronegativity is again revisited at the end of this section.

Substituent	Te	S	N	O	F
$E_g$ (PBE-GGA) / eV	0.52	1.38	1.68	2.05	2.19
$E_g$ (mBJ) / eV	0.97	2.10	2.02	2.88	3.00
$\chi$	2.10	2.58	3.04	3.44	3.98

**Table 4.11:** The PBE-GGA and PBE-GGA + mBJ calculated  $E_g$  values of substituted anatase along with the substituent's electronegativity ( $\chi$ ). *Source:*  $\chi$  values reprinted from: *CRC handbook of chemistry and physics*, 97th ed.; CRC Press: Boca Raton, FL, 2017.

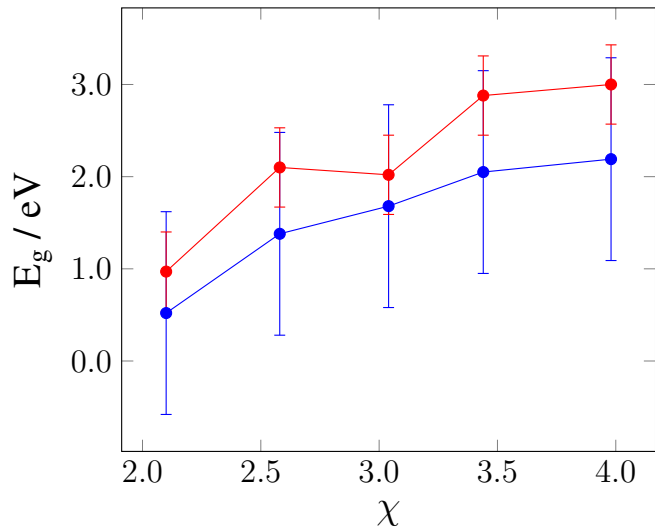


**Figure 4.25:** The PBE-GGA and PBE-GGA + mBJ calculated  $E_g$  values of substituted anatase along with the substituent's electronegativity ( $\chi$ ). *Source:* prepared using the PStricks package of L<sup>A</sup>T<sub>E</sub>X.

Table 4.12 and Figure 4.26 summarize the effect of CR on the change in  $E_g$  of substituted anatase. In Table 4.12, the crystal radius of each substituent is provided along with the calculated  $E_g$  values using both the PBE-GGA and PBE-GGA + mBJ methods. Figure 4.26 plots the changes in  $E_g$  as a function of the substituent’s CR. Error bars, as summarized in Section 4.3, are also included. In this case, the  $E_g$  value decreased with increasing CR of the substituent. One exception to this trend was the nitrogen data point in the mBJ data set (red). The trend in CR is again revisited at the end of this section.

Substituent	F	O	N	S	Te
$E_g$ (PBE-GGA) / eV	2.19	2.05	1.68	1.38	0.52
$E_g$ (mBJ) / eV	3.00	2.88	2.02	2.10	0.97
CR / Å	1.16	1.22	1.32	1.70	2.07

**Table 4.12:** The PBE-GGA and PBE-GGA + mBJ calculated  $E_g$  values of substituted anatase along with the substituent’s CR. *Source:* CR values reprinted from: Shannon, R. Revised effective ionic radii and systematic studies of interatomic distances in halides and chalcogenides. *Acta Cryst.* **1976**, *A32*, 751–767.

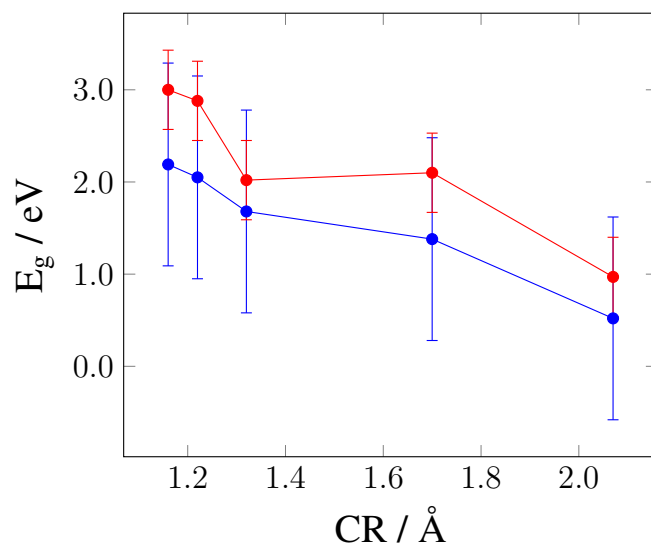


**Figure 4.26:** The PBE-GGA and PBE-GGA + mBJ calculated  $E_g$  values of substituted anatase along with the substituent’s CR. *Source:* prepared using the PSTricks package of L<sup>A</sup>T<sub>E</sub>X.

Table 4.13 and Figure 4.27 summarize the effect of IE on the change in  $E_g$  of substituted anatase. In Table 4.13, the ionization energy of each substituent is provided along with the calculated  $E_g$  values using both the PBE-GGA and PBE-GGA + mBJ methods. Figure 4.27 plots the changes in  $E_g$  as a function of the substituent’s IE. Error bars, as summarized in Section 4.3, are also included. In this case, no clear trend is observed between the calculated  $E_g$  value and the IE of the substituent. However, a trend of increasing  $E_g$  was apparent with the exception of the nitrogen-substituted calculations in both the PBE-GGA and mBJ data sets.

Substituent	Te	S	O	N	F
$E_g$ (PBE-GGA) / eV	0.52	1.38	2.05	1.68	2.19
$E_g$ (mBJ) / eV	0.97	2.10	2.88	2.02	3.00
IE / eV	9.01	10.36	13.62	14.53	17.42

**Table 4.13:** The PBE-GGA and PBE-GGA + mBJ calculated  $E_g$  values of substituted anatase along with the substituent’s IE. *Source:* IE values reprinted from: *CRC handbook of chemistry and physics*, 97th ed.; CRC Press: Boca Raton, FL, 2017.

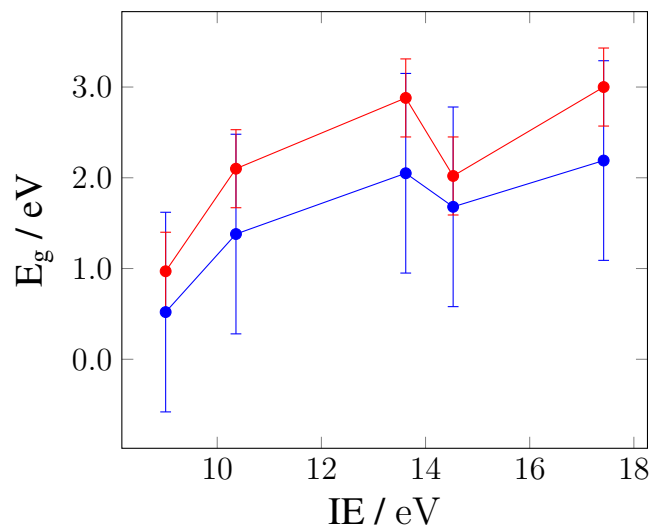


**Figure 4.27:** The PBE-GGA and PBE-GGA + mBJ calculated  $E_g$  values of substituted anatase along with the substituent’s IE. *Source:* prepared using the PSTricks package of L<sup>A</sup>T<sub>E</sub>X.

Upon examining the relationships between various chemical properties and the calculated  $E_g$  values in this section, several interesting observations were made. In the rutile substitutions, a trend of decreasing  $E_g$  was observed with increasing MP. However, this trend is difficult to justify and rationalize from a structural point of view. No clear trends were observed between Z/CR or IE and the calculated  $E_g$  values. However, clear trends were observed with the CR and  $\chi$  with respect to the changes in  $E_g$ .  $E_g$  decreased with increasing CR and increased with increasing  $\chi$ . However, an exception in the CR trend was observed with the oxygen data point in the mBJ data set.

In the anatase substitutions, the MP trend was observed again, but was not given much further consideration. While this was observed in both of the substituted systems in this work and was suggested in the literature, there is no current structural explanation of how MP would impact  $E_g$ . Similar to the rutile substitutions, no clear trends were observed between Z/CR or IE and the calculated  $E_g$  values for substituted anatase. Most notably, the  $E_g$  in substituted anatase also decreased with increasing CR. Moreover, as the  $\chi$  increased, so too did the  $E_g$  values. However, minor exceptions (nitrogen data point) to these trends still need to be addressed.

The decrease in  $E_g$  with increasing CR can be explained by again considering some general chemistry principles. Upon substituting an atom with a larger crystal radius on an oxygen site, the molecular orbitals of that substituent and the neighboring titanium atoms overlap to a greater extent. As discussed in Section 1.3, greater orbital overlap produces a greater band dispersion (total range in energy) of the bands in a band structure plot. With bands spanning greater energy, the  $E_g$  value subsequently decreases. An explanation for the increase in  $E_g$  with increasing  $\chi$  can also be rationalized by considering the effect of substitution on the molecular orbitals. As evidenced from the DOS diagrams in Sections 4.3-4.5, the substituent gives rise to -p state DOS contributions in the valence band. The addition of a more electronegative

atom in the valence band can have an effect on the other nearby orbitals, possible shifting conduction band states to higher energy or lower the energy of valence band states, and widening  $E_g$ .

With these outcomes, the hypothesis of this project has been partially refuted. While the CR and  $\chi$  clearly showed an impact on changes in  $E_g$ , differentiating between which had a greater impact was not possible. It is also important to note that these two chemical properties are related to one another and cannot be decoupled, further complicating the hypothesis. A combination of the two chemical properties was also considered. Motivated by the work of Plumley and Evanseck, various linear combinations of weighted CR and  $\chi$  were investigated in attempt to improve the data's linear fit, but these attempts were unsuccessful.<sup>109</sup> In addition, further studies will be necessary to elucidate the significance of the mid-gap states observed upon sulfur, nitrogen, and tellurium substitution.

## Chapter 5. Electronic Structure of Diamond-like Semiconductors

In addition to the electronic structure calculations carried out for substituted and un-substituted  $\text{TiO}_2$ , several collaborative projects with the Aitken research group were carried out to elucidate the electronic structure of diamond-like semiconductor materials. The results of these works are summarized in this chapter.

### 5.1 Electronic Structure of $\alpha$ - and $\beta$ - $\text{Cu}_2\text{ZnSiS}_4$

This section is partially adapted and reproduced (with permission) from the following manuscript: Rosmus, K. et al. Synchrotron X-ray powder diffraction and electronic band structure of  $\alpha$ - and  $\beta$ -  $\text{Cu}_2\text{ZnSiS}_4$ . *Z. Anorg. Allg. Chem.* **2012**, *638*, 2578–2584. All experimental work was performed by the Aitken Research Group and can be found online for support of the electronic structure calculations.

The quaternary diamond-like semiconductor,  $\text{Cu}_2\text{ZnSiS}_4$ , was synthesized by high-temperature solid-state synthesis at 1000 °C. High-resolution synchrotron X-ray powder diffraction of this product revealed the presence of two polymorphs. This data confirms that the known  $\alpha$ - $\text{Cu}_2\text{ZnSiS}_4$  exists with the wurtz-stannite structure in the noncentrosymmetric space group  $Pmn2_1$ . The new polymorph,  $\beta$ - $\text{Cu}_2\text{ZnSiS}_4$ , crystallizes in the noncentrosymmetric space group  $Pn$  with  $a = 6.134\,092(6)$  Å,  $b = 6.392\,752(5)$  Å,  $c = 7.421\,228(8)$  Å,  $\beta = 90.056(1)^\circ$ ,  $Z = 2$ ,  $\chi^2 = 5.554$ ,  $R_p = 0.0857$  and  $wR_p = 0.1173$ . Structures of the  $\alpha$  and  $\beta$  polymorphs are provided in Figure 5.1. Results of the electronic structure calculations are summarized below.

Electronic structure calculations, band structure and DOS, for both polymorphs of  $\text{Cu}_2\text{ZnSiS}_4$ , were performed using the WIEN2k computational software package (version 11.1) and the FP-LAPW method of DFT.<sup>21</sup> The refined crystal structure of  $\alpha$ - $\text{Cu}_2\text{ZnSiS}_4$  in the  $Pmn2_1$  space group (from single-crystal X-ray diffraction data) and  $\beta$ - $\text{Cu}_2\text{ZnSiS}_4$  in the  $Pn$  space group (from the Rietveld refinement of synchrotron powder diffraction data) were used to initialize the electronic structure calculations.<sup>111</sup> In these calculations, the muffin tin radii (RMT) of Cu, Zn, Si, and S were set to



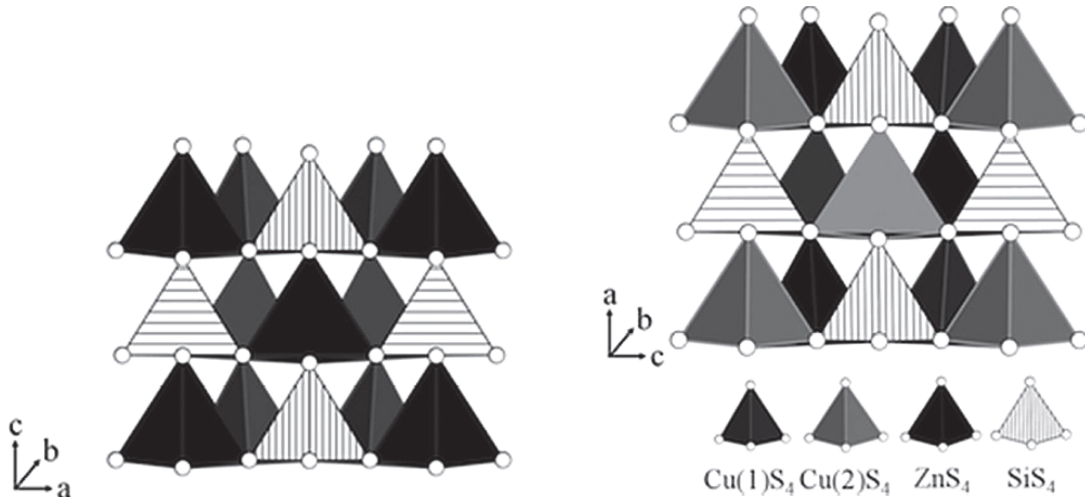


**Figure 5.1:** Polyhedral view along the  $b$  axis for  $\alpha$ - $\text{Cu}_2\text{ZnSiS}_4$  (left) and  $\beta$ - $\text{Cu}_2\text{ZnSiS}_4$  (right). *Source:* reprinted with permission from: Rosmus, K. et al. Synchrotron X-ray powder diffraction and electronic band structure of  $\alpha$ - and  $\beta$ -  $\text{Cu}_2\text{ZnSiS}_4$ . *Z. Anorg. Allg. Chem.* **2012**, 638, 2578–2584.

2.23, 2.25, 1.93, and 1.97 bohr, respectively. The PBE-GGA functional was used to treat XC effects and a total of 1000 k-points in the full Brillouin zone were used.<sup>90</sup> SCF calculations were considered converged when the change in total energy is less than 0.1 mRy per unit cell. The set of high symmetry points used for plotting the band structure in the iBZ is an automatic (arbitrary) path, based on the template files of WIEN2k.

The calculated electronic band structure and DOS of both  $\alpha$ - and  $\beta$ - $\text{Cu}_2\text{ZnSiS}_4$  are shown in Figures 5.2-5.4. The total energy was calculated to be  $-27972.6498$  Ry and  $-27972.65612$  Ry for  $\alpha$ - $\text{Cu}_2\text{ZnSiS}_4$  and  $\beta$ - $\text{Cu}_2\text{ZnSiS}_4$ , respectively. The energy difference between the two structures is 0.08476 eV. However, neither of these polymorphs have the kesterite structure, which is predicted by Chen et al. to be the ground state structure for  $\text{Cu}_2\text{ZnSiS}_4$ .<sup>112</sup> The trend in the energies of the two polymorphs are in accordance with that calculated by Chen and co-workers, showing that the  $\beta$ -phase has a lower energy.<sup>112</sup> As shown in Figure 5.2, both polymorphs exhibit a direct  $E_g$  as evidenced by the valence band maximum and the conduction band minimum existing at the  $\Gamma$ -point of the iBZ. The calculated  $E_g$  for  $\alpha$ - $\text{Cu}_2\text{ZnSiS}_4$  is 1.3 eV, whereas that

of  $\beta$ - $\text{Cu}_2\text{ZnSiS}_4$  is 1.7 eV. These calculated values are lower than the experimentally determined  $E_g$ , which are greater than 3.0 eV. The under-estimation of  $E_g$  by DFT calculations using the PBE-GGA functional is well known and has been discussed in Chapter 2.<sup>26</sup>

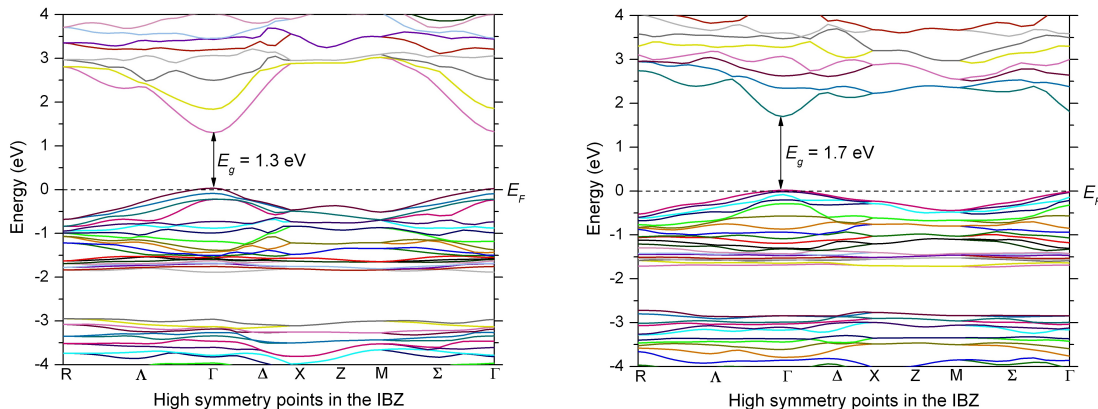


**Figure 5.2:** Calculated electronic band structure of  $\alpha$ - (left) and  $\beta$ -(right)- $\text{Cu}_2\text{ZnSiS}_4$ . The horizontal, dashed line denotes the Fermi level ( $E_F$ ). *Source:* reprinted with permission from: Rosmus, K. et al. Synchrotron X-ray powder diffraction and electronic band structure of  $\alpha$ - and  $\beta$ -  $\text{Cu}_2\text{ZnSiS}_4$ . *Z. Anorg. Allg. Chem.* **2012**, *638*, 2578–2584.

The total and partial DOS for  $\alpha$ - $\text{Cu}_2\text{ZnSiS}_4$  are shown in Figure 5.3. The total DOS in the energy interval of 10 to 10 eV is comprised of contributions from a copper atom, a zinc atom, a silicon atom, and three crystallographically unique sulfur atoms. The core bands in the energy range of 10 to 6.5 eV have major contributions from the Zn-d and Si-s orbitals. In the energy range of 6.5 to 0 eV, the major contributions are from the Cu-d and the S-p orbitals. As is the case with the Cu-III-VI<sub>2</sub> chalcopyrite DLS and the wurtz-kesterite-type  $\text{Ag}_2\text{ZnSiS}_4$ , the valence band maximum in the wurtz-stannite-type  $\text{Cu}_2\text{ZnSiS}_4$  is dominated by the hybridization of the Cu/Ag-d and chalcogen-p states.<sup>113,114</sup> The most significant contributions to the conduction band minimum from the range of 1.3 to 5 eV are from the Zn-s, Si-s, Si-p, and S-p orbitals. It should be noted that the Si-s and Si-p contributions are similar in the lowest region of the conduction band minimum, while the Si-p has greater contributions after 3 eV. The composition of the conduction band minimum in this

structure is similar to that of  $\text{Ag}_2\text{ZnSiS}_4$  except that the Si-s has greater contribution than Si-p at the lowest conduction band minimum energies for the silver analog.

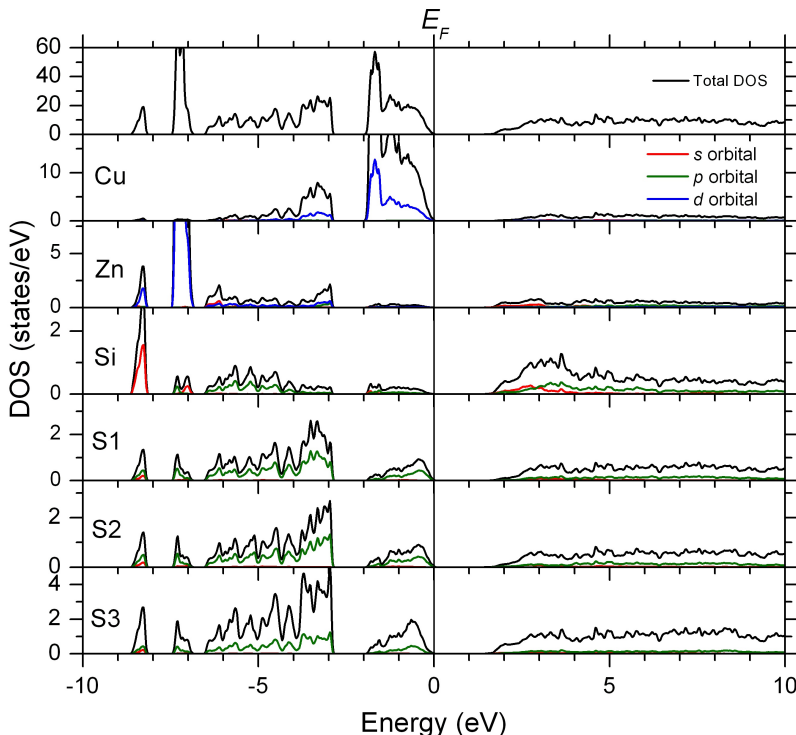


**Figure 5.3:** Calculated DOS diagram of  $\alpha\text{-Cu}_2\text{ZnSiS}_4$ . The vertical, solid line denotes the Fermi level ( $E_F$ ). *Source:* reprinted with permission from: Rosmus, K. et al. Synchrotron X-ray powder diffraction and electronic band structure of  $\alpha$ - and  $\beta$ -  $\text{Cu}_2\text{ZnSiS}_4$ . *Z. Anorg. Allg. Chem.* **2012**, 638, 2578–2584.

While the overall DOS for  $\beta\text{-Cu}_2\text{ZnSiS}_4$  is strikingly similar to that of  $\alpha\text{-Cu}_2\text{ZnSiS}_4$ , there exist some subtle differences (Figure 5.4). Although the atomic identity of the major contributors in each region is the same, the magnitude of states per eV is noticeably different for the two structures. Another minor difference is that the contributions from each of the four crystallographically unique sulfur atoms near the valence band maximum in the  $\beta$ -phase are nearly identical; however, these contributions are less evenly distributed among the three unique sulfur atoms in the  $\alpha$ -phase. Additionally, there are also differences in the partial DOS for silicon. In the  $\beta$ -phase the lowest conduction band minimum is almost entirely comprised of Si-s states, followed by a region of equal contributions from Si-s and Si-p, and lastly a higher energy region that is mainly Si-p in character.

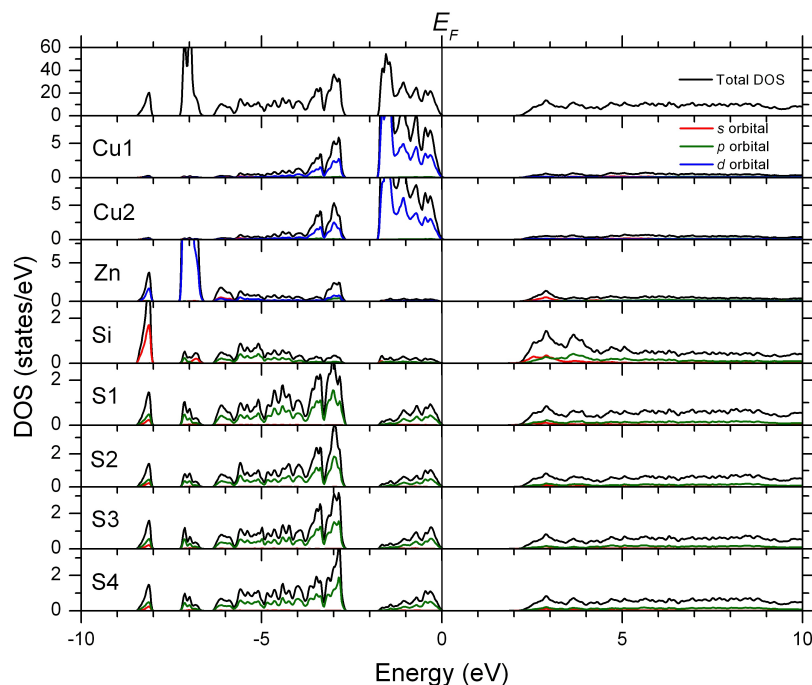


**Figure 5.4:** Calculated DOS diagram of  $\beta$ - $\text{Cu}_2\text{ZnSiS}_4$ . The vertical, solid line denotes the Fermi level ( $E_F$ ). *Source:* reprinted with permission from: Rosmus, K. et al. Synchrotron X-ray powder diffraction and electronic band structure of  $\alpha$ - and  $\beta$ -  $\text{Cu}_2\text{ZnSiS}_4$ . *Z. Anorg. Allg. Chem.* **2012**, *638*, 2578–2584.

Optical diffuse reflectance of  $\text{Cu}_2\text{ZnSiS}_4$  was obtained on a powdered sample and  $E_g$  values of 3.0 eV and 3.2 eV were assigned for the  $\alpha$  and  $\beta$  phases, respectively. The  $E_g$  of  $\text{Cu}_2\text{ZnSiS}_4$  was reported by Wold and coworkers in 1977 as 3.25 eV; and later in 1987, the same group reported the  $E_g$  as 3.04 eV.<sup>115,116</sup> Upon examining the absorption spectrum published in the 1977 paper, one can see the clear presence of a significant absorption edge tail at lower energy.<sup>115</sup> This spectrum is similar to that, which is reported herein and have assigned as resulting from a mixture of both  $\alpha$ - and  $\beta$ - $\text{Cu}_2\text{ZnSiS}_4$ .

In more recent works by Levcenco et al., several  $E_g$  values ranging from 2.97 to 3.41 eV were reported for  $\text{Cu}_2\text{ZnSiS}_4$  using polarization-dependent piezoreflectance (PzR),<sup>117</sup> surface photovoltage (SPV) spectroscopy,<sup>118,119</sup> and electrolyte electroreflectance (EER) measurements.<sup>120</sup> It is interesting to note that while the measurements performed in this work were on a powdered sample, Levcenco and Wold's

groups prepared their samples as crystals using the iodine vapor transport method. Although each group reported their material as having the wurtzstannite structure, it is quite possible that the crystals could have been an intergrowth of the  $\alpha$ - and  $\beta$ -phases. However, the diffraction methods that were used in both of these studies did not have the ability to indicate the presence of two phases since their peaks could not be resolved.

Further ambiguity in the interpretation of the optical spectra arises from the fact that, in addition to the presence of two polymorphs, there exist other accessible transitions within the band structure of each phase at the  $\Gamma$ -point. As shown in Figure 5.5, there exist four bands at the  $\Gamma$ -point, whose energies differ by ca. 250 meV for  $\alpha$ - and  $\beta$ - $\text{Cu}_2\text{ZnSiS}_4$ . The close spacing of these bands near the valence band maximum allows for the possibility of multiple electronic excitations that can be observed for the material. The observation of multiple bands with similar energies near the  $E_g$  was also observed for CZTS and CZTSe, as calculated by Persson using the LAPW method of DFT.<sup>121</sup> Likewise, Chen and co-workers have proposed similar excitonic transitions for I-III-II<sub>2</sub>-VI<sub>4</sub> and II-III-IV-V<sub>4</sub> diamondlike materials.

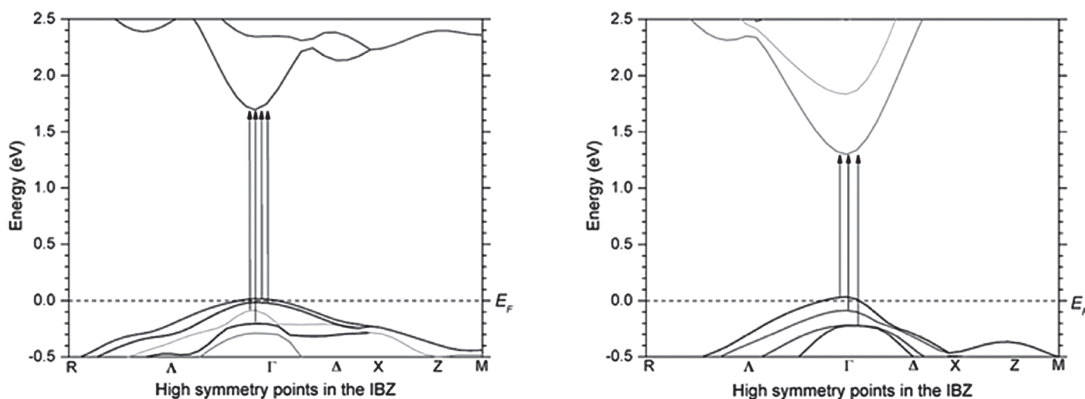


**Figure 5.5:** A zoomed view of the calculated electronic band structure showing the accessible transitions for  $\alpha$ - $\text{Cu}_2\text{ZnSiS}_4$  (left) and  $\beta$ - $\text{Cu}_2\text{ZnSiS}_4$  (right). *Source:* reprinted with permission from: Rosmus, K. et al. Synchrotron X-ray powder diffraction and electronic band structure of  $\alpha$ - and  $\beta$ -  $\text{Cu}_2\text{ZnSiS}_4$ . *Z. Anorg. Allg. Chem.* **2012**, *638*, 2578–2584.

In this work, a sample of  $\text{Cu}_2\text{ZnSiS}_4$  was characterized using high-resolution synchrotron powder diffraction. The refinement of this data confirmed the previously reported structure for  $\text{Cu}_2\text{ZnSiS}_4$  in  $Pmn2_1$  and identified a new polymorph,  $\beta$ - $\text{Cu}_2\text{ZnSiS}_4$ , crystallizing in the space group  $Pn$ . Electronic structure calculations using WIEN2k showed direct  $E_g$  of 1.3 and 1.7 eV for the  $\alpha$ - and  $\beta$ -phases, respectively. The valence band maximum was found to be dominated by the Cu-d and S-p orbitals, similar to the chalcopyrite type DLS. Electronic structure calculations and the Rietveld refinement results help to explain the observed optical absorption spectrum of  $\text{Cu}_2\text{ZnSiS}_4$ , which shows multiple absorption edges, from which  $E_g$  values of 3.0 and 3.2 eV were estimated for the  $\alpha$ - and  $\beta$ -phases, respectively. Synthesis of each polymorph as a pure-phase material is challenging due to their similar relative energies, yet this is imperative for the further physicochemical characterization of both polymorphs.

## 5.2 Electronic Structure of the $\text{Cu}_2\text{CdSnS}_4$ and $\alpha/\beta$ - $\text{Cu}_2\text{ZnSiS}_4$ Diamond-like Semiconductors

This section is partially adapted and reproduced (with permission) from the following manuscript: Rosmus, K. et al. Optical nonlinearity in  $\text{Cu}_2\text{CdSnS}_4$  and  $\alpha/\beta$ - $\text{Cu}_2\text{ZnSiS}_4$ : diamond-like semiconductors with high laser-damage thresholds. *Inorg. Chem.* **2014**, *53*, 7809–7811. All experimental work was performed by the Aitken, Jang, and Kim Research Groups and can be found online for support of the electronic structure calculations.

$\text{Cu}_2\text{CdSnS}_4$  and  $\alpha/\beta$ - $\text{Cu}_2\text{ZnSiS}_4$  meet several criteria for promising nonlinear optical materials for use in the infrared (IR) region. Structures of the polymorphs are provided in Figure 5.6. Both are air-stable, crystallize in noncentrosymmetric space groups, and possess high thermal stabilities.  $\text{Cu}_2\text{CdSnS}_4$  and  $\alpha/\beta$ - $\text{Cu}_2\text{ZnSiS}_4$  display wide ranges of optical transparency, 1.4-25 and 0.7-25  $\mu\text{m}$ , respectively, and have relatively large second-order nonlinearity as well as phase matchability for wide regions in

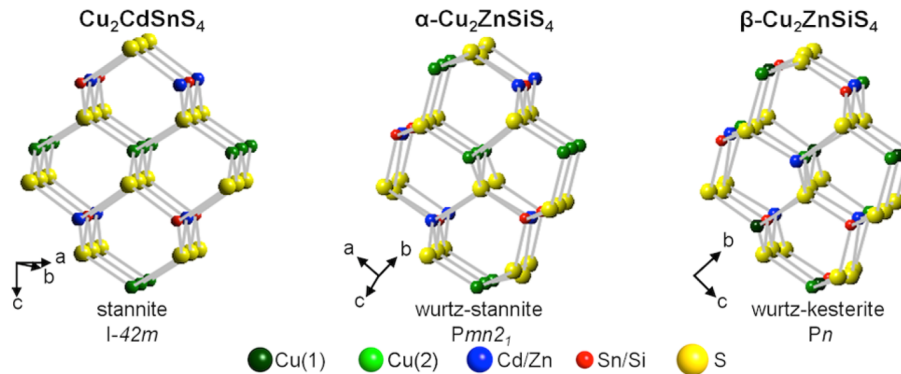


**Figure 5.6:** 3D DLS structures of  $\text{Cu}_2\text{CdSnS}_4$  and  $\alpha/\beta\text{-Cu}_2\text{ZnSiS}_4$ . *Source:* reprinted with permission from: Rosmus, K. et al. Optical nonlinearity in  $\text{Cu}_2\text{CdSnS}_4$  and  $\alpha/\beta\text{-Cu}_2\text{ZnSiS}_4$ : diamond-like semiconductors with high laser-damage thresholds. *Inorg. Chem.* **2014**, *53*, 7809–7811.

the IR. The laser-damage threshold (LDT) for  $\text{Cu}_2\text{CdSnS}_4$  is  $0.2 \text{ GW cm}^{-2}$ , whereas  $\alpha/\beta\text{-Cu}_2\text{ZnSiS}_4$  has a LDT of  $2.0 \text{ GW cm}^{-2}$  for picosecond near-IR excitation. Both compounds also exhibit efficient third-order nonlinearity. Electronic structure calculations provide insight into the variation in properties. Results of the electronic structure calculations are summarized below.

The band structure and DOS of  $\text{Cu}_2\text{CdSnS}_4$ ,  $\alpha\text{-Cu}_2\text{ZnSiS}_4$ , and  $\beta\text{-Cu}_2\text{ZnSiS}_4$  were carried out using the WIEN2k package and the FP-LAPW method of DFT for solving the KS equations.<sup>21,88,96</sup> The PBE-GGA functional was used to treat XC effects; in addition the mBJ exchange potential was used to achieve greater accuracy of the  $E_g$  energies in semiconductors.<sup>93</sup> In these calculations, the RMT of Cu, Zn, Si, and S were set to 2.39, 2.40, 1.85, and 1.96 bohr, respectively. In  $\text{Cu}_2\text{CdSnS}_4$ , the RMT values were set to 2.39, 2.50, 2.49, and 1.96 bohr for Cu, Cd, Sn, and S, respectively. SCF calculations converged when the energy difference between successive iterations fell below 0.1 mRy per unit cell. Additionally, a total of 3,000 k-points were used in the full Brillouin zone for each compound, which corresponded to 336, 630, and 240 k-points in the iBZ for the  $\text{Cu}_2\text{CdSnS}_4$ ,  $\alpha\text{-Cu}_2\text{ZnSiS}_4$ , and  $\beta\text{-Cu}_2\text{ZnSiS}_4$  structures, respectively.

An electronic structure calculation was reported for  $\text{Cu}_2\text{CdSnS}_4$ ,<sup>123</sup> but is ex-

panded upon here with the DOS and the incorporation of the mBJ potential for all compounds.<sup>93</sup> The direct  $E_g$  of  $\text{Cu}_2\text{CdSnS}_4$ ,  $\alpha\text{-Cu}_2\text{ZnSiS}_4$  and  $\beta\text{-Cu}_2\text{ZnSiS}_4$  were calculated as 0.79, 2.05, and 2.57 eV, respectively. The differences in the electronic structures of  $\text{Cu}_2\text{CdSnS}_4$  and  $\alpha/\beta\text{-Cu}_2\text{ZnSiS}_4$  can be understood by examining the partial DOS (Figures 5.7-5.9). The largest discrepancy near the Fermi level ( $E_F$ ) arises from the contributions of the IV ion orbitals at the conduction band minimum. For  $\alpha\text{-Cu}_2\text{ZnSiS}_4$ , the states at the conduction band minimum chiefly arise from the S-p, Si-s, Si-p, and Zn-s orbitals, with lesser contributions from the Zn-p and Cu-p orbitals; the partial DOS for  $\beta\text{-Cu}_2\text{ZnSiS}_4$  is similar to that of  $\alpha\text{-Cu}_2\text{ZnSiS}_4$  (Figures 5.8 and 5.9). However, in  $\text{Cu}_2\text{CdSnS}_4$ , the lowest energy states in the conduction band minimum evolve predominantly from the Sn-s and S-p orbitals. Accompanying the calculations summarized here using WIEN2k, electronic structure calculations and Mulliken population analysis were also carried out using the CASTEP code and the results are available via the web in supporting information (<http://pubs.acs.org.authenticate.library.duq.edu/doi/suppl/10.1021/ic501310d>).



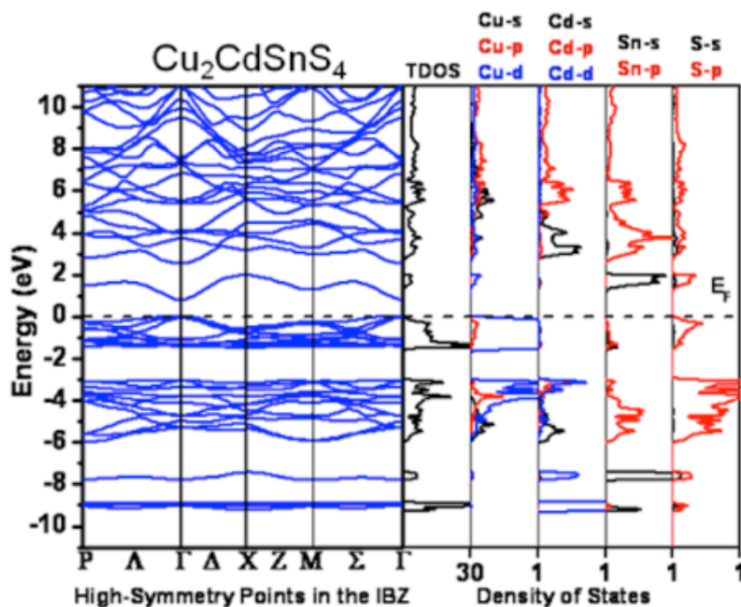


**Figure 5.7:** Calculated band structure (left) and partial DOS diagrams of  $\text{Cu}_2\text{CdSnS}_4$  via the WIEN2k computational software. The horizontal, dashed line denotes the Fermi level ( $E_F$ ). *Source:* reprinted with permission from: Rosmus, K. et al. Optical nonlinearity in  $\text{Cu}_2\text{CdSnS}_4$  and  $\alpha/\beta\text{-Cu}_2\text{ZnSiS}_4$ : diamond-like semiconductors with high laser-damage thresholds. *Inorg. Chem.* **2014**, *53*, 7809–7811.

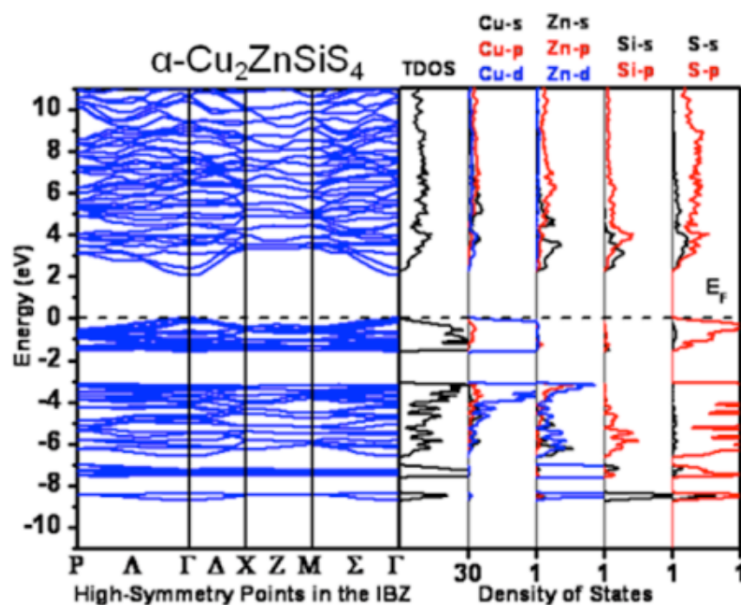


**Figure 5.8:** Calculated band structure (left) and partial DOS diagrams of  $\alpha\text{-Cu}_2\text{ZnSiS}_4$  via the WIEN2k computational software. The horizontal, dashed line denotes the Fermi level ( $E_F$ ). *Source:* reprinted with permission from: Rosmus, K. et al. Optical nonlinearity in  $\text{Cu}_2\text{CdSnS}_4$  and  $\alpha/\beta\text{-Cu}_2\text{ZnSiS}_4$ : diamond-like semiconductors with high laser-damage thresholds. *Inorg. Chem.* **2014**, *53*, 7809–7811.

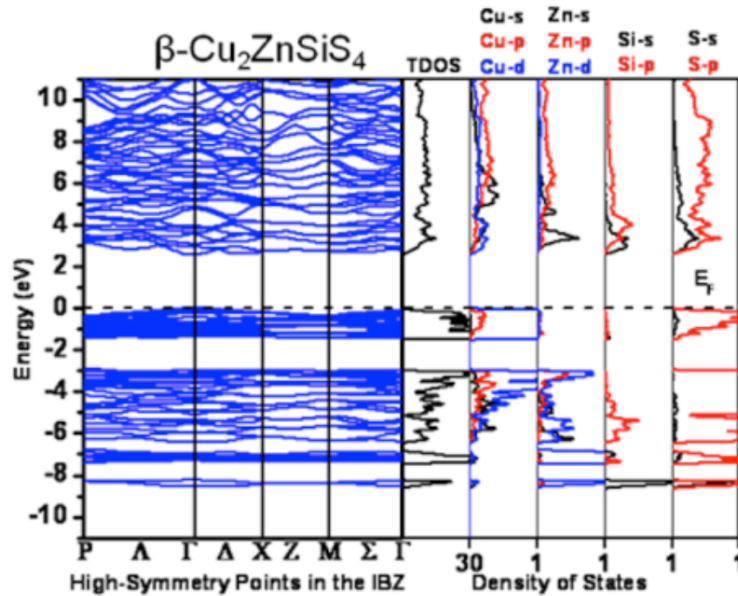


**Figure 5.9:** Calculated band structure (left) and partial DOS diagrams of  $\beta$ - $\text{Cu}_2\text{ZnSiS}_4$  via the WIEN2k computational software. The horizontal, dashed line denotes the Fermi level ( $E_F$ ). *Source:* reprinted with permission from: Rosmus, K. et al. Optical nonlinearity in  $\text{Cu}_2\text{CdSnS}_4$  and  $\alpha/\beta$ - $\text{Cu}_2\text{ZnSiS}_4$ : diamond-like semiconductors with high laser-damage thresholds. *Inorg. Chem.* **2014**, *53*, 7809–7811.

### 5.3 Electronic Structure of a Novel Diamond-like Semiconductor:

#### $\text{Li}_2\text{MnSnS}_4$

This section is partially adapted and reproduced (with permission) from the following manuscript: Devlin, K. et al. Polymorphism and second harmonic generation in a novel diamond-like semiconductor:  $\text{Li}_2\text{MnSnS}_4$ . *J. Solid State Chem.* **2015**, *231*, 256–266. All experimental work was performed by the Aitken, Jang, and Kim Research Groups and can be found online for support of the electronic structure calculations.

High-temperature, solid state synthesis in the  $\text{Li}_2\text{MnSnS}_4$  system led to the discovery of two new polymorphic compounds that were re-analyzed using single crystal X-ray diffraction. The  $\alpha$ -polymorph crystallizes in  $Pna2_1$  with the lithium cobalt (II) silicate,  $\text{Li}_2\text{CoSiO}_4$ , structure type, where  $Z=4$ ,  $R1=0.0349$  and  $wR2=0.0514$  for all data. The  $\beta$ -polymorph possesses the wurtzkesterite structure type, crystallizing in  $Pn$  with  $Z=2$ ,  $R1=0.0423$ , and  $wR2=0.0901$  for all data. These structures are provided in Figure 5.10. Rietveld refinement of synchrotron X-ray powder diffraction

was utilized to quantify the phase fractions of the polymorphs in the reaction products. The  $\alpha/\beta$ - $\text{Li}_2\text{MnSnS}_4$  mixture exhibits an absorption edge of  $\approx 2.6$ - $3.0$  eV, a

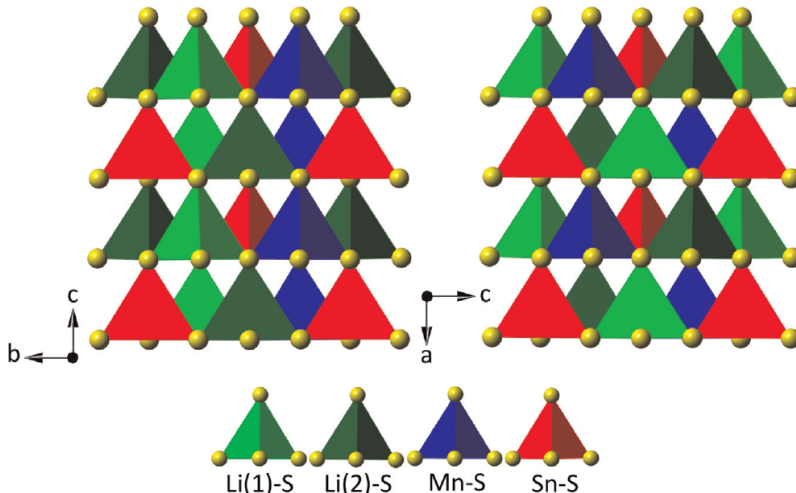


**Figure 5.10:** Polyhedral representations of  $\alpha$ - $\text{Li}_2\text{MnSnS}_4$  (left) and  $\beta$ - $\text{Li}_2\text{MnSnS}_4$  (right) shown down the crystallographic a- and b-axes, respectively. The two structures differ in the arrangement of cations. Both compounds are noncentrosymmetric as all of the tetrahedra point in one direction along the c-axis and a-axis, respectively. *Source:* reprinted with permission from: Devlin, K. et al. Polymorphism and second harmonic generation in a novel diamond-like semiconductor:  $\text{Li}_2\text{MnSnS}_4$ . *J. Solid State Chem.* **2015**, *231*, 256–266.

wide region of optical transparency in the mid- to far-IR, and moderate SHG activity over the fundamental range of 1.1-2.1  $\mu\text{m}$ . Calculations using DFT indicate that the ground state energies and electronic structures for  $\alpha$ - and  $\beta$ - $\text{Li}_2\text{MnSnS}_4$ , as well as the hypothetical polymorph,  $\gamma$ - $\text{Li}_2\text{MnSnS}_4$  with the wurtzstannite structure type, are highly similar. Results of the electronic structure calculations are summarized below.

Electronic structure calculations were carried out for  $\alpha$ - and  $\beta$ - $\text{Li}_2\text{MnSnS}_4$ , along with the hypothetical  $\gamma$ - $\text{Li}_2\text{MnSnS}_4$ , using the FP-LAPW method of DFT within WIEN2k to solve the KS equations for total energy.<sup>21,88,96</sup> For  $\alpha$ - and  $\beta$ - $\text{Li}_2\text{MnSnS}_4$ , the experimentally determined crystal structures were used as input, while the proposed fractional atomic coordinates for the hypothetical  $\gamma$ - $\text{Li}_2\text{MnSnS}_4$  in space group  $Pmn2_1$  were derived from the  $\text{Li}_2\text{CdSnS}_4$  structure,<sup>125</sup> which crystallizes in the wurtzstannite( $Pmn2_1$ ) structure type. The lattice parameters were obtained by transforming the experimentally determined lattice parameters of  $\beta$ - $\text{Li}_2\text{MnSnS}_4$  such that a, b

and *c* axes lengths of  $\beta$ -Li<sub>2</sub>MnSnS<sub>4</sub> became the *c*, *b* and *a* axes of  $\gamma$ -Li<sub>2</sub>MnSnS<sub>4</sub>.<sup>126</sup> Tables S3 and S4 in the supporting information (available on the web at <http://dx.doi.org/10.1016/j.jssc.2015.08.011>) provide the starting model details for  $\gamma$ -Li<sub>2</sub>MnSnS<sub>4</sub>.

The PBE-GGA functional was utilized to account for the XC energy along with the mBJ potential for a better approximation of the  $E_g$  in semiconductors.<sup>90,93</sup> The RMT for Li, Mn, Sn, and S were 2.10, 2.47, 2.50, and 2.02 bohr, respectively for  $\alpha$ -Li<sub>2</sub>MnSnS<sub>4</sub>; 2.05, 2.46, 2.50, and 2.01 bohr, respectively for  $\beta$ -Li<sub>2</sub>MnSnS<sub>4</sub>; and 2.12, 2.50, 2.50, and 2.04 bohr, respectively for  $\gamma$ -Li<sub>2</sub>MnSnS<sub>4</sub>. Convergence in the SCF calculations was achieved when the energy difference in consecutive iterations fell below 0.1 mRy per unit cell. The rkmax value used to establish the number of plane waves was set to 6.5. The number of k-points used in the full Brillouin zone was 3,000, which reduced to 400, 630, and 336 k-points in the iBZ for  $\alpha$ -Li<sub>2</sub>MnSnS<sub>4</sub>,  $\beta$ -Li<sub>2</sub>MnSnS<sub>4</sub>, and  $\gamma$ -Li<sub>2</sub>MnSnS<sub>4</sub>, respectively. The k-point path selected for the band structure plots of all polymorphs was of the primitive unit cell.

Spin polarization was considered in the calculations because of the unpaired electrons in the manganese atoms. The spin was treated antiferromagnetically by alternating spin up and spin down states for the manganese atoms in the unit cell. A geometry optimization of the fractional atomic coordinates was performed on the  $\alpha$ -Li<sub>2</sub>MnSnS<sub>4</sub> and  $\beta$ -Li<sub>2</sub>MnSnS<sub>4</sub> polymorphs. A volume optimization of the lattice parameters was performed on the hypothetical  $\gamma$ -Li<sub>2</sub>MnSnS<sub>4</sub> structure, followed by a geometry optimization of the fractional atomic coordinates. Tables S1 and S2 (available in the supporting information online) list the optimized fractional atomic coordinates for  $\alpha/\beta$ -Li<sub>2</sub>MnSnS<sub>4</sub>, respectively, as compared to those determined by experiment. Tables S3 and S4 (available in the supporting information online) provide the calculated lattice parameters and fractional atomic coordinates, respectively, for  $\gamma$ -Li<sub>2</sub>MnSnS<sub>4</sub> as compared to the proposed values that were input.

The electronic structures of  $\alpha$ - and  $\beta$ - $\text{Li}_2\text{MnSnS}_4$  were calculated using the single crystal structure solutions obtained at room temperature while the electronic structure for the hypothetical polymorph,  $\gamma$ - $\text{Li}_2\text{MnSnS}_4$ , was calculated using the proposed wurtzstannite structure. Figures 5.11-5.13 provide the spin up and spin down band structures of all three polymorphs.

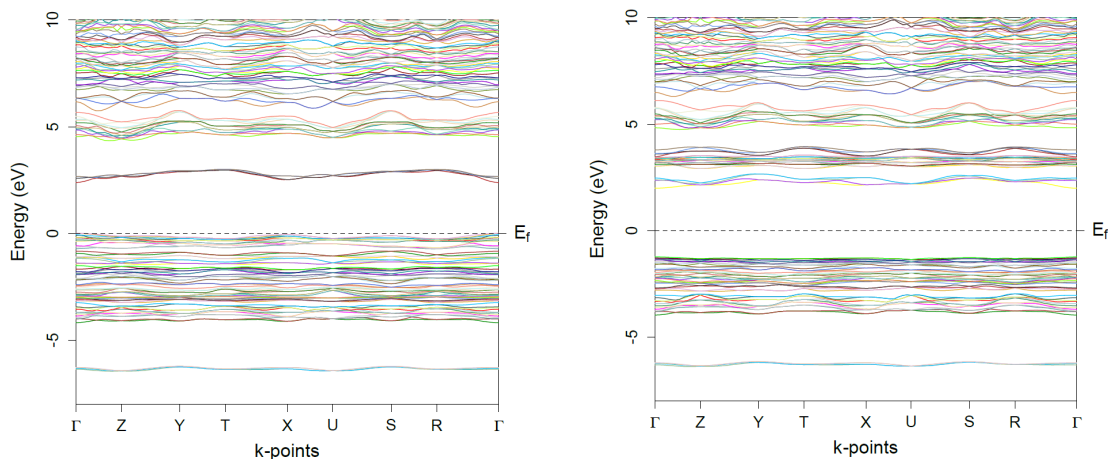


**Figure 5.11:** The spin up (left) and spin down (right) band structures of  $\alpha$ - $\text{Li}_2\text{MnSnS}_4$ . The Fermi level ( $E_f$ ) is denoted by the horizontal dashed line. *Source:* reprinted with permission from: Devlin, K. et al. Polymorphism and second harmonic generation in a novel diamond-like semiconductor:  $\text{Li}_2\text{MnSnS}_4$ . *J. Solid State Chem.* **2015**, *231*, 256–266.

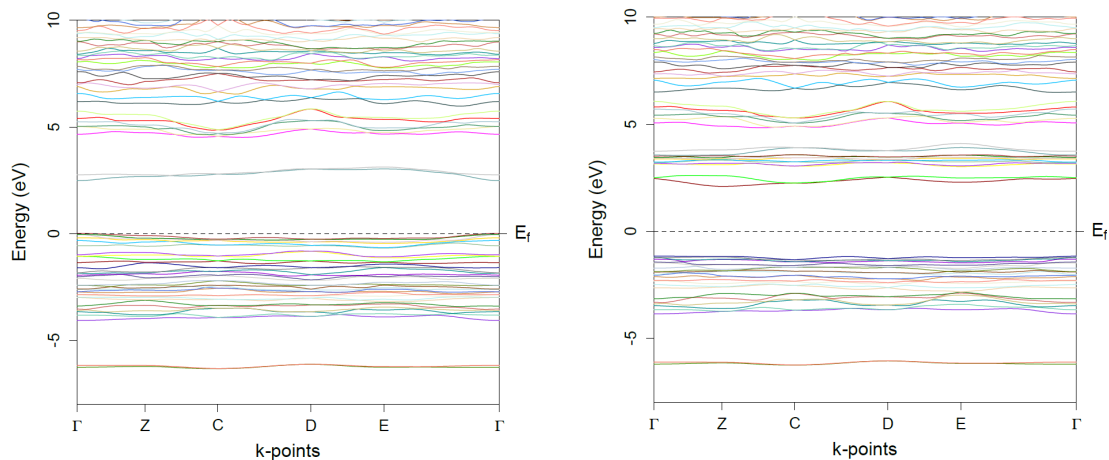


**Figure 5.12:** The spin up (left) and spin down (right) band structures of  $\beta$ - $\text{Li}_2\text{MnSnS}_4$ . The Fermi level ( $E_f$ ) is denoted by the horizontal dashed line. *Source:* reprinted with permission from: Devlin, K. et al. Polymorphism and second harmonic generation in a novel diamond-like semiconductor:  $\text{Li}_2\text{MnSnS}_4$ . *J. Solid State Chem.* **2015**, *231*, 256–266.

Direct  $E_g$  values of 2.3, 2.6, and 2.3 eV were calculated at the  $\Gamma$  point in the Brill-

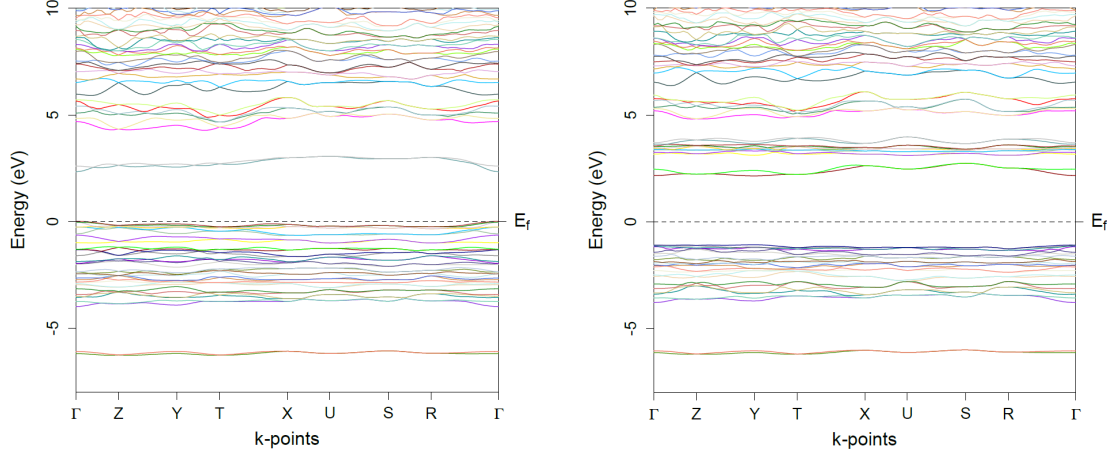


**Figure 5.13:** The spin up (left) and spin down (right) band structures of  $\gamma$ - $\text{Li}_2\text{MnSnS}_4$ . The Fermi level ( $E_f$ ) is denoted by the horizontal dashed line. *Source:* reprinted with permission from: Devlin, K. et al. Polymorphism and second harmonic generation in a novel diamond-like semiconductor:  $\text{Li}_2\text{MnSnS}_4$ . *J. Solid State Chem.* **2015**, *231*, 256–266.

lounin zone for the  $\alpha$ ,  $\beta$ , and  $\gamma$  polymorphs, respectively. These  $E_g$  values were the same for both the spin up and spin down states of all three polymorphs. Despite the implementation of the mBJ potential for improved  $E_g$  calculations in semiconductors,<sup>93</sup> the  $E_g$  values were still underestimated compared with those approximated from the measured optical absorption spectrum. This underestimation is commonly encountered in DFT calculations using the PBE-GGA method, as well as other methods, due to the inexact nature of the XC potential energy term.<sup>89,90,93,127</sup>

To better understand the origin of  $E_g$  in the polymorphs, the partial DOS were calculated and the results are provided in Figures 5.14-5.19 for the  $\alpha$ -,  $\beta$ -, and  $\gamma$ - $\text{Li}_2\text{MnSnS}_4$  polymorphs, respectively. Comparison of the DOS plots for the spin up and spin down configurations show some pronounced differences, while the DOS from polymorph to polymorph are qualitatively similar and exhibit little variation in their atomic orbital contributions. Here, the DOS for the spin up case will be described in detail and, where applicable, variations in the spin down case will be explained. The states in the valence band for the spin up configurations from -7.0 to -5.0 eV mainly arise from Sn-s, S-s, and S-p orbitals and to a much lesser extent the Li-s

and Li-p orbitals. From approximately -5.0 to -1.25eV, the states mostly originate from the Mn-d and S-p orbitals, with the Sn-p, Li-s, and Li-p orbitals providing only weak donations. The valence band maximum in the vicinity of about -1.25 to 0 eV is almost entirely composed of Mn-d and S-p states; the Sn and Li orbitals provided nearly zero influence in this energy region. The most prominent difference between the spin cases is the orbital contribution of the manganese atom. In contrast to the DOS of the spin up configuration, the Mn-d states are almost completely absent in the valence band for the DOS of the spin down configuration.

The states at the conduction band minimum,  $\approx 2.5$  eV, arise primarily from the Sn-s and S-p orbitals. Therefore, based on these electronic structure calculations, it is proposed that the transition across  $E_g$  observed in the optical spectrum of the  $\alpha/\beta$ - $\text{Li}_2\text{MnSnS}_4$  mixture principally occurs from the S-3p states at the valence band maximum to the Sn-5s states at the conduction band minimum. These results agree with the calculations performed for the chemically similar compounds  $\text{Li}_2\text{CdGeS}_4$  and  $\text{Cu}_2\text{CdSnS}_4$ ,<sup>122,128</sup> where the transition across  $E_g$  primarily occurs from S-3p states at the valence band maximum to the IV-s states at the conduction band minimum. Although the Mn-d orbitals play no role in the conduction band states in the spin up configuration, the states at the conduction band minimum have significant Mn-d character in the spin down case. In all calculations, the states higher in the conduction band of the  $\text{Li}_2\text{MnSnS}_4$  polymorphs, from  $\approx 3.2$ -6 eV, are predominantly derived from the Sn-s, Sn-p, S-s, and S-p orbitals with minor involvement of the Li-s and Li-p orbitals. The major contributions of the Li-s and Li-p orbitals are mainly spread out over the higher energy conduction band states, greater than 6 eV, due to the highly ionic bonding interaction of lithium and sulfur. Subtle variations in the states near the Fermi level of the  $\alpha$ - and  $\beta$ - $\text{Li}_2\text{MnSnS}_4$  polymorphs gives rise to the somewhat dissimilar  $E_g$  values. Although the Mn-4d states make major contributions to the valence band maximum and conduction band minimum for the spin up and spin

down configurations, respectively, the  $E_g$  observed for the  $\text{Li}_2\text{MnSnS}_4$  polymorphs is comparable to other DLS, where the II cation plays no role in defining  $E_g$ , for example  $\text{Li}_2\text{CdGeS}_4$  (3.15 eV) and  $\text{Li}_2\text{ZnSnS}_4$  (2.87 eV) that appear pale-yellow and yellow-green, respectively.<sup>125,128,129</sup>

The calculated total energies were considered in order to rationalize the difficulty encountered in separately preparing the  $\alpha$ - and  $\beta$ - $\text{Li}_2\text{MnSnS}_4$  polymorphs. The calculated total energies of  $\alpha$ -,  $\beta$ -, and  $\gamma$ - $\text{Li}_2\text{MnSnS}_4$  were  $-71\,496.2870$ ,  $-35\,748.1423$ , and  $-35\,748.1082$  Ry per unit cell, respectively. Note that since the volume of the  $\alpha$ - $\text{Li}_2\text{MnSnS}_4$  unit cell is twice that of the  $\beta$  and  $\gamma$ - $\text{Li}_2\text{MnSnS}_4$  polymorphs, its total energy is doubled. In accordance with the fact that this work provides no experimental evidence to support the existence of a  $\gamma$ - $\text{Li}_2\text{MnSnS}_4$  polymorph with the wurtzstannite structure, the calculated total energy of the hypothetical  $\gamma$ -phase registered highest. While the polymorph with the most stable structure, i.e. the lowest energy, was  $\alpha$ - $\text{Li}_2\text{MnSnS}_4$ , the total energies of all three polymorphs are considered very similar. These results help to explain the many failed attempts to synthesize the  $\alpha$ - and  $\beta$ - $\text{Li}_2\text{MnSnS}_4$  phases in pure form.



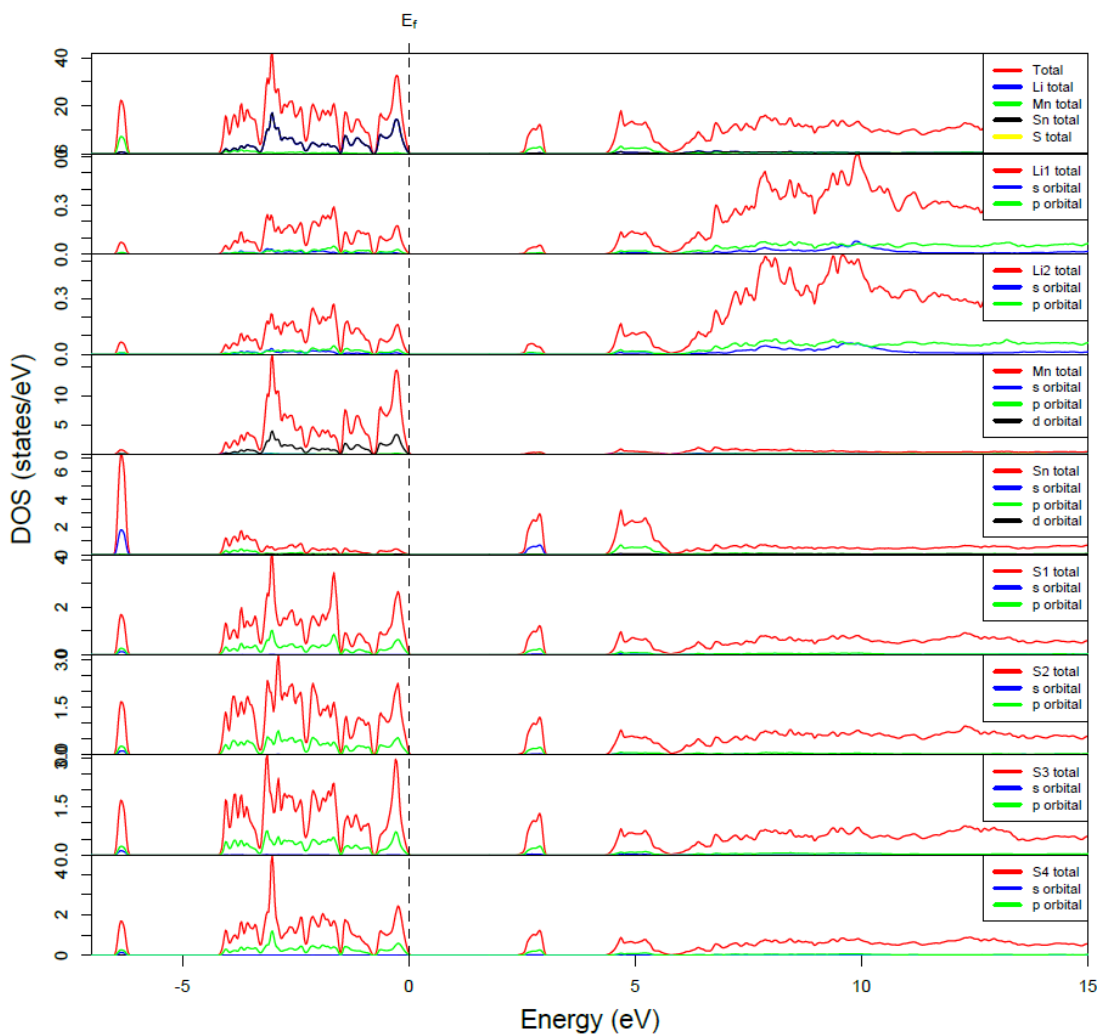


**Figure 5.14:** The spin up DOS of  $\alpha$ -Li<sub>2</sub>MnSnS<sub>4</sub>. The Fermi level ( $E_f$ ) is denoted by the vertical dashed line. *Source:* reprinted with permission from: Devlin, K. et al. Polymorphism and second harmonic generation in a novel diamond-like semiconductor: Li<sub>2</sub>MnSnS<sub>4</sub>. *J. Solid State Chem.* **2015**, *231*, 256–266.

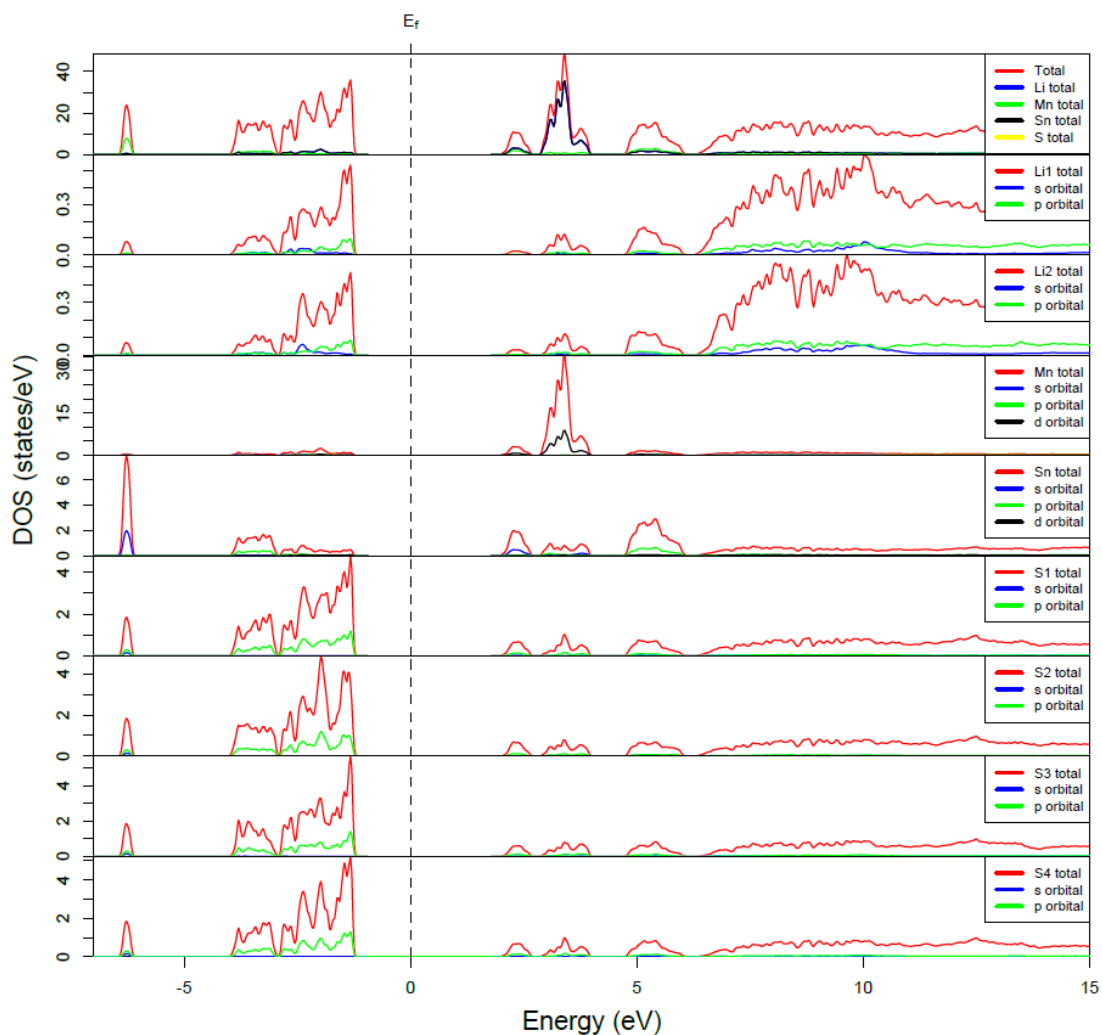


**Figure 5.15:** The spin down DOS of  $\alpha$ -Li<sub>2</sub>MnSnS<sub>4</sub>. The Fermi level ( $E_f$ ) is denoted by the vertical dashed line. *Source:* reprinted with permission from: Devlin, K. et al. Polymorphism and second harmonic generation in a novel diamond-like semiconductor: Li<sub>2</sub>MnSnS<sub>4</sub>. *J. Solid State Chem.* **2015**, *231*, 256–266.

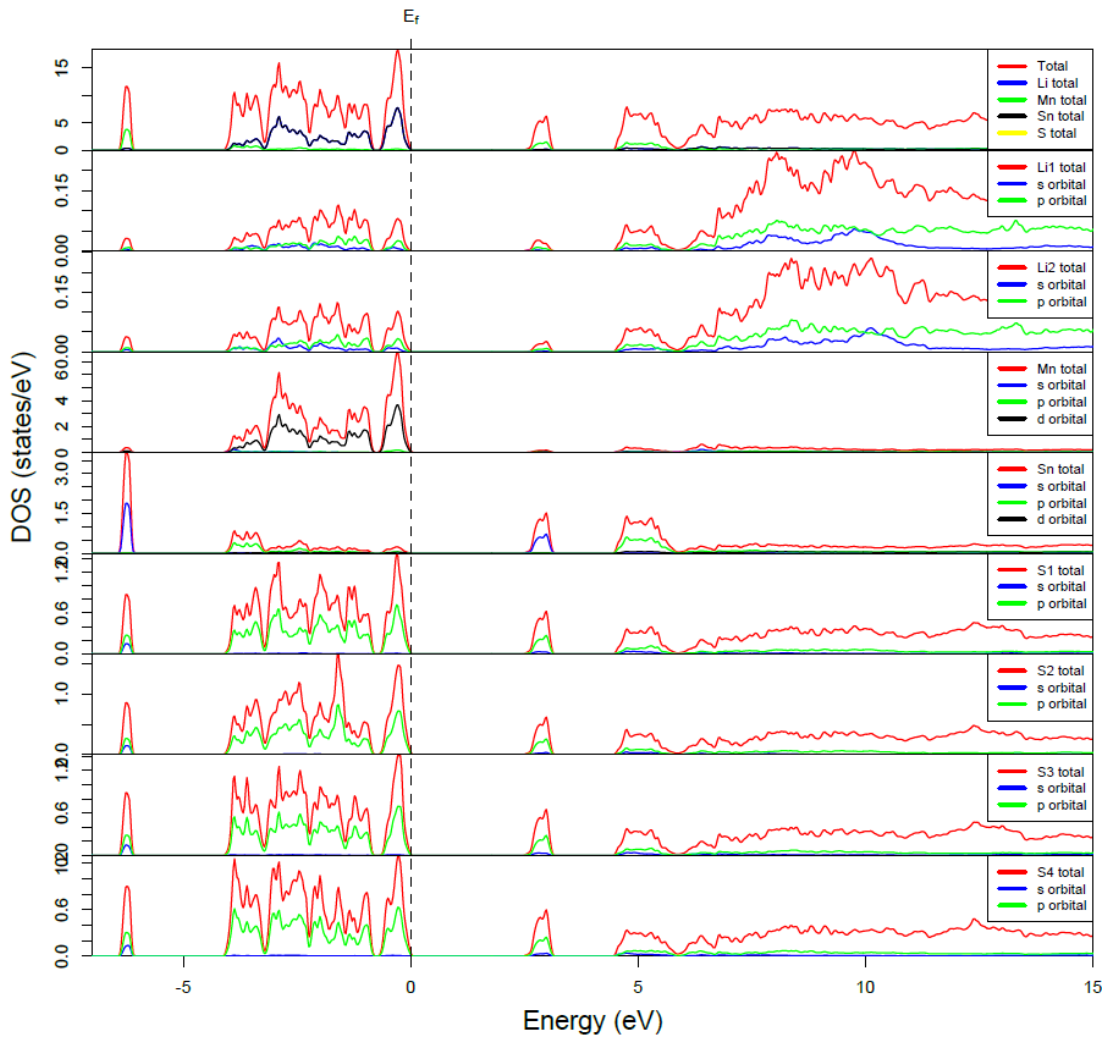


**Figure 5.16:** The spin up DOS of  $\beta$ - $\text{Li}_2\text{MnSnS}_4$ . The Fermi level ( $E_f$ ) is denoted by the vertical dashed line. *Source:* reprinted with permission from: Devlin, K. et al. Polymorphism and second harmonic generation in a novel diamond-like semiconductor:  $\text{Li}_2\text{MnSnS}_4$ . *J. Solid State Chem.* **2015**, *231*, 256–266.

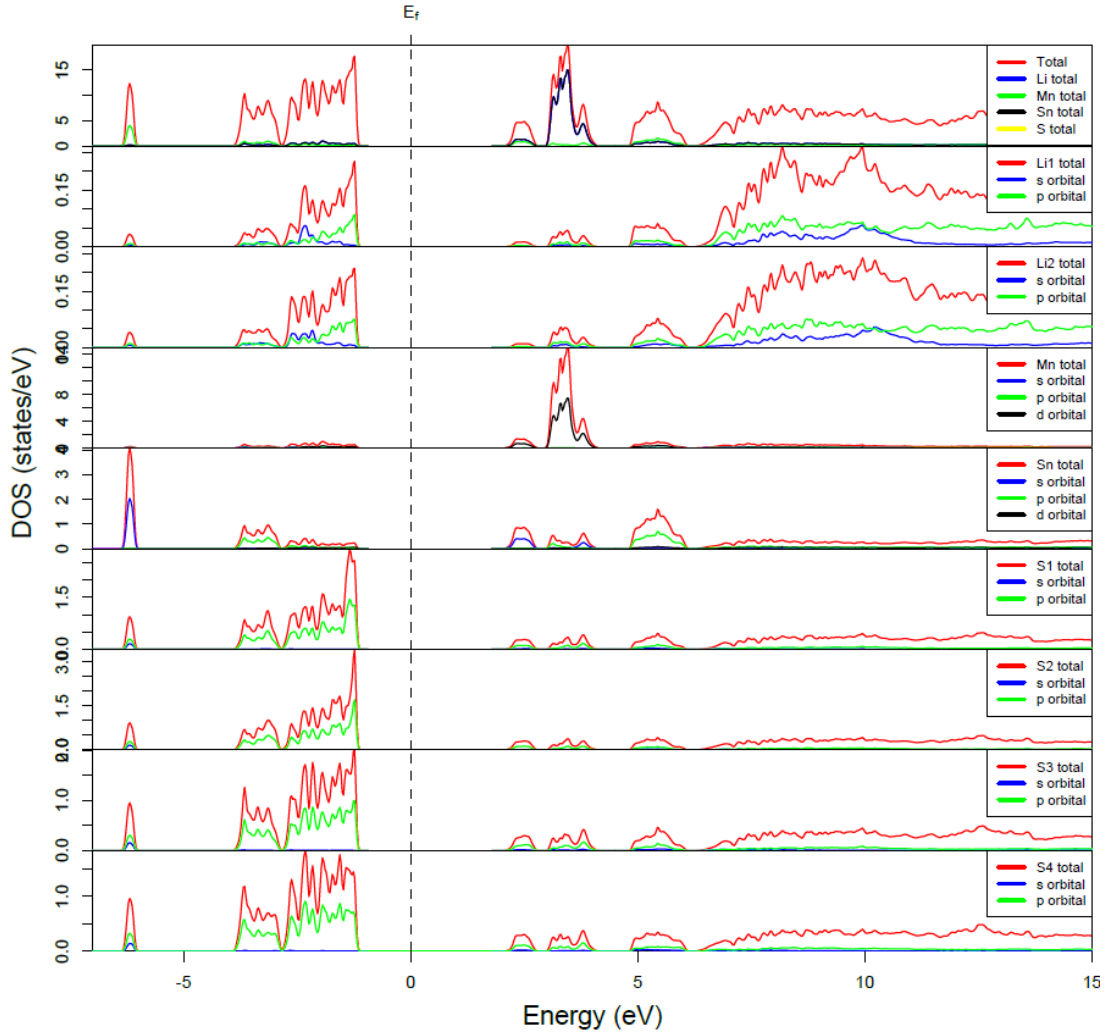


**Figure 5.17:** The spin down DOS of  $\beta$ - $\text{Li}_2\text{MnSnS}_4$ . The Fermi level ( $E_f$ ) is denoted by the vertical dashed line. *Source:* reprinted with permission from: Devlin, K. et al. Polymorphism and second harmonic generation in a novel diamond-like semiconductor:  $\text{Li}_2\text{MnSnS}_4$ . *J. Solid State Chem.* **2015**, *231*, 256–266.

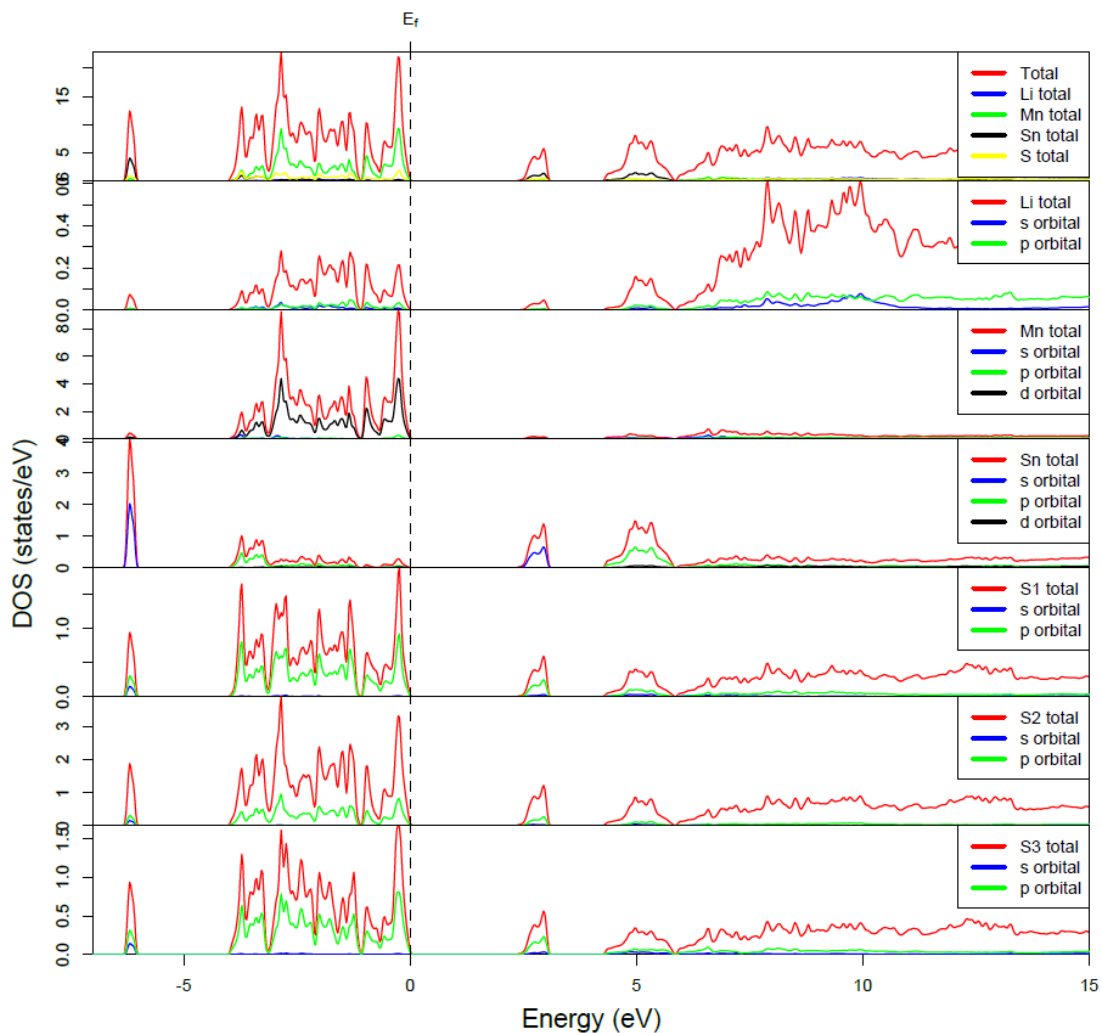


**Figure 5.18:** The spin up DOS of  $\gamma$ -Li<sub>2</sub>MnSnS<sub>4</sub>. The Fermi level ( $E_f$ ) is denoted by the vertical dashed line. *Source:* reprinted with permission from: Devlin, K. et al. Polymorphism and second harmonic generation in a novel diamond-like semiconductor: Li<sub>2</sub>MnSnS<sub>4</sub>. *J. Solid State Chem.* **2015**, *231*, 256–266.

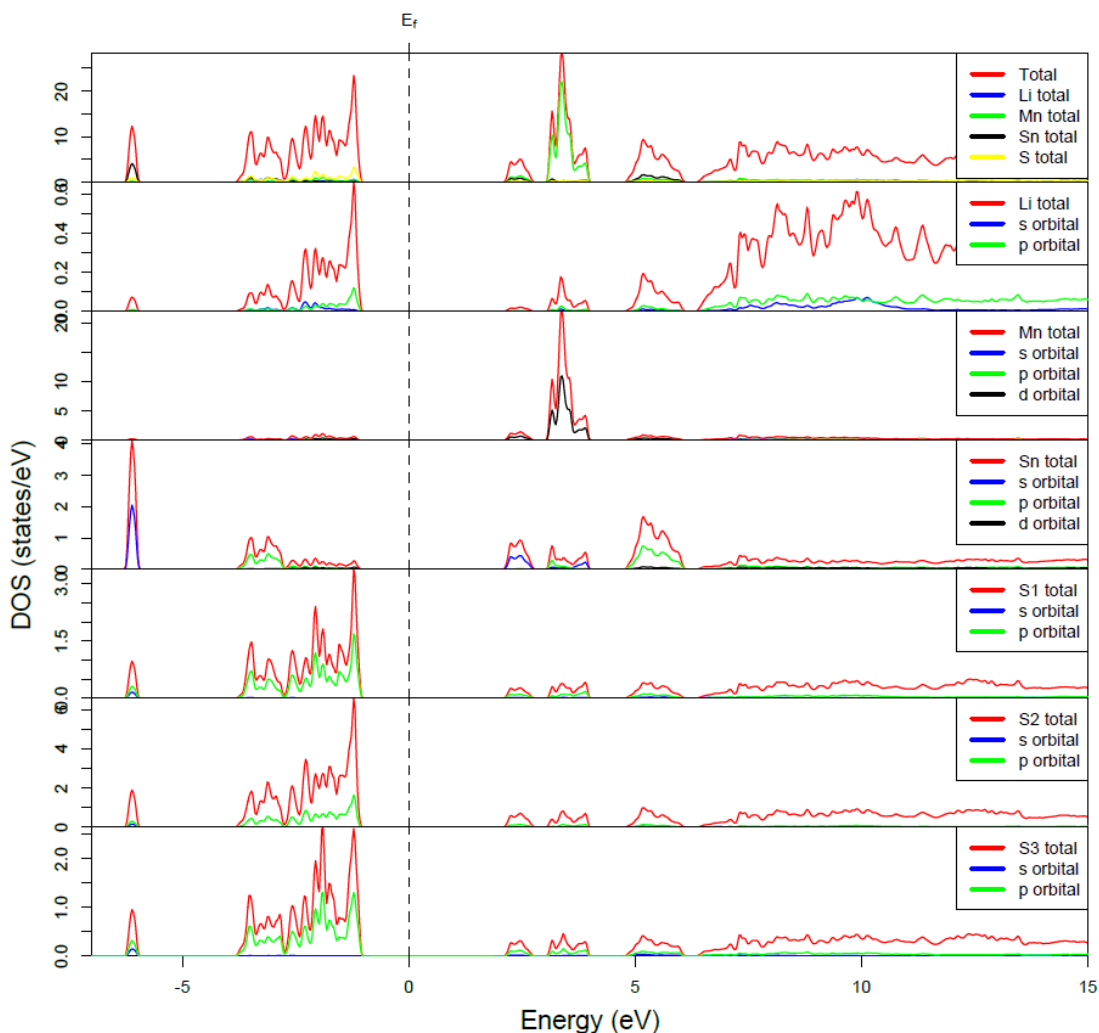


**Figure 5.19:** The spin down DOS of  $\gamma$ - $\text{Li}_2\text{MnSnS}_4$ . The Fermi level ( $E_f$ ) is denoted by the vertical dashed line. *Source:* reprinted with permission from: Devlin, K. et al. Polymorphism and second harmonic generation in a novel diamond-like semiconductor:  $\text{Li}_2\text{MnSnS}_4$ . *J. Solid State Chem.* **2015**, *231*, 256–266.

#### 5.4 Electronic Structure of Mn-Substituted $\text{AgInSe}_2$ Chalcopyrite Semiconductors

This section is partially adapted and reproduced from a manuscript in progress, titled “Structure and optical properties of Mn-substituted  $\text{AgInSe}_2$  chalcopyrite semiconductors.” All experimental work was performed by the Aitken, Mar, and Khalifah Research Groups and is summarized to support the electronic structure calculations.

Mn-substituted  $\text{AgInSe}_2$  direct  $E_g$  semiconductors were prepared by solid-state synthesis at  $850^\circ\text{C}$ . Rietveld refinement using X-ray powder diffraction data indicates

that  $\text{Ag}_{1-2x}\text{Mn}_x\text{InSe}_2$  ( $x=0-0.07$ ) and  $\text{Ag}_{1-x}\text{Mn}_x\text{InSe}_2$  ( $x=0.05$ ) are single-phase materials. The lattice parameters decrease with increasing manganese content, while the  $c/a$  ratio increases. Oxidation states after substitution were verified as  $\text{Ag}^+$ ,  $\text{Mn}^{2+}$ ,  $\text{In}^{3+}$  and  $\text{Se}^{2-}$  by X-ray photoelectron spectroscopy. All compounds are paramagnetic with small negative Weiss temperatures. Optical diffuse reflectance spectra indicate that the substitution by manganese in the  $\text{Ag}_{1-2x}\text{Mn}_x\text{InSe}_2$  series modifies both the  $E_g$  magnitude and Urbach tail broadening, though the optical gap remains direct in nature. DFT calculations predict that  $\text{AgInSe}_2$  is a direct  $E_g$  semiconductor with a  $E_g$  of 0.95 eV at the  $\Gamma$ -point. Results of the electronic structure calculations are summarized below.

Jaffe and Zunger were the first to report the electronic structures of chalcopyrite-type compounds with DFT. In this early work, a potential-variation mixed-basis (PVMB) approach was used to study chemical trends for the compounds,  $\text{CuAlVI}_2$ ,  $\text{CuGaVI}_2$ , and  $\text{CuInVI}_2$ , where VI was either sulfur or selenium.<sup>114</sup> Additionally, electronic structure calculations for several other chalcopyrite type compounds have been previously reported in the literature.<sup>130-132</sup> These calculations are generally in agreement that the chalcopyrite materials are direct  $E_g$  semiconductors, where the top of the valence band is dominated by the antibonding hybridization of the Cu or Ag-d orbitals with the chalcogen-p orbitals.<sup>114,133,134</sup> The band structure of  $\text{AgInSe}_2$  specifically has been calculated by Rashkeev and Lambrecht,<sup>130</sup> Ozaki and Adachi,<sup>131</sup> and Maeda and coworkers.<sup>132</sup> The 0.10 eV direct  $E_g$  calculated by Rashkeev and Lambrecht<sup>130</sup> was determined using the LSDA XC functional within DFT, which is known to severely underestimate the band gaps of semiconductors.<sup>135</sup> In the work of Ozaki and Adachi,<sup>131</sup> as well as that of Maeda et al.,<sup>132</sup> a pseudopotential method was used. While providing more accurate  $E_g$  values, these pseudopotential methods can be generally inaccurate in their description of the PDOS in the valence region, below the Fermi level. For these reasons, the electronic structure of  $\text{AgInSe}_2$  was

re-calculated using the FP-LAPW method of DFT, combined with the PBE-GGA functional and the application of the mBJ potential.<sup>21,93,96</sup>

The crystal structure of AgInSe<sub>2</sub>, determined by Benoit and coworkers via single crystal X-ray diffraction, was used for the electronic structure calculations.<sup>136</sup> The exchange and correlation effects were treated using the PBE-GGA and the mBJ potential.<sup>93</sup> SCF calculations converged when the energy difference between successive iterations fell below 0.1 mRy per unit cell. Additionally, the geometry of the structure was optimized. A 3,000 k-point mesh was used in the full Brillouin zone, which corresponded to 240 k-points within the iBZ. Additionally, the manganese-substituted AgInSe<sub>2</sub> was modeled by taking the parent composition's unit cell and building a 2x2x2 supercell. This produced a 64 atom supercell, upon which a single manganese atom was substituted on an indium site, which broke the symmetry and resulted in the P1 space group. The indium was then used to displace a silver atom from the supercell in order to maintain consistency with the experimental findings. Upon construction of the supercell, SCF calculations with geometry optimization were performed in order to relax the geometry of the atoms within the supercell, particularly in the vicinity of the substitution. Calculations also incorporated the spin-orbit coupling parameter to examine the effects of the coupling between the spin and orbital angular momentum on the  $E_g$  values.

The calculated band structure and DOS of AgInSe<sub>2</sub> are plotted in Figure 5.20 and 5.21 using the PBE-GGA and the PBE-GGA + mBJ methods. Band structures are plotted to the far left and the partial DOS of Ag, In, and Se are presented in the left center, right center, and right panels of each figure. It is clear that AgInSe<sub>2</sub> is a direct  $E_g$  semiconductor with a gap of 0.004 eV at the  $\Gamma$ -point from the PBE-GGA method. Incorporation of the mBJ potential brings the calculated  $E_g$  value up to 0.95 eV. The next lowest energy transition of 1.13 eV also occurs at the  $\Gamma$ -point at the intersection of two bands. Therefore, it is likely that the two absorption edges in



the optical spectrum that were fit using the direct  $E_g$  function are due to these two transitions. The calculated  $E_g$  is a little smaller than the experimental values, but the results are much closer in agreement compared to some previously reported in the literature.<sup>130,132</sup> Previously reported calculations indicate a direct  $E_g$  for  $\text{AgInSe}_2$  at the  $\Gamma$ -point;<sup>130-132</sup> however, with the exception of the work by Maeda et al.<sup>132</sup> previous works did not discuss the DOS. To better understand the origin of the  $E_g$  in  $\text{AgInSe}_2$ , the partial DOS were calculated, shown in Figure 5.20 left center, right center, and right. The valence band region from -7 to -5 eV principally originates from Se-4p and In-5s orbitals, with minor contributions from the Ag-4d and Se-4s orbitals. Approaching the top of the valence band, -5 to -2 eV, the DOS are primarily comprised of the Ag-4d and Se-4p states, with lesser participation from the In-5p states. The states in the highest energy valence band region, closest to the Fermi level ( $E_F$ ), -2 to 0 eV, evolve predominantly from Se-4p and Ag-4d orbitals. On the other side of the band gap, the minimum states in the conduction band (from +1 to +3.5 eV) chiefly arise from the Se-4s, Se-4p, and In-5s orbitals. Higher in the conduction band, +3.5 to +6 eV, the states are largely due to the Ag-4s and In-5p orbitals along with the Se-4s and Se-4p orbitals.

Based on these calculations, it can be surmised that the lowest energy direct  $E_g$  excitation observed in the optical spectrum arises primarily from the strongly hybridized Ag-4d/Se-4p states to the In-5s orbitals. Considering the large contribution of the Ag-4d orbitals near the Fermi level, it is possible that as manganese is added to the material, and silver is thus removed, the  $E_g$  might change. In fact, it has been shown that the Ag-4d-Se-4p interaction is an antibonding hybridization that is responsible for the  $E_g$  anomaly observed for chalcopyrite materials, meaning that the  $E_g$  of the chalcopyrites are considerably smaller than one would expect based on the binary analogs.<sup>134</sup> However, in the  $\text{Ag}_{1-x}\text{Mn}_x\text{InSe}_2$  series, no change is observed in the experimental  $E_g$  values. This is similar to the results found in the  $\text{CuInSe}_2$

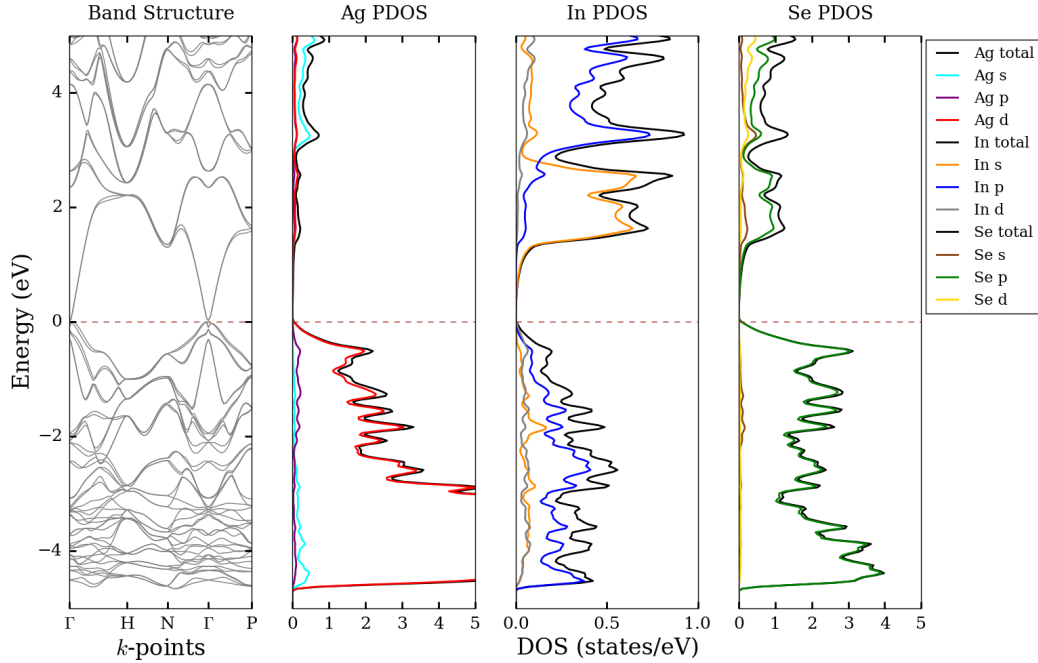


**Figure 5.20:** The band structure (left) and partial DOS of silver (left center), indium (right center), and sulfur (right) of  $\text{AgInSe}_2$  using the PBE-GGA method. *Source:* prepared using: Python Software Foundation. Python Language Reference, version 2.7. Available at <http://www.python.org>.

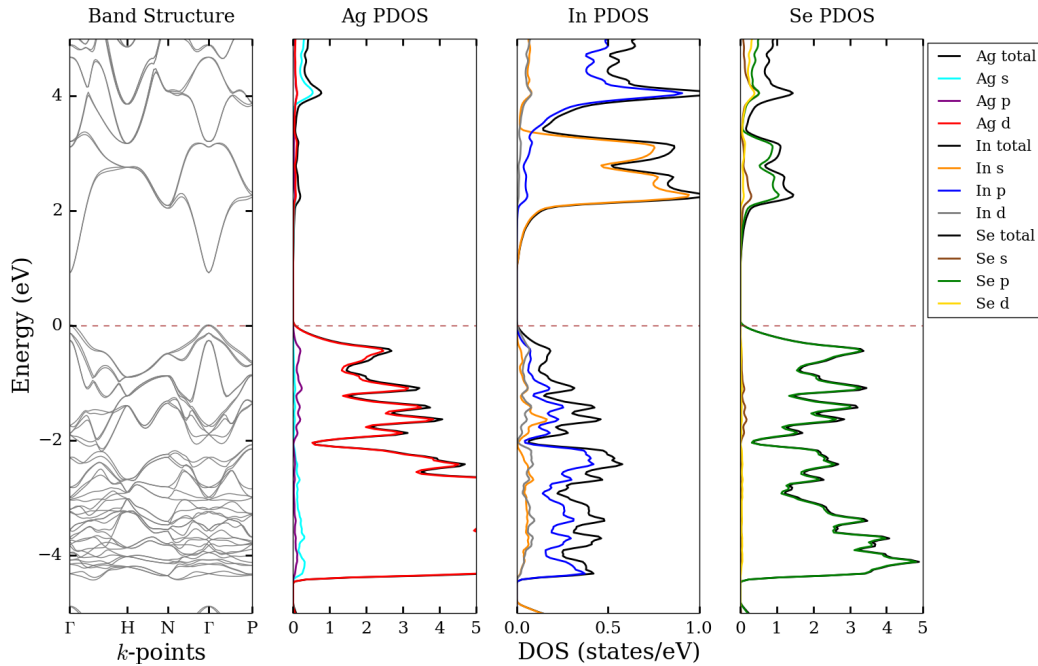


**Figure 5.21:** The band structure (left) and partial DOS of silver (left center), indium (right center), and sulfur (right) of  $\text{AgInSe}_2$  using the PBE-GGA + mBJ method. *Source:* prepared using: Python Software Foundation. Python Language Reference, version 2.7. Available at <http://www.python.org>.

system for the  $\text{CuIn}_{1-x}\text{Mn}_x\text{Se}_2$  and  $\text{Cu}_{1-y}\text{In}_{1-y}\text{Mn}_{2y}\text{Se}_2$  series.<sup>137</sup> Alternatively, in the case of  $\text{Ag}_{1-2x}\text{Mn}_x\text{InSe}_2$ , a small widening of the  $E_g$  is observed that may be due to the removal of Ag-d states at the Fermi level and a narrowing of the bands. On the other hand, the Burstein-Moss effect has been used to explain the  $E_g$  shift in several related, heavily-substituted chalcopyrites.<sup>138,139</sup> A small increase in  $E_g$  with increasing vacancies on the 4a site has also been reported in the copper deficient  $\text{CuInSe}_2$  materials,  $\text{Cu}_{0.95-x}\text{Mn}_x\text{InSe}_2$ , where  $x = 0-0.20$ .<sup>140</sup>

The results of manganese-substituted  $\text{AgInSe}_2$  are provided in Figures 5.22 - 5.27. Figures 5.22 and 5.23 correspond to spin up and spin down calculations of the manganese-substituted system using the PBE-GGA methodology. These calculations produced direct  $E_g$  values of 0.0006 and 0.0002 eV for the spin up and spin down configurations, respectively. Figures 5.24 and 5.25 correspond to spin up and spin down calculations of the manganese-substituted system using the PBE-GGA + mBJ methodology. Incorporation of the mBJ potential increases the  $E_g$  values to 0.87 eV for both the spin-up and spin-down configurations. In both the PBE-GGA and PBE-GGA + mBJ methods, a narrowing of the  $E_g$  value is observed upon manganese substitution, which is opposite of that observed experimentally. Figures 5.26 and 5.27 correspond to spin up and spin down calculations of the manganese-substituted system using the PBE-GGA + mBJ methodology with the incorporation of spin-orbit coupling. Incorporation of the spin-orbit coupling parameter produces a  $E_g$  value of 0.84 eV for both the spin up and spin down configurations. It is important to note that the spin-orbit coupling parameter is important to consider in highly correlated systems. However, in this case, a difference of only 0.03 eV was observed upon spin-orbit coupling inclusion.

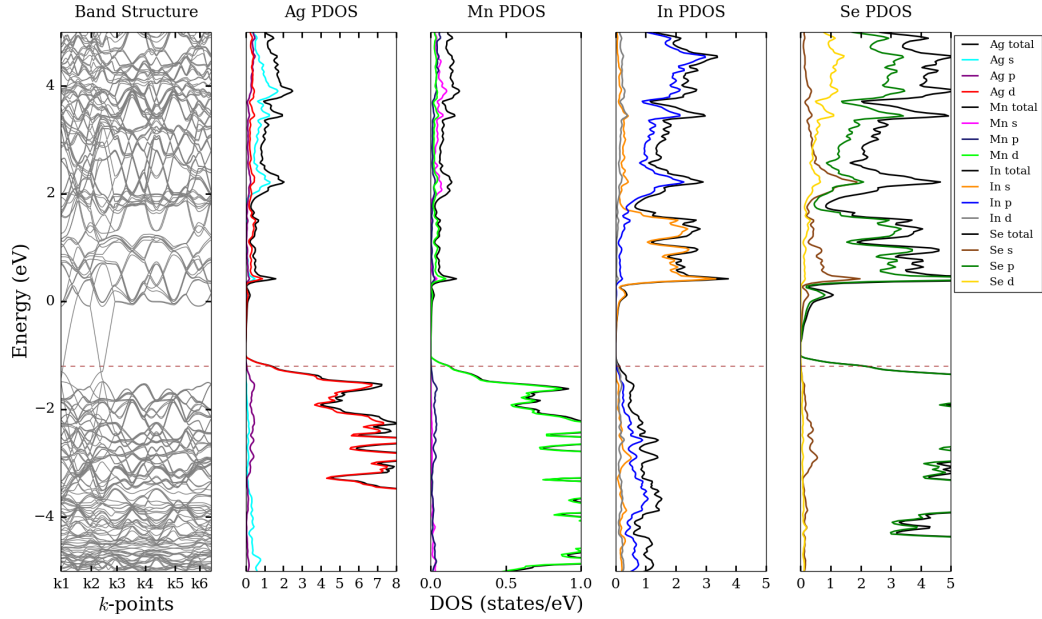


**Figure 5.22:** The band structure (panel 1) and partial DOS of silver (panel 2), manganese (panel 3), indium (panel 4), and sulfur (panel 5) for the spin up configuration of  $\text{Ag}_{0.94}\text{Mn}_{0.06}\text{InSe}_2$  using the PBE-GGA method. *Source:* prepared using: Python Software Foundation. Python Language Reference, version 2.7. Available at <http://www.python.org>.

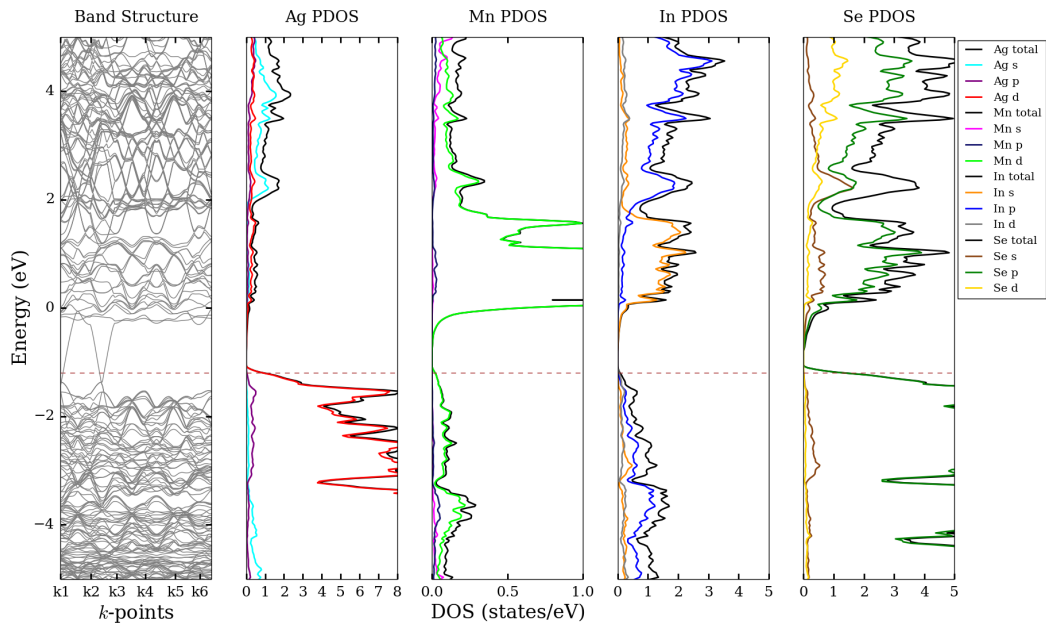


**Figure 5.23:** The band structure (panel 1) and PDOS of silver (panel 2), manganese (panel 3), indium (panel 4), and sulfur (panel 5) for the spin down configuration of  $\text{Ag}_{0.94}\text{Mn}_{0.06}\text{InSe}_2$  using the PBE-GGA method. *Source:* prepared using: Python Software Foundation. Python Language Reference, version 2.7. Available at <http://www.python.org>.

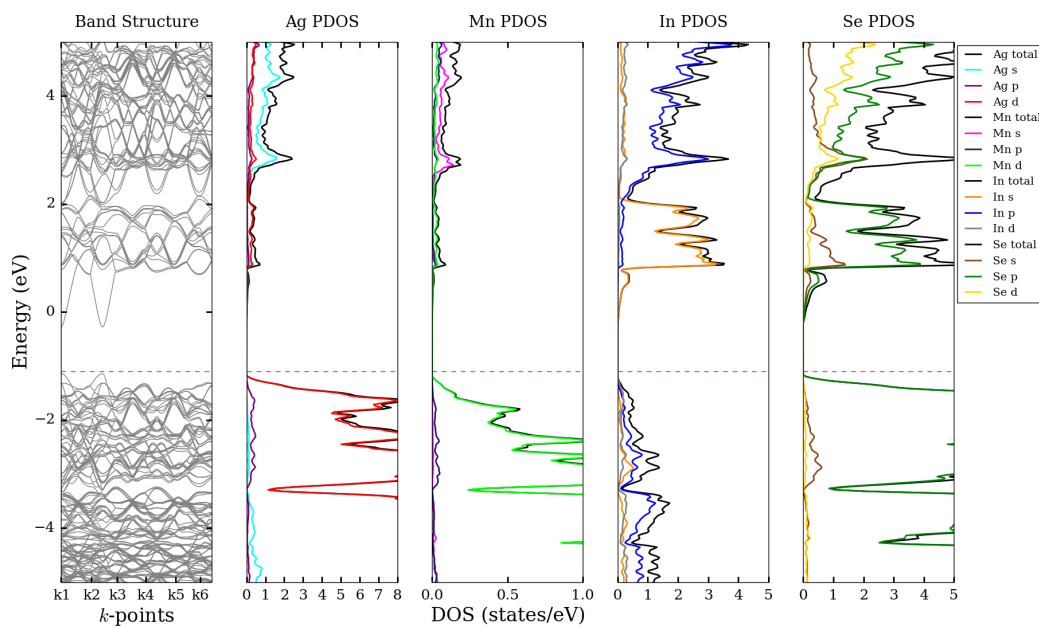


**Figure 5.24:** The band structure (panel 1) and PDOS of silver (panel 2), manganese (panel 3), indium (panel 4), and sulfur (panel 5) for the spin up configuration of  $\text{Ag}_{0.94}\text{Mn}_{0.06}\text{InSe}_2$  using the PBE-GGA + mBJ method. *Source:* prepared using: Python Software Foundation. Python Language Reference, version 2.7. Available at <http://www.python.org>.

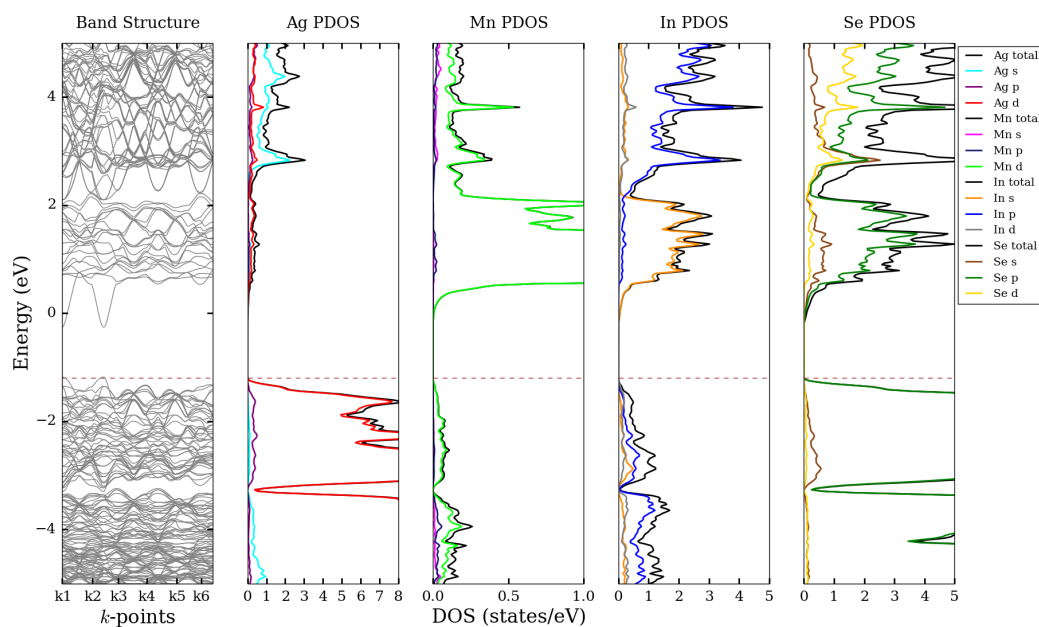


**Figure 5.25:** The band structure (panel 1) and PDOS of silver (panel 2), manganese (panel 3), indium (panel 4), and sulfur (panel 5) for the spin down configuration of  $\text{Ag}_{0.94}\text{Mn}_{0.06}\text{InSe}_2$  using the PBE-GGA + mBJ method. *Source:* prepared using: Python Software Foundation. Python Language Reference, version 2.7. Available at <http://www.python.org>.

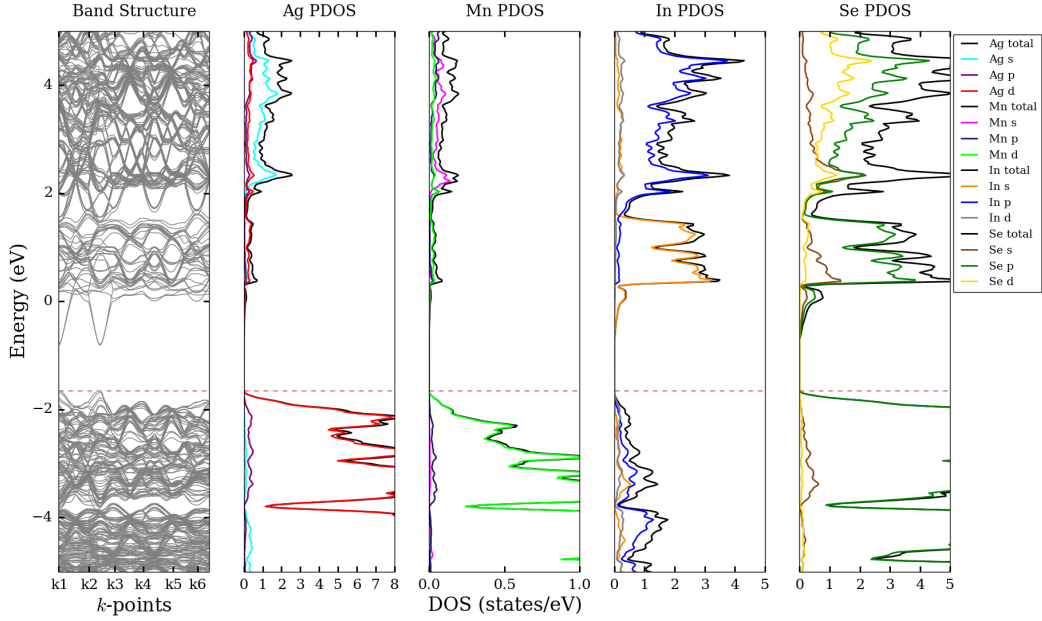


**Figure 5.26:** The band structure (panel 1) and PDOS of silver (panel 2), manganese (panel 3), indium (panel 4), and sulfur (panel 5) for the spin up configuration of  $\text{Ag}_{0.94}\text{Mn}_{0.06}\text{InSe}_2$  using the PBE-GGA + mBJ method with spin-orbit coupling. *Source:* prepared using: Python Software Foundation. Python Language Reference, version 2.7. Available at <http://www.python.org>.

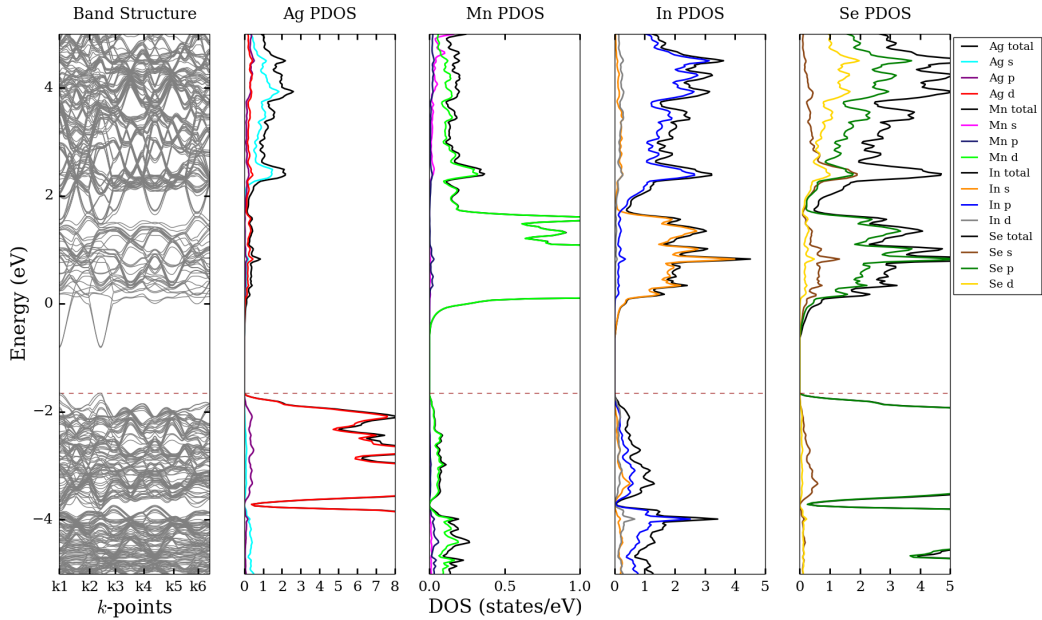


**Figure 5.27:** The band structure (panel 1) and PDOS of silver (panel 2), manganese (panel 3), indium (panel 4), and sulfur (panel 5) for the spin down configuration of  $\text{Ag}_{0.94}\text{Mn}_{0.06}\text{InSe}_2$  using the PBE-GGA + mBJ method with spin-orbit coupling. *Source:* prepared using: Python Software Foundation. Python Language Reference, version 2.7. Available at <http://www.python.org>.

## Chapter 6. Broader Impacts

### 6.1 Revisiting the Thermodynamic Model from Goldstein et al. (1992)

This section is partially adapted and reproduced (with permission) from the following e-letter in *Science*: Srnec, M.N.; Madura, J.D. “RE: Revisiting the thermodynamic model from Goldstein et al. (1992)” (2016); <http://science.sciencemag.org/content/256/5062/1425.e-letters>. The work of this chapter is not directly related to the electronic structure calculations discussed in Chapters 3-5, but is considered a broader impact of this dissertation’s focus on solid state materials. While preparing a general chemistry textbook problem based off the work of Goldstein et al.’s 1992 study, an error was discovered in the thermodynamic model utilized. The correction to this error was made available on the web in the above e-letter. In addition, a future *J. Chem. Educ.* manuscript is in progress, focusing on the use of general chemistry’s dimensional analysis to elucidate a mistake in *Science*. The results of these findings are summarized below.

Goldstein et al. showed that  $T_m$  varied with nanocrystal size, but an alternative evaluation of their data leads to improved agreement with experimental surface tension data. Various thermodynamic models (based on differences in liquid and solid surface tensions) have been reported in the literature and show that the prediction of melting point depression in nanocrystals agrees reasonably well with size-dependent melting.<sup>141–144</sup> In analyzing this data, Goldstein et al. used a form of the liquid-drop model, eq 6.1, where  $T_b$  is the bulk melting temperature,  $T_m$  is the melting temperature of the particle of radius  $R$ ,  $L$  is the molar latent heat of fusion,  $\gamma$  is the surface tension, and  $\rho$  is the density of the solid or liquid.

$$T_b - T_m = \frac{2T_m}{L\rho_{\text{sol}}R_{\text{sol}}} \left[ \gamma_{\text{sol}} - \gamma_{\text{liq}} \left( \frac{\rho_{\text{sol}}}{\rho_{\text{liq}}} \right)^{\frac{2}{3}} \right] \quad (6.1)$$

Using eq 6.1, the authors determined a difference in surface tensions ( $\gamma_{\text{sol}} - \gamma_{\text{liq}}$ ) of  $0.42 \text{ N m}^{-1}$  through a fit of  $1/T_m$  as a function of reciprocal particle radius. The

surface tension of the solid ( $2.50 \text{ N m}^{-1}$ ) was determined from the slope of a line of best fit from a plot of cadmium sulfide (CdS) lattice parameter as a function of the reciprocal particle radius (see Goldstein et al. Figure 1). Using this data, the surface tension of the liquid was determined to be  $2.08 \text{ N m}^{-1}$ .<sup>145</sup>

Attempting to reproduce the liquid surface tension value from their work, the units were inconsistent in eq 6.1. Review of the literature revealed an alternative form of eq 6.1. This alternative thermodynamic model was proposed in equation 44 of Hanszen's 1960 work and is given in eq 6.2, where  $M_{\text{CdS}}$  is the molar mass of the CdS nanocrystal.<sup>146</sup> Here, Hanszen's original equation has been rearranged, isolating  $(T_b - T_m)$ .

$$T_b - T_m = \frac{2T_b M_{\text{CdS}}}{L \rho_{\text{sol}} R_{\text{sol}}} \left[ \gamma_{\text{sol}} - \gamma_{\text{liq}} \left( \frac{\rho_{\text{sol}}}{\rho_{\text{liq}}} \right)^{\frac{2}{3}} \right] \quad (6.2)$$

Eq 6.2 is equivalent to that used by Goldstein et al. (eq 6.1) with two exceptions. The first difference is that the temperature term on the right-hand side of eq 6.1 should be  $T_b$  instead of  $T_m$ . The second difference is the presence of the molar mass term in eq 6.2, which does not appear in the work of Goldstein et al., but is necessary for unit cancellation when determining the surface tension of the liquid. The thermodynamic model of Goldstein et al. references work presented by Buffat and Borel in 1976, who appeared to drop the molecular mass term from Hanszen's original 1960 equation.

The errors in eq 6.1 were discovered via the dimensional analysis shown below. The input data utilized is provided in Table 6.1, where we have made two changes (highlighted in red) based on the literature. Values for  $\rho_{\text{sol}}$  and  $\Delta h_{\text{fs}}$  were obtained from the Handbook of Inorganic Materials,<sup>147</sup> where  $\rho_{\text{sol}}$  is the density of the solid and  $\Delta h_{\text{fs}}$  is the heat of fusion.  $\rho_{\text{liq}}$  is the density of the liquid,  $\gamma_{\text{sol}}$  is the surface tension of the solid,  $\gamma_{\text{liq}}$  is the surface tension of the liquid,  $M_{\text{CdS}}$  is the molecular mass of CdS,  $T_b$  is the bulk melting temperature, and  $\kappa$  is the isothermal compressibility.

As was shown in Goldstein et al.,<sup>145</sup> the value of  $\gamma_{\text{sol}}$  in eq 6.2 can be obtained



$\rho_{\text{sol}} = 4820 \text{ kg m}^{-3}$ $\rho_{\text{liq}} = 4200 \text{ kg m}^{-3}$ $N = \text{kg m s}^{-2}$ $1 \text{ m} = 10^{10} \text{ \AA}$	$\Delta h_{\text{ls}} = 201.669 \text{ kJ mol}^{-1}$ $M_{\text{CdS}} = 0.144 477 \text{ kg mol}^{-1}$ $J = \text{kg m}^2 \text{ s}^{-2}$ $\gamma_{\text{sol}} = ?$	$T_{\text{b}} = 1678 \text{ K}$ $\kappa = 1.56 \times 10^{-11} \text{ m}^2 \text{ N}^{-1}$ $\text{N m}^{-1} = \text{kg s}^{-2}$ $\gamma_{\text{liq}} = ?$
---	---	--

**Table 6.1:** A summary of the CdS input data utilized in the thermodynamic model and the dimensional analysis shown below.

experimentally from a linear fit of

$$\underbrace{\frac{\Delta a}{a}}_y = \underbrace{\frac{2 \cdot \gamma_{\text{sol}} \cdot \kappa}{3}}_m \cdot \underbrace{\frac{1}{R_{\text{sol}}}}_x \quad (6.3)$$

where  $\Delta a = 5.818 - a$ . The value of  $5.818 \text{ \AA}$  is the lattice parameter for the bulk CdS.

The value of  $\gamma_{\text{sol}}$  is

$$\gamma_{\text{sol}} = \frac{3 \cdot \text{slope}}{2 \cdot \kappa} = \frac{3 \cdot 0.26 \times 10^{-10} \text{ m}}{2 \cdot 1.56 \times 10^{-11} \text{ m}^2 \text{ N}^{-1}} = 2.50 \text{ N m}^{-1} \quad (6.4)$$

This value of  $\gamma_{\text{sol}}$  agrees exactly with that of Goldstein et al. and allows eq 6.2 to be rearranged, solving for  $T_{\text{m}}$

$$\left( \frac{T_{\text{m}}}{T_{\text{b}}} \right) = 1 - \frac{2 \cdot M_{\text{CdS}}}{\rho_{\text{sol}} \cdot \Delta h_{\text{ls}} \cdot R_{\text{sol}}} \left[ \gamma_{\text{sol}} - \gamma_{\text{liq}} \left( \frac{\rho_{\text{sol}}}{\rho_{\text{liq}}} \right)^{\frac{2}{3}} \right] \quad (6.5)$$

$$T_{\text{m}} = T_{\text{b}} - \frac{2 \cdot M_{\text{CdS}} \cdot T_{\text{b}}}{\rho_{\text{sol}} \cdot \Delta h_{\text{ls}} \cdot R_{\text{sol}}} \left[ \gamma_{\text{sol}} - \gamma_{\text{liq}} \left( \frac{\rho_{\text{sol}}}{\rho_{\text{liq}}} \right)^{\frac{2}{3}} \right] \quad (6.6)$$

$$\underbrace{T_{\text{m}}}_y = \underbrace{-\frac{2 \cdot M_{\text{CdS}} \cdot T_{\text{b}}}{\rho_{\text{sol}} \cdot \Delta h_{\text{ls}}}}_m \left[ \gamma_{\text{sol}} - \gamma_{\text{liq}} \left( \frac{\rho_{\text{sol}}}{\rho_{\text{liq}}} \right)^{\frac{2}{3}} \right] \cdot \underbrace{\frac{1}{R_{\text{sol}}}}_x + \underbrace{T_{\text{b}}}_b \quad (6.7)$$

where the slope,

$$m = -\frac{2 \cdot M_{\text{CdS}} \cdot T_{\text{b}} \cdot \gamma_{\text{sol}}}{\rho_{\text{sol}} \cdot \Delta h_{\text{ls}}} + \frac{2 \cdot M_{\text{CdS}} \cdot T_{\text{b}} \cdot \gamma_{\text{liq}}}{\rho_{\text{sol}} \cdot \Delta h_{\text{ls}}} \left( \frac{\rho_{\text{sol}}}{\rho_{\text{liq}}} \right)^{\frac{2}{3}} \quad (6.8)$$

and a value of  $-11 918 \text{ K \AA}$  was determined from a plot of  $T_{\text{m}}$  vs.  $\frac{1}{R_{\text{sol}}}$ . Substituting into eq 6.8 yields

$$-11 918 \text{ K \AA} = -\frac{2 \cdot 0.144 477 \text{ kg mol}^{-1} \cdot 1678 \text{ K} \cdot 2.50 \text{ N m}^{-1}}{4820 \text{ kg m}^{-3} \cdot 201.669 \text{ kJ mol}^{-1}} + \quad (6.9)$$

$$\frac{2 \cdot 0.144 477 \text{ kg mol}^{-1} \cdot 1678 \text{ K} \cdot \gamma_{\text{liq}}}{4820 \text{ kg m}^{-3} \cdot 201.669 \text{ kJ mol}^{-1}} \left( \frac{4820 \text{ kg m}^{-3}}{4200 \text{ kg m}^{-3}} \right)^{\frac{2}{3}} \quad (6.10)$$

$$-11\,918\text{ K \AA} = -1.247\,023\,1 \times 10^{-3}\text{ K N m}^2\text{ kJ}^{-1} + 5.467\,636\,694 \times 10^{-4}\text{ K m}^3\text{ kJ}^{-1} \cdot \gamma_{\text{liq}} \quad (6.11)$$

Now, converting to joules and substituting  $J = \text{kg m}^2 \text{s}^{-2}$  and  $N = \text{kg m s}^{-2}$ , produces:

$$-11\,918\text{ K \AA} = -1.247\,023\,1 \times 10^{-6}\text{ K ~~kg m m}^2\text{ s}^2\text{ kg}^{-1}\text{ m}^2 + \quad (6.12)~~$$

$$5.467\,636\,694 \times 10^{-7}\text{ K m}^3\text{ s}^2\text{ kg}^{-1}\text{ m}^2 \cdot \gamma_{\text{liq}} \quad (6.13)$$

and utilizing  $1\text{ m} = 10^{10}\text{ \AA}$ , the above expression can be simplified to:

$$-11\,918\text{ K \AA} = -12\,470.231\text{ K \AA} + 5467.636\,694\text{ K \AA s}^2\text{ kg}^{-1} \cdot \gamma_{\text{liq}} \quad (6.14)$$

combining like terms

$$552.231\text{ K \AA} = 5467.636\,694\text{ K \AA s}^2\text{ kg}^{-1} \cdot \gamma_{\text{liq}} \quad (6.15)$$

and, finally, solving for  $\gamma_{\text{liq}}$

$$\gamma_{\text{liq}} = \frac{552.231\text{ K \AA}}{5467.636\,694\text{ K \AA s}^2\text{ kg}^{-1}} = 0.100\,999\,9\text{ kg s}^{-2} = 0.101\text{ N m}^{-1} \quad (6.16)$$

The results of this fit yielded a liquid surface tension ( $\gamma_{\text{liq}}$ ) of  $0.101\text{ N m}^{-1}$ , which compares well (Table 6.2) to the molten ( $\gamma_{\text{liq}}$ ) cadmium surface tension and similar metal sulfides.<sup>148,149</sup> In addition, a linear regression of the fit between melting point

Material	MP/ $^{\circ}\text{C}$	Temperature/ $^{\circ}\text{C}$	$\gamma_{\text{liq}}/\text{N m}^{-1}$
Cd	321.1	350	0.628
FeS	1,194	1200	0.332
Ni <sub>3</sub> S <sub>2</sub>	790.9	1000	0.526
Cu <sub>2</sub> S	1,130	1200	0.386

**Table 6.2:** Liquid surface tension values of pure molten cadmium and several metal sulfides.

and liquid surface tension values for cadmium and several metal sulfides was also prepared in Figure 6.1. The calculated value of  $0.101\text{ N m}^{-1}$  for  $\gamma_{\text{liq}}$  compares better with the above sulfides in the literature than the value of  $2.08\text{ N m}^{-1}$  reported by Goldstein et al.<sup>145</sup> Utilizing Hansen's equation addresses the temperature typo and the absence of the CdS molecular mass term in eq 6.1. The inclusion of molar mass results in consistent units and improves the reasonableness of the  $\gamma_{\text{liq}}$  value compared

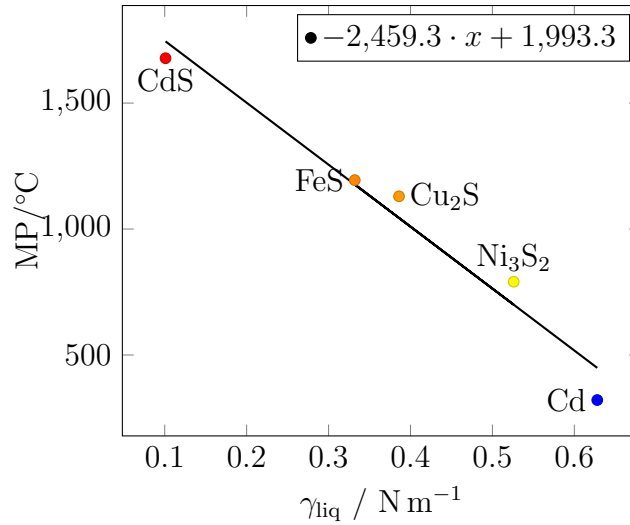


**Figure 6.1:** Fit of melting point and liquid surface tension values for pure molten cadmium and several metal sulfides. *Source:* prepared using the PSTricks package of L<sup>A</sup>T<sub>E</sub>X.

to experimental values in the literature.

In summary, this document revisits novel work published by Goldstein et al. regarding CdS. While new experimental data is not presented, an alternative analysis of their data is presented, which results in a better comparison to similar materials reported in the literature.<sup>150</sup> The analysis further supports their work and the utilization of thermodynamic models to predict surface tensions from experimental melting temperature data.

## Chapter 7. Conclusions

In this work, world energy production and consumption, as well as their consequences, were summarized. In response to these events, alternative energy materials have become a significant focus of today's materials science research. One such class of alternative energy materials is PV solar cells, whose fundamentals and research advances were extensively summarized in Chapter 1. In order to rationalize the efficiency of solar cell materials, their electronic structure must be well understood. The basics of electronic structure and reciprocal space were also summarized in Chapter 1, followed by an overview of the computational methods available to study the electronic structure in Chapter 2.

One such material that has been experimentally and computationally studied for PV solar cell applications is  $\text{TiO}_2$ , whose parent composition gives rise to  $E_g$  values that are too wide for commercial solar cell applications. As a result, several studies in the literature have proposed tuning the electronic structure via structural substitutions to narrow the  $E_g$  value. In this work, the electronic structures of three polymorphs (rutile, anatase, and brookite) of unsubstituted  $\text{TiO}_2$  were calculated. Results of the mBJ calculations for rutile, anatase and brookite produced  $E_g$  values of 2.61, 2.88 and 3.06 eV, respectively. Compared to the standard band structure calculation of rutile with PBE-GGA, these results showed significant improvement in the  $E_g$  underestimation. The  $E_g$  values calculated in this work also compared very well with experimental UV-visible spectroscopy values and the other computational methods reported in the literature. However, the method still has limitations, as evidenced by its inability to produce the same qualitative order of the  $E_g$  values compared to experiment while other methods in the literature (see Table 3.3) do predict the correct order.

Furthermore, the DOS results of Sections 3.3-3.5 agreed very well with those reported in the literature. The agreement between calculations of unsubstituted  $\text{TiO}_2$

polymorphs in this work and those reported in the literature provided validation of the method prior to the substituted calculations of Chapter 4. Inspection of the DOS near the  $E_g$ , particularly in the valence band region, revealed a significant oxygen-p state contribution. In attempt to decrease the  $E_g$  of the  $\text{TiO}_2$  polymorphs, the oxygen-p states were the primary target of structural substitutions.

In Chapter 4 the electronic structures of sulfur-, nitrogen-, and fluorine-substituted rutile were successfully calculated. Additionally, the electronic structures of sulfur-, nitrogen-, fluorine-, and tellurium-substituted anatase were also successfully calculated. These electronic structures and the calculated  $E_g$  values were compared against various chemical properties of the substituents to elucidate the cause of  $E_g$  change. Upon examining these relationships, several interesting observations were made. In the rutile substitutions, a trend of decreasing  $E_g$  was observed with increasing MP. However, this trend is difficult to justify and rationalize from a structural point of view. No clear trends were observed between  $Z/\text{CR}$  or IE and the calculated  $E_g$  values. However, clear trends were observed with the CR and  $\chi$  with respect to the changes in  $E_g$ .  $E_g$  decreased with increasing CR and increased with increasing  $\chi$ . However, an exception in the CR trend was observed with the oxygen data point in the mBJ data set.

In the anatase substitutions, the MP trend was observed again, but was not given much further consideration. While this was observed in both of the substituted systems in this work and was suggested in the literature, there is no current structural explanation of how MP would impact  $E_g$ . Similar to the rutile substitutions, no clear trends were observed between  $Z/\text{CR}$  or IE and the calculated  $E_g$  values for substituted anatase. Most notably, the  $E_g$  in substituted anatase also decreased with increasing CR. Moreover, as the  $\chi$  increased, so too did the  $E_g$  values. However, minor exceptions (nitrogen data point) to these trends still need to be addressed.

The decrease in  $E_g$  with increasing CR can be explained by again considering some

general chemistry principles. Upon substituting an atom with a larger crystal radius on an oxygen site, the molecular orbitals of that substituent and the neighboring titanium atoms overlap to a greater extent. As discussed in Section 1.3, greater orbital overlap produces a greater band dispersion (total range in energy) of the bands in a band structure plot. With bands spanning greater energy, the  $E_g$  value subsequently decreases. An explanation for the increase in  $E_g$  with increasing  $\chi$  can also be rationalized by considering the effect of substitution on the molecular orbitals. As evidenced from the DOS diagrams in Sections 4.3-4.5, the substituent gives rise to  $p$  state DOS contributions in the valence band. The addition of a more electronegative atom in the valence band can have an effect on the other nearby orbitals, possibly shifting conduction band states to higher energy or lower the energy of valence band states, and widening  $E_g$ .

With these outcomes, the hypothesis of this project was partially refuted. While the CR and  $\chi$  clearly showed an impact on changes in  $E_g$ , differentiating between which had a greater impact was not possible. It is also important to note that these two chemical properties are related to one another and cannot be decoupled, further complicating the hypothesis. A combination of the two chemical properties was also considered. Motivated by the work of Plumley and Evanseck, various linear combinations of weighted CR and  $\chi$  were investigated in attempt to improve the data's linear fit, but these attempts were unsuccessful.<sup>109</sup> In addition, further studies will be necessary to elucidate the significance of the mid-gap states observed upon sulfur, nitrogen, and tellurium substitution. In addition to the electronic structure calculations carried for unsubstituted and substituted  $\text{TiO}_2$ , the electronic structures of various DLS were also calculated and summarized in Chapter 5. Last, some of the broader impacts of this research project were presented in Chapter 6

## References

1. Enerdata. Total energy consumption. <https://yearbook.enerdata.net/> (accessed 05/31/2017).
2. EPA. Climate change indicators: greenhouse gases. <https://www.epa.gov/climate-indicators/greenhouse-gases> (accessed 05/31/2017).
3. NASA. Global temperature. <https://climate.nasa.gov/vital-signs/global-temperature/> (accessed 05/31/2017).
4. Wang, J.; Song, Y.; Liu, F.; Hou, R. Analysis and application of forecasting models in wind power integration: A review of multi-step-ahead wind speed forecasting models. *Renew. Sust. Energ. Rev.* **2016**, *60*, 960–981.
5. Shortall, R.; Davidsdottir, B.; Axelsson, G. Geothermal energy for sustainable development: A review of sustainability impacts and assessment frameworks. *Renew. Sust. Energ. Rev.* **2015**, *44*, 391–406.
6. Kaunda, C.; Kimambo, C.; Nielsen, T. Hydropower in the context of sustainable energy supply: A review of technologies and challenges. *ISRN Renew. Energ.* **2012**, *2012*, 1–15.
7. Bell, L. Cooling, heating, generating power, and recovering waste heat with thermoelectric systems. *Science* **2008**, *321*, 1457–1461.
8. DiSalvo, F. Thermoelectric cooling and power generation. *Science* **1999**, *285*, 703–706.
9. El Chaar, L.; Lamont, L.; El Zein, N. Review of photovoltaic technologies. *Renew. Sust. Energ. Rev.* **2011**, *15*, 2165–2175.
10. Parida, B.; Iniyani, S.; Goic, R. A review of solar photovoltaic technologies. *Renew. Sust. Energ. Rev.* **2011**, *15*, 1625–1636.
11. Cutnell, J.; Johnson, K. *Physics*, 9th; John Wiley and Sons: Hoboken, NJ, 2012.
12. Shockley, W.; Queisser, H. Detailed balance limit of efficiency of p-n junction solar cells. *J. Appl. Phys.* **1961**, *32*, 510.
13. Housecroft, C.; Sharpe, A. *Inorganic chemistry*, 3rd; Prentice Hall: Essex, England, 2008.
14. Hoffmann, R. How chemistry and physics meet in the solid state. *Angew. Chem. Int. Edit.* **1987**, *26*, 846–878.
15. Srnec, M.; Upadhyay, S.; Madura, J. Teaching reciprocal space to undergraduates via theory and code components of an IPython notebook. *J. Chem. Educ.* **2016**, *93*, 2106–2109.
16. Meyer, M.; Glaus, S.; Calzaferri, G. Introduction to basic terms of band structures. *J. Chem. Educ.* **2003**, *80*, 1221.
17. Gerstein, B. Chemistry, bands, bonds, and solids. A translator’s notes. *J. Chem. Educ.* **1973**, *50*, 316–322.

18. Ladd, M. The language of lattices and cells. *J. Chem. Educ.* **1997**, *74*, 461.
19. Mjöberg, P.; Ljunggren, S.; Ralowski, W. Reciprocal vectors in function space. *J. Chem. Educ.* **1975**, *52*, 212–214.
20. Kettle, S.; Norrby, L. The Brillouin zonean interface between spectroscopy and crystallography. *J. Chem. Educ.* **1990**, *67*, 1022–1028.
21. Blaha, P.; Schwarz, K.; Madsen, G.; Kvasnicka, D.; Luitz, J. WIEN2k: an augmented plane wave plus local orbitals program for calculating crystal properties user's Guide.
22. Kresse, G. VASP. <http://www.vasp.at/>.
23. Dovesi, R.; Orlando, R.; Erba, A.; Zicovich-Wilson, C.; Civalleri, B.; Casassa, S.; Maschio, L.; Ferrabone, M.; De La Pierre, M.; D'Arco, P.; Noël, Y.; Causà, M.; Rérat, M.; Kirtman, B. CRYSTAL14: A program for the ab initio investigation of crystalline solids. *Int. J. Quantum Chem.* **2014**, *114*, 1287–1317.
24. Pisanty, A. The electronic structure of graphite - a chemist's introduction to band theory. *J. Chem. Educ.* **1991**, *68*, 804–808.
25. Python Software Foundation. Python Language Reference, version 2.7. Available at <http://www.python.org>.
26. Lee, J. *Computational materials science, an introduction*; CRC Press Taylor and Francis Group: Florida, 2012.
27. Yang, J.; Banerjee, A.; Guha, S. Amorphous silicon based photovoltaics - from earth to the "final frontier". *Sol. Energ. Mat. Sol. C* **2003**, *78*, 597–612.
28. Becker, C.; Amkreutz, D.; Sontheimer, T.; Preidel, V.; Lockau, D.; Haschke, J.; Jogschies, L.; Klimm, C.; Merkel, J.; Plocica, P.; Steffens, S.; Rech, B. Polycrystalline silicon thin-film solar cells: status and perspectives. *Sol. Energ. Mat. Sol. C* **2013**, *119*, 112–123.
29. Lipiński, M.; Panek, P.; Świątek, Z.; Belltowska, E.; Ciach, R. Double porous silicon layer on multi-crystalline Si for photovoltaic application. *Sol. Energ. Mat. Sol. C* **2002**, *72*, 271–276.
30. Ferekides, C.; Marinskiy, D.; Viswanathan, V.; Tetali, B.; Palekis, V.; Selvaraj, P.; Morel, D. High efficiency CSS CdTe solar cells. *Thin Solid Films* **2000**, *361* - *362*, 520–526.
31. Pfisterer, F. The wet-topotaxial process of junction formation and surface treatments of Cu<sub>2</sub>S-CdS thin-film solar cells. *Thin Solid Films* **2003**, *431* - *432*, 470–476.
32. Tsai, H.; Thomas, S.; Chen, C.; Wang, Y.; Tsai, H.; Yen, Y.; Hsu, C.; Tsai, W.; Wang, Z.; Chueh, Y. Enhanced conversion efficiency of Cu(In,Ga)Se<sub>2</sub> solar cells via electrochemical passivation treatment. *ACS Appl. Mater. Interfaces* **2016**, *8*, 7777–7782.



33. Repins, I.; Contreras, M.; Egaas, B.; DeHart, C.; Scharf, J.; Perkins, C.; To, B.; Noufi, R. 19.9%-efficient ZnO/CdS/CuInGaSe<sub>2</sub> solar cell with 81.2% fill factor. *Prog. Photovoltaics* **2008**, *16*, 235–239.
34. Bernède, J.; Derouiche, H.; Djara, V. Organic photovoltaic devices: influence of the cell configuration on its performances. *Sol. Energ. Mat. Sol. C* **2005**, *87*, 261–270.
35. Itoh, M.; Takahashi, H.; Fujii, T.; Takakura, H.; Hamakawa, Y.; Matsumoto, Y. Evaluation of electric energy performance by democratic module PV system field test. *Sol. Energ. Mat. Sol. C* **2001**, *67*, 435–440.
36. Hara, K.; Sugihara, H.; Tachibana, Y.; Islam, A.; Yanagida, M.; Sayama, K.; Arakawa, H. Dye-sensitized nanocrystalline TiO<sub>2</sub> solar cells based on ruthenium (II) phenanthroline complex photosensitizers. *Langmuir* **2001**, *17*, 5992–5999.
37. Ju, A. Carbon nanotubes could make efficient solar cells. (accessed 01/01/2017).
38. Yablonovitch, E.; Miller, O.; Kurtz, S. In *Photovoltaics Specialists Conference*, IEEE XPlore: Austin, TX, 2012.
39. Clarke, C. San Jose solar company breaks efficiency record for PV. <https://www.kcet.org/redefine/san-jose-solar-company-breaks-efficiency-record-for-pv> (accessed 05/31/2017).
40. Reyes-Coronado, D.; Rodríguez-Gattorno, G.; Espinosa-Pesqueira, M.; Cab, C.; de Coss, R.; Oskam, G. Phase-pure TiO<sub>2</sub> nanoparticles: anatase, brookite and rutile. *Nanotechnology* **2008**, *19*, 145605 (1–10).
41. Pascual, J.; Camassel, J.; Mathieu, H. Fine structure in the intrinsic absorption edge of TiO<sub>2</sub>. *Phys. Rev. B* **1978**, *18*.
42. Amtout, A.; Leonelli, R. Optical properties of rutile near its fundamental band gap. *Phys. Rev. B* **1995**, *51*, 6842.
43. Tang, H.; Lévy, F.; Berger, H.; Schmid, P. Urbach tail of anatase TiO<sub>2</sub>. *Phys. Rev. B* **1995**, *52*, 7771.
44. Mattsson, A.; Österlund, L. Adsorption and photoinduced decomposition of acetone and acetic acid on anatase, brookite, and rutile TiO<sub>2</sub> nanoparticles. *J. Phys. Chem. C* **2010**, *114*, 14121–14132.
45. Landmann, M.; Rauls, E.; Schmidt, W. The electronic structure and optical response of rutile, anatase and brookite TiO<sub>2</sub>. *J. Phys.: Condens. Matter* **2012**, *24*, 195503 (1–6).
46. Gong, S.; Bang-Gui, L. Electronic structures and optical properties of TiO<sub>2</sub>: improved density-functional-theory investigation. *Chin. Phys. B* **2012**, *21*, 057104 (1–7).

47. Tosoni, S.; Lamiel-garcia, O.; Hevia, D.; Doña, J.; Illas, F. Electronic structure of F-doped bulk rutile, anatase, and brookite polymorphs of TiO<sub>2</sub>. *J. Phys. Chem. C* **2012**, *116*, 12738–12746.
48. Navas, J.; Sánchez-Coronilla, A.; Aguilar, T.; Hernández, N.; de los Santos, D.; Sánchez-Márquez, J.; Zorrilla, D.; Fernández-Lorenzo, C.; Alcántara, R.; Martín-Calleja, J. Experimental and theoretical study of the electronic properties of Cu-doped anatase TiO<sub>2</sub>. *Phys. Chem. Chem. Phys.* **2014**, *16*, 3835–3845.
49. Khan, M.; Song, Y.; Chen, N.; Cao, W. Effect of V doping concentration on the electronic structure, optical and photocatalytic properties of nano-sized V-doped anatase TiO<sub>2</sub>. *Mater. Chem. Phys.* **2013**, *142*, 148–153.
50. Serpone, N.; Lawless, D.; Disdier, J.; Herrmann, J. Spectroscopic, photoconductivity, and photocatalytic studies of TiO<sub>2</sub> colloids: naked and with the lattice doped with Cr<sup>3+</sup>, Fe<sup>3+</sup>, and V<sup>5+</sup> cations. *Langmuir* **1994**, *10*, 643–652.
51. Sangaletti, L.; Mozzati, M.; Galinetto, P.; Azzoni, C.; Speghini, A.; Bettinelli, M.; Calestani, G. Ferromagnetism on a paramagnetic host background: the case of rutile TM: TiO<sub>2</sub> single crystals (TM = Cr, Mn, Fe, Co, Ni, Cu). *J. Phys.: Condens. Matter* **2006**, *18*, 7643–7650.
52. Muhich, C.; Westcott, J.; Fuerst, T.; Weimer, A.; Musgrave, C. Increasing the photocatalytic activity of anatase TiO<sub>2</sub> through B, C, and N doping. *J. Phys. Chem. C* **2014**, *118*, 27415–27427.
53. Zheng, J.; Bhattcahrayya, A.; Wu, P.; Chen, Z.; Highfield, J.; Dong, Z.; Xu, R. The origin of visible light absorption in chalcogen element (S, Se, and Te) - doped anatase TiO<sub>2</sub> photocatalysts. *J. Phys. Chem. C* **2010**, *114*, 7063–7069.
54. Wang, H.; Lewis, J. Effects of dopant states on photoactivity in carbon-doped TiO<sub>2</sub>. *J. Phys.: Condens. Mat.* **2005**, *17*, L209–L213.
55. Xi, X.; Dong, P.; Pei, H.; Hou, G.; Zhang, Q.; Guan, R.; Xu, N.; Wang, Y. Density functional study of X monodoped and codoped (X = C, N, S, F) anatase TiO<sub>2</sub>. *Comp. Mater. Sci.* **2014**, *93*, 1–5.
56. Yao, J.; Aitken, J. Experimental band gap data of CuInS<sub>2</sub>, 2011.
57. Chen, W.; Yuan, P.; Zhang, S.; Sun, Q.; Liang, E.; Jia, Y. Electronic properties of anatase TiO<sub>2</sub> doped by lanthanides: a DFT+U study. *Physica B* **2012**, *407*, 1038–1043.
58. Pan, J.; Li, C.; Zhao, Y.; Liu, R.; Gong, Y.; Niu, L.; Liu, X.; Chi, B. Electronic properties of TiO<sub>2</sub> doped with Sc, Y, La, Zr, Hf, V, Nb and Ta. *Chem. Phys. Lett.* **2015**, *628*, 43–48.
59. Levi, A. *Applied quantum mechanics*; University Press: Cambridge, NY, 2003.
60. Burden, R.; Faires, J. *Numerical analysis*; Brooks and Cole, Cengage Learning: Boston, MA, 2011.

61. Hartree, D. The wave mechanics of an atom with a non-Coulomb central field. Part I. Theory and methods. *Proc. Cambridge Phil. Soc.* **1928**, *24*, 89–110.
62. Fock, V. Approach to the solution of the quantum mechanical multi-body problem. *Z. Phys.* **1930**, *61*, 126–148.
63. Levine, I. *Quantum Chemistry*; Prentice Hall: Englewood Cliffs, New Jersey, 1991.
64. Parr, R. On the genesis of a theory. *Int. J. Quantum Chem.* **1990**, *37*, 327–347.
65. Møller, C.; Plesset, M. Note on an approximation treatment for many-electron systems. *Phys. Rev.* **1934**, *46*, 618.
66. Sherrill, C.; Schaefer III., H. The configuration interaction method: advances in highly correlated approaches. *Adv. Quantum Chem.* **1999**, *34*, 143–269.
67. Čížek, J. On the correlation problem in atomic and molecular systems. Calculation of wavefunction components in Ursell-type expansion using quantum-field theoretical methods. *J. Chem. Phys.* **1966**, *45*, 4256.
68. Čížek, J. On the use of the cluster expansion and the technique of diagrams in calculations of correlation effects in atoms and molecules. *Adv. Chem. Phys.* **1966**, *14*, 35.
69. Ceperly, D.; Chester, G.; Kalos, M. Monte Carlo simulation of a many-fermion study. *Phys. Rev. B* **1977**, *16*, 3081.
70. Caffarel, M.; Claverie, P. Development of a pure diffusion quantum Monte Carlo method using a full generalized Feynman-Kac formula. I. Formalism. *J. Chem. Phys.* **1988**, *88*, 1088.
71. Hückel, E. Quantum-theoretical contributions to the benzene problem. I. The electron configuration of benzene and related compounds. *Z. Phys.* **1931**, *70*, 204–286.
72. Hückel, E. Quantitative theorems to the benzene problem. Quantitative theory of the induced polarities. *Z. Phys.* **1931**, *72*, 310–337.
73. Hückel, E. Quantum theoretical contributions to the problem of aromatic and non-saturated compounds. *Z. Phys.* **1932**, *76*, 628.
74. Hückel, E. The free radicals of organic chemistry. *Z. Phys.* **1933**, *83*, 632.
75. Srnec, M.; Upadhyay, S.; Madura, J. A python program for solving Schrödinger's equation in undergraduate physical chemistry. *J. Chem. Educ.* **2017**, *94*, 813–815.
76. Hansen, J. Schroedinger.m: a Mathematica package for solving the time-independent Schrödinger equation. *J. Chem. Educ.* **1996**, *73*, 924.
77. Tellinghuisen, J. Accurate numerical solutions of the one-dimensional Schrödinger equation. *J. Chem. Educ.* **1989**, *66*, 51.

78. Beddard, G. Solution of the Schrödinger equation for one-dimensional anharmonic potentials: an undergraduate computational experiment. *J. Chem. Educ.* **2011**, *88*, 929–931.
79. Ge, Y.; Rittenhouse, R.; Buchanan, J.; Livingston, B. Using a spreadsheet to solve the Schrödinger equations for the energies of the ground electronic state and the two lowest excited states of H<sub>2</sub>. *J. Chem. Educ.* **2014**, *91*, 853–859.
80. Johnson, J. Visualization of wavefunctions of the ionized hydrogen molecule JCE SymMath: symbolic mathematics in chemistry. *J. Chem. Educ.* **2004**, *81*, 1535.
81. Lang, P.; Towns, M. Visualization of wave functions using Mathematica. *J. Chem. Educ.* **1998**, *75*, 506–509.
82. Rioux, F. Quantum mechanics using Mathcad 3.0. *J. Chem. Educ.* **1992**, *69*, 240–241.
83. Poiars, J.; Rodrigues, S.; Marques, J. A quantum mechanics toolkit. *J. Chem. Educ.* **2008**, *85*, 591.
84. Miles Jr., D.; Francis, T. A graphical approach to the angular momentum Schrödinger equation. *J. Chem. Educ.* **2001**, *78*, 405–408.
85. Jones, E.; Oliphant, E.; Peterson, P.; Al., E. SciPy: open source scientific tools for Python. <http://www.scipy.org/> (accessed 05/31/2017).
86. Pérez, F.; Granger, B. IPython: a system for interactive scientific computing. *Comput. Sci. Eng.* **2007**, *9*, 21–29.
87. Hohenberg, P.; Kohn, W. Inhomogeneous electron gas. *Phys. Rev. B* **1964**, *136*, 864.
88. Kohn, W.; Sham, L. Self-consistent equations including exchange and correlation effects. *Phys. Rev. A* **1965**, *140*, 1133.
89. Perdew, J. Density functional theory and the band gap problem. *Int. J. Quantum Chem.* **1986**, *19*, 497–523.
90. Perdew, J.; Burke, K.; Ernzerhof, M. Generalized gradient approximation made simple. *Phys. Rev. Lett.* **1996**, *77*, 3865–3868.
91. Perdew, J.; Burke, K.; Wang, Y. Generalized gradient approximation for the exchange-correlation hole of a many-electron system. *Phys. Rev. B* **1996**, *54*, 533–539.
92. Tran, F.; Blaha, P. Implementation of screened hybrid functionals based on the Yukawa potential within the LAPW basis set. *Phys. Rev. B* **1993**, *83*, 235118 (1–16).
93. Koller, D.; Tran, F.; Blaha, P. Merits and limits of the modified Becke-Johnson exchange potential. *Phys. Rev. B* **2011**, *83*, 195134 (1–10).

94. Tran, F.; Blaha, P. Accurate band gaps of semiconductors and insulators with a semilocal exchange-correlation potential. *Phys. Rev. Lett.* **2009**, *102*, 5–8.
95. Cocula, V.; E.A., C. Introduction to solid state physics, band structure theory and periodic density functional theory.
96. Schwarz, K.; Blaha, P. Solid state calculations using WIEN2k. *Comp. Mater. Sci.* **2003**, *28*, 259–273.
97. Towns, J.; Cockerill, T.; Dahan, M.; Foster, I.; Gaither, K.; Grimshaw, A.; Hazlewood, V.; Lathrop, S.; Lifka, D.; Peterson, G.; Roskies, R.; Scott, J.; Wilkins-Diehr, N. XSEDE: Accelerating scientific discovery. *Comput. Sci. Eng.* **2014**, *16*, 62–74.
98. Kokalj, A. XCrySDen-a new program for displaying crystalline structures and electron densities. *J. Mol. Graphics Mod.* **1999**, *17*, 176–179.
99. CrystalMaker<sup>®</sup>: a crystal and molecular structures program for Mac and Windows. CrystalMaker Software Ltd, Oxford, England ([www.crystallmaker.com](http://www.crystallmaker.com)).
100. Wyckoff, R. *Crystal structures, vol. 1*; John Wiley and Sons: New York, NY, 1963.
101. Horn, M.; Schwerdtfeger, C.; Meagher, E. Refinement of the structure of anatase at several temperatures. *Z. Kristallogr.* **1972**, *136*, 273.
102. Pauling, L. The principles determining the structure of complex ionic crystals. *J. Am. Chem. Soc.* **1928**, *51*, 1010–1026.
103. Pauling, L. The nature of the chemical bond. IV. The energy of single bonds and the relative electronegativity of atoms. *J. Am. Chem. Soc.* **1932**, *54*, 3570–3582.
104. Shannon, R. Revised effective ionic radii and systematic studies of interatomic distances in halides and chalcogenides. *Acta Cryst.* **1976**, *A32*, 751–767.
105. *CRC handbook of chemistry and physics*, 97th ed.; CRC Press: Boca Raton, FL, 2017.
106. Fang, C.; de Groot, R.; Haas, C. Bulk and surface electronic structure of 1T - TiS<sub>2</sub> and 1T - TiSe<sub>2</sub>. *Phys. Rev. B* **1997**, *56*, 4455.
107. Crowley, J.; Tahir-Kheli, J.; Goddard, W. Resolution of the band gap prediction problem for materials design. *J. Phys. Chem. Lett.* **2016**, *7*, 1198–1203.
108. CamargoMartínez, J.; Baquero, R. Performance of the modified Becke-Johnson potential for semiconductors. *Phys. Rev. B.* **2012**, *86*, 195106 (1–8).
109. Plumley, J.; Evanseck, J. Periodic trends and index of boron lewis acidity. *J. Phys. Chem. A* **2009**, *113*, 5985–5992.
110. Rosmus, K.; Brunetta, C.; Srnec, M.; Karuppanan, B.; Aitken, J. Synchrotron X-ray powder diffraction and electronic band structure of  $\alpha$ - and  $\beta$ - Cu<sub>2</sub>ZnSiS<sub>4</sub>. *Z. Anorg. Allg. Chem.* **2012**, *638*, 2578–2584.

111. Nitsche, R.; Sargent, D.; Wild, P. Crystal growth of quaternary  $1_2246_4$  chalcogenides by iodine vapor transport. *J. Cryst. Growth* **1967**, *1*, 52–53.
112. Chen, S.; Walsh, A.; Luo, Y.; Yang, J.; Gong, X.; Wei, S. Wurtzite-derived polytypes of kesterite and stannite quaternary chalcogenide semiconductors. *Phys. Rev. B* **2010**, *82*, 195203.
113. Brunetta, C.; Karuppanan, B.; Rosmus, K.; Aitken, J. The crystal and electronic band structure of the diamond-like semiconductor  $\text{Ag}_2\text{ZnSiS}_4$ . *J. Alloy Compd.* **2012**, *516*, 65–72.
114. Jaffe, J.; Zunger, A. Electronic structure of the ternary chalcopyrite semiconductors  $\text{CuAl}_2$ ,  $\text{CuGaS}_2$ ,  $\text{CuInS}_2$ ,  $\text{CuAlSe}_2$ ,  $\text{CuGaSe}_2$ , and  $\text{CuInSe}_2$ . *Phys. Rev. B* **1983**, *28*, 5822.
115. Schleich, D.; Derrington, C.; Godek, W.; Weisberg, D.; Wold, A. Semiconducting properties of barium titanate and iron substituted barium titanate. *Mater. Res. Bull.* **1977**, *12*, 111.
116. Yao, G.-Q.; Shen, H.-S.; Honig, E.; Kershaw, R.; Dwight, K.; Wold, A. Preparation and characterization of the quaternary chalcogenides  $\text{Cu}_2\text{B(II)C(IV)X}_4$  [B(II)=Zn, Cd; C(IV)=Si, Ge; X=S, Se]. *Solid State Ionics* **1987**, *24*, 249–252.
117. Levenco, S.; Dumcenco, D.; Huang, Y. S.; Arushanov, E.; Tezlevan, V.; Tiong, K. K.; Du, C. H. Near band edge anisotropic optical transitions in wide band gap semiconductor  $\text{Cu}_2\text{ZnSiS}_4$ . *J. Appl. Phys.* **2010**, *108*, 073508.
118. Levenco, S.; Dumcenco, D.; Huang, Y. S.; Arushanov, E.; Tezlevan, V.; Tiong, K.; Du, C. Temperature-dependent study of the band-edge excitonic transitions of  $\text{Cu}_2\text{ZnSiS}_4$  single crystals by polarization-dependent piezoreflectance. *J. Alloy Compd.* **2010**, *506*, 46–50.
119. Levenco, S.; Dumcenco, D.; Huang, Y. S.; Arushanov, E.; Tezlevan, V.; Tiong, K.; Du, C. Absorption-edge anisotropy of  $\text{Cu}_2\text{ZnSiQ}_4$  (Q = S, Se) quaternary compound semiconductors. *J. Alloy Compd.* **2011**, *509*, 4924–4928.
120. Levenco, S.; Dumcenco, D.; Huang, Y.; Arushanov, E.; Tezlevan, V.; Tiong, K.; Du, C. Polarization-dependent electrolyte electroreflectance study of  $\text{Cu}_2\text{ZnSiS}_4$  and  $\text{Cu}_2\text{ZnSiSe}_4$  single crystals. *J. Alloy Compd.* **2011**, *509*, 7105–7108.
121. Persson, C. Electronic and optical properties of  $\text{Cu}_2\text{ZnSnS}_4$  and  $\text{Cu}_2\text{ZnSnSe}_4$ . *J. Appl. Phys.* **2010**, *107*, 053710.
122. Rosmus, K.; Brant, J.; Wisneski, S.; Clark, D.; Kim, Y.; Jang, J.; Brunetta, C.; Zhang, J.; Srnc, M.; Aitken, J. Optical nonlinearity in  $\text{Cu}_2\text{CdSnS}_4$  and  $\alpha/\beta$ - $\text{Cu}_2\text{ZnSiS}_4$ : diamond-like semiconductors with high laser-damage thresholds. *Inorg. Chem.* **2014**, *53*, 7809–7811.

123. Xiao, Z.-Y.; Li, Y.-F.; Yao, B.; Deng, R.; Ding, Z.-H.; Wu, T.; Yang, G.; Li, C.-R.; Dong, Z.-H.; Liu, L.; Zhang, L.-G.; Zhao, H.-F. Bandgap engineering of  $\text{Cu}_2\text{Cd}_x\text{Zn}_{1-x}\text{SnS}_4$  alloy for photovoltaic applications: a complimentary experimental and first-principles study. *J. Appl. Phys.* **2013**, *114*.
124. Devlin, K.; Glaid, A.; Brant, J.; Zhang, J.; Srnec, M.; Clark, D.; Soo Kim, Y.; Jang, J.; Daley, K.; Moreau, M.; Madura, J.; Aitken, J. Polymorphism and second harmonic generation in a novel diamond-like semiconductor:  $\text{Li}_2\text{MnSnS}_4$ . *J. Solid State Chem.* **2015**, *231*, 256–266.
125. Lekse, J.; Moreau, M.; McNerny, K.; Yeon, J.; Halasyamani, P.; Aitken, J. Second-harmonic generation and crystal structure of the diamond-like semiconductors  $\text{Li}_2\text{CdGeS}_4$  and  $\text{Li}_2\text{CdSnS}_4$ . *Inorg. Chem.* **2009**, *48*, 7516–7518.
126. Ramsdell, L. Studies on silicon carbide. *Am. Mineral.* **1947**, *32*, 64.
127. Godby, R.; Shlüter, M.; Sham, L. Trends in self-energy operators and their corresponding exchange-correlation potentials. *Phys. Rev. B* **1987**, *36*, 6497.
128. Brant, J. A.; Clark, D.; Kim, Y.; Jang, J.; Zhang, J.; Aitken, J.  $\text{Li}_2\text{CdGeS}_4$ , a diamond-like semiconductor with strong second-order optical nonlinearity in the infrared and exceptional laser damage threshold. *Chem. Mater.* **2014**, *26*, 3045–3048.
129. Lekse, J.; Leverett, B.; Lake, C.; Aitken, J. Synthesis, physicochemical characterization and crystallographic twinning of  $\text{Li}_2\text{ZnSnS}_4$ . *J. Solid State Chem.* **2008**, *181*, 3217–3222.
130. Rashkeev, S.; Lambrecht, R. Second harmonic generation of I-III-VI<sub>2</sub> chalcopyrite semiconductors: effects of chemical substitutions. *Phys. Rev. B* **2001**, *63*, 165212.
131. Ozaki, S.; Sasaki, M.; Adachi, S. Positive temperature variation of the bandgap energy in  $\text{AgGaSe}_2$ . *Phys. Stat. Sol. (A)* **2006**, *203*, 2648–2652.
132. Maeda, T.; Takeichi, T.; Wada, T. Systematic studies on electronic structures of  $\text{CuInSe}_2$  and the other chalcopyrite related compounds by first principles calculations. *Phys. Stat. Sol. (A)* **2006**, *203*, 2634–2638.
133. Shay, J.; Wernick, J. *Ternary chalcopyrite semiconductors: growth, electronic properties and applications*; Pergamon Press: Oxford, 1974.
134. Jaffe, J.; Zunger, A. Theory of the band-gap anomaly in  $\text{ABC}_2$  chalcopyrite semiconductors. *Phys. Rev. B* **1984**, *29*, 1882.
135. Dronskowski, R. *Computational chemistry of solid state materials*; Wiley-VCH: Weinheim, 2005.
136. Benoit, P.; Charpin, P.; Djega-Mariadassou, C. Crystal structure of chalcopyrite  $\text{AgInSe}_2$ . *Jap. J. App. Phys.* **1980**, *9*.

137. Yao, J.; Kline, C.; Gu, H.; Yan, M.; Aitken, J. Effects of Mn substitution on the structure and properties of chalcopyrite-type CuInSe<sub>2</sub>. *J. Solid State Chem.* **2009**, *182*, 2579–2586.
138. Rincón, C. A model for the band gap shrinkage in the chalcopyrite semiconductor CuInSe<sub>2</sub>. *Solid State Commun.* **1987**, *64*, 15–17.
139. Ramaiah, K.; Raja, V.; Bhatnagar, A.; Juang, F.; Chang, S.; Su, Y. Effect of annealing and  $\gamma$ -irradiation on the properties of CuInSe<sub>2</sub> thin films. *Mater. Lett.* **2000**, *45*, 251–261.
140. Yao, J.; Brunetta, C.; Aitken, J. Suppression of antiferromagnetic interactions through Cu vacancies in Mn-substituted CuInSe<sub>2</sub> chalcopyrites. *J. Phys.: Condens. Mat.* **2012**, *24*, 086006.
141. Buffat, P.; Borel, J. Size effect on the melting temperature of gold particles. *Phys. Rev. A.* **1976**, *13*, 2287–2298.
142. Pawlow, P. The dependency of the melting point on the surface energy of a solid body. *Z. Phys.* **1909**, *65*, 545–548.
143. Wronski, C. The size dependence of the melting point of small particles of tin. *Brit. J. Appl. Phys.* **1967**, *18*, 1731–1737.
144. Reiss, H.; Wilson, I. The effect of surface on melting point. *J. Colloid Sci.* **1948**, *3*, 551.
145. Goldstein, A.; Echer, C.; Alivisatos, A. Melting in semiconductor nanocrystals. *Science* **1992**, *256*, 1425–1427.
146. Hanszen, K. Theoretical investigations on the melting point of small crystals. *Z. Phys.* **1960**, *157*, 523–553.
147. Perry, D. *Handbook of inorganic compounds*, 2nd ed.; CRC Press: Boca Raton, FL, 2011, p 83.
148. Libman, E. The surface tension of molten metals with the determination of the capillary constant of copper., Urbana, 1928.
149. Hamuyuni, J. Measurement of surface tension in base metal sulfide mattes by an improved sessile drop method., Ph.D. Thesis, Stellenbosch University, 2012, pp 1–76.
150. Esparza, D.; Zarazúa, I.; López-Luke, T.; Cerdán-Pasarán, A.; Sánchez-Solís, A.; Torres-Castro, A.; Mora-Sero, I.; De La Rosa, E. Effect of different sensitization technique on the photoconversion efficiency of CdS quantum dot and CdSe quantum rod sensitized TiO<sub>2</sub> solar cells. *J. Phys. Chem. C* **2015**, *119*, 13394–13403.



## Appendix 1

### Python Installation Instructions for Windows Users

We promote the use of Python through the Anaconda open data science platform. We are aware that other installation methods exist, but have solely included the Anaconda installation instructions below due to the ease of setup and use in a classroom environment:

1. In order to download Anaconda for Windows, navigate to the following webpage:  
`https://www.continuum.io/downloads`
2. In the section labeled “Anaconda for Windows”, there are installers for Python 2.7 and Python 3.5. The reciprocal program is written for Python 2.7. *While you may want to install both versions of Python for personal use, the following instructions are provided for version 2.7 only.*
3. In the box labeled “Python 2.7”, click on the blue box labeled “WINDOWS 64-BIT GRAPHICAL INSTALLER.” If you are using Windows 32-bit, the graphical installer is provided in smaller print below the 64-bit installer.
4. Upon clicking the installer, you will notice a dialog box appear at the bottom of your web browser, indicating the download progress. Once finished, click the executable to begin the installation. If a dialog box does not appear, navigate to the downloads folder from the desktop or windows key, and double click the executable to begin installation.
5. Upon double clicking the executable, the Anaconda 64-bit Setup Wizard will open. Click “Next” to continue.
6. Click “I Agree” to accept the license agreement.

7. Select “Just Me” as the installation type. This will complete the installation without requiring administrative privileges.
8. Next, you will be prompted to select an installation location. Here, it is most likely that the default location is suitable. For example, the destination folder selected here was **C:\Users\Username\Anaconda2**.
9. You will then be prompted for two installation options (add Anaconda to my PATH environment variable and Register Anaconda as my default Python 2.7). We advise that both these boxes are checked before proceeding.
10. Click “Install”. The installation process will take some time, please be patient.
11. Upon installation, several executables are generated. In order to find these executables, open Windows’ File Explorer and navigate to the installation location directory you specified in step 8 above. Upon locating this “Anaconda2” folder, you will find a subfolder called “Menu”. This folder contains all the executables that you will utilize for running Python programs or IPython notebooks. We advise copying the important executables as shortcuts to your desktop so that they are easier to access. The executables you will use most frequently are: IPython, Jupyter Notebook, Anaconda Prompt, and Spyder.
12. Once you have created shortcuts for the above executables, open the Anaconda Prompt. Upon opening, the prompt will appear similar to Windows Command Prompt. You will notice the path of your installation location from step 8 to the left of the Anaconda Prompt, followed by a cursor.
13. In the Anaconda prompt, type **conda update conda**.
14. A list of packages to be downloaded will appear and you will be asked to proceed [yes/no]. Select “yes” to begin the download.

15. Following the download, you will also need to manually install the numpy, scipy, matplotlib, and colorama packages. In order to install each of these, use the following example for formatting purposes: **conda install numpy**. After typing each install command once, type the same command a second time to assure that the package is correctly installed. If installed, you will receive the following message upon typing the install command a second time: “All requested packages already installed.”
16. Within the Python\_Files folder (where you found this installation instructions document), you will also find the Reciprocal.py Python program (for running in an Anaconda Prompt or via Windows Command Prompt), the Reciprocal.ipynb IPython notebook (for instructor use in classrooms), and a file named **jupyter\_notebook\_config.py**
17. Using Windows File Explorer, navigate to the directory that contains the Anaconda2 folder from step 8 above. In the same directory as the Anaconda2 folder, you will find another folder named **.jupyter**. In this folder, you must place the **jupyter\_notebook\_config.py** file mentioned in step 16.
18. We also advise that you create a folder on your desktop called **Reciprocal** to place the Reciprocal.py (Python program) and the Reciprocal.ipynb (IPython notebook) documents.
19. Next, open an Anaconda Prompt and navigate to the Reciprocal desktop folder that you just created in step 18. In order to navigate directories using the Anaconda Prompt, the following Windows Command Prompt keystrokes should be utilized:
  - **dir** = list files in your current directory
  - **cd** = change directory (in order to use the **cd** command, you must first type

**cd** followed by a **space**, followed by the **name** of the folder or directory you wish to navigate to)

- **cd ..** = move back one folder level

As an example, when you open your Anaconda Prompt, the default folder should be identical to what you declared in step 8 above (**C:\Users\Username\Anaconda2**). If this is the case, you will simply type **cd Desktop\Reciprocal** to navigate to the Reciprocal folder on the desktop that you created in step 18.

20. Once you've navigated to the Reciprocal folder via the Anaconda Prompt, type **jupyter notebook** in the Anaconda Prompt. This will open Jupyter in your default web browser. When the default web browser opens, you should see the Reciprocal.py (Python program) and the Reciprocal.ipynb (IPython notebook) documents. Double click the Reciprocal.ipynb file to open the IPython notebook.
21. With the notebook open, users are encouraged to examine the options at the top of the web browser. Most importantly, the user should focus on the “play” button in the top panel, which can be used to run each cell in the IPython notebook. The Reciprocal IPython notebook is broken down into sections of **markdown** (text that explains the Reciprocal program or theory/math behind the program) and **code** (Python commands that carry out the mathematics discussed in the manuscript). When using the notebook, users should progress through the cells of the notebook one-by-one and press the play button for each cell. This will update the screen of any changes and also prompt the user for any input that the program requires. In the edit tab of the top panel, users also have the option to **run all cells**. If the user updates markdown text or Python code, they must remember to press the play button to update the screen of those changes. In some instances, the user might need to begin at the beginning of

the notebook and re-play all the cells again, or simply use the **run all cells** function.

22. When finished, the IPython notebook should be closed. However, the main Jupyter web browser will remain open and the IPython notebook will show **Running** in green. Click on the green **Running** button and an option will appear to **Shutdown** the notebook. Click **Shutdown** before closing the main Jupyter notebook web browser. Last, press CTRL+C in the Anaconda Prompt to terminate the Jupyter notebook process.
23. If users wish to simply run the Reciprocal.py program in the Anaconda Prompt (without the use of the IPython notebook), repeat step 19 above. Once you've navigated to the desktop folder containing the Reciprocal.py program, type **python Reciprocal.py**. Here, the program will run in the Anaconda window with various user input prompts.

### Python Installation Instructions for OSX Users

1. In order to download Anaconda for OSX, navigate to the following webpage:  
`https://www.continuum.io/downloads`
2. In the section labeled “Anaconda for OSX”, there are installers for Python 2.7 and Python 3.5. The reciprocal program is written for Python 2.7. *While you may want to install both versions of Python for personal use, the following instructions are provided for version 2.7 only.*
3. In the box labeled “Python 2.7”, click on the blue box labeled “MAC OSX 64-BIT GRAPHICAL INSTALLER.” *If you select the graphical installer, double-click on the downloaded .pkg file and follow the instructions in the installer window. These instructions will be very similar to those in steps 5-11 in the aforementioned Windows Installation Instructions.*

4. Below the blue graphical installer box, you will also notice a “MAC OSX 64-BIT COMMAND-LINE INSTALLER.” If you are more comfortable using MAC Terminal, select this download.
5. If using the COMMAND LINE INSTALLER, once the download completes, navigate to the downloads folder, type **bash Anaconda2-4.1.1-MacOSX-x86\_64.sh**, and follow the instructions printed to the MAC Terminal. *If you need a refresher on using MAC Terminal commands, please reference the following document: <https://ubuntudanmark.dk/filer/fwunixref.pdf>. Some basic examples are as follows:*
  - **ls** = list files in current directory
  - **cd** = change directory (in order to use the **cd** command, you must first type **cd** followed by a **space**, followed by the name of the folder or directory you wish to navigate to)
  - **cd ..** = move back one folder level
6. Regardless of your installation method (graphical or command line installer), you must now open a MAC Terminal and follow the instructions below:
7. In the MAC Terminal, type **conda update conda**
8. A list of packages to be downloaded will appear and you will be asked to proceed [yes/no]. Select “yes” to begin the download.
9. Following the download, you will also need to manually install the numpy, scipy, matplotlib, and colorama packages. In order to install each of these, use the following example for formatting: **conda install numpy**. After typing each install command once, type the same command a second time to assure that the package is correctly installed. If installed, you will receive the following mes-

sage upon typing the install command a second time: “All requested packages already installed.”

10. Within the Python\_Files folder (where you found this installation instructions document), you will also find the Reciprocal.py Python program (for running in an Anaconda Prompt or via MAC Terminal), the Reciprocal.ipynb IPython notebook (for instructor use in classrooms), and a file named **jupyter\_notebook\_config.py**
11. Using the MAC Terminal, navigate to the directory that contains the Anaconda2 folder from the installation in step 4/5. In the same directory as the Anaconda2 folder, you will find another folder named **.jupyter**. In this directory, you must place the **jupyter\_notebook\_config.py** file mentioned in step 10.
12. We also advise that you create a folder on your desktop called **Reciprocal** to place the Reciprocal.py (Python program) and the Reciprocal.ipynb (IPython notebook) documents.
13. Using MAC Terminal, navigate to the Reciprocal directory you just created in step 12. Once there, type **jupyter notebook** in the Terminal. This will open Jupyter in your default web browser. When the default web browser opens, you should see the Reciprocal.py (Python program) and the Reciprocal.ipynb (IPython notebook) documents. Double click the Reciprocal.ipynb file to open the IPython notebook.
14. With the notebook open, users are encouraged to examine the options at the top of the web browser. Most importantly, the user should focus on the “play” button in the top panel, which can be used to run each cell in the IPython notebook. The Reciprocal IPython notebook is broken down into sections of

**markdown** (text that explains the Reciprocal program or theory/math behind the program) and **code** (Python commands that carry out the mathematics discussed in the manuscript). When using the notebook, users should progress through the cells of the notebook one-by-one and press the play button for each cell. This will update the screen of any changes and also prompt the user for any input that the program requires. In the edit tab of the top panel, users also have the option to **run all cells**. If the user updates markdown text or Python code, they must remember to press the play button to update the screen of those changes. In some instances, the user might need to begin at the beginning of the notebook and re-play all the cells again, or simply use the **run all cells** function.

15. When finished, the IPython notebook should be closed. However, the main Jupyter web browser will remain open and the IPython notebook will show **Running** in green. Click on the green **Running** button and an option will appear to **Shutdown** the notebook. Click **Shutdown** before closing the main Jupyter notebook web browser. Last, press CTRL+C in the Terminal to terminate the Jupyter notebook process.
16. If users wish to simply run the Reciprocal.py program in the MAC Terminal (without the use of the IPython notebook), navigate to the Reciprocal folder on the desktop again. Once you've navigated to the desktop folder containing the Reciprocal.py program, type **python Reciprocal.py**. Here, the program will run in the terminal window with various user input prompts.



## Appendix 2

### Pedagogical Framework for Incorporating Reciprocal.py Program in the Classroom

This tool is best suited for materials science and physical chemistry classrooms. Instructors should evaluate their curriculum and identify the proper place for introducing the topic of reciprocal space. Unfortunately, most physical chemistry texts save solid-state materials for special topics or chapters later in the book, which sometimes are not covered for the sake of time. We anticipate this topic and tool will find its home at the conclusion of the quantum mechanics semester of physical chemistry. Solid materials are typically discussed following spectroscopy and it is strongly encouraged to discuss reciprocal space and the Python tools provided on the web (<http://pubs.acs.org/doi/suppl/10.1021/acs.jchemed.6b00392>) as a bridge to connect crystal lattices and unit cells to the electronic properties of solids.

In preparation for presenting/discussing this topic in class, instructors should encourage their students to read the following manuscripts prior to the class it will be covered.

Srnec, M. et al. Teaching reciprocal space to undergraduates via theory and code components of an IPython notebook. *J. Chem. Educ.* **2016**, *93*, 2106–2109.

Pisanty, A. The electronic structure of graphite - a chemist's introduction to band theory. *J. Chem. Educ.* **1991**, *68*, 804–808.

This allows students time to refresh their linear algebra and practice the matrix math operations prior to class, ultimately enhancing the classroom discussion and allowing students to follow along more closely in class. It is strongly advised that students follow the installation instructions document provided in Appendix 1 and attempt to install/use the Python software on their personal computer (if available) prior to class. However, if students only read the manuscript and familiarize themselves with the terminology, concepts, and mathematics in advance, it will still aid significantly in the lecture's success.

Before class, it is imperative that the instructor has the IPython notebook working properly via Jupyter<sup>86</sup> on the campus computer in their classroom or on their own personal laptop for connection to the classroom's AV equipment. This tool is best utilized when students also have computer access. Here, the instructor must evaluate which is most appropriate in their classroom. We anticipate that most students will have laptops available, but if this is not the case, the instructor may need to reserve a computer lab and install the Python software on these machines for the students, so that they can also interact with the IPython notebook. If this cannot be accomplished, the instructor should simply have their computer prepared to run the notebook, and allow students to come up in groups and examine the notebook's functions. The instructor can also reserve time outside of class for students to work with the IPython notebook in groups and answer the associated questions.

To begin class, instructors should first discuss the importance of solids and their properties while also covering basic terminology of crystals. This serves as a nice means of introducing reciprocal space. We anticipate that this will be best achieved as an open discussion with the class. Following this brief 5-10 min discussion on the topic's significance, the instructor should transition to the IPython notebook via Jupyter. The power of this tool is that it allows the instructor to simultaneously present conceptual/theoretical content (text and equations) and their computer code (the `Reciprocal.py` Python program) in the same environment (Figure A2.1). Prior to the use of IPython, instructors were limited to screen-jumping between their lecture notes and a separate program to run computer code. Here, within the IPython notebook, instructors can present their theory in the markdown sections of the notebook followed by code sections of the notebook, which allows the instructor to run pieces of their Python program. This provides a single, clear resource for presenting the content to students, allowing them to focus on the material, rather than being distracted by the instructor transitioning between resources (Figure A2.2).

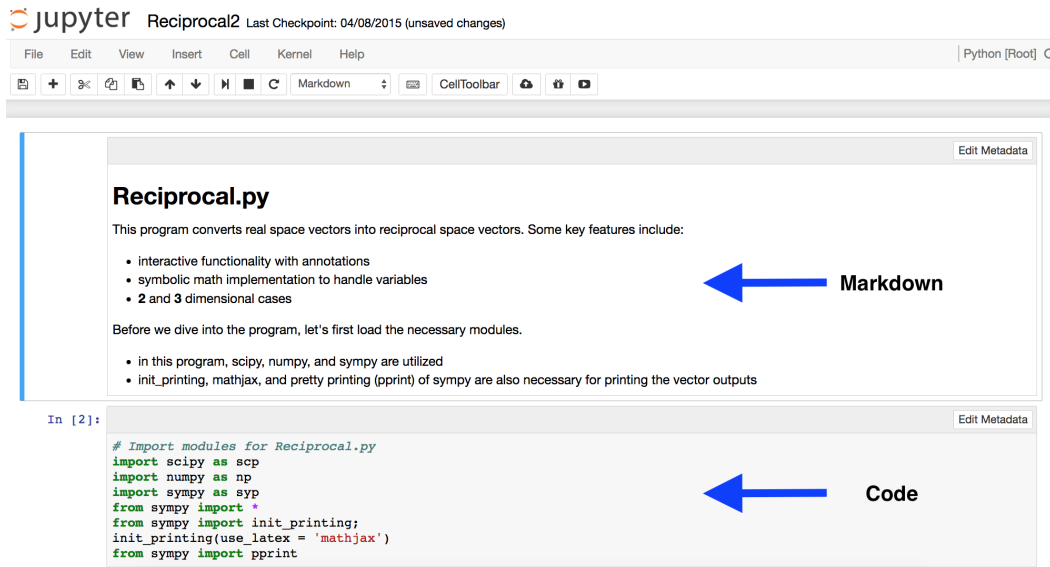


**Figure A2.1:** A screenshot of the IPython notebook via Jupyter, illustrating the simultaneous presentation of concept, theory, and notes in the markdown section and Python programming commands in the code section. *Source:* prepared using Jupyter notebook: Pérez, F.; Granger, B. IPython: a system for interactive scientific computing. *Comput. Sci. Eng.* **2007**, *9*, 21–29.

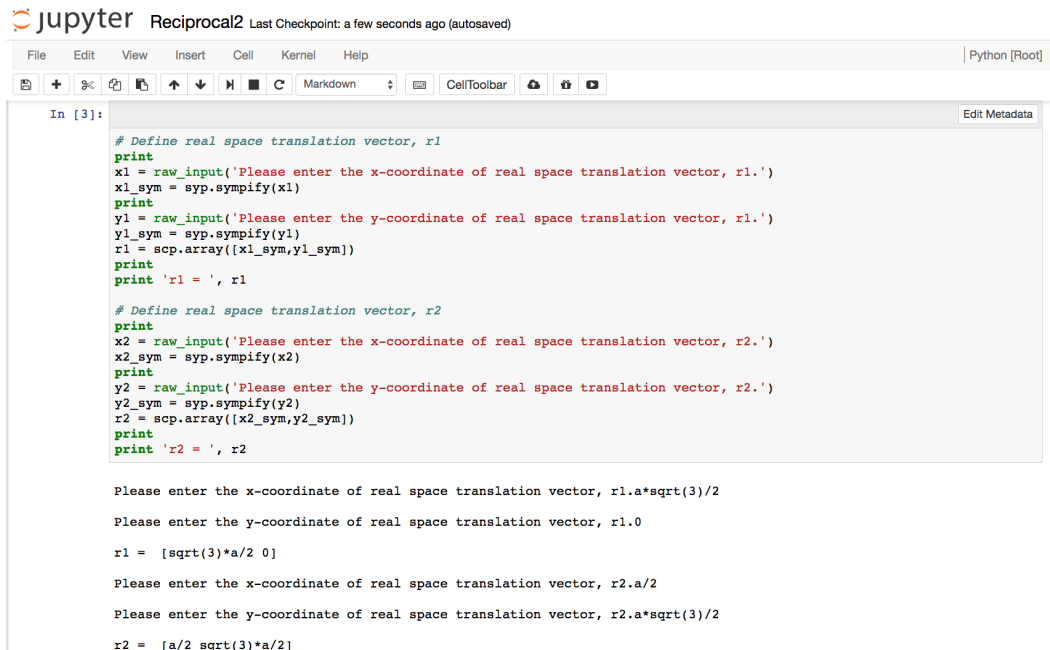


**Figure A2.2:** A screenshot of the IPython notebook via Jupyter, illustrating the Python programming commands (top) followed by the interactive comments (bottom) that are returned to the user as the program runs. *Source:* prepared using Jupyter notebook: Pérez, F.; Granger, B. IPython: a system for interactive scientific computing. *Comput. Sci. Eng.* **2007**, *9*, 21–29.

Utilizing the IPython notebook via Jupyter, instructors are advised to quickly (10-15 min) revisit the mathematical steps for converting real space translation vectors to reciprocal space vectors via the two-dimensional graphite example in Section 1.4. This is provided in the markdown section of the IPython notebook. Once students are comfortable with this mathematical conversion, the instructor can proceed to the code section of the notebook and illustrate that these tedious mathematical processes can be translated into a series of computer-interpreted commands and the Python software can be utilized to quickly calculate the same values. Using the Python code within the IPython notebook, instructors should focus on first using the tool to validate the results that students obtained by carrying out the calculation by hand.

Next, instructors should allow students to interact with the computer in small groups. Here, they will get a feel for the IPython notebook prior to the end of class. This will be valuable experience so that the students can successfully answer the associated questions outside of class. The instructor should remain after class to handle any Python installation questions and also make him/herself available outside of class to help students getting the software setup on their personal machines. If the instructor will have the software pre-installed on campus computers or will be allowing students to use his/her computer, this step is unnecessary. The instructor can choose how they wish to evaluate students on this topic. We suggest an assignment consisting of the questions in Section 1.4. Here, students can work in small groups and should have access to computers for utilizing the IPython notebook.

### Appendix 3

This is an example assignment to supplement the content from Section 2.2 and serves to reinforce several concepts discussed in undergraduate physical chemistry. Such examples include: particle in an infinite well, particle in a finite well, particle in a double finite well of equal depth, particle in a double finite well of unequal depth, particle in a harmonic well, particle in Morse potential energy well, and particle in a Kronig-Penney potential. Moreover, this assignment also provides experience working with the Python programming language and a numerical method for solving Schrödinger's equation. For background information, methods employed, and instructions for getting started, please see the corresponding manuscript and supporting information referenced in Section 2.2. This assignment is suitable as an individual or group project. A single write-up should be submitted that summarizes the Schrödinger program(1-2 paragraphs), answers the questions outlined in each case (include figures where directed), and discusses (1-2 paragraphs) how these examples can be related back to chemical systems that encountered in chemistry.

#### Cases and Questions

Each of the following sections briefly describes a case of the Schrodinger.py program, outlines the variables to modify, presents a sample plot, and lists several questions to be answered. In *ALL* cases, the following questions should also be answered *ALONG WITH* the specific questions for each case:

1. What happens to the energy levels as the width of the potential energy well,  $W$ , increases/decreases?
2. What happens to the spacing between wavefunctions with increasing energy?
3. What is the general rule for the number of nodes of a wavefunction? Does what you observe agree with the general rule?

### *Case 1. Particle in an Infinite Potential Energy Well*

The first case to investigate is the particle in an infinite potential energy well. Here, the width of the potential energy well ( $W$ ) and the number of wavefunctions for plotting can be modified.  $\hbar$  and  $m$  are both set to 1 in all calculations so that energies are calculated in au. Upon calculating the eigenvectors (wavefunctions) and the eigenvalues (energies), the results are plotted. An example plot of the wavefunctions and energies for this case is provided in Figure A3.1. The input parameters are  $W = 5$  au and number of wavefunctions = 7.

Users should compare the energies calculated to the exact energies predicted by

$$E = \frac{n^2 h^2}{8mW^2}$$

where  $n$  is the energy level,  $h$  is Planck's constant,  $m$  is the mass of an electron,  $W$  is the *total width* of the well,  $\hbar$  and  $m$  are 1, and  $h = 2\pi$ . For  $n = 1$ , the predicted energy (in atomic units) is

$$E = \frac{1^2 \cdot (2\pi)^2}{8 \cdot 5^2} = 0.0987 \text{ au}$$

How well do the calculated energy values from the program compare to the energies for a particle-in-a-box discussed above? Compare these energy values for various values of  $n$ .

In addition to the general questions described previously, students should answer the following questions in their write-up for case 1:

1. Briefly summarize Case 1 of the Schrodinger.py program. Comment specifically on the modifiable input variables.
2. When  $W = 3$  au, what is the energy value of the 7th bound wavefunction? Include a plot of your results.

3. Comment on the accuracy of the 3-point finite-difference method in approximating the energy calculated above.
4. Try 2 additional sets of inputs for Case 1 and include the plots in your write-up. Be sure to explain what variable(s) was/were changed and the significance they had on the results.
5. For the 2 additional sets of inputs, also include a plot of the probability density for each. Provide an explanation of how this probability density differs from the plots in question #4 above.

*Case 2. Particle in a Finite Potential Energy Well*

In addition to the width of the potential energy well ( $W$ ), the depth ( $D$ ) of the well can be modified in this case. An example plot of the wavefunctions and energies for this case is provided in Figure A3.2. The input parameters are:  $W = 1$  au and  $D = 100$  au.

In addition to the general questions described previously, students should answer the following questions in their write-up for Case 2:

1. Briefly explain the differences between Cases 1 and 2. In particular, comment on the definition of zero energy in these two cases. Why is there such a significant difference? Is the zero energy at the top or bottom of the infinite well in Case 1? Likewise, is the zero energy at the top or bottom of the finite well in Case 2?
2. How many bound energy levels are capable of existing in the finite potential energy well if  $W = 5$  au and  $D = 400$  au? Include a plot of your results.
3. Are the wavefunctions permitted to exist outside the finite potential energy well barriers? If so, what is this phenomenon called? Provide a brief description of the phenomenon.

4. When  $W = 3$  au and  $D = 52$  au, what is the energy of the 5th bound wavefunction? Include a plot of your results.
5. Try two additional sets of inputs for Case 2 and include the plots in your write-up. Be sure to explain what variable(s) was/were changed and the significance they had on the results.
6. For the 2 additional sets of inputs, also include a plot of the probability density for each. Provide an explanation of how this probability density differs from the plots in question #5 above.

*Case 3. Particle in a Double Finite Potential Energy Well of Equal Width and Depth*

In addition to the width ( $W$ ) and depth ( $D$ ) of the finite potential energy well, users can also vary the distance ( $B$ ) between wells in this case. An example plot of the wavefunctions and energies for this case is provided in Figure A3.3. The input parameters are:  $W = 1$  au,  $D = 50$  au, and  $B = 2$  au.

In addition to the general questions described previously, students should answer the following questions in their write-up for Case 3:

1. Briefly explain the differences between Case 3 and Cases 1 and 2.
2. How many bound energy levels are capable of existing in the finite potential energy well if  $W = 4$  au,  $B = 2$  au, and  $D = 80$  au? Include a plot of your results.
3. Does the phenomenon discussed in Case 2 likewise exist in Case 3?
4. When  $W = 3$  au,  $B = 4$  au, and  $D = 150$  au, what is the energy of the 6th bound wavefunction? Include a plot of your results.
5. What do you observe as  $W$ ,  $B$ , and  $D$  are changed individually?



6. Considering the inputs in question 2 of this case, what unique feature do you notice about the wavefunctions? In quantum mechanics, what term is given to this phenomenon?
7. Choose a width (W) and depth (D) of the finite potential energy wells. Incrementally decrease the distance between the wells from the maximum allowed value to the minimum allowed value. What do you notice about the wavefunction behavior as the wells are brought to the minimum separation distance? Discuss what is occurring in the context of a chemical system.
8. Provide an example of a chemical system that this case represents. Do you think that the square potentials depicted in the plots are an accurate representation of atomic potentials in molecules? How would you expect the potential energy wells of these atoms to be different than the step potentials used in the Schrodinger.py program?

*Case 4. Particle in a Double Finite Potential Energy Well of Unequal Depth and Width*

In this case, students can enter unequal widths (W1 and W2) and depths (D1 and D2) of their wells. An example plot of the wavefunctions and energies for this case is provided in Figure A3.4. The input parameters are: W1 = 0.5 au, W2 = 1.0 au, B = 0.8 au, D1 = 30 au, and D2 = 75 au.

In addition to the general questions described previously, students should answer the following questions in their write-up for Case 4:

1. Briefly explain the differences between Case 4 and Cases 1,2, and 3.
2. How many bound energy levels are capable of existing in the finite potential energy well if W1 = 2 au, W2 = 4 au, B = 2 au, D1 = 50 au, and D2 = 150 au? Include a plot of your results.

3. Does the phenomenon discussed in cases 2 and 3 likewise exist in case 4?
4. When  $W_1 = 0.8$  au,  $W_2 = 1.3$  au,  $B = 4$  au,  $D_1 = 30$  au, and  $D_2 = 65$  au, what is the energy of the 4th bound wavefunction? Include a plot of your results.
5. What do you observe as  $W_1$ ,  $W_2$ ,  $B$ ,  $D_1$ , and  $D_2$  are changed individually?
6. Choose a width ( $W$ ) and depth ( $D$ ) of the finite potential energy wells. Incrementally decrease the distance between the wells from the maximum allowed value to the minimum allowed value. What do you notice about the wavefunction behavior as the wells are brought to the minimum separation distance? Discuss what is occurring in the context of a chemical system.
7. In the context of chemical systems, how does Case 4 differ from Case 3?

*Case 5. Particle in a Harmonic Potential Energy Well*

The force constant and the depth ( $D$ ) of the well can be modified in this case. An example plot of the wavefunctions and energies for this case is provided in Figure A3.5. The input parameters are: force constant = 0.5 and  $D = 4$  au.

In addition to the general questions described previously, students should answer the following questions in their write-up for Case 5:

1. Briefly explain how this case differs from the previous cases.
2. How many bound energy levels are capable of existing in the finite potential energy well if force constant = 0.6 and  $D = 10$  au? Include a plot of your results.
3. Are the wavefunctions permitted to exist outside the harmonic potential energy well? If so, what is this phenomenon called? Provide a brief description of the phenomenon.

4. When  $W = 0.8 \text{ au}$  and  $D = 6 \text{ au}$ , what is the energy of the 5th bound wavefunction? Include a plot of your results.
5. Try two additional sets of inputs for case 5 and include the plots in your write-up. Be sure to explain what variable(s) was/were changed and the significance they had on the results.
6. For the 2 additional sets of inputs, also include a plot of the probability density for each. Provide an explanation of how this probability density differs from the plots in question #5 above.

*Case 6. Particle in a Morse Potential Energy Well*

The force constant and the depth ( $D$ ) of the well can be modified in this case. An example plot of the wavefunctions and energies for this case is provided in Figure A3.6. The input parameters are: force constant = 0.3 and  $D = 2 \text{ au}$ .

In addition to the general questions described previously, students should answer the following questions in their write-up for Case 6:

1. Briefly explain how this case differs from the previous cases.
2. How many bound energy levels are capable of existing in the finite potential energy well if force constant = 0.4 and  $D = 4 \text{ au}$ ? Include a plot of your results.
3. Are the wavefunctions permitted to exist outside the finite potential energy well barriers? If so, what is this phenomenon called? Provide a brief description of the phenomenon.
4. When force constant = 0.7 and  $D = 5 \text{ au}$ , what is the energy of the 5th bound wavefunction? Include a plot of your results.
5. Try two additional sets of inputs for case 6 and include the plots in your write-up. Be sure to explain what variable(s) was/were changed and the significance they had on the results.

6. For the 2 additional sets of inputs, also include a plot of the probability density for each. Provide an explanation of how this probability density differs from the plots in question #5 above.

*Case 7. Kronig-Penney Finite Well*

The width (W) and depth (D) of repeating finite wells, the distance between finite wells (B) and the number of repeating wells (n) can be modified in this case. An example plot of the wavefunctions and energies for this case is provided in Figure A3.7. The input parameters are:  $W = 1.0$  au,  $D = 30$  au,  $B = 1.0$  au, and  $n = 5$ .

In addition to the general questions described previously, students should answer the following questions in their write-up for Case 7:

1. Briefly explain how this case differs from the previous cases. Hint: Consider the boundary conditions.
2. How many bound energy levels are capable of existing in the finite potential energy wells if  $W = 2$  au,  $D = 50$  au, and  $B = 1$  au? Include a plot of your results.
3. Are the wavefunctions permitted to exist outside the finite potential energy well barriers? If so, what is this phenomenon called? Provide a brief description of the phenomenon.
4. When  $W = 1$  au,  $D = 80$  au, and  $B = 1$  au what is the energy of the 5th bound wavefunction? Include a plot of your results.
5. Try two additional sets of inputs for case 7 and include the plots in your write-up. Be sure to explain what variable(s) was/were changed and the significance they had on the results.
6. For the 2 additional sets of inputs, also include a plot of the probability density

for each. Provide an explanation of how this probability density differs from the plots in question #5 above.

7. Finite size effects arise when treating periodic systems because treating a few wells periodically is different than treating an infinite number of wells. How does the energy of the ground state change as more periodic wells are included?

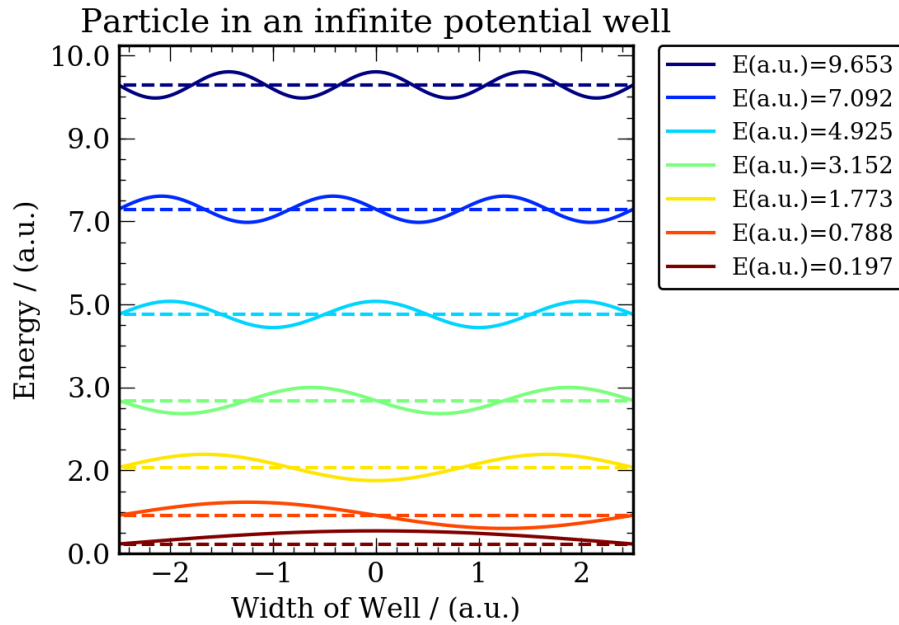


**Figure A3.1:** An example plot of the seven lowest energy wavefunctions and their energies for a particle in an infinite well of width = 5 au. *Source:* prepared using Python 3.5: Python Software Foundation. Python Language Reference, version 2.7. Available at <http://www.python.org>.

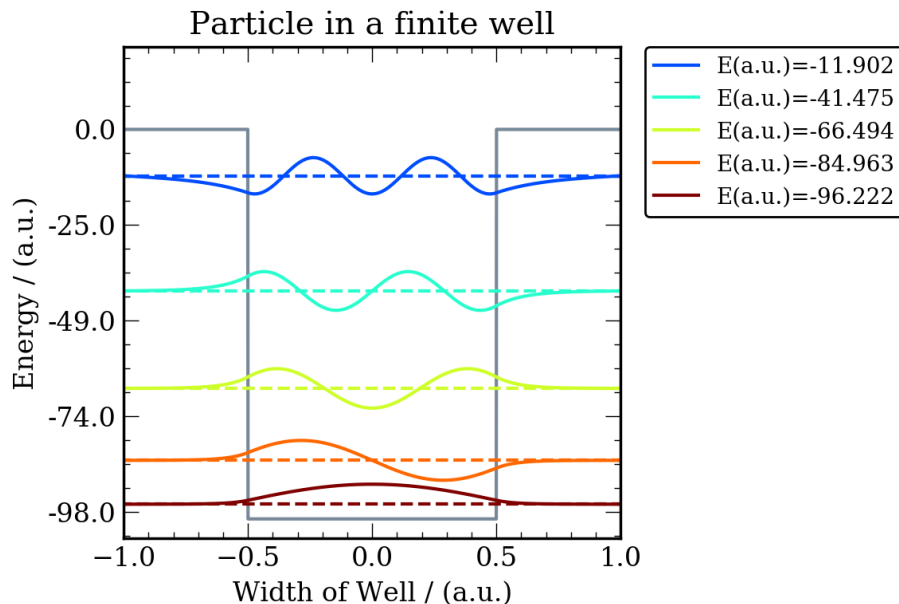


**Figure A3.2:** An example plot of the five lowest energy wavefunctions and their energies for a particle in a finite well of width = 1 au and depth = 100 au. *Source:* prepared using Python 3.5: Python Software Foundation. Python Language Reference, version 2.7. Available at <http://www.python.org>.

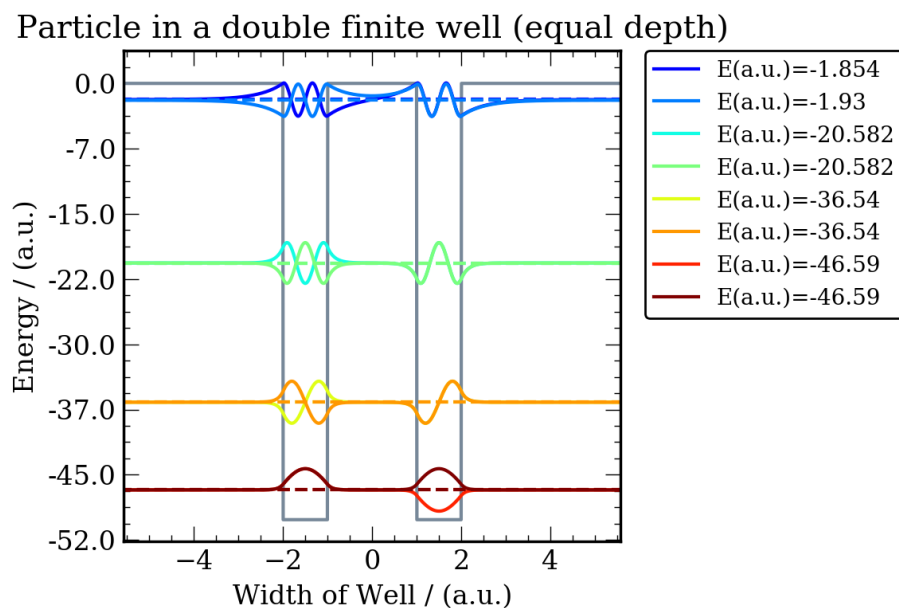


**Figure A3.3:** An example plot of the eight lowest energy wavefunctions and their energies for a particle in a double finite well (equal depth) with width = 1 au, depth = 50 au, and spacing between wells = 2 au. *Source:* prepared using Python 3.5: Python Software Foundation. Python Language Reference, version 2.7. Available at <http://www.python.org>.

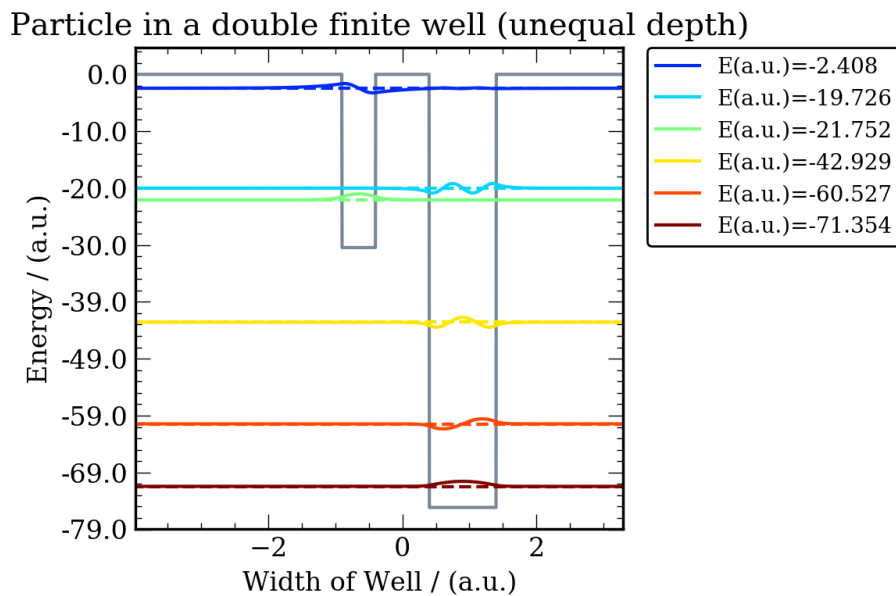


**Figure A3.4:** An example plot of the six lowest energy wavefunctions and their energies for a particle in a double finite well of unequal depth. The input parameters are: width 1 = 0.5 au, width 2 = 1.0 au, spacing between wells = 0.8 au, depth 1 = 30 au, and depth 2 = 75 au. *Source:* prepared using Python 3.5, <https://www.python.org/>.

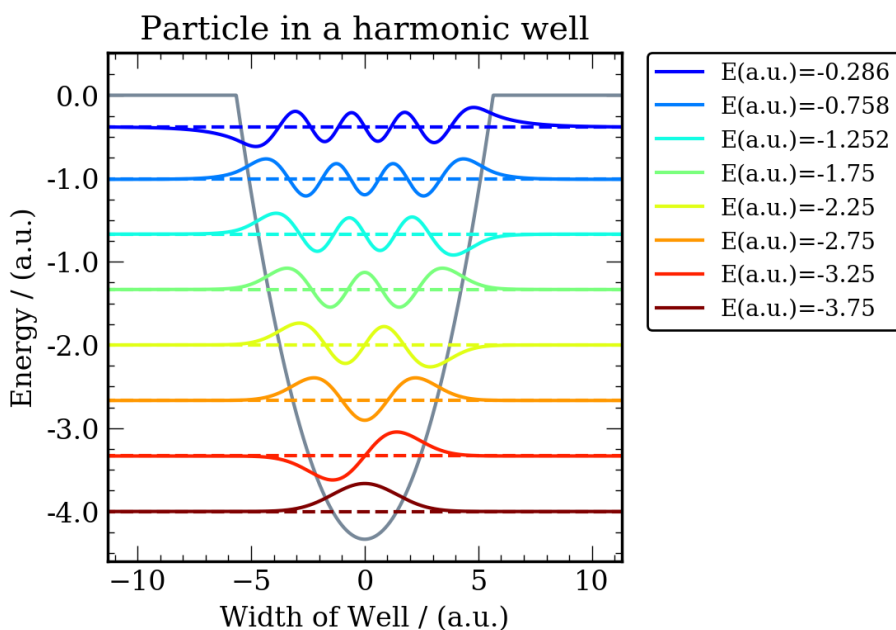


**Figure A3.5:** An example plot of the eight lowest energy wavefunctions and their energies for a particle in a harmonic well. The force constant = 0.5 and the depth of the well = 4 au. *Source:* prepared using Python 3.5: Python Software Foundation. Python Language Reference, version 2.7. Available at <http://www.python.org>.

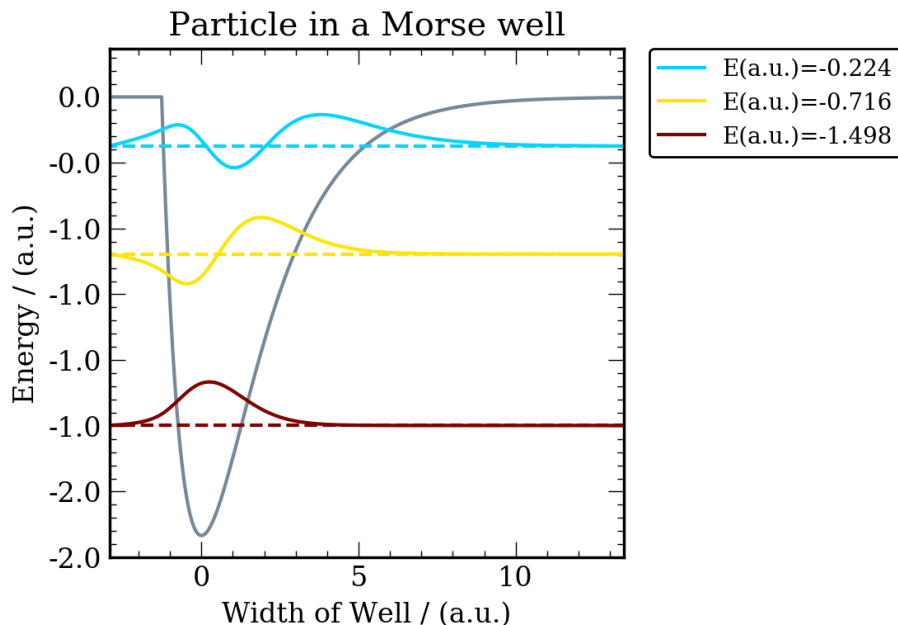


**Figure A3.6:** An example plot of the three lowest energy wavefunctions and their energies for a particle in a Morse potential energy well. The force constant = 0.3 and the depth of the well = 2 au. *Source:* prepared using Python 3.5, <https://www.python.org/>.

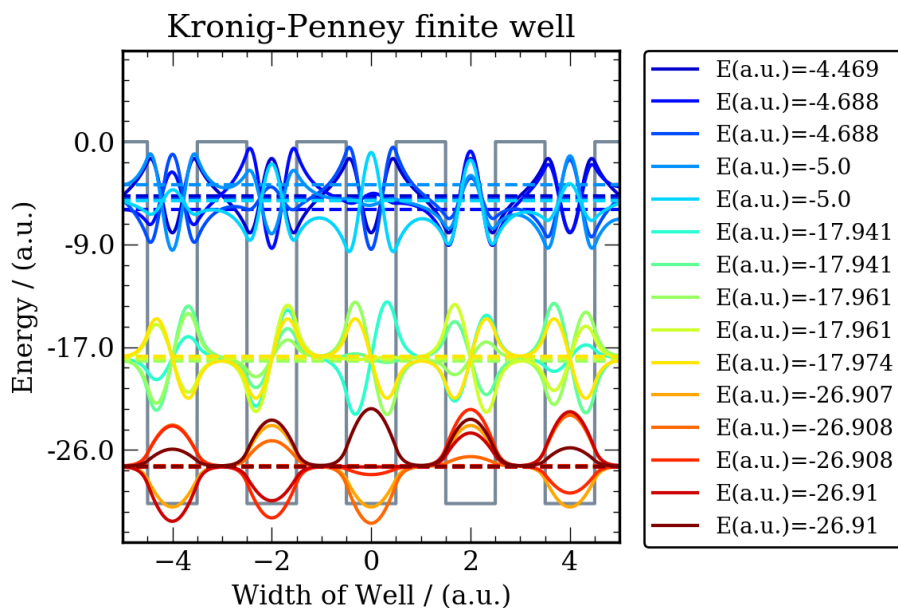


**Figure A3.7:** An example plot of the 15 lowest energy wavefunctions and their energies for a particle in a Kronig-Penney finite well. The width of the wells is = 1.0 au, the depth of the wells = 30 au, the spacing between the wells = 1.0 au, and  $n = 5$ . *Source:* prepared using Python 3.5: Python Software Foundation. Python Language Reference, version 2.7. Available at <http://www.python.org>.



## Appendix 4

### Schrödinger Program Pre-Assignment Survey

Please answer the following questions pertaining to the Schrödinger program assignment.

1. Do you have experience in computer programming / scripting?  
A. Yes B. No
2. Have you had a course in numerical methods / analysis?  
A. Yes B. No
3. Do you have experience using a computer to solve numerical problems in physics, biology or chemistry?  
A. Yes B. No
4. What is your level of computer skill?  
A. Poor B. Below average C. Average D. Above Average E. Strong
5. The energy levels of a 1-dimensional particle in a box decrease as the length of the box increases.  
A. True B. False
6. The spacing between wavefunctions increases with increasing energy for the 1-dimensional particle in a box.  
A. True B. False
7. The number of nodes in a 1-dimensional particle in a box is equal to (n-2).  
A. True B. False
8. For a particle in a finite potential energy well, the particle is permitted to exist outside of the well.  
A. True B. False
9. For a particle in a finite potential energywell, the amount of tunneling decreases for particles with higher energy.  
A. True B. False
10. The energy of a particle in an infinite potential energy well is  
$$\frac{n^2 h^2}{8mL}$$
  
A. True B. False

**Schrödinger Program Post-Assignment Survey**

Please answer the following questions pertaining to the Schrödinger program assignment.

1. Did you find it difficult to use the Schrödinger.py script for this assignment?  
A. Yes B. No
2. Do you feel that this assignment enriched your understanding of quantum mechanics?  
A. Yes B. No
3. Did you find the assignment easy to follow?  
A. Yes B. No
4. The energy levels of a 1-dimensional particle in a box decrease as the length of a well increases.  
A. True B. False
5. The spacing between wavefunctions increases with increasing energy for the 1-dimensional particle in a box.  
A. True B. False
6. The number of nodes in a 1-dimensional particle in a box is equal to (n-2).  
A. True B. False
7. For a particle in a finite potential energy well, the particle is permitted to exist outside of the well.  
A. True B. False
8. For a particle in a finite potential energy well, the amount of tunneling decreases for particles with higher energy.  
A. True B. False
9. The energy of a particle in an infinite potential energy well is

$$\frac{n^2 h^2}{8mL}$$

- A. True B. False